Evolution of surface hydrography in the Eastern Arabian Sea during the Late Quaternary:

Perspectives gained from sedimentary records of past Sea surface temperature and salinity

Thesis submitted to the Department of Marine Sciences, Goa University, Goa, India, for the degree of Doctor of Philosophy in Marine Sciences

By

Mahesh Badanal

Research Supervisor

Dr. Virupaxa K Banakar

January 2011

Dedicated

To My

Beloved Parents...

Appa

Amma

Contents   Page

Statement of the Candidate

As required under the university ordinance O.9.9 (ii), I hereby state that the present thesis entitled "Evolution of surface hydrography in the Eastern Arabian Sea during the Late Quaternary: Perspectives gained from the sedimentary records of past sea surface temperature and salinity", is my original contribution and the same has not been submitted on any previous occasion. To the best of my knowledge, the present study is the first comprehensive work of its kind from the area mentioned.

The literature related to the problem investigated has been cited. Due acknowledgements have been made wherever facilities and suggestions have been availed of.

January 25^{th,} 2011

Mahesh Badanal
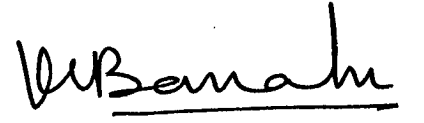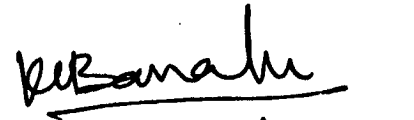
Certificate

As required under the university ordinance OB.9.9. (vi), I certify that the thesis entitled "Evolution of surface hydrography in the Eastern Arabian Sea during the Late Quaternary: Perspectives gained from the sedimentary records of past sea surface temperature and salinity", submitted by Mr. Mahesh Badanal for the award of the degree of Doctor of Philosophy in Marine Science, is based on original studies carried-out by him under my supervision. The thesis or any part of thereof has not been previously submitted for any other degree or diploma in any university or institution.

Dr. Virupaxa K Banakar

All the corrections suggested by the examiners are incorporated

12.12.2011

(V. K. Banakar)

Acknowledgements

Preface

Climate change refers to a statistically significant variation in either the mean state of the climate or in its variability, persisting for an extended period (typically decades or longer). It may be due to nature's internal processes or by external forcing, or by persistent anthropogenic intrusion in the otherwise considerably stable Earth System. Climate change is no more just an environmental concern, but is one of the key economic issues of the present Anthropocene Era. It has emerged as the most serious challenge the world faces at present, whose consequences go far beyond its effects on the environment.

The economics of south Asia is very much dependant on the Indian monsoon. The Indian monsoon, a major climatic system over south Asia caters to a population of more than one billion. Any change in this system would affect a majority of the population in a huge way. Hence, it is necessary to know how the monsoon varied in past and how it is going to be in future. However, to make any such predictions, a deep understanding of how the Indian monsoons have varied through the past geological time when the human effect was absent is very much essential. Understanding past climate helps us to explain how current environment evolved.

The studies have been carried out to decipher the subtleties of the Indian monsoon, which have revealed different perspectives time and again. Paleoclimatology also provides data, which we can use to model and predict both current and future climate change scenarios. Earth being such a complex system, it is a daunting task for scientists to make projections for future climate changes in turn monsoons and how it will affect the environment. The palaeoclimatic data is used as a standard background by climate scientists for providing crucial information on the anthropogenic effect on the modern climate.

The ability to predict future monsoons significantly depends on the reliability and accuracy of information derived from the past behavior of the monsoon systems under different conditions. When this natural change is subtracted from the cumulative change it is possible to quantify the impact of human activity on climate. As the monsoon system is a component of the Earth's climate system it may be possible to understand the response of monsoons to climate change. Hence, it is necessary to obtain

accurate information on changes in the surface hydrography of the Arabian Sea, which directly responds to the regional well-known monsoon system. The Arabian Sea sediment repository holds records of past monsoons in the form of changes in it's biological and chemical signatures. The sediment deposited in productive regions above the CCD contains abundant skeletons of microorganisms made up of calcite (coccoliths and foraminifera) and those deposited below CCD contain dominant siliceous skeletons of diatoms and radiolaria. These biogenic hard-parts of the organisms are secreted mostly in equilibrium with the surrounding seawater, hence they are expected to incorporate signatures of ambient physicochemical conditions prevailed during their life span. Thus the sea surface temperature and surface salinity signatures are effectively preserved in planktonic foraminiferal calcite skeletons in the form of variable $^{18}O/^{16}O$ ($\delta^{18}O$) and skeleton building element concentrations.

With a perspective to find out how the Indian monsoon has varied in the past and responded to global climate as a whole, I reconstructed a few index elements of the ocean surface (surface temperature and surface salinity), which respond directly to the monsoon variability in key area (Eastern Arabian Sea) of the northern Indian Ocean for the past ~100 kyr. To achieve this, I have utilized geochemical tools such as Oxygen Isotope ratios ($^{18}O/^{16}O$), Mg/Ca ratios, and radiocarbon (^{14}C) locked-in calcite skeletons of planktonic foraminifera preserved in sediment cores. It should be noted that, so far published palaeomonsoon studies were largely based on indirect proxies such as $\delta^{18}O$ variation or changes in abundance of upwelling sensitive foraminifera, organic matter preserved in sediment etc. The hydrographic changes based studies are very limited. Therefore, the present study is expected to contribute significantly to the regional palaeoclimatic knowledge. Although, precisely isolating the relative importance of past variability in summer and winter monsoon intensities is not viable from past sea surface climatology (hydrography), it is feasible to qualitatively understand their variations in light of modern analogue.

The Eastern Arabian Sea, a key region for monsoon studies, is a complex and dynamic water body that responds instantly to any changes in the modern Indian monsoon strength. Thus the surface climatology structure of this region is modulated by the Indian monsoons both in space and time.

There have been evidences for the modern Indian monsoon linkage with major climatic features such as the Inter Tropical Convergence, El Nino-Southern Oscillation, Indian Ocean Dipole, snow cover over the Tibetan Plateau, transfer of heat to the Indian sub continent through the Eurasian land mass and also with the northern high-latitude climate. Therefore, such linkages in the past also must have existed. Unscrambling such teleconnections on sub-glacial and interglacial time-scales utilizing novel proxies is important in terms of paleo-monsoon studies. I have used "sub" glacial-interglacial because the time-resolutions of paleo-reconstructions presented in my thesis are coarser than the high-frequency Dansgard-Oeschger variability, but adequately finer to resolve the subtle variations within the glacial-interglacial time-scales.

The thesis is presented in seven chapters and a brief outline of the layout of the thesis is given below.

Chapter 1 provides an introduction to palaeoclimate studies in reference to the Earth's early climatic history and the role of various geochemical proxies in understanding the past climate and monsoon variability. A detailed description of the study area is given in **Chapter 2,** which includes the bathymetry, tectonic features, air-sea interaction, upwelling and the biogeochemistry along with the vertical depth profiles of salinity and temperatures in the study region. The sample descriptions are given in **Chapter 3.** **Chapter 4** provides detailed description of the methodology and experimental work carried-out to extract the information on the proxies from sediment cores. The results are given in **Chapter 5,** which includes details of AMS ^{14}C dates and linear sedimentation rates obtained for radiocarbon dated sections of the four sediment cores, variation of oxygen-isotopes with depth in sediment cores, Quality Control results of Mg/Ca measurement, and measured Mg/Ca ratios in the planktonic calcite tests. The discussion of the results is presented in **Chapter 6.** The **Chapter 7** is dedicated for summary of the present study. The thesis contains twenty-two tables and thirty-seven figures inserted at appropriate places in the text to provide ready reference.

Abbreviations used in this thesis

(Only the abbreviations are used in subsequent sections)

AABW	Antarctica Bottom Water (Forms in the Southern Ocean)
AMS	Accelerator Mass Spectrometer (Instrument used in radiocarbon dating)
ASHSW	Arabian Sea High Salinity Water (Forms in northernmost Arabian Sea)
BoB	Bay of Bengal (Eastern arm of the northern Indian Ocean)
Ga	Billion Years (Unit of time in to the past equivalent to 10^9 years)
CDW	Circumpolar Deep Water (Combination of AABW and NADW)
CLIMAP	Climate Long-Range Investigation, Mapping and Prediction (Research project of the 1970s & 80s to produce a map of climatic conditions during the LGM)
C/N	Carbon /Nitrogen (ratios used to decipher provenance of organic matter)
DIC	Dissolved Inorganic Carbon (sum of inorganic carbon species in seawater)
D-O	Dansgaard-Oeschger (High-frequency climate fluctuations occurring at a frequency of ~1000 years recorded in GISP ice cores)
EAS	Eastern Arabian Sea (Study region in western Indian Margin)
EACC	East African Coastal Current (Circulation off East African Coast fed by SEC)
EC	Equatorial Current (A perennial west flowing circulation)
EICC	East Indian Coastal Current (Circulation off east coast of India)
EIO	Equatorial Indian Ocean (Indian Ocean between 10° N and 10° S)
EMC	East Madagascar Current (western boundary currents of the subtropical gyre in the southern Indian Ocean)
ENSO	El-Nino Southern Oscillation (A major climatic feature in Pacific Ocean)
E-P	Evaporation minus Precipitation (An indicator of salinity status of a region)
EPICA	European Project for Ice Coring in Antarctica (multinational European project for deep ice core drilling in Antarctica)
EPILOG	Environmental Processes of the Ice age: Land, Ocean and Glacier (An international project to assess state of the Earth's surface during the LGM)
EUC	Equatorial Under Current (subsurface current flowing eastward along the equator just a few meters below the equator: ~ 100 m depth in Indian Ocean)
ICP AES	Inductively Coupled Plasma Atomic Emission Spectroscopy (Instrument used to measure concentration of elements – Mg, Ca, Al, Mn and Fe in this study)
IOD	Indian Ocean Dipole (A climatic feature in the Indian Ocean)
ITF	Indonesian Through Flow (Circulation connecting Pacific and Indian Ocean at ~10°S latitude)
ITCZ	Inter Tropical Convergence Zone (Global tropical climatic feature)
JGOFS	Joint Global Ocean Flux Study (Core Project of the International Geosphere-Biosphere Programme)
kyr	kilo-years (Thousand years) (Unit of time)
LGM	Last Glacial Maximum (Immediately preceding Earth's coldest climatic state)
LH	Lakshadweep High (Feature evident in summer monsoon off Lakshadweep Island)
LL	Lakshadweep Low (Feature evident in winter monsoon off Lakshadweep Island)

Ma	Million years ago (Unit of time in to the past equivalent to 10^6 years before)
MARGO	Multiproxy Approach for the Reconstruction of the Glacial Ocean Surface (an international community effort of more than 50 scientists, who pursued the goal to reconstruct SST during the Last Glacial Maximum)
MAT	Modern Analogue Technique (quantifies faunal changes within deep-sea cores in terms of modern oceanographic conditions)
MIS	Marine Isotope Stage (Defines the climate events- Cold and Warm in oxygen isotope records)
NADW	North Atlantic Deep Water (Forms in the northern Atlantic Ocean)
NBS	National Bureau of Standards (Analytical Standards used in measurements)
NEC	North Equatorial Current (A significant current that flows east-to-west between 10° N and 20° N)
NEMC	North East Madagascar Current (Oceanic circulation off Madagascar which feeds the Agulhas current)
NIDW	North Indian Deep Water (Forms from combination of RSW, PGW and ASHSW)
ORV	Ocean Research Vessel (Ship used in oceanic research)
PCC	Poleward Coastal Current (northward circulation advecting low saline BoB water into the EAS)
PDB	Pee Dee Belemnite (Global reference standard for normalizing oxygen and carbon-isotopes prepared from fossil *Belemnitella Americana* carbonate deposit of Pee Dee Formation in South Carolina)
PGW	Persian Gulf Water (Persian Gulf origin found in AS at 200-300 m depth)
PMIP	Paleoclimate Modeling Intercomparison Project
psu	practical salinity unit (Unit of salinity)
QC	Quality Control (a process employed to ensure quality of analyzed results)
RSW	Red Sea Water (Red Sea origin found at 300-800 m depth in AS)
SC	Somali Current (Circulation off Somali coast)
SECC	South Equatorial Counter Current (Ocean current in the Indian Ocean that flows west-to-east at approximately five degrees north)
SEC	South Equatorial Current (Ocean current in the Indian Ocean that flows east-to-west between the equator at about 20° S)
SG	Somali Gyre (Rotating ocean current off Somali)
SK	Sagar Kanya (An Indian Ocean Research Vessel)
SMC	Summer Monsoon Current (Flow towards equator and BoB)
SPECMAP	Spectral Mapping and Climate Modeling of the Past (A composite stacked oxygen isotopes reference curve derived from planktonic foraminifera, which was smoothed, filtered and tuned to the known cycles of astronomical variables)
SST	Sea Surface Temperature (Surface water temperature)
Sv	Sverdrup (Amount of water transferred i.e., 10^6 cubic meters per second)
TFN	Total Foraminiferal Number (Total number of foraminifera in 1 gm of sediment)
WMC	Winter Monsoon Current (Flow towards AS from BoB)
WICC	West Indian Coastal Current (Coastal current which flows northward during November-February and southward during April-September)

List of Tables

List of Figures

CHAPTER 1

INTRODUCTION

1.1. Paleoclimate

Climate is the result of interaction between atmospheric and oceanic systems of the rotating Earth around the Sun, which strictly follow the laws of physics. These two fluids (air and water) flow and interact within a geographic setting determined primarily by the arrangements of land and sea, the orientation of mountains and lowlands on continents, the depths of oceans, and the location of ocean gateways. Paleoclimatology is the study of variability of this climate system throughout the evolutionary history of the Earth. The basis for paleoclimate is to have a thorough understanding of present climatic conditions based on which the variations in the past climate that are well beyond the instrumental records could be deduced (see Bradley and Eddy, 1991 and references therein). The ultimate aim of paleoclimate is to understand the physicochemical and biogeochemical processes, which were instrumental in variation of climate over the time and also to minimize the uncertainties associated in predicting the likely climate in the future. Numerous paleo-records are used to provide understanding of the patterns, ranges and causes of natural climatic variability, including how such variability is affected by alteration in biogeochemical forcing of oceans and physical forcing of atmosphere. Paleoclimatology also provides a framework for testing how much effective are the predictive models to simulate the response of climate system components to altered forcing. In addition, the paleoclimate records provide baseline information that is long enough to unambiguously separate anthropogenic environmental change superimposed over the natural background.

The Earth's climate system is extremely complicated and depends on the interplay of many factors ranging from events occurring in the Sun to microscopic organisms that inhabit the oceans. The climate system consists of external components such as changes in insolation received by Earth's surface due to changes in its orbital geometry and internal components such as atmosphere, hydrosphere, biosphere, cryosphere and lithosphere. Various components of these entities such as albedo, extent of snow cover, heat capacity of land and oceans, landmass distribution, hydrological regimes and biomass etc play definite role in dictating the climate system on variable time-scales. The famous dictum by James Hutton - *"Present is key to the Past"* is the

2

thumb-rule for paleoclimate reconstructions. It is assumed that the causes for past and present climate variability are of the same kind, have the same energy, and produce the same effects (Bradley and Eddy, 1991). The 4.6 billion years old (Ga) Earth has undergone innumerable changes from the Hadean Eon (4.5 - 3.8 Ga) to the present Holocene. The entire surface of the Earth was covered by ice (termed as Snowball Earth) at ~700 million years (Ma) (Harland, 1964). This 'Snowball Ice Age' condition is believed to have terminated at ~635 Ma due to rapid warming caused by destabilization of huge amounts of methane-hydrates of the permafrost paleo-equatorial regions (Kennedy, 2008). Thus, there are evidences for long 'glacial' conditions in distant past history of the Earth.

The hydrosphere, atmosphere, biosphere, lithosphere and cryosphere have been interacting through geological past in a tightly coupled manner, but with random variations to attain a regular pattern, e.g., establishment of rhythmic alternating warm and cold events in the beginning of Pleistocene. The Pleistocene characterizing initiation of the classic Ice-Age rhythm is now shown to have begun at 2.6 Ma, instead of previously thought 1.8 Ma, thus shifting the age of the beginning of Pleistocene backward by 0.8 Ma i.e., in to the upper part of the Pliocene (Mascarelli, 2009). The oceans covering majority of Earth's surface have played a pivotal role in past climate variability. As compared to the continental landmass and atmosphere, the oceans store vast amount of heat energy (latent heat) in the tropics. This stored heat energy is transferred to high latitudes through thermohaline circulation, which is considered to be the primary mechanism that regulates and drives the global climate. Temperature is the primary representative state of the climate system. Further, the temperature of oceans is critical because oceans are the single most important component of the Earth, which have ability to store, release and redistribute the heat. Majority of the heat content of oceans is stored in upper few meters (~100 m) of the water column and the interaction of this water column with troposphere results in the exchange of heat between oceans and atmosphere.

The dynamic interactions of the hydrosphere-lithosphere-biosphere-atmosphere-cryosphere coupled processes are very important feedback mechanisms operating in

3

global climate system. The insolation associated with orbital parameters acts as the primary fuel for climate variability and associated feedbacks. The conditions which govern the climate today have not been the same in past and are unlikely to remain same in the future. Our ability to predict future climatic changes rests in how well we understood the past variations of the Earth's climate and factors that were influencing the changes. Hence, in order to understand the future climate within natural framework, it is very much necessary to know the past dynamics of climatic system and also to have good understanding of those factors, which induced changes. The climate over the entire Earth's history has been varying on different time-scales (millennial, centennial and decadal). A wide variety of archives, both natural and documented records are available to unravel past climate patterns on geological and historical time-scales respectively. The natural records could extend well beyond Ma, while the documented records are very recent (covering the past ~150 years). However, the proxy signatures preserved in natural material provide large range of information to understand past climate changes.

Advancement in dating techniques significantly assisted the researchers to unlock geological history of the climate with considerable accuracy. The sources of paleoclimate proxies are many. They include glaciological (ice cores), geological (marine sediment cores) and biological (tree rings, pollens, plant macrofossils, corals) etc. Most reliable and abundant proxy records have been obtained from ice cores obtained from polar ice caps, continental glaciers and oceanic sediments. The temporal record of several paleoclimate proxies such as grain size, organic molecules, isotopes of oxygen, carbon, and nitrogen, biological productivity, elemental ratios, faunal transfer functions etc can be obtained from marine sediment cores. Each one of these has specific application to understand particular processes in the oceans, which produce distinct response to climate forcing. It is much easier to document the evidence of climate variability and past climate change than to determine it's underlying mechanisms because, the climate is influenced simultaneously by multiple factors, which operate at altogether different time-scales.

1.2. Earth's climatic history

Geologically, the Earth's history is divided into series of eons, eras and periods based on evolutionary changes in flora and fauna. The Hadean is the earliest era while the Cenozoic is the recent era. The latter is further subdivided into Tertiary and Quaternary periods. Cenozoic encompasses the last ~65 Ma with Tertiary forming the major period and the Quaternary covering the last 2.6 Ma. The Quaternary is further subdivided into two epochs: a) Pleistocene, meaning 'most recent' (2.6 Ma to the last 10 ka) and b) the Holocene, meaning 'wholly recent' (10 ka to Present). Further, Crutzen and Stoermer (2000) coined the term Anthropocene (18th century onwards) in which the Earth's climate is being mostly influenced by anthropogenic activity (Zalaseiwicz *et al.*, 2008). Though the Earth had entered the Anthropocene era 6-8 kyr ago with the beginning of human settlements and community living (Crowley, 2003), the visible effect has become more prominent only since the 18th century, i.e., following the industrial revolution.

The Earth's first atmosphere was established during the Precambrian. This primordial atmosphere mostly contained water vapor (80%), carbon dioxide (10%), hydrogen sulfide (7%) and smaller amounts of nitrogen, carbon monoxide, hydrogen, methane and inert gases (Walker *et al.*, 1977). The primordial oceans started to form due to cooling of Earth's surface resulting in first precipitation of vapour. The secondary atmosphere evolved around 3.8 Ga comprised of nitrogen as the primary constituent. The late Archaean Era (3.8 - 2.5 Ga) witnessed the evolution of oxygen from the photosynthetic algae. The geological records showed a relatively warm climate in Archaean, but for a cold glacial phase around 2.4 Ga (Walker *et al.*, 1977). During this period, the continents also stabilized followed by the development of red beds (strata of reddish-colored sedimentary rocks such as sandstone, siltstone or shale that were deposited under warm and oxidizing conditions). The end of banded-iron-formation episode during the Phanerozoic marks a shift from reducing atmosphere to an oxidizing atmosphere during which oxygen-breathing metazoan life forms began to appear (Holland, 1994; Farquhar *et al.*, 2000; Dobson and Brodholt, 2005).

The first three quarters of Earth's history are marked with only one major glaciation, just before the appearance of Ediacaran ~635 Ma. The Earth's climate has varied from large-scale extensive ice cover over the Earth's surface (coldest climate) to ice cover limited only to Polar Regions (warmest climate). The time-scale for this variation is rather large (of the order of ~100 Ma), which depended on the Earth's rotation around the sun. The Precambrian period has witnessed a major glaciation event wherein most of the Earth's surface was covered by snow/ice giving rise to popularly known "Snowball Earth" (Harland, 1964; Kirschvink, 1992; Walker, 2003). Earth's atmosphere warmed up during the Late Proterozoic Eon and by the dawn of Cambrian life forms became abundant with the "Cambrian Explosion", where the global average temperatures rose to ~22°C (Whittington, 1979). Variation in the Sun, volcanic ash and exhalations, relative movements of Earth towards the Sun, tectonically induced effects, water sheds and orbital oscillations are the major drivers for climate change in the earliest history of our planet. Ice ages on Earth are first documented about 2.3 Ga, followed by an immensely long interval of warm climate for about 1.3 Ga. Several glaciations occurred since the Late Precambrian through Late Permian. Continental ice sheets then disappeared and only began to wax again about 25 Ma. Continental glaciers have thus appeared and disappeared on the Earth through geological time (Hambrey and Harland, 1981).

An estimated ~10°C was found to be the difference in global mean temperatures between a fully glacial Earth and the ice-free Earth, wherein, the difference was large at high latitudes and small at low latitudes (Frakes, 1979; Lang et al., 1999). The Quaternary, which includes the present day climate, is the most important period with most extraordinary changes in climate that took place over the globe and incidentally was also the start of the hominid evolution. Starting from the late Neogene, the global climate began to cool down in a "see-saw" pattern from colder climate to warmer conditions along with waxing and waning of the continental ice sheets and the polar ice caps (Tripati et al., 2005). The cold periods were long lasting (many tens of thousands of years) and slow paced termed as the "glacial periods". During the glacial periods, there was high accumulation of ice over the continents where polar ice caps expanded

and mountain snow line moved down ultimately resulting in nearly 30% of the Earth's surface covered under ice as compared to modern ice cover of ~10% (Figure 1).
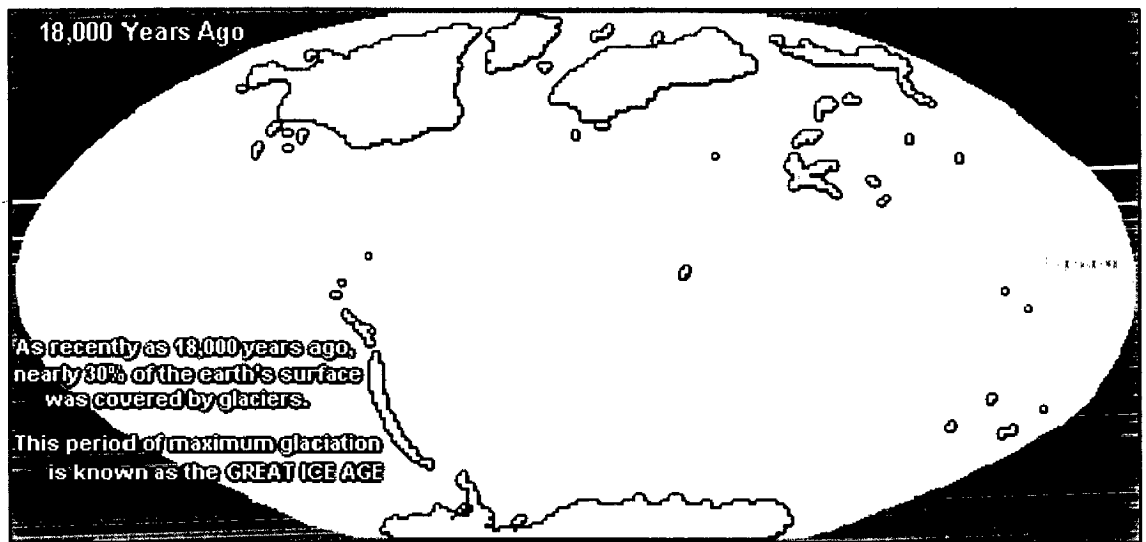
Figure 1. Ice cover (white patches) during the last glacial maximum (~18 kyr ago). Note the entire Canadian Shield covered by the glacial ice popularly known as Laurentide Ice Sheet. (Figure Source: http://home.comcast.net).

These glacial episodes have terminated rapidly to lead in to relatively shorter warm events called the "interglacials". It has been observed that the cold glacials progress gradually but their termination into warm interglacial conditions occur in one big rapid step (Imbrie and Imbrie, 1979). In some parts of the globe, the variation between the glacial and interglacial atmospheric temperature has been as high as 15°C. Through the last two millions years, the long glacial episodes (~100 ka) are followed by rapid deglaciation culminating in the interglacial stages. As many as ten glacial/interglacial cycles have been found in the last 800,000 years, while as many as fifty glacial/interglacial cycles have been recognized in the entire Quaternary (Shackleton et al., 1990). The climatic changes induced by these variations have been very significant. The waxing and waning of the continental glaciers and also the mountain glaciers produced an enormous change in the landforms and vegetation resulting in varied weathering rates and pedogenic processes, varying temperature and precipitation rates, changes in river courses etc. Compared to the modern sea level, the sea levels during glacial maximums have fallen by ~120 m (due to buildup of

7

continental ice sheets) affecting the whole flora and fauna related to it and rose by more than ~6 m during the warmest parts of the interglacials again affecting the entire Earth System.

The signatures of the climate changes that have occurred during Quaternary have been well preserved in marine sediments. These changes can be reconstructed using various proxies, which form the basis for understanding climatic changes over the globe through geological time. Venetz (1821) first recognized the occurrence of a cold period before the present time. Later, Agassiz (1842) hypothesized the reason for those glacial climates. In the following years, it was verified that there were several glacial/interglacial periods that spanned the Late Quaternary. This period in the geological time has recorded maximum number of glacial/interglacial variations in regular pattern as compared to any of the other periods in past. The ice age is primarily governed by the insolation changes depending upon the eccentricity of Earth's orbit around the Sun followed by obliquity and precession of it's rotation axis (Milankovitch Cycles). These orbital parameters dictate the extent of snow cover. Scottish geologist James Croll (1867) proposed that recurring variations in orbital eccentricity (the deviation of Earth's orbit from a perfectly circular path) were responsible for alternating glacial and interglacial periods. In early 20th century the Serbian mathematician and astronomer Milutin Milankovitch refined the Croll's hypothesis, which became the foundation of paleoclimatology. Milankovitch (1941) not only confirmed the Croll's hypothesis but also mathematically elucidated the orbital parameters responsible for climate variability. The three orbital parameters, which are primary components to force changes in global climate, are: a) eccentricity (~100 kyr cycle), b) obliquity (~41 kyr cycle) and c) precession (~21 kyr cycle). These phases line up together to impinge on Earth's surface resulting in either maximum or minimum net insolation, in particular to northern hemisphere during summer. Such changes in resultant insolation (fundamental energy) control the melting or build-up of continental ice sheets leading to warming or cooling of the Earth's climate. The accumulation rate of ice in winter will be more than the melting rate in the summer, i.e., when the summers are colder (summers which occur during aphelion), the snow accumulated during the previous winter doesn't melt

completely. Hence, in the forthcoming winter more snow is added leading to extensive build up of ice. When this process continues for many thousands of years, ice sheets begin to extend towards the mid-latitudes. The glacial ages have been observed to coincide with the phases when orbital eccentricity, axis of tilt and the precession of the equinoxes were all superimposed in such way to produce lowest insolation over the northern hemisphere. The increased albedo due to expanded ice surface produced a positive feedback that helped further cooling and sustain the cold climate for longer time resulting in vast expansion and build-up of ice sheets causing intense cooling in northern hemisphere (Manabe and Broccoli, 1985; Wilson, Drury and Chapman, 2000 for more detailed description of glacial-interglacial climate cycles).

1.3. Role of oxygen isotopes in paleoclimate studies

The oxygen isotopes have provided basis for basic understanding of past climate. The oxygen isotopic ratio has been used extensively as a powerful tool for not only deriving the relative chronology for the sediment column but also to extract important clues of climate variability. Urey (1947) first recognized potential of these isotopes. Later, McCrea (1950), Epstein (1953), Emiliani (1954), and Shackleton (1974) developed this method and made it an integral part of the paleoclimate study. The changes in $^{18}O/^{16}O$ ratios of the seawater reflect loss or gain of water from or to oceanic reservoir respectively. The loss of water would occur when the climate is cold wherein most of the water evaporated from the oceanic reservoir gets locked in to the ice at high-latitude and high-altitude glaciers and polar ice caps (during glacials). The gain of water would be due to melting of such ice during warm episodes (interglacials). This climate forced dynamics of ocean reservoir has led to the rise or fall in sea level relative to modern level. This climate driven changes in the volume of ocean water can be tracked by using the fundamental property of isotope fractionation during transformation of matter in to different states.

According to Rayleigh's isotopic fractionation, the lighter isotopes preferentially stay in vapor state while the heavier isotope preferentially precipitate or stays in liquid state. This thumb-rule dictates the $^{18}O/^{16}O$ ratio expressed as $\delta^{18}O$ of the global oceans. During long-term loss of water from oceans in cold glacial periods, the oceanic reservoir

enriched with ^{18}O, while reverse happened during warm interglacial due to return of the lost water back to the oceans by melting of ice-sheets. It is estimated that nearly 3% of the oceanic water was locked-up as ice during the glacial maximum resulting in ~120 m drop in eustatic sea level leading to global ocean $\delta^{18}O$ increase of ~1.2‰ (Shackleton, 2000). In other words, every 10 m fall in global sea level would cause $\delta^{18}O$ enrichment in the global oceans by 0.1‰.

This $\delta^{18}O$ can be measured (e.g., in calcareous foraminifera) with precision using isotope ratio mass spectrometer. The study is quite robust when applied to samples which are well above the foraminiferal lysocline. The fractionation between ^{18}O and ^{16}O is predominantly thermodynamically mediated with minor contribution from CO_3 ion concentration and vital effects and hence can be used as paleotemperature proxy after deducting the global ice volume effect and changes in evaporation and precipitation (E-P) i.e., local salinity variations. Epstein *et al.* (1953) first proposed a "paleotemperature equation" based on $\delta^{18}O$ of calcite precipitated by mollusks in both controlled experiments and field samples. Their analysis yielded a sensitivity of ~0.2‰ change in the $\delta^{18}O$ / °C change in the calcification temperature. The variation in $^{18}O/^{16}O$ ratio of seawater is mostly linear to that of salinity. Hence, salinity can be calculated from $\delta^{18}O$ of seawater (Schmidt, 2004). These various possibilities of obtaining indirect quantifiable information about oceanic environment from the oxygen isotopes have revolutionized the paleoclimate study.

Emiliani (1955) further made a systematic examination of the marine oxygen isotope records, which were generated from planktonic foraminifera of the Caribbean Sea sediment cores. The glacial-interglacial cycles observed down-core showed a cyclic pattern of low and high $\delta^{18}O_{FORAMINIFERA}$ values for the last 525,000 years. The temperature changes and difference in $\delta^{18}O$ values were in the order of 5 - 10°C and 1.5 - 2.0‰ respectively for the glacial to interglacial shifts. Further, the negative shifts were designated as warm stages (interglacials: "odd" numbered) and positive shifts as cold stages (glacials: "even" numbered), which are well known as Marine Isotope Stages (MIS1, MIS2, MIS3...etc back in the past). The MIS1 refers to present interglacial interval (Holocene) that we are living in; MIS2 refers to the immediate preceding glacial

period and the MIS5e represents the last interglacial which has experienced more or less similar conditions as that of the Holocene. Prell *et al.* (1986) added "events" of isotopic extremes within the glacials and interglacial periods to establish finer divisions. For example, events in MIS1 were designated as 1a, 1b, 1c and so on. These were further revised as 1.1, 1.2, 1.3 etc. The 'odd' numbers in the series (e.g., 1.1, 1.3, 1.5 etc) represent warm interstadials and the 'even' numbers (e.g., 1.2, 1.4, 1.6 etc) represent cold stadial events within the main glacial or interglacial stages (Imbrie *et al.*, 1984). Using the past variations in the insolation as basis for numerical time-scale, further refinements to the marine oxygen isotope stratigraphy were made (Imbrie *et al.*, 1984; Martinson *et al.*, 1987). The SPECMAP $\delta^{18}O$ record (Figure 2) generated by stacking planktonic foraminifera $\delta^{18}O$ records for several long deep-sea cores from all over the world oceans and tuning it to the insolation cycle has become the standard reference curve for deriving chronology for sediment cores. This SPECMAP based chronology however has poor precision (~5000 years) (Imbrie *et al.*, 1984), hence suitable mostly as relative dating rather than absolute chronology required for high resolution studies of the Late Quaternary. This limitation is overcome by the advent of radiocarbon dating (^{14}C), which now stands valid for dating up to MIS4.

On the other hand, the climate records from the Greenland Ice-Cores revealed much more complex variability characterized by rapid fluctuations within few decades (Dansgaard *et al.*, 1993). As many as 24 warm interstadials within the last glacial cycle (115 - 15 kyr BP) were identified and named as D-O oscillations. These D-O oscillations are the dominant type of climatic changes scaling over millennia for ~1500 years (Bond and Lotti, 1995; Bond *et al.*, 1997; Grootes and Stuiver, 1997; Mayewski *et al.*, 1997), which have been most prominent in the Northern high-latitude oceans but have been expressed faintly in Antarctic ice-cores (EPICA Members, 2006).

Ice Volume
Planktonic Foraminifera O^{18} as Proxy
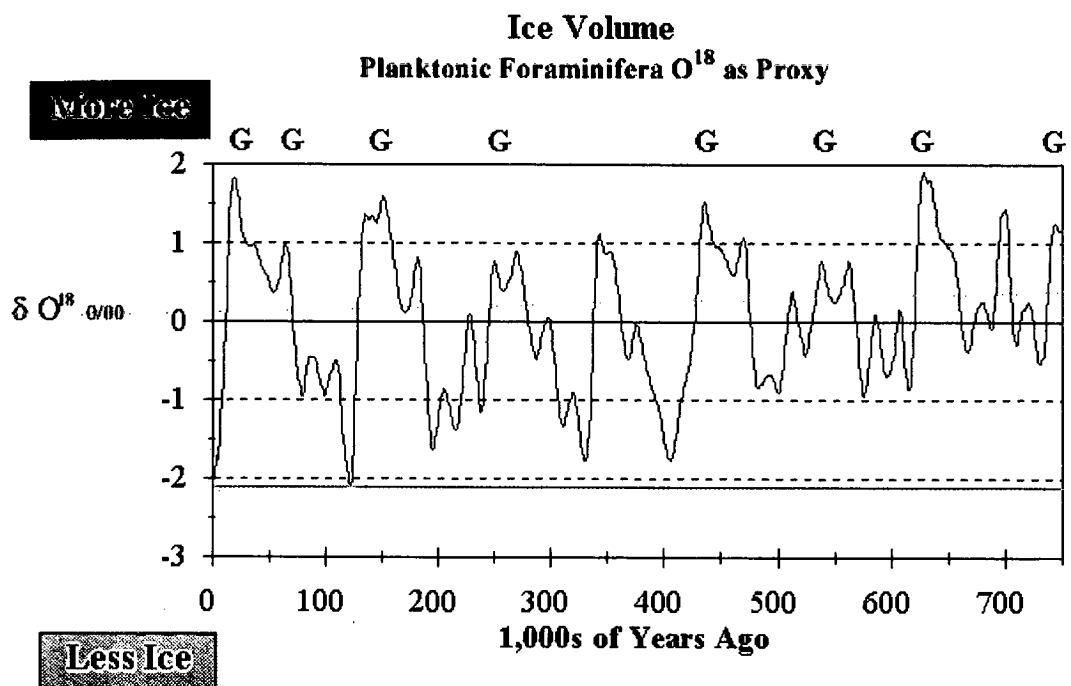
Figure 2. SPECMAP derived from stacking the oxygen isotope variation in planktonic foraminifera from global oceans. This curve has become the reference curve for demarcating glacial-interglacial boundaries identified in marine sediment cores. 'G' - denotes Glacial Period. The original curve was derived by Emiliani (1955). (Figure Source: www.museum.state.il.us).

1.4.   Indian Monsoons

The Indian monsoon forms a significant component of global climate system due to its vast expanse of ocean-atmospheric coverage (more than half of the tropics and near a quarter of the global surface area). The geographical setting of monsoon over the Indian sub-continent plays a vital role in the lifeline of over a billion people directly. The Indian monsoon is also notable for its amazing recurrence during summer and winter seasons every year. These monsoons are driven by seasonal reversal of winds. It is a dynamic land-ocean-atmosphere phenomenon prevailing in the Northern Indian Ocean, also having remote connections with ENSO system of tropical Pacific. The origin of Indian monsoons could be traced back to middle Miocene (i.e., since the rise of Himalaya to half its present height required to establish pressure gradient between land and ocean to initiate monsoon circulation: Valdiya, 1993, 1998). During the Late Miocene (11 to 7.5 Ma), the Himalayas became high enough to disrupt west-to-east flow of winds and push low-pressure area over the northern India, which attracted moist

12

summer winds from the Indian Ocean. The Indian monsoon system is punctuated by seasonal reversal of winds called the summer monsoon (southwesterly winds) and the winter monsoon (northeasterly winds) (Slingo, 2002). It is also influenced by the northern high-latitude climate or by the transfer of heat from Eurasian landmass to the Indian sub-continent (Goes et al., 2005). The Indian monsoons are driven by the differential heating of the land and ocean (land-sea thermal contrast) between the Eurasian landmass and the Southern Indian Ocean (Webster et al., 1998) and tropospheric latent heat (Clemens et al., 1991). However, recent work also suggests that the Indian monsoon is an integral part of the ITCZ and the manifestation of the seasonal migration of the ITCZ (Chao and Chen, 2001; Gadgil, 2003). As the Indian monsoons have links with other major climatic features such as ITCZ, ENSO (Krishna Kumar et al., 1999), Indian Ocean Dipole (Saji et al., 1999), snow cover over the Tibetan Plateau (Kutzbach et al., 1993), transfer of heat to the Indian sub continent through the Eurasian land mass (Goes et al., 2005) etc., predicting the modern monsoon has been tough and challenging task for meteorologists. However, long-term monsoon variability on geological time-scale has shown some systematic rhythm in accordance with climate variability pattern. It has been shown that during warm interglacials the summer monsoons were stronger and weakened during cold glacials (see Duplessy, 1982; Anderson and Prell, 1993; Rostek et al., 1993; Reichart et al., 1998; Banakar et al., 2005; Chodankar et al., 2005; and references therein). Further, the Indian monsoons have distinctly fluctuated during the late Holocene as evident from sediments of local freshwater reservoirs (Shankar et al., 2006; Warrier and Shankar, 2009).

The past monsoon variations can be reconstructed from various proxies that are preserved in marine sediments. The monsoon wind system closely regulates the surface circulation and hydrography in the northern Indian Ocean, which is depicted by changes in the evaporation and precipitation (E-P). The sea surface salinity (henceforth 'salinity') directly responds to changes in the freshwater flux or E-P balance in the basin. Hence, by reconstructing the time-series salinity variation, past monsoon intensity variation can be understood. Understanding of monsoon trends in the geological past depends on reliability of information that could be retrieved from sedimentary proxies.

13

1.5. Oceanography and climate of the study area

The Indian Ocean with a surface area of 74,110,000 sq km occupies about 20% of the world ocean surface area. It is the youngest and tectonically more complex among the three major oceans (Tomczak and Godfrey, 1994) with about $3.5 \times 10^6 \, km^3$ of water (Groves and Hunt, 1980). It is roughly triangular in shape, which is circumscribed by the Indian sub-continent in the north, Africa and Atlantic Ocean in the west, Indo-China, the Sunda Islands, Australia and the Pacific Ocean in the east and Southern Ocean in the South. Indian Ocean differs from Atlantic and Pacific oceans in several aspects. It is the only ocean which is not connected to the north polar ocean and hence unique in its geographical setting. Towards the north of the Indian Ocean is the large Asian landmass providing a continental barrier at all depths preventing a connection to northern polar seas, thus rendering this ocean as most vibrant region with respect to global-climate. The Indian Ocean has no deep-water formation cells like north Atlantic or Antarctic Margin. The major rivers debouching into Indian Ocean are Brahmaputra, Ganges, Indus, Irrawaddy, Zambezi, Jubba etc. The Indian Ocean receives ~4532 billion cubic meters of freshwater through river discharge annually (Dai and Trenberth, 2003). The Arabian Sea in the west, and Bay of Bengal (BoB) in the east form two distinct basins of the northern Indian Ocean. The hydrography of these basins changes seasonally owing to seasonal reversing of the monsoon winds (Wyrtki, 1971). Arabian Sea is one of the most productive regions of the world due to upwelling of nutrient rich thermocline waters driven by strong summer monsoon winds (Currie, 1963; Schott, 1983; Currie, 1992) and intense deep mixing during winter (Madhupratap et al., 1996).

1.6. Water masses in the northern Indian Ocean

The water masses in the northern Indian Ocean bear characteristic signature of the ocean surface of a particular area where they are originated and transported by circulation either horizontally or to deeper levels all over the world oceans. Each layer has different temperature and salinity combinations that form discrete water masses of different densities with lighter water overlaying denser water. The density difference is the primary driving force responsible for deep water circulations. In the Indian Ocean, the deep waters are mainly of north Atlantic origin, while the bottom waters are

14

exclusively of Antarctic origin. The circulation of deepwater is slow and can be inferred from their distribution of properties (2°C and 34.8 psu) similar to that in the Pacific Ocean depths (Millero, 1996). A hydrochemical front near 10°S across the tropical Indian Ocean chemically separates Northern Indian Ocean waters from Subantarctic waters at intermediate depths (Wyrtki, 1971).

Properties of the Indian Ocean water masses are influenced by indirect and direct input from remote regions such as Mediterranean Seas, Persian Gulf, Red Sea and Indonesian Through Flow. Rochford (1964) first documented three distinct high salinity water masses in the Northern Indian Ocean: a) Northern Arabian Sea High Salinity Water (ASHSW), b) Persian Gulf Water (PGW) and c) the Red Sea Water (RSW). The high salinity RSW spreads in the Arabian Sea between 300-800 m with a temperature of 13-14°C and salinity of ~36.5 psu. The PGW has lower density than RSW (due to its higher temperature) and hence stays above the main thermocline than penetrating it. Hence, the PGW can be found at a depth of 200-300 m overlying highest salinity RSW (Tomczak and Godfrey, 1994). The Arabian Sea High Salinity Water (ASHSW) spreads south between 60 and 100 m depth in the Arabian Sea and becomes indistinguishable further south across the equator. The mixture of ASHSW, PGW and RSW, which flow southwards, is collectively called as North Indian Deep Water. The Circumpolar Deep Water (CDW), which is a mixture of NADW and deepwater forming at Antarctic margin, fills most of the northern Indian Ocean depths below ~2000 m.

1.7. Surface circulation in northern Indian Ocean

The surface circulation south of 10°N resembles the general pattern similar to that of the Pacific and the Atlantic Oceans. However, towards the North of 10°N it is modulated by seasonal reversing monsoon winds, which differs markedly from that in the Atlantic and Pacific Oceans for the same latitudes. Shankar *et al.* (2002) have published an excellent synthesis of the surface circulation in this region (see Figure 3). In the Eastern Indian Ocean (EIO), the eastward flowing South Equatorial Counter Current (SECC) exists between the westward flowing North Equatorial Current (NEC) and the South Equatorial Current (SEC). The NEC, SEC and SECC exist throughout the year along the equatorial Indian Ocean. During the intermonsoon times (April-May and

15

October-November), an intense eastward flowing current called Equatorial Jet (Wyrtki, 1973) appear around the equator. These characteristic circulations in general dictate the salt balance between Arabian Sea and BoB.

The surface circulation in the Arabian Sea also undergoes reversal owing to the reversing monsoon winds (Figure 3). The Summer Monsoon Current (SMC) flows eastward during the summer (May-September) and the Winter Monsoon Current (WMC) flows westward during the winter (November-February). These monsoon currents extend from the Somali coast to the eastern BoB. The major surface currents are evident normally up to ~50 m depth largely defining the mixed layer. However, the effect of surface circulations may sometime penetrate even up to 100 m when the turbulent wind mixing is intense during peak summer monsoons. These local circulations exist as trans-basin flows (Shankar *et al.*, 2002). During these trans-basin flows, the salinity over the Northern Indian Ocean is adjusted between the Arabian Sea and BoB. In other words, the high-salinity Arabian Sea water enters the BoB during summer monsoons, while the low-salinity BoB water is advected into the Arabian Sea during winter monsoons.
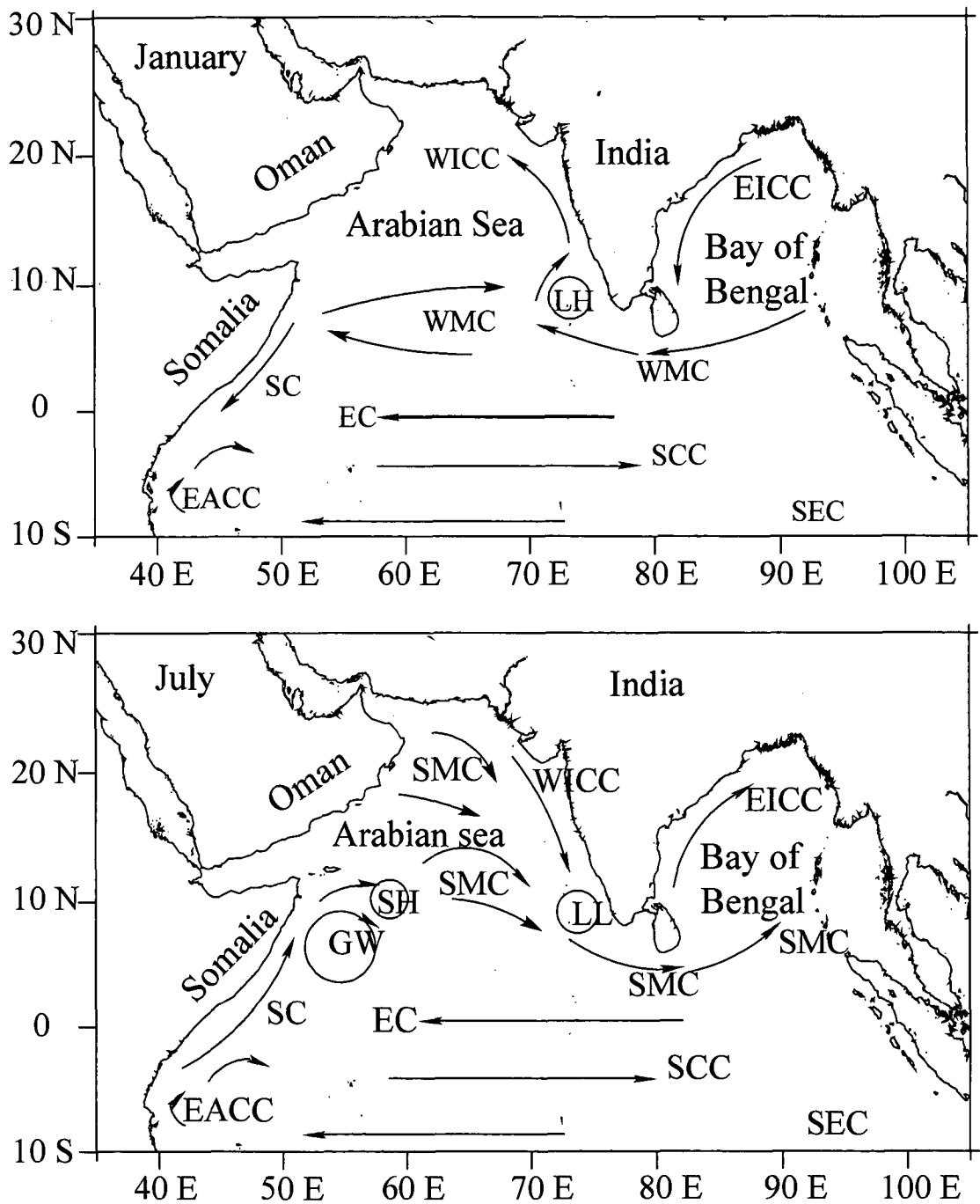
Figure 3. Surface circulation over the Indian Ocean during northeast monsoon (upper panel) and during southwest monsoon (lower panel). EICC – East Indian Coastal Current, WICC – West India Coastal Current, SMC – Summer Monsoon Current, WMC – Winter Monsoon Current, LL – Lakshadweep Low, LH – Lakshadweep High, SC – Somali Current, SG – Somali Gyre, EACC – East African Coastal Current, SECC – South Equatorial Counter Current, SEC – South Equatorial Current, NEMC – North East Madagascar Current, SEMC – South Eastern Madagascar Current. (Figure source: Shankar *et al.*, 2002).

17

The WMC forms at the southern edge of BoB during the winter monsoon period, which is fed by the East India Coastal Current (EICC) initially and later the WMC is mainly fed by the waters at southern BoB. The WMC breaks into two arms, where one arm moves further west along the southern Arabian Sea and feeds the Somali Current, while the other branch flows poleward along the west coast of India as poleward coastal current. This poleward current is of special interest in the present study as it is one of the main components that freshens the Eastern Arabian Sea (EAS: the study area) (Shetye *et al.*, 1991; Shankar *et al.*, 2002). The other components which are responsible for freshening the EAS are, a) intense overhead precipitation, b) mountain river runoff during summer monsoons and c) advection of low-salinity water from BoB during the winter as poleward coastal current.

All the above listed three primary drivers for reducing salinity in the EAS are associated with strength of the summer monsoon precipitation on sea and rains on Indian subcontinent. Therefore, it is possible to reconstruct the relative changes in the past summer monsoon intensity utilizing the time-series of 'salinity' reconstructed from sedimentary proxies from the EAS.

1.8. Productivity and upwelling in the Arabian Sea

The western Arabian Sea is the region of intense upwelling and hence has definite control in regulating atmospheric CO_2 (Currie, 1963). The upwelling occurs as a consequence of offshore turning boundary current (Ekman transport) in response to winds blowing parallel to the coast (Schott and Quadfasel, 1982; Swallow et al., 1983). Strong steady winds during the summer monsoon season (May-August) generate coastal and oceanic upwelling zones of great extent and upward transport of nutrient rich deep-water to the surface layer. The upwelling regions here are characterized by relatively low temperature, higher salinity, higher nutrients, greater primary productivity and rich plankton biomass (Ramasastry and Myrland, 1959; Varadachari, 1961; Sankaranarayanan and Quasim, 1969). The contribution of upwelled water from the western Arabian Sea to the central and eastern Arabian Sea due to advection facilitates high productivity (Prasanna Kumar et al., 2001). Large-scale upwelling is also observed off southwest India (Banse, 1968; Shetye, 1984) during the summer monsoons. During the winter monsoon (December-January), cold and dry air blowing from the continent over the sea (north to south) enhances evaporation setting up strong vertical convection in the northernmost Arabian Sea (Madhupratap et al., 1996), which sinks to the bottom of mixed layer and spreads southward contributing nutrient rich water to the EAS (Prasanna Kumar and Prasad, 1999) resulting in increased productivity. In the EAS, extensive areas of high fertility with Chlorophyll-a concentration of over 30 mg m^{-3} and surface production rate as high as 232 mg Cm^{-3}d^{-1} have been observed along the southwest coast of India induced by upwelling during summer monsoons (Rao et al., 1989). This fairly high production is sustained till the month of November. Intrusion of low salinity water from the BoB into the EAS during winter (Shetye, 1991) leads to an increase in chlorophyll concentrations in the southern region of the west-coast of India (Prasanna Kumar et al., 2004). Thus, the biogeochemistry of Arabian Sea in general and EAS in particular responds to monsoon variability.

1.9. Modern Sea Surface Temperature

The sea surface temperature (SST) governs the near-surface ocean responses throughout the monsoon seasons over the Arabian Sea. The sea surface warming or cooling in this region occurs through air-sea heat exchange and associated upwelling. In the Northern Indian Ocean the SSTs range between 25°C and 29°C (Fieux, 1987; Reverdin, 1987). The surface cooling is observed over most of the basin during November to January and June to August, whereas, warming occurs during the remainder of the year. The temperature is as high as 30°C during the lull periods i.e., during the inter-monsoon periods and cooling occurs during summer and winter monsoons through air-sea heat exchange due to intense winds. The phenomenon of surface cooling in the Arabian Sea is most intense during the summer monsoon period when the northern and western Arabian Sea experiences intense upwelling (Duing and Leetma, 1980; McCreary and Kundu, 1988). The upwelling and surface heat exchange creates thermal anomalies in the western Arabian Sea (Brown and Evans, 1981), which are believed to modify monsoon rainfall over India (Shukla, 1975; Raman *et al.*, 1992).

In all four seasons of the year SSTs show clear north-to-south increasing trend (Figure 4). The lowest annual SSTs (~27°C) observed over the northwestern Arabian Sea is due to perennial upwelling off Oman and advection of Somali upwelled waters. The highest SSTs are found towards the southern EAS with temperatures as high as 29°C. This increasing trend towards south probably reflects the combination of increasing insolation towards the Equator and reduced effect of advected waters from intense upwelling regions. During inter-monsoon periods the northerly winds are weak along with high insolation, which leads to the development of highly stratified upper layer with high SSTs. The annual SSTs in the EAS (study region) range between 28 and 29°C, which provide the basis for evaluating reliability of paleo-SST reconstructions.
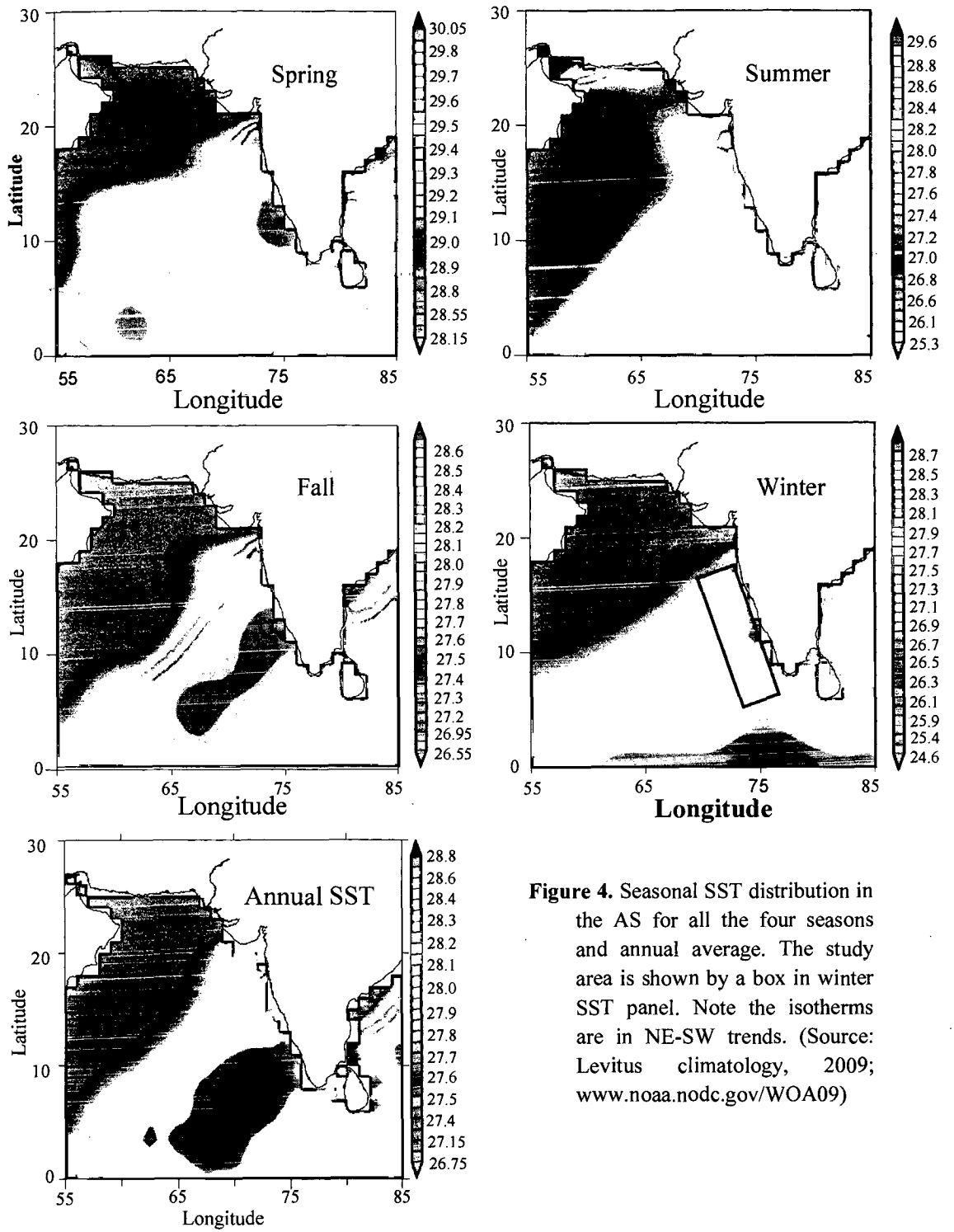
Figure 4. Seasonal SST distribution in the AS for all the four seasons and annual average. The study area is shown by a box in winter SST panel. Note the isotherms are in NE-SW trends. (Source: Levitus climatology, 2009; www.noaa.nodc.gov/WOA09)

21

1.10. Modern Sea Surface Salinity

The Arabian Sea surface salinity follows the E-P distribution. The Arabian Sea exhibits E-P always >1, hence significantly saline (>36 psu) as compared to its eastern counterpart, the BoB (E-P always <1; salinity <34 psu) (Figure 5). The summer monsoon E-P lies between -1 and -1.5 m y^{-1} towards the east of 70°E and south of 20°N while during the winter monsoons, the E-P remains positive (1.5 m y^{-1}) and is almost constant to the north of 10°N (Prasad, 1997). The annual salinity distribution pattern in the EAS also indicates that the rate of evaporation is higher than the precipitation in the study area. Most saline water (~37 psu) occurs in the entire northern- and central-Arabian Sea. Salinities > 37 psu are also found in the outflow regions of the Red Sea and the Persian Gulf. Low salinity water (~35 psu) is found along the coastal margin of western India (EAS). Intermediate salinity water (~36 psu) occupies the western and eastern region of the Arabian Sea (Figure 5). In the northern Arabian Sea, the salinity is found to be the highest during spring and winter (~37.3 psu) due to highest evaporation rates. Lowest salinity (~34 psu) water is found along the western margin of southern India during all the seasons but for summer. This low salinity water in EAS is due to inflow of BoB water in the form of northward flowing poleward coastal current during winter and spring. During summer, the salinity in EAS rarely exceeds 36 psu owing to the intense overhead precipitation. It has earlier been shown that the salinity in EAS is dictated by summer monsoon intensity as the low salinities in both Arabian Sea and BoB feeding the surface waters of EAS depend mainly upon the summer monsoon associated overhead precipitation and river discharge. Therefore, it is feasible to understand the summer monsoon intensity variability in the past by paleo-salinity reconstructions from EAS sediment.
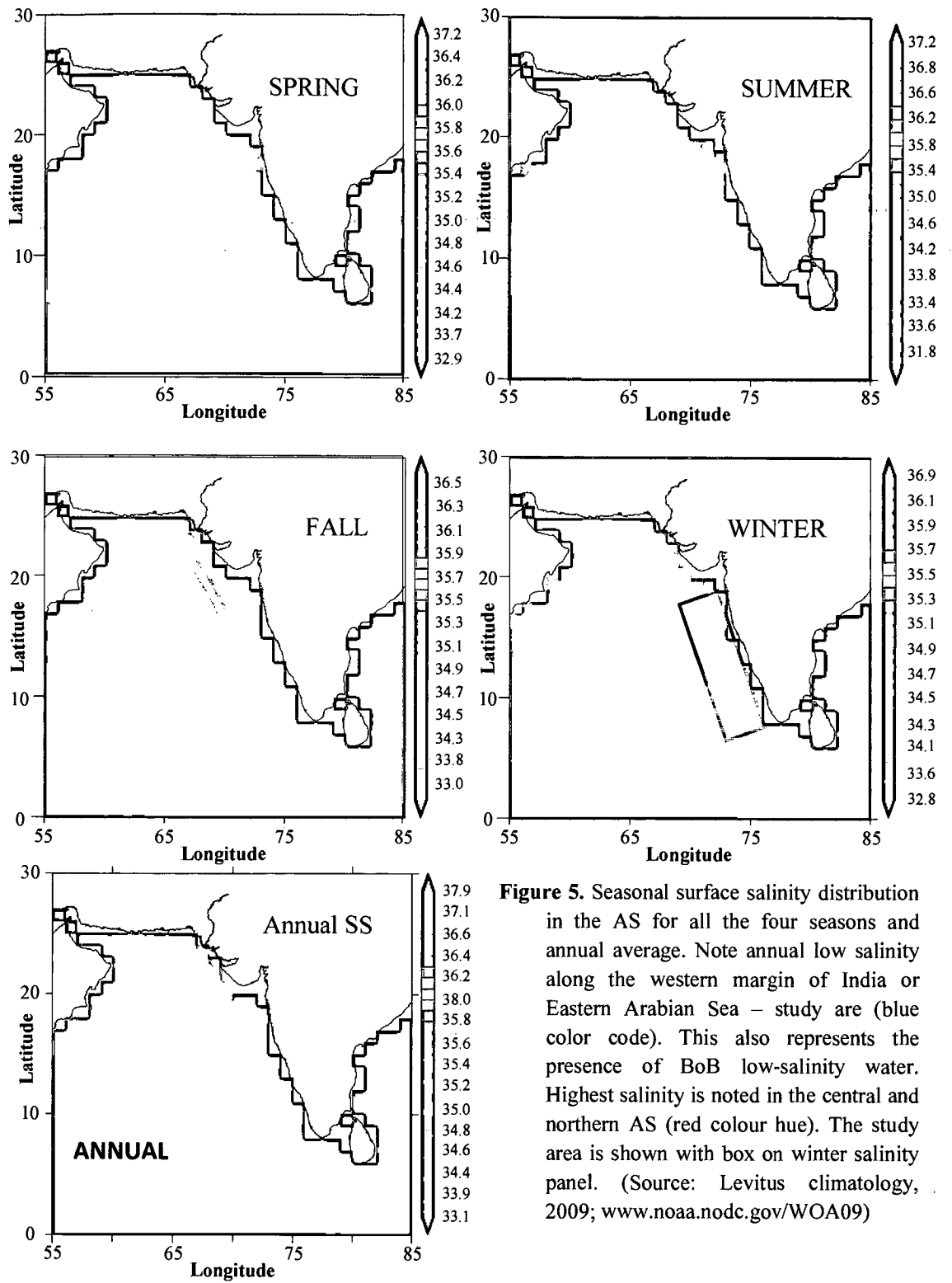
Figure 5. Seasonal surface salinity distribution in the AS for all the four seasons and annual average. Note annual low salinity along the western margin of India or Eastern Arabian Sea – study are (blue color code). This also represents the presence of BoB low-salinity water. Highest salinity is noted in the central and northern AS (red colour hue). The study area is shown with box on winter salinity panel. (Source: Levitus climatology, 2009; www.noaa.nodc.gov/WOA09)

23

1.11. Objectives of the Present Study

The aim of present study is to understand the evolution of Late Quaternary Indian monsoons by tracking changes in surface hydrography of the EAS. The time-series of SST and salinity reconstructed from planktonic foraminifera is used to reconstruct changes in surface hydrographic properties. To achieve this objective the following investigations were defined for the present thesis:

a. Reconstruction of oxygen-isotope variation in planktonic foraminifera extracted from sediment cores: The oxygen isotopes are important tools for paleoclimate studies as they reflect the global climate and also provide information on E - P when used in conjunction with SST, in addition to their potential as chronometer.

b. Reconstruction of SST from Mg/Ca ratios in planktonic foraminifera extracted from the sediment cores. Generate paired data of oxygen isotopes and Mg/Ca to obtain reliable information on salinity changes.

c. Reconstruction of surface salinity by combining foraminiferal Mg/Ca-SST and $\delta^{18}O$: As the surface salinity varies as a function of E-P, it should be feasible to understand the past variability of monsoons.

I have selected four sediment cores from the EAS for accomplishing above objectives. The oxygen-isotope data for two sediment cores was readily available from published literature. Therefore, only Mg/Ca data was generated for these two cores using same sub-sections and same species of foraminifera as were used for oxygen isotopes, to maintain strict-pairing of the data while strictly paired measurement (aliquots from same sample) of oxygen-isotope and Mg/Ca was carried out for remaining two sediment cores.

2.1. Regional hydrographic setting

The Sahyadris (Western Ghats or Deccan Mountains) play an important role in not only concentrating precipitation over the EAS regions (Sarker, 1966; Xie *et al.*, 2006), but also is drained by several medium to small seasonal rivers debouching in the EAS. The freshwater input received by the EAS through river flux is low (~498 Billion m^3) as compared to that of the BoB (~1475 billion m^3) (source Water and Related Statistics, Central Water Commission, India - 2007, http://www.cwc.nic.in/). Most of the overhead precipitation (~90%) in EAS occurs during summer monsoon period with negligible precipitation during winters.

The study region experiences net heat and freshwater loss during winter and net heat and freshwater gain during summer (Weller *et al*, 1998; Prasanna Kumar and Prasad, 1999). The increase in monsoon wind intensity and duration, either during summer or winter, would result in SST cooling along with increased productivity in the EAS due to upwelling induced by the stronger winds. This wind driven response in the Arabian Sea has been observed by a coupled ecosystem model for the Indian monsoon variations (Murtugudde *et al.*, 2007). Consequently, seasonal fluctuations in SSTs of the EAS apparently could be the result of relative strength of monsoon winds. The surface salinity structure in the EAS in general shows a decrease from north to south and presence of a low-salinity tongue along the western coast of India (see Figure 5). The width of this low-salinity water intrusion extends up to over 400 km in southwestern part and tapers to around 200 km in the northern-EAS. This salinity structure of EAS is thought to have been maintained by combination of excess evaporation in northern region (Prasanna Kumar and Prasad, 1999) and low-salinity water inflow from BOB via Sri Lanka and southern tip of India (Darbyshire, 1967; Shetye *et al.*, 1991) during the winter monsoon and spring inter-monsoon periods.

2.2. Regional tectonic features and bathymetry

The western continental margin of India is a passive margin which is characterized by: a) NW-SE trending wide continental shelf, b) remarkably straight edge limited by ~200 m isobaths, c) a narrow continental slope bounded between 200 and 2000 m isobaths, d) deep sedimentary basins and e) several structural features. The shelf is ~300 km wide in Kutch-Saurashtra area and gradually narrows towards southward to ~50 km in Kerala offshore area. Complimentary to this, the continental slope is narrow in the north and widens towards the south (Biswas, 1987). Geographically, the EAS lies between the eastern end of the Laxmi-Laccadive Ridges and adjacent continental slope of India (Figure 6). These basins were developed during the evolution of the western continental margin since the Late Cretaceous.
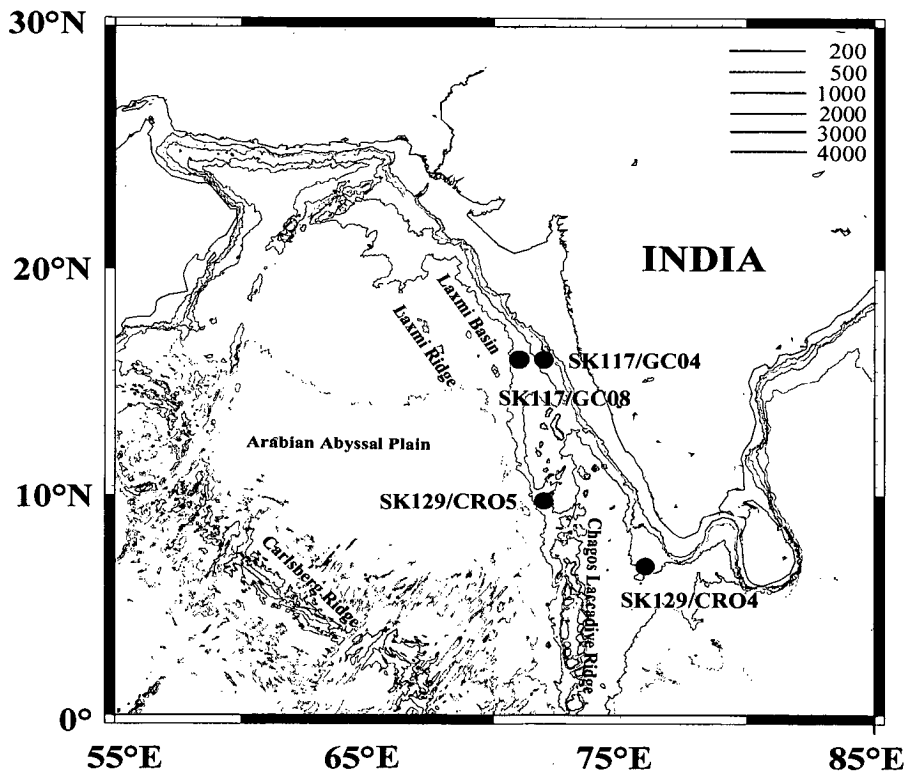
Figure 6. Major tectonic features of Arabian Sea along with bathymetry. The core locations are shown as red filled circles. The water depths of the cores vary between 2000-2500 m.

27

2.3. Upwelling in the EAS

The contribution of the upwelled water from the western Arabian Sea through lateral advection to central and eastern parts facilitates high productivity in the EAS (Prasanna Kumar *et al.*, 2001). Large- scale upwelling is also observed off southwest coast of India during the southwest monsoons up to 15°N (Banse, 1968; Sharma, 1978; Shetye, 1984), although its intensity is low when compared to western Arabian Sea (Shetye *et al.*, 1990). During the northeast monsoon (December-January), cold and dry air blowing from the north enhances evaporation leading to strong vertical convection in the northernmost Arabian Sea resulting in upwelling of nutrient rich water, which further is contributed to the EAS surface nutrient pool (Madhupratap *et al.*, 1996). Such spreading of nutrient rich water from northern Arabian Sea in to the EAS forces higher productivity in this region during winter. Therefore, in general the EAS could be considered as productive region.

The vertical sections of temperature (Figure 7) and salinity (Figure 8) for the EAS are presented up to a depth of 200 m. These depth profiles are representative of four seasons - summer, fall, winter and spring. The blue code in salinity vertical cross-section (see Figure 8) represents the low-salinity BoB water whose prominence wanes off further north. All the four sediment cores lie in the proximity of the here presented sections.
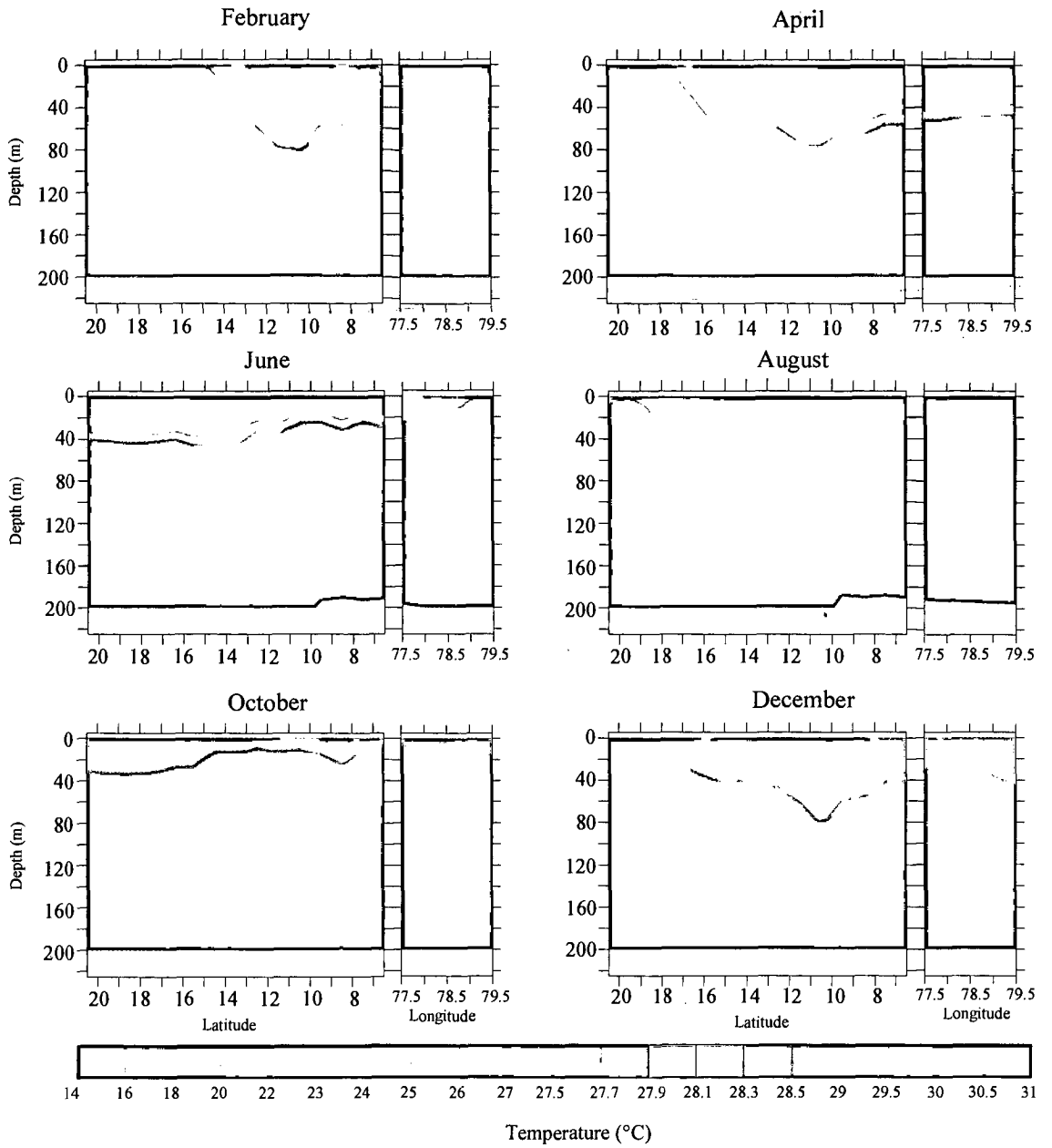
Figure 7. Vertical temperature cross-sections across EAS in North-South transect up to 200 m depth. (Figure source: www.noaa.nodc/gov/WOA09, refined processing of the data used in this figure is by A.Chatterjee).
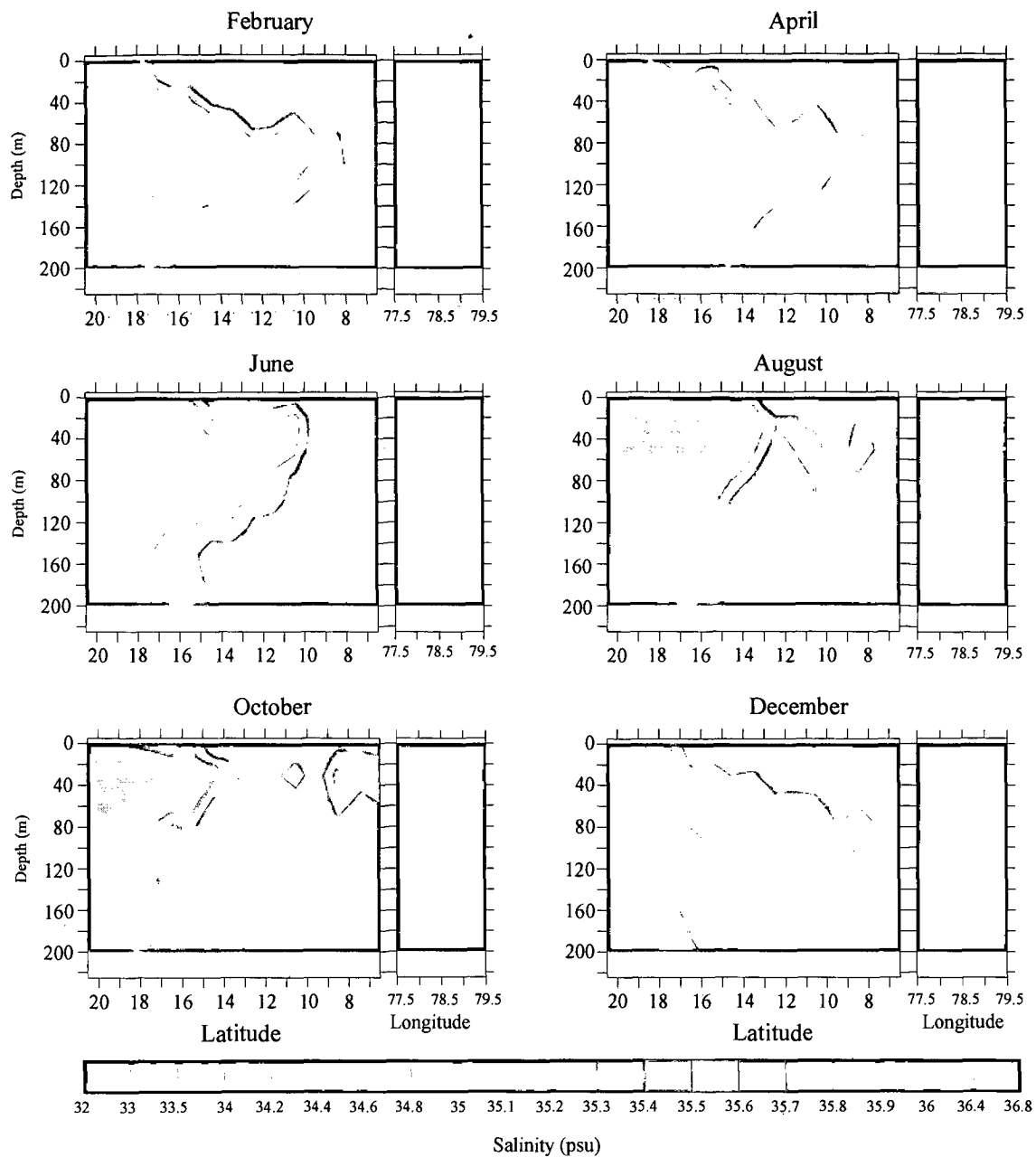
Figure 8. Vertical salinity cross-section across EAS in North-South transects up to 200 m water depth. Note: The deep blue red colour represents the BoB low-salinity water. (Figure source: www.noa.nodc/gov/WOA09, refined processing of the data used in this figure is by A.Chatterjee).

2.4. Productivity in the EAS

In the EAS, extensive areas of high fertility with Chlorophyll-a concentration of over 30 mg m^{-3} and surface production rate as high as 232 mg C m^{-3}d^{-1} have been observed along the southwest coast of India during the upwelling induced by the southwest monsoon (Krey and Babenerd, 1976; Sumitra and kumari, 1989). This fairly high production is sustained till the month of November. Intrusion of low salinity water from the BoB into the AS during winter (Shetye, 1991) leads to an increase in chlorophyll concentrations in the southern region of the western coast of India (Prasanna Kumar et al., 2004). The maximum productivity in the EAS is 1782 mg Cm^{-2}d^{-1} (Prasanna Kumar et al., 2001) as compared to 2668 mg Cm^{-2}d^{-1} in the western Arabian Sea (Owens et al., 1993) during the summer monsoons, indicating weak upwelling.

2.5. SST and Salinity variation in the EAS

Seasonally reversing monsoon system could be considered as the fundamental force that controls the physical and biogeochemical properties of the EAS. It may be of worth to mention that some of the local processes superimpose on the broader monsoon driven changes in the EAS. The region off Goa experiences phytoplankton bloom during the winter season due to the advection of the nutrient enriched ASHSW, while the region off Kochi experiences upwelling during the summer monsoons induced by the monsoon winds blowing parallel to the coast. Hence, in order to assess the influence of these forces, a basic understanding of hydrography at the core locations is required. The vertical depth profiles of SST and salinity at each core location are presented in the next chapter.

3.1. Sediment cores

The sediment cores used for the present study were retrieved onboard ORV Sagar Kanya during different cruises (SK-117: October 1996 and SK-129: December 1997) undertaken by the National Institute of Oceanography respectively *(see the respective Cruise reports for more details)*. Out of four sediment cores used in this study, two were located off Goa (SK117/GC04 & GC08), one off Kochi (SK129/CR05) and one off southern-tip of India (SK129/CR05) (Figure 9). The relevant details of sediment cores are provided in Table 1. All the sediment cores were from locations beyond the depth of modern oxygen minimum zone (200-1000 m) and well above the foraminiferal lysocline depth (3300 m; Cullen and Prell, 1984) and also the carbonate compensation depth (~4800 m) (Berger and Winterer, 1974; Kolla *et al.*, 1981; Banakar *et al.*, 1998).

Table 1. Location details of the studied sediment cores from the Eastern Arabian Sea

Core ID	Latitude N	Longitude E	Water Depth m	Total core length (cm)	Number of Sub-sections
SK117/GC08*	15° 29.67`	71° 00.98`	2500	415	207
SK117/GC04	15° 29.85`	71° 54.20`	2100	596	298
SK129/CR04	06° 29.67`	75° 58.68`	2000	520	260
SK129/CR05*	09° 21.00`	71° 54.20`	2300	552	276

(*The oxygen-isotope data for these two sediment cores are from previously published datasets: Banakar *et al.*, 2005; Chodankar *et al.*, 2005)
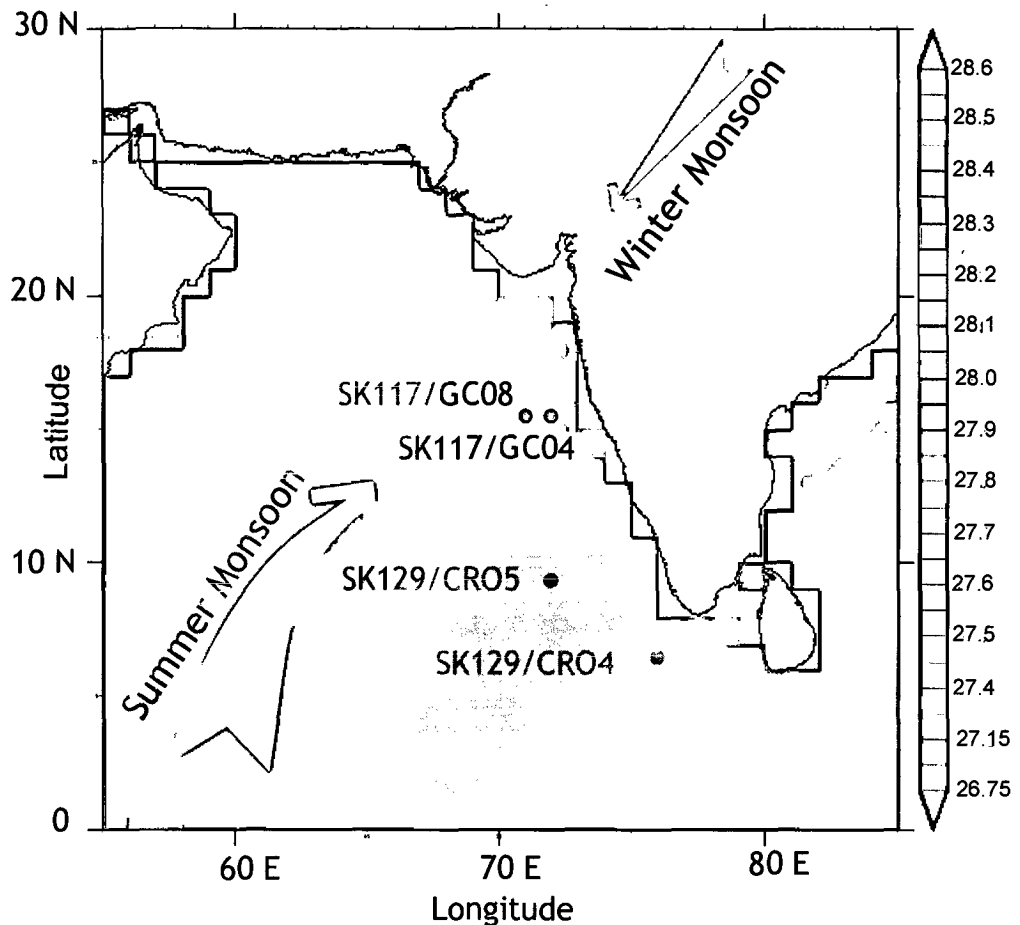
Figure 9. Sediment core locations shown on annual surface temperature (°C) distribution map. The general trend of two seasonally reversing monsoon systems, which affect surface hydrology and biology of the study region, are shown with labeled gray colored arrows. The thickness of arrow tentatively indicates relative significance of these two monsoon systems. The 'deep red' indicates high-SST end and 'pink' indicates low-SST end. (Map source: www.noaa.nodc.gov).

3.2. Vertical depth profiles of temperature and salinity at core locations

As the modern hydrography varies significantly in the EAS, I have selected four sediment cores so as to represent the entire EAS. The depth profiles of modern salinity and SST in these core locations would provide an idea about what type of water is present in the thermocline (below 20 °C isotherm), which normally upwells and modifies the surface water properties. The past changes in SST and salinity are expected to have been forced either by changes in E-P or by changes in upwelling intensity. Therefore, it may necessitate an assessment of surface hydrological changes in light of both these two processes. The vertical distribution of SST and salinity presented as Figure 10 are the annual averages of Levitus climatology data for the core locations.

34
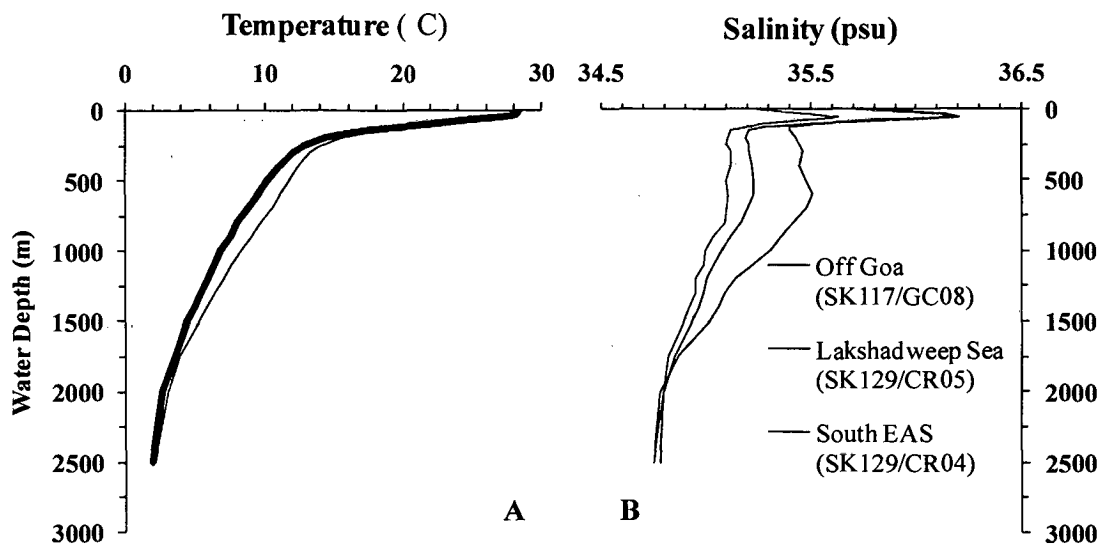
Figure 10. Vertical distribution of annual average SST (A) and salinity (B) at core locations. The figure shows that the temperature remains almost same at four locations and salinity varies significantly. (Compiled: www.noaa.nodc.gov).

From Figure 10, it is evident that the temperature variation with depth is mostly similar at all four locations, where the upper thermocline extends from ~100 m to 400 m and lower thermocline between 400 and 1000 m water depths. On the other hand, the off Goa location (SK117- GC8 & GC4) records higher salinity at both the thermocline and mixed layer as compared to southern-EAS locations (SK129/CR4 & CR5). This pattern of salinity distribution is expected as the northern-EAS cores are under the influence of high salinity ASHSW, whereas the southern-EAS cores are under the direct influence of low-salinity BoB water. These characteristic modern hydrographic properties at each of the sediment core locations would provide the baseline information to compare the past changes in climatology of the EAS in response to climate variability.

CHAPTER 4
METHODS

As discussed in previous chapters, the paleoclimate reconstructions require extraction of indirect information preserved by sedimentary proxies. Various components of sediments (biogenic or lithogenic or authigenic) hold clues about the environment under which they have been generated, transported and deposited on the seafloor. Unscrambling such proxy information is complex and inherently contains certain uncertainties. Such uncertainties could be minimized by: a) selecting a proxy which has single source of origin, or b) quantifying and subtracting the effect of unwanted influence on the selected proxy. For example, extracting SST signals from the oxygen isotopes of planktonic foraminifera requires quantification of ice volume/sea level changes through time. Whereas, the SST estimation by Mg/Ca from planktonic foraminifera is straightforward because, this ratio in calcite secreted by foraminifera is predominantly controlled thermodynamically (Nurnberg et al., 1996) (others being biological fractionation, vital effects, salinity and pH are of minor significance) having a single source of origin, i.e., ambient seawater. In the following sections, I present Mg/Ca-Thermometry in detail and well-known radiocarbon dating in brief. The fundamentals of oxygen isotope technique are already given in 'Introduction Section' and only measurement method is described here.

In order to develop a stratigraphic framework, the depth (from top to bottom) within each of the studied sediment core needs to be translated in to time-scale. A relative time-scale could be obtained using oxygen isotopic ratios and absolute time-scale using radiocarbon. Here, I have utilized earlier published oxygen-isotope records for SK117-GC08 and SK129-CR04 sediment cores (Chodankar, 2004; Banakar *et al.*, 2005; Chodankar *et al.*, 2005), and generated new oxygen-isotope data for SK117-CR05 and SK117-GC04 utilizing *Globigerinoides sacculifer*, a planktonic foraminifera. The sedimentation rate between two dated intervals (in case of radiocarbon) or between two adjacent MIS boundaries (in case of oxygen isotopes) were calculated. The sedimentation rate in turn was used to convert 'depth-in-core' into 'time-in-past'. In order to obtain time-series records of SST and salinity strictly paired measurement of Mg/Ca ratios and oxygen isotopes was carried out utilizing same species of same size range from same sub-sections of the sediment core.

Identifying the climate events from the down-core depth profile of the oxygen-isotope is essential to identify warm and cold events, which have link to the surface climatology (SST & salinity) in general. The climate-events from the oxygen isotope variations for the four cores were identified by comparing the measured oxygen isotopic time-series profile with the Benthic Oxygen Isotopic Stack of Lisiecki and Raymo (2005), which is popularly known as LR04 Benthic Stack. The LR04 is superior to SPECMAP oxygen isotope reference curve (Imbrie *et al.*, 1984 Bassinot *et al.*, 1994), because the LR04 curve represents changes in the deep-water oxygen isotopes that are well-insulated from the local surface ocean-atmosphere influences. Therefore, it represents exclusively the changes occurred in global ice-volume (sea level) reflecting the climate status.

The calendar age chronology (absolute ages) for all the sediment cores is established by AMS ^{14}C dates. Finally, I have integrated all the proxy records to discuss the changes in EAS surface hydrography in response to climate change on different lines of evidences to produce an overall paleoclimate synthesis. Before presenting the results, few basic aspects of the proxies utilized in this study are described below.

4.1. The proxy used: *Globigerinoides sacculifer*

Foraminifera are the single-celled marine microorganisms, which secrete calcium carbonate (calcite) tests mostly in equilibrium with their ambient water properties. Around 40 planktonic (free-floating in photic zone) species have been identified. These along with bottom dwelling benthic foraminifera constitute about 2.5% of all fauna known and have come in to existence in the earliest Cambrian period (Loeblich and Tappan, 1964). However, the modern oceanic foraminifera originated during the Neogene (Kucera and Schonfeld, 2007). The planktonic foraminifera represent the upper ocean conditions, which are dynamic due to direct interaction with the atmosphere. Therefore, the planktonic foraminifera are ideal for studying the ocean-atmosphere coupled processes such as monsoons.

The microorganisms are highly sensitive for any change in their environment and hence are useful in the reconstruction of paleoenvironments and paleoecology. The calcite test is normally well preserved in marine sediments over millions of years,

particularly when deposited well above the CCD. As they are inorganic ($CaCO_3$) in nature, the post-depositional diagenetic alterations are absent unlike in organic matter. They are ubiquitous in nature and whole tests can be retrieved even from a small quantity of marine sediment. Hence, there is no limit on the material availability. These aspects render the foraminifera as an ideal tool used for past climate reconstructions.

For the present study, the species *Globigerinoides sacculifer* (*G. sacculifer*), a planktonic foraminifer belonging to the kingdom Protista, Phylum Protozoa, Class Reticularea (Be`, 1960) is used. This spinose foraminifera exhibits lunar reproductive cycle (Bijma *et al.*, 1994). It is an upper mixed layer dwelling species found to be largely restricted to 20-40 m water depth (Be`, 1980). It is widely distributed in the tropical and sub-tropical oceans between $40^{\circ}N$-$40^{\circ}S$ and is most resistant to dissolution amongst all globigerinoides species (Delaney *et al.*, 1985; Brown and Elderfield, 1996; Dekens *et al.*, 2002). During gametic (reproductive) stage, this species migrates to deeper depths and develops a sac-like terminal chamber (Be`, 1980; Hemleben *et al.*, 1989) that records physicochemical signatures of deeper water, which is very different from the mixed layer in which it basically lives for most of its life-span. This sac-like chamber adds as much as ~20 - 30% calcite to its shell at greater depths (Be` 1980) and hence, not suitable for studying surface ocean properties. Therefore, I have picked only those tests which do not possess terminal-sac for the present study (see Figure 11).

Figure 11. *G. sacculifer* without terminal sac (left), which is used in the present study. The right hand side picture is of the *G. sacculifer* with terminal sac (within box). The terminal-sac forms during gametogenesis at deep waters (below mixed layer). Hence species with this chamber are not suitable for studying ocean-atmosphere coupled processes.

It is observed that *G. sacculifer* is consistently present in the marine sediments retrieved from the study area irrespective of whether the sediment is from the glacial or interglacial period.

4.2. Extracting planktonic foraminifera from the sediment

About 5 g of air dried sediment was dispersed in water in presence of 10% w/v sodium hexametaphosphate [$(NaPO_3)_6$] for about eight hours. The dispersed sediment was wet sieved over 63 μm standard sieve using soft jet of water to separate coarse fraction. The dried coarse fractions (+63 μm) were preserved in labeled vials. The coarse fraction was further sieved using mini-sieve set of 250 and 355 μm to restrict the size of coarse fraction to a narrow range of ~100 μm to ensure that the *G. sacculifer* tests used in the paired measurements were of nearly uniform size.

Around 100 tests of *G. sacculifer* were picked from above size-range coarse fractions under a binocular microscope. Sufficient care was taken to pick intact and clean tests to minimize the influence of contaminants and artifact on the results. The picked tests were stored in clean glass micro-thimbles. Before describing the methodology adopted for instrumental measurements, the fundamental aspects of techniques are described in brief in the following paragraphs.

4.3. Mg/Ca Ratio Thermometry

The compositional variations of elements such as Mg, Cd, Ba and Sr in the skeletons of planktonic foraminifera have been of great interest in paleoceanographic studies (Savin and Douglas, 1973; Bender *et al*, 1975; Graham *et al*, 1982; Delany *et al*, 1985). These elements are amongst several divalent cations, which substitute for Ca during calcification of the tests and have close relationship to environmental parameter such as temperature, salinity, productivity and pH. Element-to-calcium ratio in $CaCO_3$ depends on the corresponding element-to-calcium activity ratio of ocean water and the distribution coefficients of these elements between the carbonate mineral and seawater.

Of all the temperature proxies developed over the past decade to reconstruct SST, the Mg/Ca thermometer has been considered as most reliable method (Bijma *et al.*, 1990; Nurnberg *et al.*, 1996; Bemis *et al.*, 1998; Elderfield and Ganssen, 2000). Chave (1954) first elucidated that the calcite test precipitated by a microorganism in marine environments is a function of temperature in which that organism lives. Through presently available analytical tools, it is possible to quantify the Mg/Ca ratios with a

precision better than 1%. The basis for Mg/Ca thermometry is that the substitution of Ca by Mg in calcite lattice is temperature dependant (Chave, 1952; Goldsmith *et al.*, 1955). At equilibrium, the partitioning constants between the two pure mineral phases depend on temperature since the substitution of Mg in to calcite is associated with a change in enthalpy or heat of reaction, which is sensitive to temperature. The Mg^{2+} ion replaces Ca^{2+} ion in the lattice structure of $CaCO_3$ forming aragonite. As the substitution of Mg in to calcite is an endothermic reaction, the Mg/Ca ratio of calcite is expected to increase with increasing temperature (Mucci and Morse, 1990; Rosenthal *et al.*, 1997). Incorporation of Mg into biogenic calcite tests is found to increase exponentially by about 8 - 10% for every one degree rise in calcification temperature (Rosenthal *et al.*, 1997; Lea *et al*, 1999), which was consistent with experimental results on Mg incorporation into inorganically precipitated calcites (Katz, 1973; Oomori *et al.*, 1987; Burton and Walter, 1991). Since this process is physiologically mediated, wherein the incorporation of Mg into calcite is temperature related, the ratio of Mg to Ca provided a reliable scale for SST. Thus the variation in Mg/Ca ratios in modern foraminifer tests is a result of influence of temperature on the calcification process. The Mg/Ca ratios are measured in foraminifera extracted from sediments that has deposited above the lysocline to minimize the influence of dissolution on ratios, as Mg/Ca was found to be affected by dissolution with increasing depth (Brown and Elderfield, 1996; Lea *et al*, 2000).

The oceanic residence time for Mg and Ca is 10^6 and 10^7 years respectively (Holland, 1978), i.e., much longer than the oceanic mixing time ($\sim 10^3$ y). Thus, the long residence times of these two elements ensure not only their homogeneous distribution throughout the global oceans, but also maintain their constancy through time at least on glacial- and interglacial- time scales. Further, the inter-oceanic fractionation of these elements is highly unlikely (or not evident) due to their long residence time. Therefore, substantial uncertainties that otherwise could have been caused by spatiotemporal fractionation is minimized. This property of Mg and Ca render them as valuable proxy for ocean water temperature reconstructions. The SSTs obtained by this method for the surficial sediments at different locations spread over large geographical zones were

found to be closely comparable to the modern day temperatures validating this technique as a most faithful tool for SST reconstruction.

To be able to extract temperature signals from Mg/Ca in biologically precipitated calcite requires appropriate calibration. The calibrations used for translating Mg/Ca ratios in to water temperature are species specific, since uptake of these elements is different in different species even within the same habitat. Lea *et al.* (1999) showed through culture experiments measurable differences in uptake between species during calcification. It has been observed that the Mg/Ca ratios measured for foraminiferal calcite are generally 1-2 orders of magnitude lower than those predicted by the thermodynamics of inorganic precipitates. This is suggestive of the fact that the biogenic calcification is undoubtedly influenced by the physiological processes involved in calcification (Stephen *et al.*, 2005).

The Mg/Ca method has major advantages over other methods like alkenone unsaturation indices because, a) the Mg/Ca ratio remains unchanged even after the calcite test settle to the seafloor unlike the organic matter in which alkenones are preserved, b) even if the calcite tests have undergone dissolution, the correction to measured Mg/Ca could be made to obtain Mg/Ca that was present under pristine state (Dekens *et al.*, 2002), and c) as these elements are associated within the calcite lattice, the same tests can be used for both oxygen isotope and Mg/Ca measurements providing strictly paired data, which is highly desirable.

4.3.1. Temperature calibrations and limitations

As mentioned earlier, different calibrations are needed for different species of foraminifera since the uptake of Mg in their calcareous tests is species specific and biologically mediated (Rosenthal *et al.*, 1997). These calibrations are determined by using three different approaches: a) culture based calibrations, b) sediment trap calibrations, and c) core top calibrations. In culture based calibrations, the planktonic foraminifera are grown under controlled laboratory conditions i.e., by varying any one of the hydrographic parameters (in this case temperature) and maintaining other parameters constant (in this case salinity, pH, nutrients and light) (Nurnberg *et al.*, 1996; Lea *et al.*, 1999; Mashiotta *et al.*, 1999; Russell *et al.*, 2004; Langen *et al.*, 2005). Anand *et al.* (2003) and McConnell and Thunell (2005) conducted measurements for planktonic foraminifera species (*G. sacculifer, G. ruber and G. bulloides*) collected in sediment traps deployed in the North Atlantic and Gulf of California and found that the Mg/Ca ratios changed in accordance with ambient water temperatures. The core top calibrations were derived for foraminifera extracted from surface sediments (Nurnberg *et al.*, 1995; Nurnberg *et al.*, 1996; Mashiotta *et al.*, 1999; Elderfield and Ganssen, 2000; Lea *et al.*, 2000; Dekens *et al.*, 2002; Rosenthal and Lohmann, 2002; Hathorne *et al.*, 2003; McKenna and Prell, 2004). The Mg/Ca ratios were found to be affected by post depositional dissolution with increasing depth (Brown and Elderfield, 1996; Lea *et al*, 1999; Rosenthal *et al.*, 2000). However, after applying depth-dissolution corrections, estimated SSTs were closely comparable to the modern SSTs at their respective locations.

Availability of culture based calibrations is limited to a few numbers of species. The temperature sensitivity of these combined experiments is about 9.7 ± 0.9% change in Mg/Ca per °C, which affirms the direct evidence for temperature control on planktonic foraminiferal Mg/Ca similar to the inorganic experiments. The multi-species core top calibration by Elderfield and Ganssen (2000) suggests temperature sensitivity of 9.5 ± 0.5% change in Mg/Ca per °C. The good agreement between the multi-species calibrations and sediment trap sample based calibrations along with culture experiments

(Table 2) provide evidence of robustness of the temperature signal imprinted during test formation and faithfully transferred into the sediment.

Majority of works related to estimating Mg/Ca - Temperature calibrations are done from the Pacific and Atlantic Oceans and virtually none for the Indian Ocean (see Table 2). The reconstruction of temperature for the Indian Ocean therefore requires use of calibrations developed either for Atlantic or for Pacific depending on how closely the physico-chemical features between the regions resemble each other. In the present study the calibration derived for *G. sacculifer* of tropical Pacific (Dekens *et al*., 2002) is used to calculate SSTs from the Mg/Ca$_{G.\ sacculifer}$, since the hydrological setup of both the tropical Indian Ocean and tropical Pacific are nearly similar.

Table 2. Summary of published Mg/Ca-Temperature calibrations for multiple and single species of planktonic foraminifera (Mg/Ca in mmol/mol and T in °C) (Source: Marcel and Vernal, 2007)

Species	Mg/Ca = B exp^{AT}		Material	Region	T- Range	Reference
	B	A				
Multiple-species equations						
Two planktonic species	0.47	0.082	Core tops	Atlantic and Pacific	0 - 30	Nurnberg et al., 1996
Eight planktonic species	0.52	0.100	Core tops	North Atlantic	8 - 22.	Elderfield and Ganssen, 2000
Eight planktonic species	0.78	0.095	Core tops	North Atlantic	9 - 22.	Rosenthal and Lohmann, 2002
Ten planktonic species	0.38	0.090	Sediment trap	North Atlantic	15 - 28	Anand and Elderfield, 2003
Single-species equations						
G. sacculifer	0.39	0.089	Culture		19-30	Nurnberg et al., 1996
O. universa	1.36	0.085			16-25	Lea et al, 1999
O. universa	0.85	0.096			15-25	Russell et al., 2003
G. bulloides	0.53	0.100			16-25	Lea et al, 1999
G. bulloides	0.47	0.107	Culture/core tops		10-25.	Mashiotta et al., 1999
N. pachyderma	0.51	0.104	Culture		9-19.	Langen et al., 2005
G. ruber (white: 250 - 350 µm)	0.34	0.102	Sediment trap	North Atlantic	22-28	Anand et al., 2003
G. ruber (white: 250 - 350 µm)	0.48	0.085		North Atlantic	22-29	Anand et al., 2003
G. ruber (white: 212 - 350 µm)	0.69	0.068		Gulf of California	20-33	McConnell and Thunell, 2005
G. sacculifer with sac (350 - 500 µm)	0.67	0.069		North Atlantic	22-28	Anand et al., 2003
G. sacculifer without sac (350 - 500 µm)	1.06	0.048		North Atlantic	22-29	Anand et al., 2003
G. bulloides (212 - 355 µm)	1.20	0.057		Gulf of California	16-31	McConnell and Thunell, 2005
G. ruber (white: 250 - 350 µm)	0.30	0.089	Core tops	Equatorial Pacific	24-29	Lea et al., 2000
G. sacculifer	0.38	0.090		Atlantic and Pacific	21-29	Dekens et al., 2002
O. universa	0.95	0.086		North Atlantic	8 - 22.	Hathorne et al., 2003
G. bulloides	0.56	0.100		North Atlantic	9 – 22	Elderfield and Ganssen, 2000
G. bulloides	0.81	0.081		North Atlantic	10-22	Elderfield and Ganssen, 2000
N. pachyderma	0.55	0.099		Norwegian Sea	1-12	Nurnberg., 1995
N. pachyderma	0.41	0.083		South Atlantic	0-15.	Nurnberg., 1996
G. truncatulinoides	0.36	0.098		Indian Ocean	8-25.	McKenna and Prell, 2004

B = pre exponential constant; A = exponential constant; T-Range = Temperature range for which the above constants are valid.

The Mg/Ca and temperature relationships were found to be mostly exponential. Based on various calibrations (Brown and Elderfield, 1996; Lea et al., 1999; Elderfield and Ganssen, 2000; Dekens et al., 2002; Rosenthal et al., 2002; Anand et al., 2003; Hathorne et al., 2003; McKenna and Prell, 2004), the Mg/Ca ratio can be translated into calcification temperature using equation:

$$Mg/Ca = B \exp (A * T)$$

Where "B" is the pre-exponential constant, "A" is the exponential constant and T is the calcification temperature in '°C'. In this relationship, the exponential constant reflects the Mg/Ca response to a given temperature change (in mmol/mol per °C), implying increased sensitivity with temperature and the pre-exponential constant determines the absolute temperature and is species specific.

Since there is no Mg/Ca - Temperature calibration available for the Arabian Sea in general and EAS in particular, I have used Dekens et al. (2002) calibration for the Tropical West Pacific derived from G. sacculifer [Mg/Ca=0.37 exp 0.09 (T- 0.36*core depth in km) – 2°C]. This calibration is most ideal for the Arabian Sea, because, a) the ocean-atmosphere coupled processes in this region are nearly similar to that of the western tropical Pacific, b) in general the SST pattern in Pacific and northern Indian Ocean are similar (Millero, 1996), and c) the extermination of G. ruber - pink variety has occurred simultaneously only from tropical Indo-Pacific region ~125 ky ago, but not from the tropical Atlantic (Thompson et al., 1979). These observations indicate a hydrographic similarity between tropical Pacific and tropical Indian Ocean. Further, these two regions experience similar large scale coupled processes such as ENSO (Pacific Pacific) and IOD (Indian Ocean). Therefore, it is reasonable to assume that the Mg/Ca - Temperature calibrations derived for western Pacific would be more or less similar for entire tropical Indian Ocean for a given species of planktonic foraminifera

4.3.2. Cleaning of foraminifera tests for Mg/Ca measurement

The calcite tests of foraminifera extracted from the sediment are filled with clays, coated with organic matter and oxides, and invariably contain secondary calcite. Before dissolving the tests for Mg/Ca measurements, it is essential to eliminate these contaminants to bring the tests nearest to their pristine condition. Without achieving this, the Mg/Ca ratios are meaningless and fraught with non-correctible errors. Therefore, a series of elaborate cleaning protocol using ultra-pure/supra-pure reagents (see Barker *et al.*, 2003) is involved before dissolving the tests for measurement. The cleaning steps are as follows.

The *G. sacculifer* tests were crushed softly between two glass-plates to break-open all the chambers to expose filled contaminants, so that it can be removed. A drop of DI-water (18M Ω - henceforth "water") was added to the crushed fraction and agitated with a fine brush under a microscope. Clay lumps, mineral grains, Mn-coated and stained fragments were physically separated under microscope and discarded. The visibly clean tests were transferred to acid cleaned 1.5 ml micro-centrifuge tubes.

The clays are composed of significant amount of Mg and can be leached by even mild acids. Therefore, clay removal is most important in Mg/Ca thermometry. This step involves washing of skeletal fragments in water and methanol. The physically separated fragments were washed by squirting 200 µl of water and sonicating it for 1 minute. The supernatant water that contains suspended clays was removed immediately with the help of micropipette. This step was repeated five times to eliminate most of the clays. The final clay removal was done by adding 200 µl of methanol and sonication. The supernatant was removed and the fragments were washed twice with water. This step was repeated three times. Methanol, which is of lower density (0.792 g/cm³) helps in suspending extremely fine clay particles. The organic coatings formed over the settling particles in marine waters normally scavenge several trace elements, which could introduce significant contamination in measured Mg/Ca. Therefore, their removal is necessary. The clay-free fractions were treated in presence of 200 µl of hydrogen peroxide (H_2O_2) buffered with 10 % sodium hydroxide (NaOH), in a boiling water bath for 20 minutes. To ensure complete oxidation of organic coatings the sample tubes were

repeatedly agitated by sonication at regular intervals. The supernatant reaction mixture was removed and the test fragments were washed twice. As the oxide-coated fragments were physically removed under the microscope in the beginning, no separate chemical treatment step was adopted as followed in few previous studies (see Pena *et al.*, 2005; Saraswat *et al.*, 2005; Dahl and Oppo, 2006; Weldeab, 2006).

The calcite tests after settling to seafloor and subsequently buried are exposed for a long time to pore-water containing several reactive elements. The secondary calcite may deposit over the original tests significantly obliterating the pristine Ca/Mg ratios. Therefore, removal of such secondary calcite was done by treating the clay- and organics-free fragments with 0.001 M HNO_3 under sonication. This step also effectively detaches most of the fine Fe-Mn oxide coating material along with secondary calcite. The supernatant was removed and the fragments were quickly washed twice with water to prevent dissolution. With completion of this step, the foraminiferal calcite tests should attain their original status. Thus cleaned fragments were re-examined under the microscope to ensure completeness of cleaning protocol. Finally, the clean calcite fragments (closest to their pristine condition) were dissolved in 0.075 M HNO_3 under sonication. The solution was then centrifuged at ~ 10 000 rpm (~ 3354 g) for about 15 minutes to ensure settling of any extremely fine (colloidal size) particles. The supernatant solution was then transferred to acid cleaned 1.5 ml capacity microtubes for Mg/Ca ratio measurement following intensity ratio (IR) calibration technique developed by DeVilliers *et al.* (2002) on Perkin-Elmer Optima 2000 DV ICP-OES at the National Institute of Oceanography.

4.3.3. Mg/Ca ratio measurement

First, all the solutions were analyzed for Mg, Ca, Al, Mn and Fe following standard calibration. Then, the Ca-contents in the sample solutions were adjusted to ~70 ppm by dilution and reanalyzed for Mg and Ca. In IR calibration method, most consistent ratios with highest precision were obtained when the Ca content in the solutions was 50 to 80 ppm (De Villiers *et al.*, 2002). Hence, the solutions with extremely low Ca (< 40 ppm) were either not used or were again prepared, while solutions with high Ca were diluted to ~70 ppm level and reanalyzed. The IRs obtained

for five standards containing variable Mg/Ca (mmol/mol) were used to establish IR-calibration (Figure 21 to 24). Then the Mg/Ca IRs of sample solutions were converted in to Mg/Ca (mmol/mol) ratios using this calibration. Along with Mg and Ca, other index elements for contamination such as Al and Fe (clays), Mn (oxides) were also measured. The Al/Mg provides a good indication of clay contamination while Mn/Mg monitors the oxide contamination. The presence of high levels of Fe and Al can increase the values of Mg/Ca ratios indicating leaching of clays during cleaning process (Barker *et al.*, 2003). Therefore, the solutions containing > 0.03 mmol/mmol of Al or Fe or Mn / Mg ratios were rejected or samples subjected to repeat cleaning protocol.

The affirmation of the quality of analyzed data is a pre-requisite in any analytical measurements. In order to validate the long term reliability and assess the precision of analytical results of the measured Mg/Ca data, Quality Control (QC) solutions of known values for all the five elements (Mg, Ca, Fe, Mn and Al) were analyzed regularly along with the sample solutions. The QC was run after every six sample solutions. In all, four QC solutions (2.720 mmol/mol, 4.128 mmol/mol, 5.128 mmol/mol, 5.144 mmol/mol) comparable to the expected ranges of sample Mg/Ca were utilized. The range of Mg/Ca in *G. sacculifer* from tropical oceans was found to vary between ~2.5 to 5.5 mmol/mol based on published results, which formed the basis for preparing QC solutions. The four QC solutions were run over a period of two years, the time taken for generating Mg/Ca data for all the four sediment cores. The results of QC measurements are given in Table 9. A detailed assessment of QC data is presented in Discussion chapter.

4.4. Oxygen isotope measurement

Oxygen has three stable isotopes: a) ^{16}O (99.763% abundant), b) ^{17}O (0.0375% abundant) and c) ^{18}O (0.1995% abundant). The ratio (relative amount) between any of the two oxygen isotopes in seawater changes with climate because of fractionation during evaporation or precipitation according to Rayleigh's Law of isotopic fractionation. This law suggests that the lighter isotope of an element preferentially stays in gas (vapour) phase as compared to heavier isotope of the same element in a given material. Thus, evaporation and condensation influence the ratio of heavy oxygen (^{18}O) to light oxygen (^{16}O) in the ocean water. Since the relative change in $^{18}O/^{16}O$ is required

49

to infer paleoclimatic changes, the $^{18}O/^{16}O$ ratio of a sample is expressed as change with respect to a standard either Pee-Dee Belemnite (PDB) in case of biogenic calcites or with respect to Standard Mean Ocean Water (SMOW) in case of water. This helps to ensure global consistency in the oxygen isotope data produced. Thus, the oxygen isotopic variations are expressed with delta notation - $\delta^{18}O$, where:

$$\delta^{18}O_{CALCITE} = [(^{18}O/^{16}O_{\ CALCITE} - {}^{18}O/^{16}O_{STANDARD}) \times {}^{18}O/^{16}O_{STANDARD}] \times 10^3$$

The temperature dependant preferential removal of ^{16}O from liquid (water) to its gaseous phase (vapor) owing to high vapor pressure of ^{16}O as compared to ^{18}O, leads to distinct differences in the isotopic composition of the foraminiferal tests formed from seawater of varying isotopic composition and temperature. Thus, the isotopic composition of the foraminiferal tests is a combined measure of seawater oxygen isotopic composition and seawater temperature at the time of precipitation of the test. Thus, the oxygen isotopic composition of a foraminiferal species can be resolved as:

$$\Delta\delta^{18}O_{CALCITE} = \Delta\delta^{18}O_{SEAWATER} + \Delta T_{SEAWATER}$$

The oxygen isotopic composition of seawater reflects variation in the global ice volume and local E-P and ambient water temperature (Shackleton, 1987; Shackleton, 2000). The global ice volume accounts for ~70% of the change in oxygen isotopic composition of the foraminiferal calcite over glacial-interglacial transitions. The remaining will be accounted for the local climatology. Therefore, the $\delta^{18}O_{CALCITE}$ could be defined as,

$$\Delta\delta^{18}O_{CALCITE} = \Delta\delta^{18}O_{GLOBAL\ ICE\ VOLUME} + \Delta\delta^{18}O_{LOCAL\ E-P} + \Delta T_{SEAWATER}$$

To understand the glacial-interglacial climate change impact on local/regional climatology and biogeochemical processes, it is essential to subtract the global ice effect from the calcite $\delta^{18}O$, which can be removed using Shackleton's (2000) corrections. The resultant oxygen isotopic changes reflect the local E-P and seawater temperature. The relationship between foraminiferal calcite and temperature is expressed by Epstein *et al.*'s (1953) equation:

$$T \ (°C) = a + b \ (\delta^{18}O_{CALCITE} - \delta^{18}O_{SEAWATER}) + c \ (\delta^{18}O_{CALCITE} - \delta^{18}O_{SEAWATER})^2$$

50

Where a, b and c are species-specific constants. To obtain information on past E-P (i.e., local salinity) the temperature component in the calcite $\delta^{18}O$ needs to be subtracted. This is achieved only by estimating the SST.

As mentioned in material section, the oxygen isotope data was available for two sediment cores (SK117/GC08 and SK129/CR04; Banakar *et al*, 2005; Chodankar *et al.*, 2005), whereas, for SK117/GC04 and SK129/CR05 it was generated. It should be noted here that only the same interval samples as those for oxygen-isotope measurements of published two sediment cores were used for Mg/Ca ratio measurement. In case of other two sediment cores, the crushed foraminifer's tests were split in to two fractions. One fraction was used for oxygen isotope measurement and another for Mg/Ca measurements. Thus, the oxygen-isotope and Mg/Ca data presented in this thesis are from strictly paired measurements.

The fragments of *G. sacculifer* tests were sonicated for ~30 seconds in ~200 µl of 30% H_2O_2 to oxidize organic contaminants and washed in water. The cleaned and dried fragments were transferred to glass vials and sealed with a screw cap holding a silicon-septa and PCTFE-washer. The sample was made to react with 100% orthophosphoric acid at 90°C in an automatic carbonate dissolution system "Micromass Multicarb Sample Preparation System". The CO_2 released by the samples following the reactions:

$$[3CaCO_3+2H_3PO_4 \rightarrow 3CO_2\uparrow+3H_2O+Ca_3(PO_4)_2]$$

The CO_2 produced was rendered moisture free by passing through cryogenic cold-traps and transferred cryogenically into a VG PRISM -IRMS. The measurement of ^{18}O and ^{16}O was done using mass discriminator at 46 ($^{12}C^{18}O^{16}O$) and 44 ($^{12}C^{16}O^{16}O$) respectively. Results are reported with reference to an international standard NBS19 calibrated with PeeDee Belmenite. The precision of oxygen isotope analysis is within ± 0.08 ‰. The measurement of oxygen isotopes was done at the Godwin Laboratory, University of Cambridge, UK. While, all pre-processing work was carried-out at ICP-AES laboratory of National Institute of Oceanography.

4.5. Surface Salinity Estimation

The paleo-salinity can be estimated from a combination of measurement of oxygen isotopes and Mg/Ca of planktonic foraminifera. The obtained SSTs were utilized in Epstein *et al.*'s (1953) paleo-temperature equation to calculate $\delta^{18}O_{SEAWATER}$. The $\delta^{18}O_{SEAWATER}$ was further corrected for global ice volume effect given by Shackleton (2000). Thus, the residual $\delta^{18}O_{SEAWATER}$ obtained reflects the local salinity (or summer monsoon intensity) in the study region. Both the local salinity and residual $\delta^{18}O_{SEAWATER}$ vary as a function of E-P and hence are linearly related. Thus obtained local $\delta^{18}O_{SEAWATER}$ can be translated into salinity using any of the calibrations given for the Arabian Sea (Rostek *et al.*, 1993; Delaygue *et al.*, 2001; Dahl and Oppo, 2006). Dahl and Oppo's (2006) calibration ($y = 0.57x - 20$) is used in the present study since it has superior linear correlation coefficient ($r = +0.95$) compared to other two calibrations and the samples used by them to develop this calibration are distributed across the Arabian Sea and hence most representative. In the equation, 'y' is salinity and 'x' is residual $\delta^{18}O_{SEAWATER}$.

4.6. Radiocarbon dating

Radiocarbon or ^{14}C dating is one of the most significant discoveries of the 20th century, which is widely used as an essential part of the paleoclimate and archaeological research. It is the best-known absolute dating methods till present, which was developed by J. R. Arnold and W. F. Libby in 1949. The ^{14}C was the first cosmogenic isotope to be detected (Ruben and Kamen, 1941; Libby, 1946). It is a cosmogenic nuclide produced by cosmic radiation interacting with atmospheric nitrogen (Masarik and Beer, 1999), and enters the global carbon cycle as $^{14}CO_2$, which is well mixed within the atmosphere. This $^{14}CO_2$ is incorporated into the terrestrial organic matter through the process of photosynthesis, while it is present as a dissolved inorganic carbon species in seawater. Any carbonate material precipitated from seawater at a given time preserves the ^{14}C composition of the seawater in its body.

The ^{14}C isotope is radioactive and decays back to ^{14}N by β-decay with a half-life of 5730 ± 40 years. Naturally, ^{14}C represents only 1 ppt of all the carbon on Earth. Due

to its radioactive nature, the ^{14}C can be used as chronometer. It's half-life of 5730 y restricts the age determination to ~50 kyr BP with reference to 1950 AD. The modern accelerator mass-spectrometric (AMS) techniques are capable of measuring few atoms of ^{14}C with exceptionally high precision. In older samples, there is not enough ^{14}C left to date them accurately. The 1950 AD is the reference point for the paleoclimate chronology as this year has witnessed a large input of radiocarbon in the Earth's system due to explosion of atom bombs that significantly altered the natural ^{14}C inventory.

Because of ocean circulation, the radiocarbon ages derived for different marine regions differ depending upon the difference between the contemporary atmospheric ^{14}C content and the local ^{14}C content of seawater. The difference in age caused due to this mismatch is known as the "reservoir age" and requires to be subtracted from the measured ages from marine carbonate samples. By convention, the correction is of 400 years (Stuvier and Braziunas, 1993), but varies from region to region with maximum of 1600 years for Southern Oceans and < 300 years in sub-tropical gyre region. These differences in the reservoir ages are due to combination of different patterns in air-sea interaction, upwelling, deepwater circulation, sea ice cover etc. The so far known best model output for pre-anthropogenic reservoir age is that of Butzin et al. (2005), which suggests 620 years for tropical oceans (ice free oceans) (Stuvier and Braziunas, 1993; Butzin et al., 2005). However, the Marine Reservoir Correction database gives a slightly lower reservoir age for the EAS. Here in this study, I have taken the average of the reservoir ages available for EAS (~600 y) (http://calib.qub.ac.uk/marine/).

The AMS ^{14}C dates were obtained from NSF-AMS dating facility of Physics Department of the Arizona University, USA. For radiocarbon measurements, around 1000 tests (equivalent to ~10 mg of $CaCO_3$) of G. sacculifer and G. ruber (white variety) were picked from 100 to 350 μ size fractions. In total, 33 such sections from four sediment cores were prepared for dating. These sections were younger than 40 ka as per the SPECMAP oxygen-isotope chronology. The radiocarbon dates were corrected for the reservoir age (600 y) defined for EAS region. The reservoir corrected dates were converted in to calendar age using on-line CalPal-2007_HULU calibration (www.intcal.qub.ac.uk; Danzeglocke et al., 2009).

5.1. Chronology of the sediment cores

Well-defined and closely comparable depth variations of $\delta^{18}O_{G.\,sacculifer}$ in all the four sediment cores with those of standard reference curve, and progressive decay of ^{14}C with depth in sediment cores together clearly rule out any possibility of mixing or slumping of the recovered sediment. This confirmation is a primary requirement for any paleoclimate study utilizing sediment cores. Absolute ages for the sediment cores on calendar-year time-scale were obtained by calculating the sedimentation rates between two adjacent radiocarbon dated sections. Beyond the radiocarbon dated sections, the chronology was established using sedimentation rates obtained between two adjacent MIS boundaries. The isotope stage boundaries in the studied sediment cores were identified by comparing their $\delta^{18}O_{G.sacculifer}$ depth-profiles to LR04 benthic stack of Lisiecki and Raymo (2005) and tuned to their ages.

5.2. Radiocarbon ages

The radiocarbon ages (measured solar ages and converted calendar ages) for the dated sections of the sediment cores are given in Table 3. From the table, it is clear that none of the four sediment core-tops are completely preserved. Recent most depositional history of sedimentation ranging from ~1800 y BP to ~5500 y BP has been erased from these sediment cores due to loss of core-tops during sample collection or by natural erosion of the younger sediment by bottom currents (Banakar et al., 1991). However, in all the sediment cores major portion of the Holocene Period (present interglacial) is still intact, hence allows comparison of reconstructed Holocene climatology with that of preceding cold period (LGM) climatology.

Table 3. Details of AMS ^{14}C dates obtained for four sediment cores. (Calendar age was calculated after correcting ^{14}C age for reservoir age: 600 yr).

Sediment core	Depth in core (cm)	^{14}C Measured Age		Calendar Age	
		yr BP	± yr	cal yr BP	± yr
SK117/GC08	1	2847	26	2259	64
	15	7775	52	8000	37
	25	11546	74	12887	100
	49	16031	91	18519	298
	79	21660	150	25214	393
	103	25910	230	30180	230
	125	30140	450	33805	433
	149	30550	460	34124	402
SK129/CR04	1.5	2533	38	1885	42
	20	7144	53	7466	38
	40	12616	85	14005	224
	48	14190	110	16563	383
	70	19060	120	22073	327
	80	21660	360	25216	535
	100	23940	190	28100	243
	120	26160	260	30556	481
	150	28370	340	32369	364
SK129/CR05	2	3497	39	3048	67
	19	4763	45	4710	88
	39	11405	60	12784	71
	49	12290	64	13575	142
	69	16016	92	18498	303
	77	18430	120	21365	365
	89	18960	150	22005	336
	99	19830	140	23003	295
	119	24550	240	28816	423
	149	28660	340	32564	386
SK117/GC04	1	5314	42	5456	99
	25	10285	56	11039	139
	39	11297	61	12683	57
	65	14549	77	17202	215
	81	15670	110	18279	248
	91	15900	120	18395	300
	101	17241	97	19912	302
	119	18300	110	21112	325
	149	20000	150	23177	315

5.3. Sedimentation rates

Rate of sedimentation in marine regimes provides insights into mass accumulation rate of various components (originated both within the sea and on land) at the seafloor through particle settling. The sedimentation rates for a given region also provide necessary tool to establish stratigraphy of sediment core with which the past-events can be distinguished. The average Holocene sedimentation rate obtained for the studied sediment cores ranges between 2.4 cm/kyr (SK117/GC08) and 8.3 cm/kyr (SK129/CR05). The sedimentation rates during the LGM (MIS 2) have nearly doubled in SK117/GC08 and SK129/CR04, while increased only marginally in SK129/CR05 (Table 4).

Table 4. Sedimentation rates obtained from four sediment cores for Holocene (MIS-1) and LGM (MIS-2) sections.

Sediment core	Sedimentation rate (cm/kyr)	
	MIS 1	MIS 2
SK117/GC08	2.44	4.30
SK117/GC04	6.48	Incomplete*
SK129/CR05	8.32	9.05
SK129/CR04	3.18	5.60

*Radiocarbon data for GC04 is available only for last 23 kyr, hence MIS2 is incomplete

5.4. Variation of oxygen-isotopes with depth in sediment cores

Tables 5 to 8 contain oxygen isotope variations with age in studied sediment cores. The depth values corresponding to the age values are not provided in these tables, but are presented as age-depth relationship figures.

Table 5. Variation of $\delta^{18}O_{G.\ sacculifer}$ with age extracted from SK117/GC08 core

Age cal kyr BP	$\delta^{18}O_{G.\ sacculifer}$ v PDB ‰	Age cal kyr BP	$\delta^{18}O_{G.\ sacculifer}$ v PDB ‰
4.72	-1.436	25.62	0.450
5.54	-1.453	26.04	0.358
6.36	-1.532	26.45	0.421
7.18	-1.294	26.87	0.307
8.00	-1.650	27.28	0.285
8.98	-0.946	27.69	0.168
9.95	-1.053	28.11	0.290
10.93	-0.530	28.52	0.293
11.91	-0.654	28.94	0.277
12.89	-0.545	29.35	0.228
13.36	-0.241	29.76	0.102
13.83	-0.225	**30.18**	0.098
14.30	0.052	30.51	0.046
14.76	0.032	30.84	-0.109
15.23	0.022	31.17	-0.070
15.70	0.019	31.50	-0.060
16.17	0.165	31.83	-0.124
16.64	0.286	32.16	-0.072
17.11	0.210	32.49	-0.141
17.58	0.144	32.82	-0.217
18.05	0.140	33.15	-0.060
18.52	0.396	33.48	-0.176
20.30	0.308	**33.81**	-0.299
20.75	0.278	33.83	-0.254
21.19	0.411	33.86	-0.328
21.64	0.311	33.89	-0.151
22.08	0.328	33.91	-0.084
22.53	0.352	33.94	0.140
22.98	0.378	33.96	0.008
23.42	0.363	33.99	-0.049
23.87	0.347	34.01	0.026
24.31	0.470	34.04	-0.166
24.76	0.326	34.07	-0.028
		34.12	-0.050

Bold numbers are radiocarbon ages. Core-top age is 2.26 ky BP for which $\delta^{18}O$-data not available. The $\delta^{18}O$-data is from Banakar *et al.*, 2005; Chodankar *et al.*, 2005.

From Table 5, it is evident that the lowest (lightest) $\delta^{18}O_{G.sacculifer}$ (-1.65‰) occurs at 15 cm depth corresponding to 8 cal kyr BP. The $\delta^{18}O$ variation is marginal in the upper 19 cm section. The highest (heaviest) $\delta^{18}O$ (0.47‰) occurs at 75 cm. The Termination-1 (mid-point of the heaviest and the lightest $\delta^{18}O$ $_{G.}$ $_{sacculifer}$) is evident at 25 cm depth 12.89 cal kyr BP. The $\delta^{18}O$ $_{G.\ sacculifer}$ shows a rapid decrease between 49 and 19 cm depth sections, i.e., ~18.5 and 10 cal kyr BP respectively. The sections between 85 and 49 cm (26.5 to 18.5 cal kyr BP) show marginal variation (within ±0.1‰). Below 79 cm depth until the end of the radiocarbon dated section (149 cm, i.e., ~34 cal kyr BP) the isotopic variation is moderate. The age-depth model for this core is given in Figure 12.
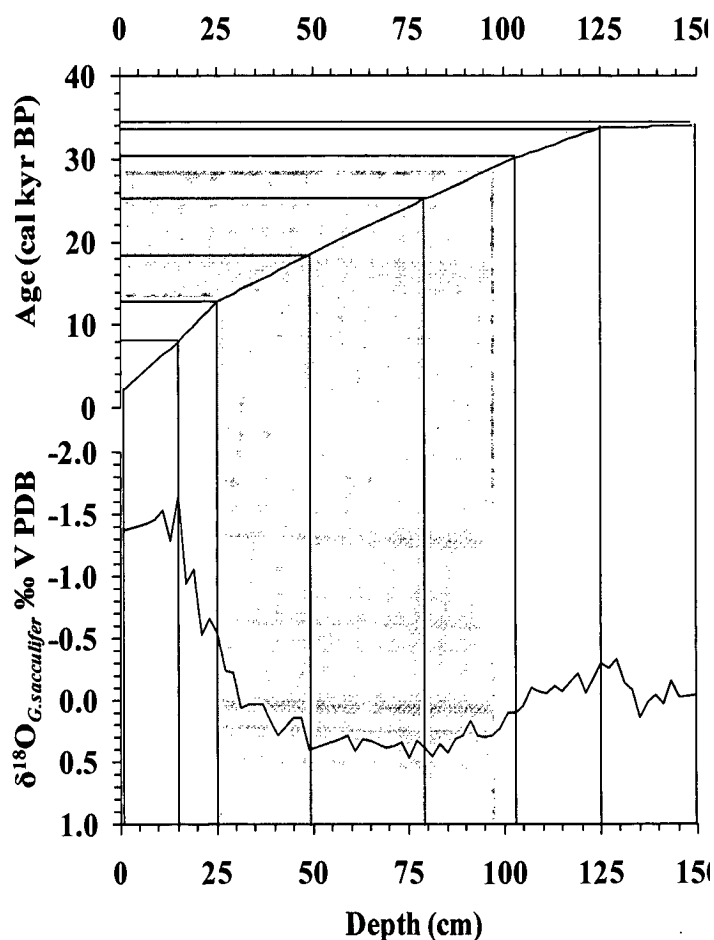
Figure 12. The age model derived for sediment core SK117/GC08 based on radiocarbon dates. The LGM is shown by shaded region. The radiocarbon dated section depths (cm) are shown with vertical lines and corresponding calendar age is shown with connecting horizontal lines. Age-depth curve shows changes in sedimentation rates.

Table 6. Variation of $\delta^{18}O_{G.\ sacculifer}$ with age extracted from SK117/GC04

Age cal kyr BP	$\delta^{18}O_{G.\ sacculifer}$ v PDB ‰	Age cal kyr BP	$\delta^{18}O_{G.\ sacculifer}$ v PDB ‰
5.45	-1.517	18.01	0.214
5.92	-1.212	18.15	0.220
6.38	-1.528	**18.28**	0.196
6.85	-1.823	18.30	0.282
7.31	-1.608	18.33	0.208
7.78	-1.813	18.35	0.145
8.25	-1.969	18.38	0.201
8.71	-1.493	**18.40**	0.337
9.18	-1.388	18.70	0.252
9.64	-1.553	19.00	0.138
10.11	-1.318	19.31	0.244
10.58	-1.334	19.61	0.070
11.04	-1.459	**19.91**	0.125
11.27	-1.524	20.04	0.181
11.51	-1.179	20.17	0.137
11.74	-0.734	20.30	0.176
11.98	-0.659	20.44	0.222
12.21	-0.724	20.57	0.288
12.44	-0.709	20.70	0.225
12.68	-0.704	20.84	0.241
13.03	-0.659	20.97	0.247
13.37	-0.524	**21.11**	0.414
13.72	-0.339	21.24	0.190
14.07	-0.695	21.38	0.287
14.42	-0.509	21.51	0.263
14.76	-0.263	21.65	0.612
15.11	-0.317	21.78	0.108
15.46	-0.391	21.91	0.255
15.80	0.085	22.05	0.161
16.15	-0.560	22.18	0.157
16.50	-0.034	22.32	0.304
16.84	0.002	22.45	0.320
17.20	0.228	22.58	0.206
17.34	0.095	22.72	0.113
17.47	0.111	22.85	0.269
17.60	0.097	22.99	0.278
17.74	0.183	**23.12**	0.315
17.88	0.139		

Bold numbers are radiocarbon ages

60

From Table 6 it is evident that the lowest $\delta^{18}O_{G.\ sacculifer}$ (-1.97‰) is recorded at 13 cm depth corresponding to 8.25 cal kyr BP. The variation in $\delta^{18}O_{G.\ sacculifer}$ from 25 cm depth to core-top corresponding to 11.27 to 5.45 cal kyr BP is about ±0.4‰ around a mean of −1.6‰. From 63 cm depth (16.84 cal kyr BP) the $\delta^{18}O_{G.\ sacculifer}$ decreases rapidly from 0.00‰ to -1.46‰ at 25 cm depth (11.04 cal kyr BP). The Termination-1 is evident at 39 cm depth 13 cal kyr BP. Below 65 cm until the end of radiocarbon dated section the variation in $\delta^{18}O_{G.\ sacculifer}$ is within ±0.2‰ around a mean of 0.3‰ (Figure 13).
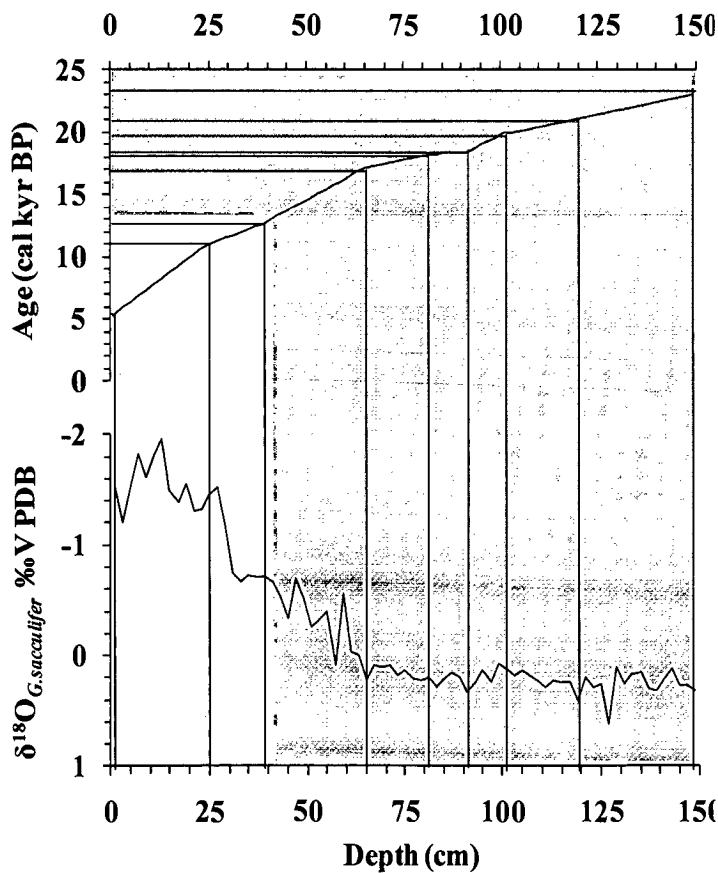
Figure 13. The age model derived for sediment core SK117/GC04 based on radiocarbon dates. The LGM is shown by shaded region. The radiocarbon dated section depths (cm) are shown with vertical lines and corresponding calendar age is shown with connecting horizontal lines. Age-depth curve shows changes in sedimentation rates.

Table 7. Variation of $\delta^{18}O_{G.\ sacculifer}$ with age extracted from SK129/CR05

Age cal kyr BP	$\delta^{18}O_{G.\ sacculifer}$ v PDB ‰	Age cal kyr BP	$\delta^{18}O_{G.\ sacculifer}$ v PDB ‰
3.05	-1.857	20.65	-0.260
3.34	-1.762	**21.36**	-0.260
3.54	-2.127	21.47	-0.262
3.73	-1.982	21.58	-0.064
3.93	-1.707	21.68	0.043
4.12	-1.712	21.79	-0.164
4.32	-1.937	21.90	-0.200
4.51	-1.983	**22.00**	-0.096
4.71	-1.858	22.20	-0.102
5.52	-1.953	22.40	-0.047
6.32	-1.966	22.60	-0.163
7.13	-1.918	22.80	-0.098
7.94	-1.871	**23.00**	-0.023
8.75	-1.843	23.58	-0.269
9.55	-1.816	24.17	-0.255
10.36	-1.708	24.75	-0.170
11.17	-1.440	25.33	-0.256
11.98	-1.073	25.91	-0.272
12.78	-0.895	26.49	-0.368
12.94	-0.897	27.07	-0.293
13.10	-0.775	27.65	-0.409
13.26	-0.647	28.23	-0.484
13.42	-0.730	**28.82**	-0.490
13.57	-0.552	29.07	-0.415
14.07	-0.335	29.32	-0.491
14.56	-0.267	30.32	-0.573
15.05	-0.169	30.56	-0.638
15.54	-0.082	30.81	-0.492
16.04	-0.235	31.06	-0.467
16.53	-0.177	31.31	-0.520
17.02	-0.084	31.56	-0.576
17.51	-0.167	31.81	-0.691
18.01	-0.059	32.06	-0.565
18.50	0.088	32.31	-0.640
19.21	-0.044	**32.56**	-0.684
19.93	-0.187		

Bold numbers are the radiocarbon ages.

The core-top (0-4 cm) $\delta^{18}O$ _G. sacculifer_ in SK129/CR05 is -1.86‰ and the lowest $\delta^{18}O_{G.\ sacculifer}$ (-2.13‰) is recorded at 7 cm depth corresponding to 3.54 cal kyr BP (Table 7). The $\delta^{18}O_{G.\ sacculifer}$ vary marginally in 33 and 2 cm section that corresponds to 10.4 to 3.05 cal kyr BP time-slab. The heaviest $\delta^{18}O$ is recorded at 71 cm depth having an age of 19.21 cal kyr BP. The Termination-1 is evident at 41 cm depth 13 cal kyr BP. The $\delta^{18}O$ value shows rapid decrease from –0.044 to –1.708‰ from 71 cm to 33 cm (Figure 14). The $\delta^{18}O_{G.\ sacculifer}$ shows marginal variation between 71 and 99 cm. From end of the radiocarbon-dated interval (149 cm) to 99 cm depth the $\delta^{18}O$ exhibit gradual increasing trend from –0.684‰ to –0.023‰ corresponding a time-interval of 32.56 to 23 cal kyr BP (Figure 14).
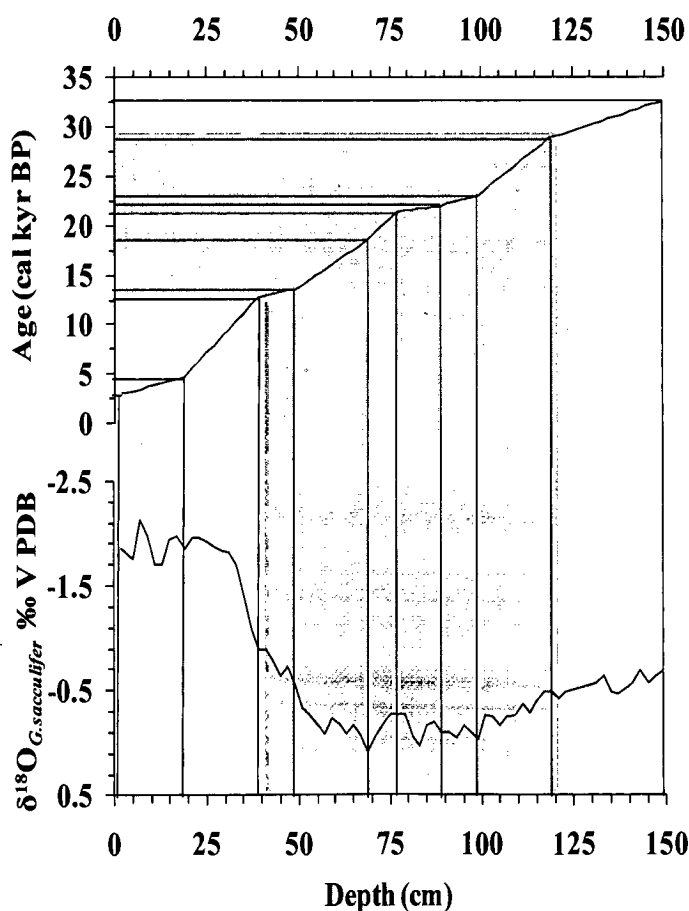
Figure14. The age model derived for sediment core SK129/CR05 based on radiocarbon dates. The LGM is shown by shaded region. The radiocarbon dated sections (depth-cm) are shown by vertical lines and corresponding calendar age is shown by connecting horizontal lines. Age-depth curve shows changes in sedimentation rates.

Table 8. Variation of $\delta^{18}O_{G.\ sacculifer}$ with age extracted from SK129/CR04

Age cal kyr BP	$\delta^{18}O_{G.\ sacculifer}$ v PDB ‰	Age cal kyr BP	$\delta^{18}O_{G.\ sacculifer}$ v PDB ‰
1.89	-1.777	25.36	-0.595
2.19	-1.816	25.94	-0.320
3.54	-1.762	26.51	-0.437
4.75	-1.883	27.09	-0.529
5.96	-2.043	27.67	-0.327
8.12	-1.975	28.22	-0.518
11.39	-1.366	28.72	-0.600
14.00	-0.804	29.21	-0.520
15.61	-0.488	29.70	-0.732
16.57	-0.535	30.07	-0.748
16.82	-0.583	30.32	-0.551
17.82	-0.361	**30.57**	-0.617
18.82	-0.487	30.75	-0.586
19.57	-0.440	30.93	-0.665
20.07	-0.110	31.11	-0.559
20.82	-0.506	31.35	-0.736
21.57	-0.230	31.53	-0.868
22.07	0.004	31.65	-0.646
22.70	-0.158	31.83	-0.652
23.33	-0.601	32.07	-0.570
24.27	-0.455	**32.37**	-0.716
25.22	-0.525		

Bold numbers are radiocarbon ages. $\delta^{18}O$ data is from Chodankar, *et al.*, 2005.

Table 8 contains the depth profile of oxygen isotope variation of *G. sacculifer* along with radiocarbon ages The $\delta^{18}O_{G.sacculifer}$ in core-top section (1.5 cm corresponding to 1.89 cal kyr BP) is -1.78‰. The lowest $\delta^{18}O_{G.sacculifer}$ is recorded at 15 cm depth dating to 6.0 cal kyr BP while heaviest (0.004‰) is recorded at 70 cm depth corresponding to an age of 22 cal kyr BP. The $\delta^{18}O_{G.sacculifer}$ shows a rapid decrease from 70 cm (i.e., 22 cal kyr BP) to 32 cm depth (i.e., 11.39 cal kyr BP) and its variation from last radiocarbon-dated section (149 cm; 32.37 cal kyr BP) up to 40 cm (14 cal kyr BP) is between –0.9 and 0.0‰ (Figure 15). Termination-1 is evident at 36 cm (13 cal kyr BP).
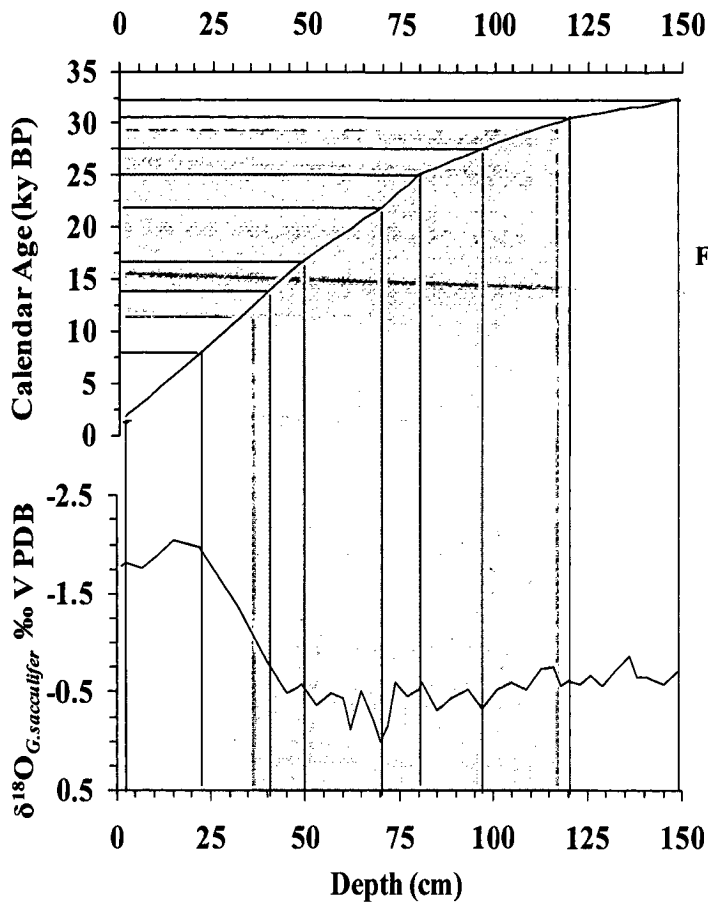
Figure 15. The age model derived for sediment core SK129/CR04 based on radiocarbon dates. The LGM is shown by shaded region. The radiocarbon dated sections (depth-cm) are shown by vertical lines and corresponding calendar age is shown by connecting horizontal lines. Age-depth curve shows changes in sedimentation rates.

5.5. Quality control results of Mg/Ca measurement

High-precision measurements of Mg and Ca are required for obtaining reliable paleo-SST data. The quality is normally achieved by analyzing a QC-solution having known Mg/Ca (mmol/mol) compatible to expected range of Mg/Ca (mmol/mol) in the solutions prepared from dissolving *G. sacculifer* tests. This QC solution also contains the appropriate levels of elements such as Al, Mn, and Fe representing contaminants. Analyzing QC at regular intervals while analyzing the sample solutions would help in assessing the precision and accuracy of the results. The results of QC analyses over a long period (~2 years) of sample measurement are given in Table 9.

Table 9. Mg/Ca ratios measured in QC-solutions along with sample solutions of different sediment cores.

[Actual Mg/Ca (mmol/mol) of QC-solutions is given in parentheses against each of them. Two different concentration QC solutions were used to assess the consistency of results at both higher- and lower-ends of the expected Mg/Ca ratios in planktonic foraminifera skeletons of tropical oceans].

SK117/GC08 QC-1 (2.76)	SK117/GC04 QC-2 (5.15)	SK129/CR05 QC-3 (5.14)	SK129/CR04 QC-4 (2.76)
2.740	5.365	5.168	2.753
2.738	5.155	5.066	2.701
2.717	5.105	5.190	2.642
2.671	5.127	5.150	2.649
2.675	5.034	4.982	2.646
2.683	5.076	5.018	2.668
2.681	5.254	5.168	2.684
2.643	5.365	5.087	2.587
2.692	5.380	5.095	2.593
2.622	5.348	5.186	2.581
2.663	5.255	5.111	2.627
2.774	5.281	5.267	2.618
2.715	5.231	5.220	2.551
2.729	5.336	5.105	2.756
2.773	5.263	5.251	2.764
2.755	5.225	5.266	2.753
2.806	5.077	5.099	2.664
2.783	5.124	5.393	2.674
2.785	5.204	5.046	2.633
2.788	5.224	5.029	2.736
2.740	5.139	5.004	2.689
2.683	5.206	5.039	2.642
2.603	5.082	5.037	2.613
2.625	5.101	4.978	2.682
2.740	5.183	4.955	2.690
2.688	5.203	5.162	
2.633	5.276	5.159	
2.644	5.209	5.189	
2.707	5.176	5.023	
2.642	5.231	5.216	
2.665	5.185	5.133	
2.678	5.211	5.180	
		5.301	
		5.134	
		5.104	
		5.092	
		5.104	
		5.100	

Please note: The statistics of the QC results is discussed in next chapter.

5.6. Mg/Ca and contaminant elements

Tables 10 through 13 below contain elemental ratios calculated from the measured values. The ratios of Mg to Ca are from intensity calibration technique, while other element-to- Mg or Ca ratios are obtained from the IR measured concentrations using standard calibration.

Table 10. Temporal variation of Mg/Ca in SK117/GC08 sediment core along with Ca and Mg normalized data of contaminant elements. (Bold fonts in age column are radiocarbon dated sections)

Age (cal kyr BP)	mmol/mol				mol/mol		
	Mg/Ca	Fe/Ca	Al/Ca	Mn/Ca	Fe/Mg	Al/Mg	Mn/Mg
2.26	4.009	0.140	0.047	0.206	0.035	0.012	0.051
4.72	3.937	0.133	0.039	0.157	0.035	0.010	0.041
5.54	3.789	0.166	0.051	0.155	0.045	0.014	0.042
6.36	3.688	0.212	0.058	0.136	0.059	0.016	0.038
7.18	3.774	0.136	0.063	0.173	0.036	0.218	0.046
8.00	3.496	0.183	-0.028	0.170	0.052	-0.003	0.049
8.98	3.547	0.085	0.045	0.186	0.024	0.014	0.053
9.95	3.693	0.195	0.046	0.199	0.053	0.034	0.054
10.93	3.843	0.181	0.026	0.103	0.047	0.007	0.027
11.91	3.871	0.144	-0.005	0.090	0.037	-0.001	0.023
12.89	3.940	0.142	0.027	0.097	0.036	0.001	0.080
13.36	3.975	0.173	0.046	0.117	0.044	0.067	0.117
13.83	3.995	0.172	0.020	0.118	0.043	0.001	0.090
14.30	3.338	0.184	0.000	0.113	0.056	0.000	0.113
14.76	3.640	0.084	0.000	0.110	0.023	0.000	0.030
15.23	3.637	0.093	0.000	0.119	0.026	0.000	0.033
15.70	3.542	0.193	0.000	0.111	0.054	-0.001	0.005
16.17	3.545	0.151	-0.056	0.126	0.042	-0.004	0.099
16.64	3.073	0.150	-0.040	0.157	0.048	-0.003	0.112
17.11	3.556	0.173	-0.020	0.130	0.048	-0.001	0.111
17.58	3.301	0.148	-0.050	0.142	0.045	-0.004	0.095
18.05	3.132	0.203	-0.087	0.186	0.064	-0.007	0.094
18.52	3.290	0.165	-0.140	0.229	0.050	-0.011	0.120
20.30	3.268	0.195	-0.048	0.265	0.062	-0.003	0.129
20.75	3.330	0.190	-0.097	0.281	0.057	-0.008	0.121
21.19	3.273	0.209	-0.111	0.231	0.063	-0.008	0.141
21.64	3.355	0.135	-0.042	0.279	0.040	-0.003	0.152
22.08	3.467	0.173	-0.074	0.230	0.050	-0.004	0.097
22.53	3.440	0.190	-0.071	0.257	0.055	-0.005	0.130
22.98	3.609	0.170	-0.042	0.223	0.047	-0.002	0.114

23.42	3.204	0.201	-0.034	0.234	0.062	-0.002	0.155
23.87	3.115	0.211	-0.098	0.211	0.067	-0.008	0.159
24.31	3.257	0.161	-0.050	0.228	0.049	-0.004	0.138
24.76	3.080	0.162	-0.046	0.240	0.052	-0.003	0.131
25.21	3.312	0.114	-0.033	0.267	0.034	-0.010	0.080
25.62	3.180	0.105	-0.005	0.283	0.033	-0.002	0.090
26.04	3.122	0.079	-0.006	0.270	0.026	-0.002	0.089
26.45	3.224	0.088	-0.013	0.251	0.029	-0.004	0.082
26.87	3.291	0.086	-0.019	0.256	0.027	-0.006	0.081
27.28	3.132	0.097	-0.004	0.284	0.033	-0.001	0.095
27.69	3.245	0.004	0.005	0.145	0.002	0.003	0.076
28.11	3.341	0.074	-0.046	0.243	0.022	-0.014	0.073
28.52	3.276	0.083	-0.017	0.268	0.027	-0.005	0.087
28.94	3.289	0.084	-0.005	0.236	0.026	-0.002	0.072
29.35	3.216	0.169	-0.105	0.223	0.053	-0.010	0.132
29.76	3.353	0.093	-0.053	0.225	0.028	-0.016	0.068
30.18	3.351	0.107	-0.067	0.243	0.033	-0.020	0.074
30.51	3.202	0.084	-0.031	0.211	0.027	-0.010	0.068
30.84	3.271	0.171	-0.087	0.209	0.053	-0.008	0.141
31.17	3.313	0.169	-0.048	0.229	0.051	-0.004	0.141
31.50	3.363	0.154	-0.026	0.233	0.046	-0.008	0.069
31.83	3.327	0.097	-0.031	0.227	0.029	-0.009	0.069
32.16	3.395	0.103	0.000	0.217	0.030	0.000	0.064
32.49	3.475	0.191	-0.004	0.259	0.056	-0.001	0.075
32.82	3.597	0.101	-0.010	0.220	0.029	-0.003	0.062
33.15	3.598	0.149	0.037	0.254	0.042	0.002	0.139
33.48	3.408	0.145	-0.106	0.214	0.043	-0.031	0.063
33.81	3.405	0.121	-0.004	0.221	0.036	-0.001	0.065
33.83	3.761	0.150	0.047	0.254	0.041	0.003	0.147
33.86	3.823	0.221	0.043	0.248	0.058	0.011	0.066
33.89	3.657	0.177	0.000	0.218	0.048	0.000	0.059
33.91	3.439	0.173	0.000	0.227	0.050	0.000	0.065
33.94	3.577	0.087	0.000	0.222	0.024	0.000	0.061
33.96	3.481	0.213	0.057	0.247	0.062	0.017	0.072
33.99	3.563	0.217	0.037	0.242	0.061	0.010	0.159
34.01	3.418	0.216	0.000	0.244	0.064	0.000	0.072
34.04	3.639	0.169	0.047	0.275	0.047	0.013	0.077
34.07	3.575	0.191	0.062	0.254	0.054	0.018	0.072
34.12	3.597	0.131	0.000	0.266	0.037	0.000	0.075

Table 11. Temporal variation of Mg/Ca in SK117/GC04 sediment core along with Ca and Mg normalized data of contaminant elements. (Bold fonts in age column are radiocarbon dated sections)

Age (cal kyr BP)	mmol/mol				mol/mol		
	Mg/Ca	Fe/Ca	Al/Ca	Mn/Ca	Fe/Mg	Al/Mg	Mn/Mg
5.45	4.285	0.636	0.029	0.252	0.147	0.007	0.058
5.92	4.134	0.255	7.407	0.081	0.089	0.000	0.028
6.38	4.115	0.281	0.000	0.131	0.068	0.000	0.032
6.85	4.285	0.243	0.000	0.123	0.052	0.000	0.027
7.31	4.281	0.237	0.000	0.115	0.055	0.000	0.027
7.78	4.125	0.125	0.014	0.090	0.031	0.003	0.022
8.25	4.083	0.218	0.000	0.106	0.049	0.000	0.024
8.71	4.041	0.095	0.024	0.064	0.024	0.006	0.016
9.18	4.232	0.107	0.021	0.068	0.025	0.005	0.016
9.64	4.326	0.126	0.011	0.070	0.029	0.002	0.016
10.11	4.448	0.249	0.016	0.096	0.055	0.004	0.021
10.58	4.374	0.106	0.033	0.060	0.024	0.008	0.014
11.04	4.273	0.117	0.000	0.063	0.027	0.000	0.015
11.27	4.456	0.211	0.016	0.077	0.047	0.004	0.017
11.51	4.464	0.206	0.060	0.072	0.046	0.014	0.016
11.74	4.571	0.175	0.000	0.073	0.038	0.000	0.016
11.98	4.247	0.203	0.029	0.111	0.048	0.007	0.026
12.21	3.869	0.075	0.030	0.065	0.019	0.008	0.017
12.44	4.061	0.307	0.086	0.140	0.076	0.021	0.035
12.68	3.803	0.113	0.029	0.078	0.030	0.008	0.021
13.03	3.771	0.170	0.034	0.070	0.045	0.009	0.019
13.37	3.736	0.094	0.040	0.056	0.025	0.011	0.015
13.72	3.775	0.107	0.026	0.066	0.029	0.007	0.018
14.07	3.912	0.104	0.018	0.050	0.027	0.005	0.013
14.42	3.987	0.172	0.138	0.066	0.043	0.035	0.017
14.76	4.102	0.166	0.100	0.067	0.041	0.025	0.017
15.11	4.137	0.247	0.134	0.073	0.048	0.026	0.014
15.46	4.172	0.213	0.117	0.064	0.051	0.028	0.015
15.80	4.107	0.149	0.113	0.066	0.036	0.028	0.016
16.15	3.997	0.193	0.122	0.071	0.048	0.031	0.018
16.50	4.162	0.197	0.092	0.067	0.048	0.022	0.016
16.84	3.982	0.220	0.127	0.077	0.055	0.032	0.019
17.20	3.934	0.191	0.122	0.067	0.049	0.031	0.017
17.34	3.931	0.228	0.074	0.091	0.058	0.019	0.023
17.47	3.763	0.225	0.111	0.074	0.052	0.026	0.017
17.60	4.016	0.196	0.089	0.073	0.049	0.022	0.018
17.74	3.958	0.219	0.104	0.074	0.055	0.026	0.019

17.88	3.899	0.186	0.087	0.066	0.048	0.022	0.017
18.01	4.133	0.349	0.146	0.115	0.085	0.035	0.028
18.15	3.766	0.270	0.158	0.118	0.072	0.042	0.031
18.28	3.794	0.313	0.107	0.109	0.082	0.028	0.029
18.30	4.198	0.432	0.146	0.176	0.103	0.035	0.042
18.33	4.208	0.343	0.099	0.132	0.082	0.024	0.031
18.35	4.363	0.317	0.096	0.152	0.073	0.022	0.035
18.38	4.199	0.672	0.218	0.223	0.121	0.039	0.040
18.40	4.034	0.338	0.105	0.183	0.070	0.022	0.038
18.70	3.870	0.390	0.104	0.179	0.074	0.020	0.034
19.00	3.705	0.457	0.106	0.116	0.095	0.022	0.024
19.31	3.541	0.266	0.090	0.090	0.057	0.019	0.019
19.61	3.377	0.286	0.171	0.156	0.069	0.041	0.037
19.91	3.212	0.112	0.083	0.099	0.035	0.026	0.031
20.04	3.071	0.126	0.094	0.092	0.041	0.031	0.030
20.17	3.394	0.205	0.107	0.104	0.061	0.032	0.031
20.30	3.123	0.154	0.095	0.104	0.049	0.031	0.033
20.44	3.140	0.108	0.088	0.096	0.034	0.028	0.031
20.57	3.320	0.229	0.096	0.127	0.068	0.029	0.038
20.70	3.339	0.108	0.107	0.088	0.032	0.032	0.026
20.84	3.729	0.200	0.044	0.096	0.054	0.012	0.026
20.97	3.534	0.125	0.100	0.097	0.036	0.028	0.028
21.11	3.298	0.256	0.078	0.115	0.078	0.024	0.035
21.24	3.303	0.073	0.085	0.092	0.022	0.026	0.028
21.38	3.982	0.193	0.090	0.147	0.048	0.022	0.037
21.51	3.561	0.256	0.060	0.097	0.072	0.017	0.027
21.65	4.039	0.179	0.093	0.109	0.044	0.023	0.027
21.78	4.176	0.262	0.049	0.133	0.047	0.009	0.024
21.91	4.313	0.328	0.063	0.154	0.067	0.013	0.031
22.05	3.821	0.100	0.093	0.115	0.026	0.025	0.030
22.18	4.313	0.226	0.102	0.153	0.053	0.024	0.036
22.32	4.012	0.269	0.158	0.164	0.067	0.039	0.041
22.45	4.461	0.290	0.058	0.084	0.065	0.013	0.019
22.58	3.669	0.187	0.098	0.089	0.051	0.027	0.024
22.72	3.529	0.171	0.103	0.137	0.049	0.029	0.039
22.85	3.701	0.287	0.120	0.202	0.061	0.026	0.043
22.99	3.873	0.185	0.100	0.182	0.048	0.026	0.047
23.12	3.787	0.859	0.112	0.227	0.177	0.023	0.047

Table 12. Temporal variation of Mg/Ca in SK129/CR05 sediment core along with Ca and Mg normalized data of contaminant elements. (Bold fonts in age column are radiocarbon dated sections)

Age (cal kyr BP)	mmol/mol				mol/mol		
	Mg/Ca	Fe/Ca	Al/Ca	Mn/Ca	Fe/Mg	Al/Mg	Mn/Mg
3.05	4.463	0.361	1.723	0.083	0.081	0.387	0.019
3.34	4.294	0.537	0.200	0.082	0.126	0.047	0.019
3.54	4.125	0.145	0.159	0.069	0.035	0.039	0.017
3.73	4.426	0.125	0.266	0.218	0.028	0.060	0.049
3.93	4.186	0.936	1.522	0.606	0.212	0.344	0.137
4.12	4.549	0.235	2.641	0.070	0.053	0.593	0.016
4.32	4.455	0.184	1.096	0.086	0.041	0.246	0.019
4.51	4.594	0.097	0.118	0.049	0.022	0.027	0.011
4.71	4.346	0.117	1.001	0.050	0.027	0.231	0.011
5.52	4.273	0.196	1.309	0.044	0.045	0.300	0.010
6.32	4.404	0.173	1.517	0.077	0.039	0.345	0.018
7.13	4.263	0.108	0.896	0.083	0.025	0.210	0.020
7.94	4.417	0.073	0.852	0.095	0.017	0.193	0.021
8.75	4.091	0.040	0.124	0.068	0.009	0.028	0.015
9.55	4.054	0.052	0.096	0.053	0.012	0.022	0.012
10.36	4.469	0.085	0.672	0.631	0.019	0.151	0.142
11.17	4.467	0.123	1.073	0.052	0.028	0.241	0.012
11.98	4.591	0.024	0.111	0.056	0.005	0.025	0.013
12.78	4.533	0.100	1.083	0.722	0.022	0.239	0.160
12.94	4.143	0.077	0.398	0.063	0.019	0.096	0.015
13.10	3.986	0.067	0.521	0.051	0.017	0.131	0.013
13.26	4.160	0.036	0.135	0.061	0.009	0.032	0.015
13.42	4.348	0.059	8.252	0.060	0.014	1.900	0.014
13.57	4.346	0.060	0.727	0.074	0.014	0.167	0.017
14.07	3.902	0.052	0.157	0.059	0.013	0.040	0.015
14.56	4.264	0.092	0.086	0.050	0.025	0.023	0.014
15.05	4.078	0.093	0.276	0.061	0.023	0.068	0.015
15.54	4.022	0.098	0.144	0.073	0.025	0.036	0.018
16.04	4.101	0.087	0.148	0.073	0.022	0.036	0.018
16.53	3.633	0.168	0.110	0.068	0.047	0.031	0.019
17.02	3.517	0.178	0.148	0.114	0.045	0.037	0.029
17.51	3.779	0.201	0.165	0.126	0.051	0.042	0.032
18.01	3.999	0.026	0.138	62.380	0.005	0.009	0.029
18.50	3.840	0.035	0.178	87.330	0.005	0.017	0.042
19.21	3.587	0.233	0.181	0.158	0.065	0.050	0.044
19.93	3.886	0.277	0.232	0.183	0.059	0.050	0.039
20.65	3.957	0.185	0.159	0.138	0.045	0.039	0.033

21.36	3.984	0.296	0.148	0.145	0.073	0.037	0.036
21.47	4.074	0.263	0.172	0.137	0.064	0.042	0.033
21.58	3.922	0.417	0.183	0.162	0.103	0.045	0.040
21.68	3.834	0.241	0.131	0.118	0.060	0.032	0.029
21.79	3.699	0.216	0.148	0.182	0.055	0.038	0.047
21.90	3.760	0.203	0.126	0.157	0.053	0.033	0.041
22.00	3.889	0.234	0.133	0.178	0.057	0.033	0.044
22.20	3.603	0.941	0.150	0.210	0.191	0.030	0.043
22.40	3.824	0.198	0.143	0.168	0.051	0.037	0.043
22.60	3.851	0.222	0.113	0.185	0.053	0.027	0.044
22.80	3.849	0.386	0.103	0.196	0.094	0.025	0.048
23.00	3.489	-0.036	0.135	0.147	-0.010	0.037	0.040
23.58	3.362	0.284	0.169	0.196	0.081	0.048	0.056
24.17	3.327	0.240	0.128	0.174	0.070	0.037	0.051
24.75	3.090	0.058	0.109	0.143	0.015	0.027	0.036
25.33	3.290	0.066	0.087	0.124	0.019	0.025	0.036
25.91	3.122	0.069	0.092	0.141	0.018	0.024	0.036
26.49	3.161	0.083	0.108	0.110	0.022	0.029	0.029
27.07	3.200	0.102	0.114	0.145	0.026	0.029	0.037
27.65	3.071	0.118	0.077	1.017	0.035	0.023	0.302
28.23	3.308	0.042	0.087	0.121	0.012	0.026	0.036
28.82	3.437	0.127	0.092	0.146	0.033	0.024	0.038
29.07	3.217	0.035	0.079	0.151	0.009	0.021	0.040
29.32	3.250	0.060	0.074	0.162	0.016	0.020	0.044
30.32	3.342	-0.058	0.130	0.131	-0.015	0.033	0.033
30.56	3.277	0.032	0.680	0.142	0.008	0.169	0.035
30.81	3.213	0.366	1.607	0.186	0.090	0.393	0.046
31.06	3.268	0.110	0.907	0.181	0.026	0.216	0.043
31.31	3.441	0.111	1.354	0.133	0.027	0.330	0.032
31.56	3.643	0.166	0.098	0.142	0.042	0.025	0.036
31.81	3.397	0.038	0.113	0.115	0.010	0.028	0.029
32.06	3.465	0.290	0.108	0.167	0.072	0.027	0.041
32.31	3.480	0.396	0.179	0.159	0.099	0.045	0.040
32.56	3.484	0.622	2.046	0.198	0.178	0.584	0.057

Table 13. Temporal variation of Mg/Ca in SK129/CR04 sediment core along with Ca and Mg normalized data of contaminant elements. (Bold fonts in age column are radiocarbon dated sections)

Age (cal kyr BP)	mmol/mol				mol/mol		
	Mg/Ca	Fe/Ca	Al/Ca	Mn/Ca	Fe/Mg	Al/Mg	Mn/Mg
1.89	3.876	0.737	0.164	0.069	0.186	0.037	0.017
2.19	3.966	0.737	0.164	0.069	0.186	0.037	0.017
3.54	3.793	1.335	0.000	0.167	0.353	0.000	0.044
4.75	3.762	0.753	0.000	0.104	0.202	0.000	0.028
5.96	3.971	0.998	0.000	0.095	0.256	0.000	0.024
8.12	3.773	0.547	0.000	0.132	0.147	0.000	0.036
11.39	3.879	0.488	0.000	0.136	0.129	0.000	0.036
14.00	3.894	3.183	0.000	0.217	0.821	0.000	0.056
15.61	4.132	0.744	0.000	0.203	0.181	0.000	0.049
16.57	3.919	0.744	0.000	0.203	0.181	0.000	0.049
16.82	3.707	0.872	0.000	0.251	0.239	0.000	0.069
17.82	3.627	1.451	0.000	0.506	0.331	0.000	0.116
18.82	3.340	0.686	0.000	0.199	0.211	0.000	0.061
19.57	3.741	0.890	0.000	0.151	0.244	0.000	0.041
20.07	3.443	0.102	0.000	0.050	0.030	0.000	0.015
20.82	3.635	0.371	0.000	0.131	0.103	0.000	0.036
21.57	3.181	0.177	0.000	0.047	0.056	0.000	0.015
22.07	3.259	0.243	0.000	0.066	0.075	0.000	0.020
22.70	3.231	0.336	0.000	0.149	0.106	0.000	0.047
23.33	3.370	0.427	0.000	0.113	0.130	0.000	0.034
24.27	3.507	0.754	0.000	0.194	0.221	0.000	0.057
25.22	3.345	0.754	0.000	0.194	0.221	0.000	0.057
25.36	3.183	0.473	0.000	0.172	0.154	0.000	0.056
25.94	3.631	0.467	0.000	0.145	0.128	0.000	0.040
26.51	3.278	0.321	0.000	0.137	0.098	0.000	0.042
27.09	3.434	0.529	0.000	0.199	0.157	0.000	0.059
27.67	3.398	0.192	0.000	0.069	0.059	0.000	0.021
28.22	3.532	0.575	0.000	0.236	0.166	0.000	0.068
28.72	3.703	0.205	0.000	0.068	0.056	0.000	0.018
29.21	3.680	0.191	0.000	0.079	0.053	0.000	0.022
29.70	3.784	0.193	0.000	0.073	0.052	0.000	0.020
30.07	3.610	0.340	0.000	0.247	0.097	0.000	0.071
30.32	3.440	0.315	0.000	0.214	0.092	0.000	0.062
30.57	3.402	0.182	0.000	0.095	0.053	0.000	0.028
30.75	3.331	0.138	0.000	0.070	0.042	0.000	0.021

30.93	3.440	0.396	0.000	0.246	0.118	0.000	0.073
31.11	3.579	0.451	0.000	0.235	0.131	0.000	0.068
31.35	3.423	0.132	0.000	0.067	0.040	0.000	0.020
31.53	3.440	0.363	0.000	0.207	0.111	0.000	0.063
31.65	3.852	0.129	0.000	0.080	0.033	0.000	0.021
31.83	3.456	0.108	0.000	0.067	0.031	0.000	0.019
32.07	3.564	0.108	0.000	0.077	0.030	0.000	0.021
32.37	3.636	0.134	0.172	0.065	0.036	0.041	0.017

5.7. Mg/Ca SST and estimated salinity

Tables 14 through 17 below contain age, SST and salinity calculated from the measured values. The SST was derived from Mg/Ca ratios and the salinity was estimated from the residual $\delta^{18}O_{SEAWATER}$, which was calculated by incorporating SST and $\delta^{18}O_{G.sacculifer}$ data in Epstein's (1953) equation (see Method section). Ice-volume correction (Shackleton, 2000) of 1 kyr interval was interpolated to the ages of each section of the studied sediment cores. This value was subtracted from $\delta^{18}O_{G.\ sacculifer}$ to obtain ice-corrected $\delta^{18}O$ of calcite which was further calculated for residual $\delta^{18}O_{SEAWATER}$ to obtain salinity (see Method section).

Table 14. Temporal variation of SST and salinity estimation from SK117/GC08 sediment core for the last 100 kyr. (Bold fonts in age column are radiocarbon dated sections)

Age	SST	Salinity	Age	SST	Salinity
cal kyr BP	°C	psu	cal kyr BP	°C	psu
2.26	29.1	36.2	22.98	28.2	37.9
4.72	29.0	36	23.42	27.2	37.9
5.54	28.6	36.1	23.87	27.0	37.7
6.36	28.4	36.1	24.31	27.3	37.9
7.18	28.6	36.4	24.76	26.9	37.9
8.00	27.9	35.8	**25.21**	27.5	37.9
8.98	28.1	36.7	25.62	27.1	37.9
9.95	28.4	36.7	26.04	27.0	37.7
11.91	28.8	36.9	26.45	27.3	38.0
12.89	29.0	36.6	26.87	27.4	38.1
13.36	29.0	37.0	27.28	27.0	38.1
13.83	29.1	36.9	27.69	27.3	37.7
14.76	28.3	37.0	28.11	27.5	37.8
15.23	28.3	36.9	28.52	27.4	38.0
15.70	28.0	37.0	28.94	27.4	38.2
16.17	28.1	37.2	29.35	27.2	38.2
17.11	28.1	37.3	29.76	27.6	37.9
17.58	27.4	37.4	**30.18**	27.6	37.9
18.05	27.0	37.5	30.51	27.2	37.9
18.52	27.4	37.6	30.84	27.4	37.7
20.30	27.4	37.6	31.17	27.5	37.7
20.75	27.5	37.5	31.50	27.6	37.8
21.19	27.4	37.8	31.83	27.5	37.7

Age cal kyr BP	SST °C	Salinity psu	Age cal kyr BP	SST °C	Salinity psu
21.64	27.6	37.7	32.16	27.7	37.7
22.08	27.9	37.7	32.49	27.9	37.5
22.53	27.8	37.8	32.82	28.2	37.3
33.15	28.2	37.5	51.06	28.1	37.8
33.48	27.7	37.4	51.62	27.6	37.9
33.81	27.7	37.3	52.19	28.2	37.8
33.83	28.6	37.3	52.75	27.3	37.9
33.86	28.7	37.1	53.32	28.1	37.2
33.89	28.3	37.5	53.88	28.4	37.1
33.91	27.8	37.7	54.44	27.9	37.6
33.94	28.1	38.0	55.01	28.6	37.4
33.96	27.9	37.8	55.58	28.0	37.4
33.99	28.0	37.7	56.14	28.3	37.6
34.01	27.7	37.9	57.00	28.7	37.4
34.04	28.3	37.5	57.75	28.2	37.7
34.07	28.1	37.7	58.32	27.8	37.8
34.12	28.2	37.7	58.70	28.6	37.5
34.68	28.1	37.9	59.07	27.3	37.6
35.25	28.9	37.5	59.45	26.9	37.7
36.38	28.5	37.3	59.83	27.0	37.7
36.95	28.6	37.4	60.20	26.7	37.4
37.51	28.4	37.4	60.58	27.4	37.2
38.07	27.8	37.7	60.96	27.4	37.4
38.92	28.0	37.5	61.52	27.1	37.3
40.05	28.4	37.5	62.09	27.4	37.5
43.43	28.8	37.8	62.46	27.3	37.2
45.69	28.1	37.4	62.84	27.3	37.1
46.54	26.9	37.1	63.22	27.5	37.2
47.11	27.9	37.2	63.60	27.5	37.3
47.67	27.2	37.7	63.97	27.5	37.5
48.24	27.1	37.4	64.35	26.9	37.4
48.80	28.1	37.4	64.73	27.0	37.2
49.65	27.5	37.2	65.10	27.4	37.4
50.49	27.5	37.7	65.48	27.9	36.9

Age cal kyr BP	SST °C	Salinity psu	Age cal kyr BP	SST °C	Salinity psu
65.86	29.2	36.8	85.00	28.4	37.1
66.23	27.6	37.0	85.75	28.2	37.0
66.61	27.9	36.7	86.50	28.1	37.2
67.00	28.6	36.8	87.00	27.9	37.2
67.55	27.8	36.8	87.39	28.2	37.4
68.12	28.2	36.5	87.78	28.4	37.3
68.50	28.0	36.4	88.17	28.2	36.9
69.06	28.0	36.6	88.56	27.3	37.2
69.63	27.8	36.7	88.95	28.2	37.0
70.00	28.0	36.6	89.34	29.6	37.2
70.75	28.4	36.5	89.74	28.5	37.0
71.50	28.5	36.3	90.52	28.9	37.3
72.63	28.2	36.6	90.91	28.5	37.2
73.75	27.9	37.1	91.30	27.9	37.0
74.50	28.3	36.6	92.08	28.7	37.0
75.25	28.8	36.9	92.47	28.7	36.6
76.00	28.8	36.9	92.87	29.3	36.4
76.75	28.4	36.6	93.26	29.3	36.0
77.50	28.4	37.0	93.65	29.4	36.1
78.25	28.5	36.7	94.04	27.8	36.3
79.00	28.9	36.6	94.43	28.7	36.2
79.75	28.4	36.6	94.82	28.6	36.1
80.50	28.6	36.7	95.21	28.6	36.1
81.25	28.4	36.5	95.61	28.4	36.1
82.00	28.4	36.8	96.00	29.0	35.7
82.50	28.7	36.8	96.38	28.5	36.2
83.00	27.8	37.7	96.78	28.0	36.5
83.50	28.3	37.6	97.17	28.7	36.6
84.00	28.4	37.8	97.76	28.9	36.8
84.50	28.4	37.2			

Table 16. Temporal variation of SST and salinity estimation from SK129/CR05 sediment core for the last 33 kyr. (Bold fonts in age column are radiocarbon dated sections)

Age cal kyr BP	SST °C	Salinity psu	Age cal kyr BP	SST °C	Salinity psu
3.05	30.0	35.1	20.65	28.9	36.5
3.34	29.7	35.3	**21.36**	29.0	36.5
3.54	29.3	34.8	21.47	29.2	36.5
3.73	29.9	35.0	21.58	28.9	36.9
3.93	29.4	35.5	21.68	28.7	37.1
4.12	30.2	35.5	21.79	28.3	36.8
4.32	30.0	35.1	21.90	28.5	36.7
4.51	30.3	35.0	**22.00**	28.8	36.9
4.71	29.8	35.2	22.20	28.1	37.0
5.52	29.6	35.1	22.40	28.6	37.0
6.32	29.9	35.2	22.60	28.7	36.9
7.13	29.6	35.2	22.80	28.7	37.0
7.94	29.9	35.2	**23.00**	27.8	37.2
8.75	29.2	35.1	23.58	27.5	36.7
9.55	29.2	35.3	24.17	27.4	36.7
10.36	30.0	35.4	24.75	26.8	37.0
11.17	30.0	35.7	25.33	27.3	36.8
11.98	30.3	36.0	25.91	26.9	36.6
12.78	30.1	35.9	26.49	27.0	36.8
12.94	29.3	35.9	27.07	27.1	37.2
13.10	29.0	36.1	27.65	26.8	36.8
13.26	29.4	36.3	28.23	27.4	36.6
13.42	29.8	36.0	**28.82**	27.7	36.8
13.57	29.8	36.3	29.07	27.2	37.1
14.07	28.8	36.6	29.32	27.2	36.9
14.56	29.6	36.7	30.32	27.5	36.8
15.05	29.2	36.5	30.56	27.3	36.8
15.54	29.1	36.7	30.81	27.1	37.0
16.04	29.3	36.4	31.06	27.3	37.1
16.53	28.2	36.6	31.31	27.7	37.0
17.02	27.9	36.8	31.56	28.2	36.8
17.51	28.5	36.7	31.81	27.6	36.7
18.01	29.0	37.0	32.06	27.8	36.9
18.50	28.7	37.0	32.31	27.8	36.7
19.21	28.1	36.7	**32.56**	27.8	36.6
19.93	28.8	36.6			

Table 17. Temporal variation of SST and salinity estimation from SK129/CR04 sediment core for the last 150 kyr. (Bold fonts in age column are radiocarbon dated sections)

Age cal kyr BP	SST °C	Salinity psu	Age cal kyr BP	SST °C	Salinity psu
1.89	28.65	36.8	30.75	27.33	38.1
2.19	28.85	36.7	30.93	27.61	38.0
3.54	28.46	36.7	31.11	27.95	38.1
4.75	28.38	36.5	31.35	27.57	37.9
5.96	28.86	36.4	31.53	27.61	37.7
8.12	28.41	36.4	31.65	28.59	38.0
11.39	28.66	37.2	31.83	27.65	38.1
14.00	28.69	37.2	32.07	27.91	38.2
15.61	29.22	37.2	**32.37**	28.09	37.8
16.57	28.75	37.2	34.61	27.24	38.0
16.82	28.26	37.1	36.85	28.48	37.5
17.82	28.07	37.8	39.83	27.91	37.8
18.82	27.35	37.3	42.82	28.01	37.7
19.57	28.34	37.4	45.80	28.10	38.0
20.07	27.62	38.2	48.79	28.13	38.0
20.82	28.08	37.4	51.03	28.05	38.0
21.57	26.94	38.1	52.52	27.98	38.4
22.07	27.14	38.6	54.76	28.19	37.8
22.70	27.07	38.4	57.00	27.63	38.2
23.33	27.43	37.5	57.59	27.82	38.3
24.27	27.77	37.6	58.18	28.25	38.2
25.22	27.37	37.7	58.77	28.35	38.0
25.36	26.94	37.5	59.36	27.96	37.9
25.94	28.08	37.7	59.95	27.70	37.9
26.51	27.19	37.9	60.54	28.61	37.7
27.09	27.59	38.0	61.13	27.37	37.8
27.67	27.50	38.1	61.72	27.27	37.9
28.22	27.84	37.7	62.32	27.36	37.6
28.72	28.25	37.8	62.91	27.33	37.8
29.21	28.19	38.1	63.50	27.28	38.1
29.70	28.44	37.7	64.09	27.82	37.9
30.07	28.02	37.7	64.68	28.30	37.7
30.32	27.61	38.1	65.56	27.68	37.8
30.57	27.51	38.1	66.75	27.85	37

Age cal kyr BP	SST °C	Salinity psu	Age cal kyr BP	SST °C	Salinity psu
67.93	27.74	37.5	98.52	27.92	37.2
69.11	28.16	37.2	99.35	28.52	36.9
70.00	28.61	37.7	100.19	28.67	36.9
71.00	28.03	37.4	101.45	28.54	37.0
75.25	28.08	37.2	102.71	28.51	37.0
76.38	28.57	37.6	103.55	28.50	36.7
77.50	27.51	37.4	104.39	28.38	36.7
78.25	27.94	37.4	105.22	28.80	36.9
79.00	27.44	37.3	106.06	28.23	36.6
79.75	28.38	37.2	106.90	28.23	36.2
80.50	29.02	37.6	107.74	29.34	36.6
81.25	28.52	37.3	109.00	27.92	36.8
82.00	28.02	37.2	111.21	29.82	36.4
82.29	28.48	37.4	113.42	28.47	36.3
82.57	28.19	37.9	115.63	29.32	35.9
82.86	28.32	37.8	117.84	29.52	36.4
83.14	28.21	38.2	120.05	28.73	36.3
83.43	28.56	38.4	123.00	29.00	36.1
83.71	27.40	38.4	124.47	30.02	36.7
84.00	28.84	38.0	125.94	29.15	36.6
84.28	27.66	38.0	127.42	29.76	37.1
84.57	27.92	38.2	128.89	29.34	37.2
85.00	28.62	37.6	131.10	30.16	37.6
85.43	27.31	37.8	134.05	28.66	36.8
85.86	28.38	37.7	136.26	29.93	36.8
86.43	28.17	37.7	137.73	29.03	36.6
87.00	27.94	37.9	139.94	29.00	36.4
89.40	28.31	37.8	142.89	28.41	36.9
91.20	29.24	37.4	145.84	27.50	37.6
93.00	29.56	36.9	148.79	28.24	37.7
94.80	27.76	36.9			
96.00	28.62	36.1			
96.84	28.13	36.5			
97.68	29.38	36.7			

The sedimentation rates, time-series of $\delta^{18}O_{G.\ sacculifer}$, SST and salinity for radiocarbon dated sediment sections covering the last ~ 35 kyr in the four sediment cores from EAS and the results obtained for sediment sections beyond the radiocarbon dated intervals of two sediment cores (SK117/GC08 and SK129/CR04) are discussed separately in this chapter. It is well known that most of the biogeochemical processes in the Arabian Sea unambiguously respond to changes in monsoon intensities. Interestingly, the modern Indian monsoon is shown to have remote connections including high latitude climates (Goes et al., 2005, and references therein). The interlinked regional monsoon and global climate perhaps induce significant changes in local climatology. Therefore, it is possible to understand the climate forced changes in monsoon activity in the geological past by recovering proxy signatures preserved in the sediment. The local sea surface climatology if reconstructed accurately would provide valuable information on teleconnections observed between modern and paleo-monsoon and the global climate.

6.1. Sedimentation rates in the EAS

The sedimentation rates in a given region provide a preliminary understanding about the climate and associated biogeochemical processes. The overall distribution of sediments in the Arabian Sea depends on few primary factors. The prevailing climate is one such factor, which greatly influences the formation and dispersion of sediments, both terrigenous as well as biogenous. As a result, latitude and climate-dependant patterns in sediment distribution could be expected. The Arabian Sea acts as a natural reservoir in stacking various monsoon related proxies in its sediments as the region comes under the direct influence of the monsoons.

The sediments undergo compaction after sedimentation which is driven towards lower porosities and higher densities as a function of increasing stress and chemical reactions. By accounting for post-depositional compaction, accurate accumulation rates can be calculated for each dated time interval. Data such as porosity, dry bulk sediment and mass accumulation rates are needed to determine the compaction of the sediments. However, these parameters were not generated as the focus was on SST and salinity

reconstructions. Hence, the rate of sedimentation addressed here is based on raw calculation only i.e., interpolating between two radiocarbon dated sections.

The sedimentation rates vary from marginal to a factor of two between the Holocene and LGM (Table 4). Based on sedimentation rates, the time-resolution obtained for the studied sediment cores is between ~ 200 and 600 yr. The sedimentation rates were nearly double during the LGM in two sediment cores (SK117/GC08 and SK129/CR04) while the core located in the central EAS (SK129/CR05) shows marginal increase.

Two important mechanisms which govern changes in the sedimentation rates in the EAS during Quaternary are: a) changes in glacio-eustatic sea level and b) monsoon climate. Sediment transportation to the marginal seas must have enhanced during lowered sea level i.e., during the glacial period. Because, during this period the drainage basin enlarges through exposure of the continental shelf and by enhancing the river-competence due to lowering of their base level (i.e., the mean sea level). The eolian transport of fine-grained terrigenous material is also expected to enhance during the cold and dry glacial climate. Thus, the climate transitions leave clear impressions in the seabed sediment in the form of changing sedimentation rates.

The location of the studied sediment cores are such that they have nearly equal latitudinal spacing representing most of the EAS region (Figure 9). The terrigenous sediment accumulation in most of the marginal EAS is by erosion by rivers draining the Sahyadris (Western Ghats or Deccan Mountains). The Indus river input is mostly limited to northern Arabian Sea margin and deep basin. Other than the fluvial derived terrigenous sediments, the wind derived dust from Arabia is also significant particularly during the LGM (Sirocko *et al.*, 2000) as a result of expanded deserts (Sarnthein, 1978). The studied region, however, has spatially variable water column productivity, which is another factor in determining the type of sedimentation in EAS.

The lower sedimentation rates in the EAS during the Holocene (Table 4) therefore largely are due to lowered terrigenous input and productivity. The previous studies have indicated that the summer monsoons were stronger during interglacial periods than during the glacial periods and *vice-versa* during the glacial periods (Duplessy, 1982; Prell and Van Campo, 1986; Clemens and Prell, 1990; Anderson and

Prell, 1993; Rostek *et al.*, 1993; Emeis *et al.*, 1995; Reichart *et al.*, 1998; Banakar *et al.*, 2005). In that case the fluvial erosion in Sahyadris would have been stronger and such input should have been significant in dictating the sedimentation rates. However, these mountain rivers are seasonal and small resulting in less significant role in the Holocene sedimentation in the EAS as compared to a major role of rivers controlling the sedimentation in BoB. On the other hand, the enhanced sediment accumulation rates during the LGM can be explained by intensified winter monsoons resulting in increased flux of wind derived terrigenous material into the EAS. This suggestion is well supported by the studies on past changes in Thar Desert. The southward extension of the Thar desert has been shown to have reached the Orsang Basin (22° 5' N, 73° 35' E), a tributary of the Narmada River (Somayajulu *et al.*, 1999). The expansion of this desert due to enhanced aridity is expected resulting in increased wind-borne sediment supply to the EAS. The increased biological production in the EAS due to increased injection of nutrient rich subsurface waters in to the mixed layer during LGM (Thamban *et al.*, 2001; Banakar *et al.*, 2005) might also have contributed to the overall increase in sedimentation rates in the EAS. The lowered sea level exposing the shelf for erosion might further add-up to the material transport to marginal sea such as EAS (Chodankar, 2004). *Thus, the glacial-interglacial difference in sedimentation in the study region has been mainly due to relative changes in the input of terrigenous material and productivity driven by the relative strength of monsoons.*

6.2. Past variations in $\delta^{18}O_{G.sacculifer}$

The past variations in $\delta^{18}O_{G.sacculifer}$ and major climatic events recorded in the EAS sediment cores are described here. The salient features of $\delta^{18}O$ variability along with their time and magnitude are listed in Table 18.

Table 18. Magnitude of $\delta^{18}O_{G.\ sacculifer}$ variation at different climate markers recorded in four sediment cores (Age in cal kyr BP)

Parameters	SK117				SK129			
	GC08		GC04		CR05		CR04	
	$\delta^{18}O$	Age	$\delta^{18}O$	Age	$\delta^{18}O$	Age	$\delta^{18}O$	Age
^{14}C dated max. age	34		23		33		32	
Core-top value	-1.37	2.26	-1.52	5.45	-1.86	3.05	-1.77	1.89
Lowest	-1.65	8	-1.97	8	-2.13	3.54	-2.04	6
Highest	0.411	21.19	0.41	21.1	0.09	18.5	0.004	22
Holocene (avg.) (‰)	-1.6		-1.51		-1.87		-1.87	
LGM (avg.) (‰)	0.12		0.21		-0.28		-0.51	
Difference (‰)	-2.0		-2.38		-2.22		-2.04	
Remainder after sea level correction (‰)	0.86		1.18		1.02		0.84	
MIS 1/2 boundary	-0.53	12.89	-0.66	13	-0.77	13		13
Mean of LGM $\delta^{18}O$	0.41± 0.08‰	26-18	0.41± 0.08‰	23-18	0.04± 0.08‰	25-18	0.17± 0.08‰	26-18
Deglaciation beginning	0.14	18	0.23	18	-0.17	18		18
Age of attainment of Holocene Optimum		9		11		10		8
MIS 2/3 boundary		29		-		29		29
Total variation within last glacial period (‰)	± 0.22		± 0.22		± 0.2		± 0.2	

6.2.1. Climate events in SK117/GC08 (see Figure 12)

Radiocarbon dated section of the core SK117/GC08 covers a time period of last ~34 kyr. The MIS 2/1 and 3/2 boundaries occur at 12.89 cal kyr BP and 29 cal kyr BP respectively (Table 5). The age of core-top section (0-2 cm) is 2.26 cal kyr BP and the $\delta^{18}O_{G.\ sacculifer}$ is -1.37‰. The highest $\delta^{18}O_{G.\ sacculifer}$ (0.41‰) occurs at 21.19 cal kyr BP and the lowest (-1.65‰) at ~8 cal kyr BP. The average $\delta^{18}O_{G.\ sacculifer}$ during the Holocene and LGM are -1.6 ‰ and 0.4‰ respectively with glacial-interglacial contrast of -2.06‰. An amount of 1.2‰ of this difference is caused by the global ice volume (Shackleton, 2000). The remainder 0.86‰ should be therefore due to changes in local surface climatology, i.e., SST and salinity. The highest $\delta^{18}O_{G.\ sacculifer}$ (0.41±0.08‰) occur between 26 and 18 cal kyr BP, which may be considered as LGM. Within the Holocene, a distinct decrease in $\delta^{18}O_{G.sacculifer}$ by ~0.2‰ at 8 cal kyr BP is observed. The transition from LGM to Holocene has been gradual. The beginning of deglaciation appears to have initiated at ~18 cal kyr BP to attain the Holocene optimum at ~9 cal kyr BP. The $\delta^{18}O_{G.\ sacculifer}$ of the entire glacial period shows marginal variation within ±0.22‰.

6.2.2. Climate events in SK117/GC04 (see Figure.13)

The radiocarbon dated sediment core spans a period of the last 23 cal kyr BP. The age of core-top section (0-2 cm) is 5.45 cal kyr BP indicating loss of most of the late Holocene record. The MIS 2/1 boundary is evident at 13 cal kyr BP (Table 6). The $\delta^{18}O_{G.\ sacculifer}$ in core-top is -1.52‰. The highest $\delta^{18}O_{G.\ sacculifer}$ (0.41 ‰) occurs at ~21 cal kyr BP and the lowest (-1.97‰) at ~8 cal kyr BP with glacial-interglacial contrast of 2.38‰. The global ice volume corrected difference in $\delta^{18}O_{G.\ sacculifer}$ between LGM and Holocene is 1.18‰, which can be attributed to changes in local climatology. The heaviest $\delta^{18}O_{G.\ sacculifer}$ within the measurement precision band of ±0.08‰ are concentrated between 23 to 18 cal kyr BP representing the LGM. The average $\delta^{18}O_{G.\ sacculifer}$ during the Holocene and LGM are -1.51‰ and 0.21‰. The beginning of deglaciation is observed at ~18 cal kyr BP while Termiantion-1 is recorded at ~13 cal kyr BP. The Holocene optimum is attained at ~11.5 cal kyr BP. Within the Holocene, an increase in $\delta^{18}O_{G.\ sacculifer}$ by about 0.5‰ is observed at ~6 and 7.3 cal kyr BP.

6.3. $\delta^{18}O$ variation and climate events

Table 19 presents timing and magnitude synthesis of important climatic events viz., LGM, Deglaciation and Holocene optimum based on the observations made from four sediment cores which are listed in Table 18.

Table 19. Synthesis of LGM, Deglaciation and Holocene optimum

Climate events	SK117		SK129	
	GC08	GC04	CR05	CR04
	Age cal kyr BP	Age cal kyr BP	Age cal kyr BP	Age cal kyr BP
LGM	26-18	23-18	25-18	26-18
Beginning of deglaciation	18	18	18	18
Attainment of Holocene Optimum	9	11	10	8

Based on the $\delta^{18}O_{G.sacculifer}$ structure depicted in all four studied sediment cores, the LGM-Holocene boundary (MIS2/1) is evident at ~13 kyr BP, while the MIS3/2 boundary is at ~29 kyr BP (Figure 16). The MIS3/2 boundary in particular in these sediment cores shows considerable (5 kyr) timing-offset and MIS2/1 boundary shows ~1 kyr offset as compared to SPECMAP (24 and 11 Ka respectively: Imbrie et al., 1984). Where as, such timing offset is negligible when compared with LR04-Benthic Stack (MIS2/1 at 13 kyr BP and MIS3/2 at 29 kyr BP: Lisiecki and Raymo, 2005). This observation confirms that the important climate events recorded in the studied sediment cores in the form of oxygen-isotope variability are robust and faithful.

6.3.1. Last Glacial Maximum

The LGM (MIS2) is defined as the period of maximum growth and expansion of global ice in most recent geological past preceding the Holocene. This event is reflected as most-enriched $\delta^{18}O$ in calcite-skeletons secreted by foraminifera within the last glacial cycle (between beginning of the MIS-4 or 74 ka and Termination-1 or ~12 ka). The LGM is an important paleoclimatic event since it represents highly contrasting climate of the immediate past as compared to the present day climate. The international

89

CLIMAP dataset forms the basic reference for understanding the ice-age climate. The climate state of the Earth during the LGM was influenced mainly by the global ice sheets (Clark *et al.*, 2009). The LGM is reasonably close to an equilibrium state of climate in which short-term fluctuations were relatively smaller (Mix *et al.*, 2001). Since, the LGM is within the range of precise dating methods (^{14}C and U-Th), it provides a potential source for unified chronologies for both land and marine proxies.

Conventionally, the LGM is defined in sediment cores a point-event of highest $\delta^{18}O_{FORAMINIFERA}$ within the last glacial cycle (74-12 Ka) (Mix *et al.*, 2001), but was not considered as an event that has covered certain period of time. However, the LGM cannot be a spike-like point-event, but is expected to cover a time-period that has witnessed coldest temperatures or lowest sea level stand within the last glacial cycle. *Therefore, in the present study, the LGM is defined as a continuous period within the last glacial cycle that has recorded heaviest $\delta^{18}O_{G.sacculifer}$ fluctuating within the measurement precision band of ±0.08‰.* This most enriched-$\delta^{18}O$ band occurs for a period of 6 to 8 kyr mostly between 26 and 18 cal kyr BP in the present four sediment cores. This observation suggests that, in the Arabian Sea in general and EAS in particular recorded the influence of LGM climate for around 6 to 8 kyr (say ~7 kyr) between 26 and 18 cal kyr BP.

The delimiting of LGM has always been of great debate since the study of paleoclimate gained importance and it is generally thought to have occurred around ~18 kyr BP. It is very unlikely that all the ice sheets and glaciers on the earth reached their maximum growth synchronously at one given point of time. However, the timing, duration and extent of ice cover at LGM differ spatially. The CLIMAP benchmarked the LGM age at 18 kyr BP (Shackleton and Opdyke, 1973), similar to the one defined as midpoint of MIS-2 (24-12 kyr BP) (Shackleton *et al.*, 1977). A multi-proxy approach for the reconstruction of glacial ocean surface (MARGO Project Members, 2009) rigorously assessed the LGM and defined it as period between 23 and 19 cal kyr BP. According to EPILOG (Environmental Processes of the Ice age: Land, Ocean and Glacier: EPILOG), the best method of defining LGM interval was based on the lowest sea level after removing local isostatic effects. Accordingly, they defined the LGM from 23 to 19 kyr B.P. This 4 kyr event, centered on 21 kyr BP, encompasses the center of MIS-2, which

was considered as the actual LGM that was coeval with the lowest sea level stand (Yokoyama *et al.*, 2000).

The LGM recognized in EAS sediment cores from the present study covers 26 to 18 cal kyr BP (Table 18), which nearly concurs with that defined by the EPILOG team (Mix *et al.*, 2001), and is in excellent agreement with global ice sheet dynamics that has reached its maximum growth at 26 kyr BP and sustained until 19 kyr BP (Clark *et al.*, 2009). Clark *et al.* (2009) have arrived at this time-slice for LGM after evaluating 5704 radiocarbon, [10]Be and [3]He data spanning 10 to 50 kyr BP, and corresponding global ice-sheets and mountain-glacier extents. *Thus the LGM identified presently in the EAS sediment as a period covering ~7 kyr between 26 and 18 cal kyr BP is closely comparable to rigorously evaluated global LGM and hence is unambiguously most realistic as compared to previously published definitions, which considered it as a most recent-past heaviest $\delta^{18}O$.*

6.3.2. Last deglaciation

The period during which the Earth's climate switched from cold and dry glacial climate to a warm and wet interglacial climate is known as "deglaciation" or "deglacial transition". During this transition, the marine sedimentary records have been punctuated with several melt-water pulses and Heinrich events characterized by coarse-grained moraine beds within the fine-grained marine sediment deposition. During this time, the terrestrial vegetation began to transform into rain forests from grasslands (Shackleton, 1973). The global deglacial climate shift was initiated due to higher insolation received at Earth's surface resulting from changes in eccentricity of its elliptical orbit around the Sun and in the tilt of its rotation axis (Milankovitch, 1941), which has forced the cold and dry climate of the LGM to change into warm climate of the Holocene.

This climate transition has distinctly influenced the oxygen isotopic composition of the oceanic reservoir, in which most of the ice-locked ^{16}O-enriched water during the LGM began to re-enter the ^{18}O-enriched (or ^{16}O-depeted) oceans. This shift is also associated with rapid lifting of sea level to modern level from its lowered stand by around 120 m during the LGM. The change in $\delta^{18}O$ of global ocean water due to LGM to Holocene climate shift has been quantified as equivalent to 1.2‰ (Shackleton, 2000).

The LGM-Holocene gradient in $\delta^{18}O_{G.\ sacculifer}$ is between 2 and 2.38‰ in the EAS sediment cores. This gradient is closely comparable to other reported values from the AS (Rostek et al., 1993; Sonzogni et al., 1998; Cayre and Bard, 1999; Banakar et al., 2005; 2010; Chodankar et al., 2005; Saher et al., 2007; Anand et al., 2008). The variation in $\delta^{18}O_{G.\ sacculifer}$ within the last glacial period (MIS 2 and latest part of MIS 3) is marginal (± 0.2‰). This marginal fluctuation indicates at the outset that the EAS has not witnessed any major changes in its climatology between ~35 and 18 cal kyr BP.

The beginning of deglaciation (rapid negative excursion of $\delta^{18}O$) in the present sediment cores is recorded at ~18 cal kyr BP and the Holocene-optimum was attained between 8 and 10 cal kyr BP (Table 19). The reorganization of climate from cold LGM to warm Holocene thus appears to have completed within a period of ~8 kyr. *The deglaciation transitions in the present $\delta^{18}O_{G.\ sacculifer}$ records appear mostly progressive and continuous indicating an affinity towards the Antarctic climate variability rather than with D-O type oscillations, which has intermittent fluctuations.* However, the time-resolution achieved in the present sediment cores is not adequate to clearly resolve D-O type climate pattern recorded in the Greenland ice sheets. *As the longest cold interval (stadial: Younger Dryas) in D-O type climate variability is also not reflected in the present $\delta^{18}O_{G.\ sacculifer}$ records (Figures 12 to 15), it is reasonable to draw a link between Antarctic climate and EAS hydrography.*

The beginning of deglaciation is not synchronous across the globe as evidenced at different locations by different proxies. Clark et al. (2009) and Yokoyama et al. (2000) placed the beginning of deglaciation between 22 and 19 kyr BP based on the lowest sea-level stand from dated geological records on tectonically stable northern Australian continental shelf. The beginning of deglaciation recorded in the Atlantic sedimentary records is 17 kyr BP (Bard et al., 2000), ~19 kyr BP in Pacific (Kiefer and Kienast, 2005), ~17 kyr BP in Greenland (Grootes et al., 1993), and ~19 kyr BP in Antarctica (EPICA Community Members, 2006). The deglaciation transition, in general, lasted for ~ 8 kyr between 21 and 11ka (Broecker et al., 1998; Clark et al., 2009). *The beginning of deglaciation and its transition pattern recorded in the EAS sediment cores are closely comparable to LR04 benthic $\delta^{18}O$ record (Figure 16). The timing of initiation and completion of deglacial transition in the EAS sedimentary records*

correlate well with the LGM-Holocene transition recorded in Antarctic ice-core records (Figure 16) (EPICA Community Members, 2006). These observations clearly suggest that the tropical climate pattern appears to have responded to changes in global climate.

6.3.3. $\delta^{18}O_{G.\ sacculifer}$ gradient over the EAS

A north-to-south decreasing $\delta^{18}O_{G.\ sacculifer}$ in core-top sections is evident in the sediment cores from the EAS (Table 18). Core-top $\delta^{18}O_{G.sacculifer}$ in the northern-EAS sediment cores are heavier (~-1.4‰) (SK117/GC04; SK117/GC08) than the core-top values (~-1.8‰) of the central- and southern-sediment cores (SK129/CR05; SK129/CR04). This clear N-S gradient in $\delta^{18}O_{G.\ sacculifer}$ is closely comparable to modern surface salinity structure in the EAS. The southern-EAS is under the perennial influence of low salinity water and the northern-EAS is perennially under high salinity water (Figure 5). *Thus, it appears that the local N-S salinity gradient is the primary driver of the observed differences in core-top $\delta^{18}O_{G.\ sacculifer}$ distribution in EAS.* This relationship provided the basis for relating the $\delta^{18}O_{SEAWATER}$ with salinity in the AS (Rostek *et al.*, 1993; Delaygue *et al.*, 2001). However, there are limitations in this relationship as the said relationship was not found to be strictly linear (see Rohling, 2000).

The time-series of $\delta^{18}O_{G.\ sacculifer}$ for all four cores and its N-S contrast therefore should provide the information on past changes in salinity regime of the EAS. The core-top ages of these sediment cores vary between 1.89 and 5.45 cal kyr BP. As there have been short-term changes in the summer monsoon intensities within the given climate stages, it is necessary to consider only those $\delta^{18}O$ values having similar ages. The SK117/GC04 has the oldest core-top of 5.45 cal kyr BP hence is taken as a reference to compare the N-S variation in $\delta^{18}O_{G.\ sacculifer}$ in other three sediment cores. Accordingly the $\delta^{18}O_{G.\ sacculifer}$ for SK129/GC08 and SK117/GC04 (northern cores) are -1.45‰ and -1.52 ‰ respectively at ~5.5 cal kyr BP, while it is -1.95 ‰ in central –EAS core (SK129/CR05) and -2.04 ‰ for the southern core (SK129/CR04). Here, it can be clearly observed that the $\delta^{18}O_{G.\ sacculifer}$ decreased from north to south even at ~5.5 cal kyr BP. The difference between the northern and southern core is ~ 0.5‰. Assuming that, a) the global ice effect at ~5.5 kyr BP was nearly similar at all the locations, which in fact was,

b) the SST regime at ~5.5 kyr BP was similar to that of today, and, c) the $\delta^{18}O_{SEAWATER}$ salinity relation was the same at 5.5 cal kyr BP as observed today, then, 0.5‰ can be equated to the existing surface salinity gradient of ~1 psu between northern- and southern-EAS (Figure 5). The empirical relationships of salinity and $\delta^{18}O_{SEAWATER}$ obtained for modern seawater also exhibit similar equivalents (see Delaygue *et al.*, 2001; Rostek *et al.*, 1993), hence, the present time-series $\delta^{18}O_{G.\ sacculifer}$ data could be utilized to reconstruct time-series of the EAS salinity. At the LGM (reference age 21 cal kyr BP), the $\delta^{18}O_{G.\ sacculifer}$ in northern-EAS (SK117/GC08) is 0.41‰ and -0.51‰ in the southern-EAS (SK129/CR04), i.e., a difference of ~0.92‰ between northen-EAS and southern-EAS locations. *Compared to N-S difference of 0.5‰ during the Holocene (reference age 5.5 kyr BP), the observed difference for LGM (0.92‰) is significantly higher, suggesting much larger salinity gradient (~1.8 psu) between northern- and southern-EAS during the LGM.*
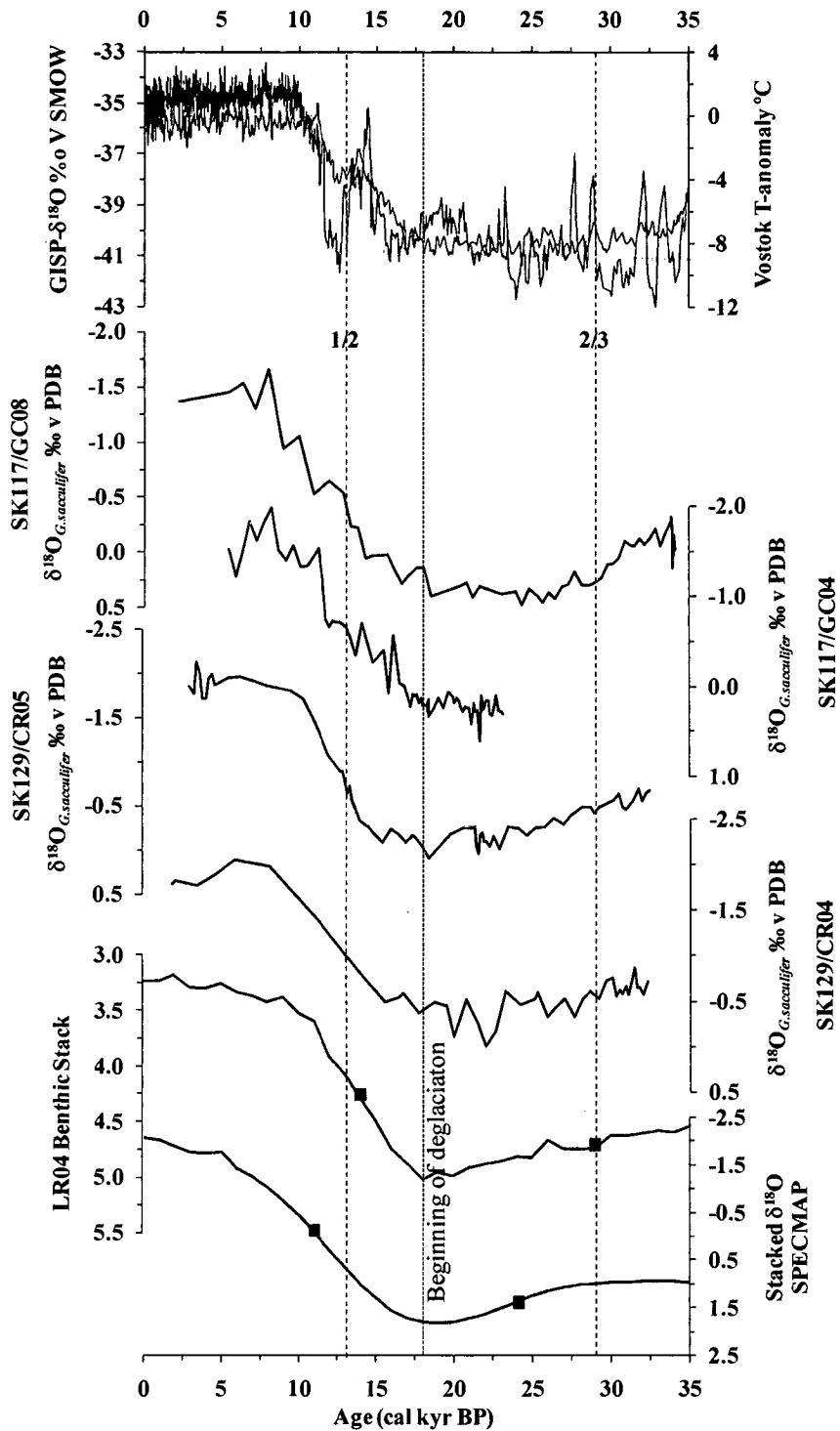
Figure 16. Time-series of EAS oxygen isotope records compared with Antarctic T- Anomaly (Petit *et al.*, 1999), Greenland Ice oxygen-isotopes (Dansgaard *et al.*, 1993), LR04 Benthic Stack (Lisiecki and Raymo, 2005), SPECMAP (Imbrie *et al.*, 1984). Broken line indicates MIS boundaries in the studied EAS sediment cores. Dotted line indicates the beginning of deglaciation. The red and black color filled squares on LR04 benthic record and SPECMAP indicate MIS 2/1 and MIS3/2 in those respective records.

6.4. Reliability of Mg/Ca-Temperatures

Validation of a proxy (here Mg/Ca ratio in *G. sacculifer* calcite) is necessary to establish the fidelity of that proxy in preserving paleoclimatic information without post-depositional alterations. Further, it is also essential to assess the errors associated with any instrumentally generated data. Precise and accurate measurement of Mg/Ca ratios is prerequisite to use this proxy as a tool for SST reconstruction. An ideal approach to ensure quality of the results from chemical analysis is that the matrices of calibration standards and samples should be identical to the extent possible. I have used HNO_3 as the matrix due to its relative freedom from chemical and spectral interferences as compared to acids containing Cl, S, F or P ions. Further, ultra-pure (supra-pure) grade reagents and 18 M Ω de-ionised-water are used throughout the calcite cleaning and dissolution protocols to obtain minimum effect from blank. The multi-element calibration curves having regression coefficient (R^2) of < 0.999 were rejected and re-calibrated. The replicate measurements of solutions having CV > 1% were also repeated until CVs reduced to < 1%. These analytical conditions are expected to yield accurate results as evident in the results obtained for QC solutions (Table 9).

The analytical values of QC solutions measured at different times over a long period of time were averaged and accuracy of the results was calculated. Deviation from actual Mg/Ca in QC was estimated at every sixth sample and appropriate correction was applied to the sample Mg/Ca. Even though the analytical errors in Mg/Ca of QC were very low (< 2.5%: Table 20), correction applied to the sample solutions at every set ensures most accurate results. During analysis of SK117/GC08 core samples, the QC solution having Mg/Ca ratio of 2.72 mmol/mol was used, which has yielded a measured mean Mg/Ca of 2.73 ± 0.06. A QC solution having 5.13 mmol/mol was used while analyzing samples of SK117/GC4 yielded a ratio of 5.137 ± 0.092 mmol/mol. The measured Mg/Ca for the same QC at different time while analyzing samples of SK129/CR5 was 5.126 ± 0.097. For SK129/CR4, the QC used was of 2.761 mmol/mol yielded a ratio of 2.664 ± 0.059 (Table 20).

Table 20. Statistical evaluation of the results of QC-solution analaysis

Parameters	SK117		SK129	
	GC08	GC04	CR05	CR04
*n	32	32	38	28
Actual QC value	2.761	5.151	5.144	2.761
Long term average of QC	2.702	5.207	5.126	2.664
Standard Deviation	0.055	0.092	0.097	0.059
% error	2.05	1.76	1.88	2.2

*n= number of times the QC solution was analyzed at different times. Mg/Ca ratios in mmol/mol.

Although the cleaning steps eliminate most of the contaminants from the final analyte solution, it is advisable to ensure the reliability of cleaning methods by analyzing elements characteristic of the contaminant. Banakar *et al.* (2010) have utilized simple scatter diagrams obtained by plotting 'contaminant elements/Ca' vs 'Mg/Ca' to assess their effect on sample Mg/Ca. Their reasoning was that, if the Mg/Ca ratios were contaminated by Mg or Ca associated with clays or oxides then the above variations are expected to be linear, if not, then their relationship would be random.

The amount of lattice-bound Fe, Al, and Mn in biogenic calcite is negligible and would provide typically < 0.3 mmol/mol of Fe/Ca, Al/Ca and Mn/Ca. Therefore, Mg/Ca ratios associated with > 0.3 mmol/mol of these element/Ca ratios should be rejected. The Fe/Ca, Al/Ca and Mn/Ca for most of the samples from all sediment cores rarely exceeded 0.05 mmol/mol. Whenever these ratios were higher than acceptable the data was regenerated following complete cleaning protocol. The scatter plots of Fe/Ca, Al/Ca, and Mn/Ca (mmol/mol) *vs.* Mg/Ca (mmol/mol) (Figures 17 to 20) showed insignificant relationships (R^2 < 0.3), suggesting that the present Mg/Ca data is mostly free from contamination and hence the estimated SSTs are reliable except for Al/Ca vs Mg/Ca in GC08. Although the R^2 in this case is 0.4, the Al/Ca rarely exceed 0.05 mmol/mol and majority of samples show negative Al contents (i.e, below detection limit) (see Figure 17 caption). Therefore, the contamination by clays (represented by Al) could be considered as negligible.
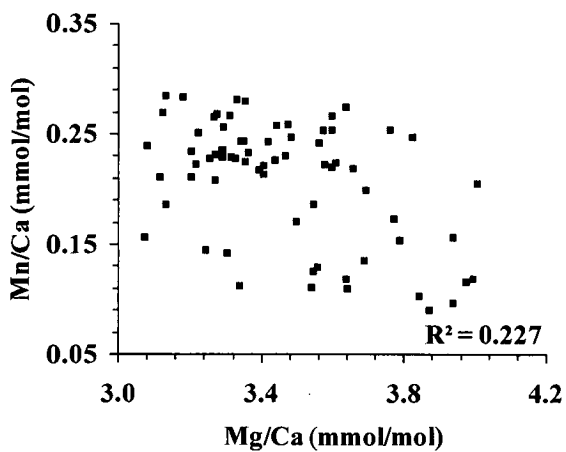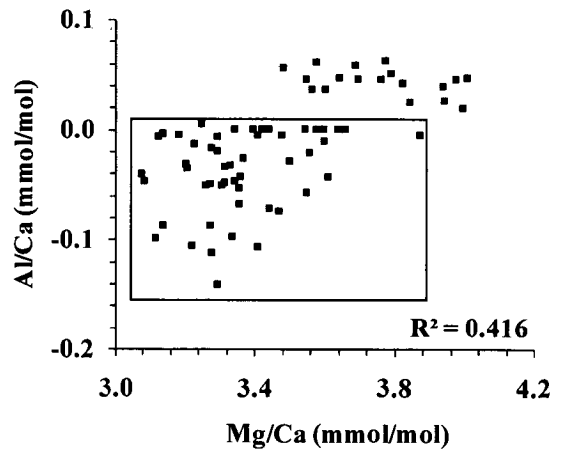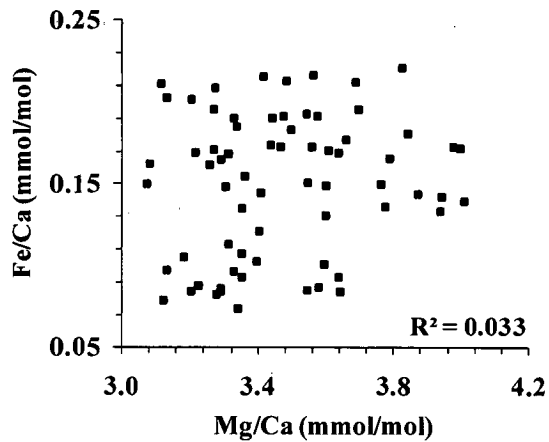
Figure 17. X-Y scatter plots of Fe/Ca, Al/Ca and Mn/Ca (mmol/mol) versus Mg/Ca (mmol/mol) for SK117/GC08 sediment core. The data points enclosed by box in Al/Ca vs Mg/Ca panel indicate Al content below detection limit. The remaining quantifiable Al/Ca (outside the box) do not show any relationship with Mg/Ca.
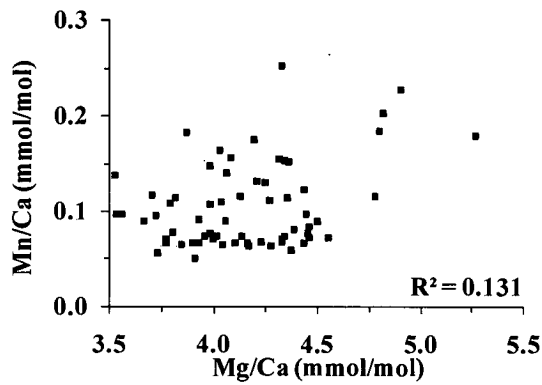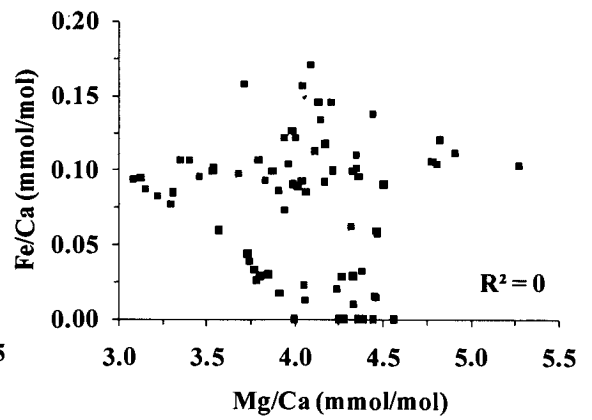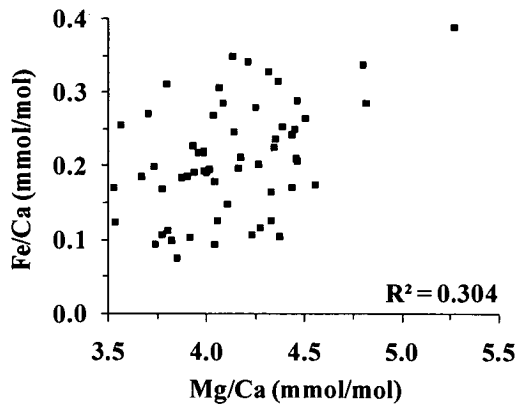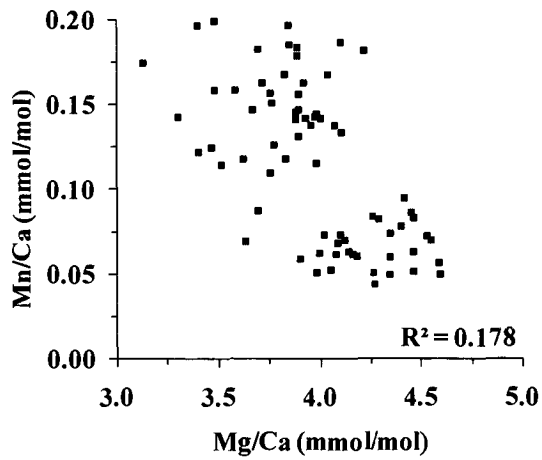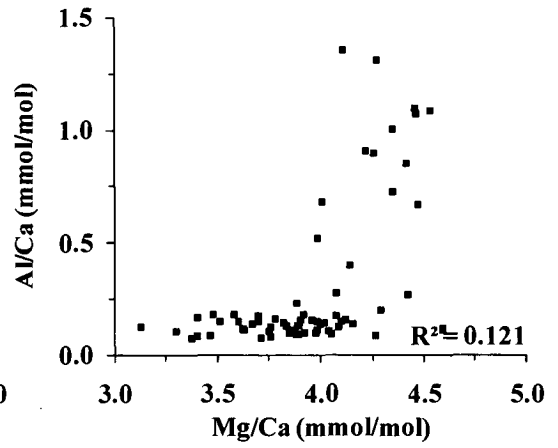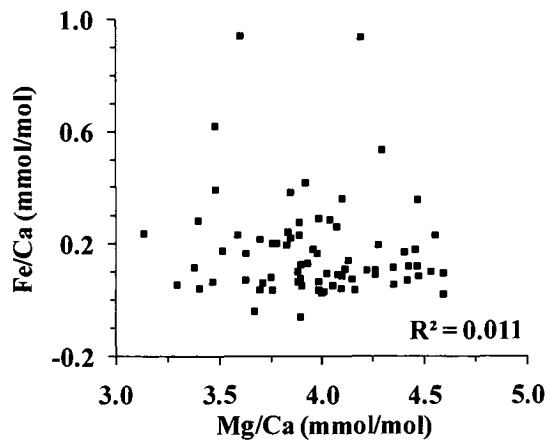
Figure 18. X-Y scatter plots of Fe/Ca, Al/Ca and Mn/Ca (mmol/mol) versus Mg/Ca (mmol/mol) for SK117/GC04 sediment core.

Figure 19. X-Y scatter plots of Fe/Ca, Al/Ca and Mn/Ca (mmol/mol) versus Mg/Ca (mmol/mol) for SK129/CR05 sediment core.
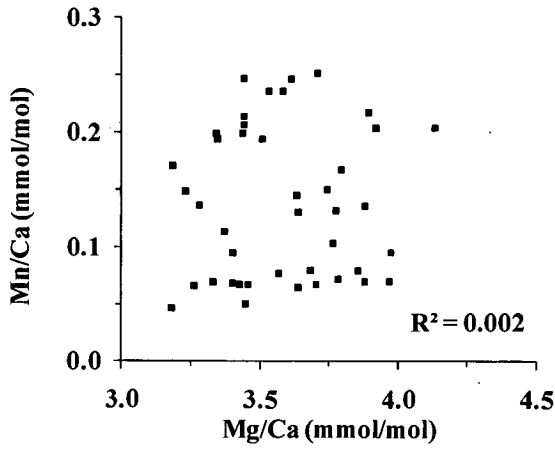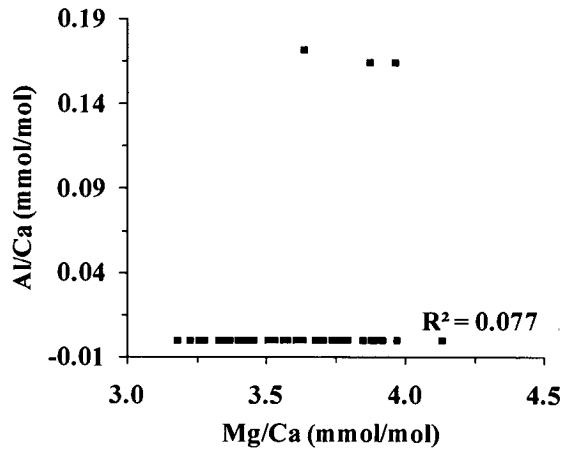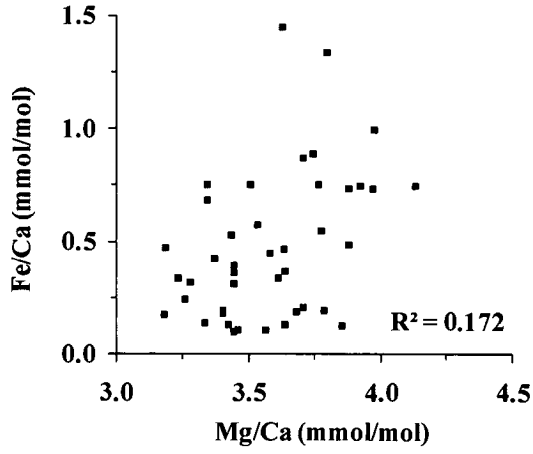
Figure 20. X-Y scatter plots of Fe/Ca, Al/Ca and Mn/Ca (mmol/mol) versus Mg/Ca (mmol/mol) for SK129/CR04 sediment core.

6.5. Intensity-ratio calibration

The precision and accuracy of analytical results from the ICP-AES technique depends to certain extent, upon the calibration technique. Multi-element, multi-standard routine calibrations are known to yield linear calibration curves with dynamic range of linearity maintained even up to four orders of magnitude. The analytical results based on such calibrations generally have precision and accuracy better than 5%. However, in case of foraminiferal calcite where the Ca-content is three orders of magnitude higher than that of Mg, and the SST estimates are sensitive to small changes in their ratios, the generally obtained precision is not sufficient (De Villiers *et al.*, 2002). Calcium is most sensitive element in ICP and has been observed to display self-absorption in addition to causing high backgrounds on other elements (Ramsey *et al.*, 1987) such as Mg. In order to negate these matrix effects, which would result in a reduced reproducibility, an alternative calibration viz., Intensity Ratio Calibration (IRC) procedure was developed to achieve highest possible precision and reproducibility (see De Villiers *et al.*, 2002). The IRC technique was found to be least sensitive to matrix effect simply because, the effect of Ca on Mg is minimized by taking ratios of intensity of Ca and Mg as the calibration tools instead of their individual concentrations. This technique under best analytical set-up could yield results precise within 0.3% (De Villiers *et al.*, 2002). The IRC procedure overcomes errors arising from evaporation of solution due to preservation or room temperature changes on concentration of elements. As the element ratios of the samples are calculated directly from their intensities, there is no propagation of the errors associated with calibration of individual element concentrations. The IRC technique assumes that all errors are in the "*y*" values (intensity ratios) and the "*x*" values (actual element ratios in standards) are error free (Miller and Miller, 1988). Hence, R^2 of the calibration curves obtained by IRC standards indicate the accuracy with which the IRC standards are prepared. The sample Mg/Ca ratios are calculated from the best-fit line equations obtained for the IRC curves established at every analytical session. The IRC data for all four sediment core analyzed here are given so as to provide an evaluation of their long-term reproducibility. The IRCs have yielded highly significant correlations ($R^2 = 0.99995$: see Figures 21 to 24).

Hence, the Mg/Ca ratios measured using IRC is mostly devoid of matrix effect and the IRC standards used for IRC calibrations were accurate.
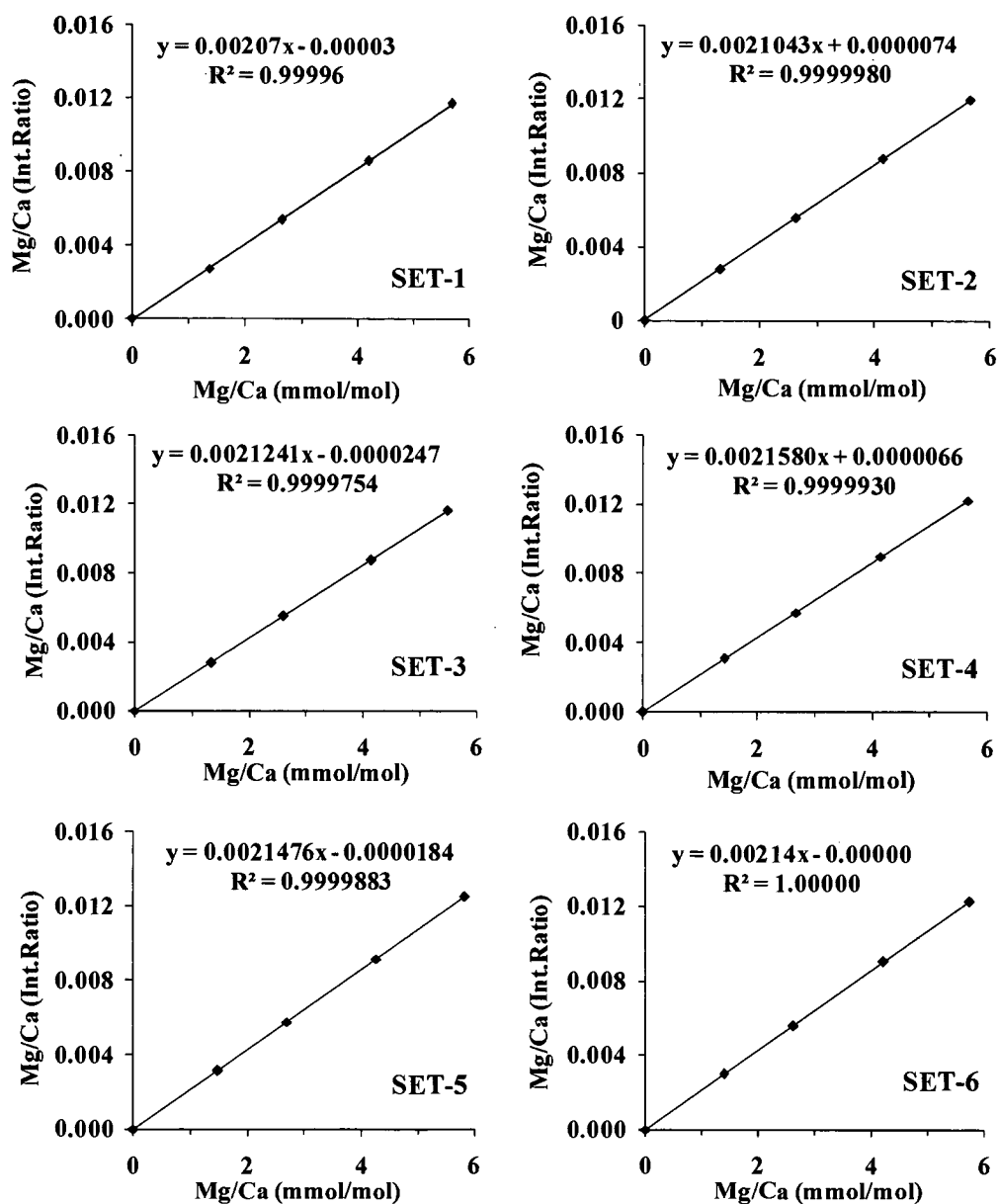

Figure 21. Intensity ratio calibration curves with their line equations used for SK117/GC08 samples solutions analyzed in six sessions.
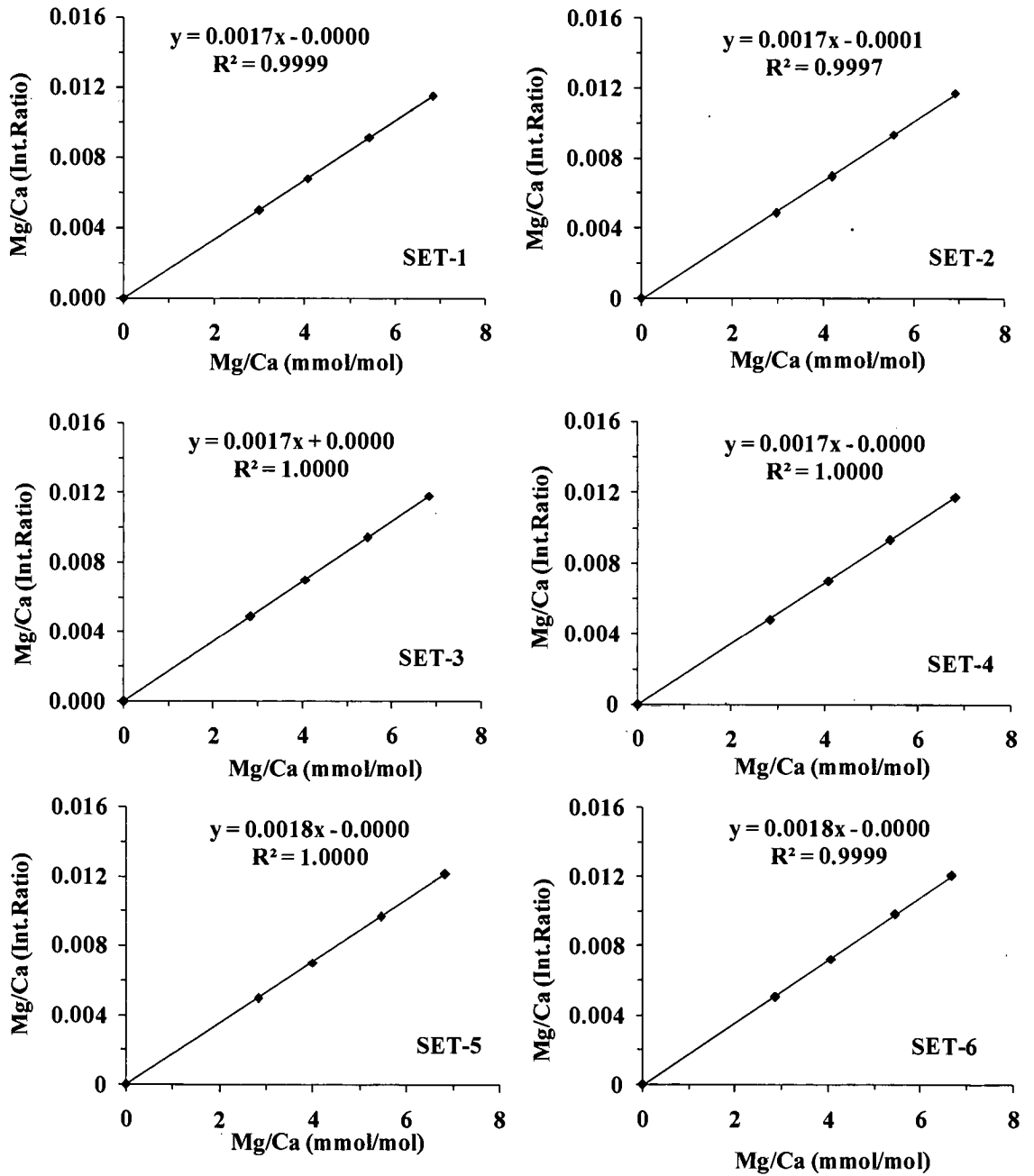
Figure 22. Intensity ratio calibration curves with their line equations used for SK117/GC04 sample solutions analyzed in six sessions.
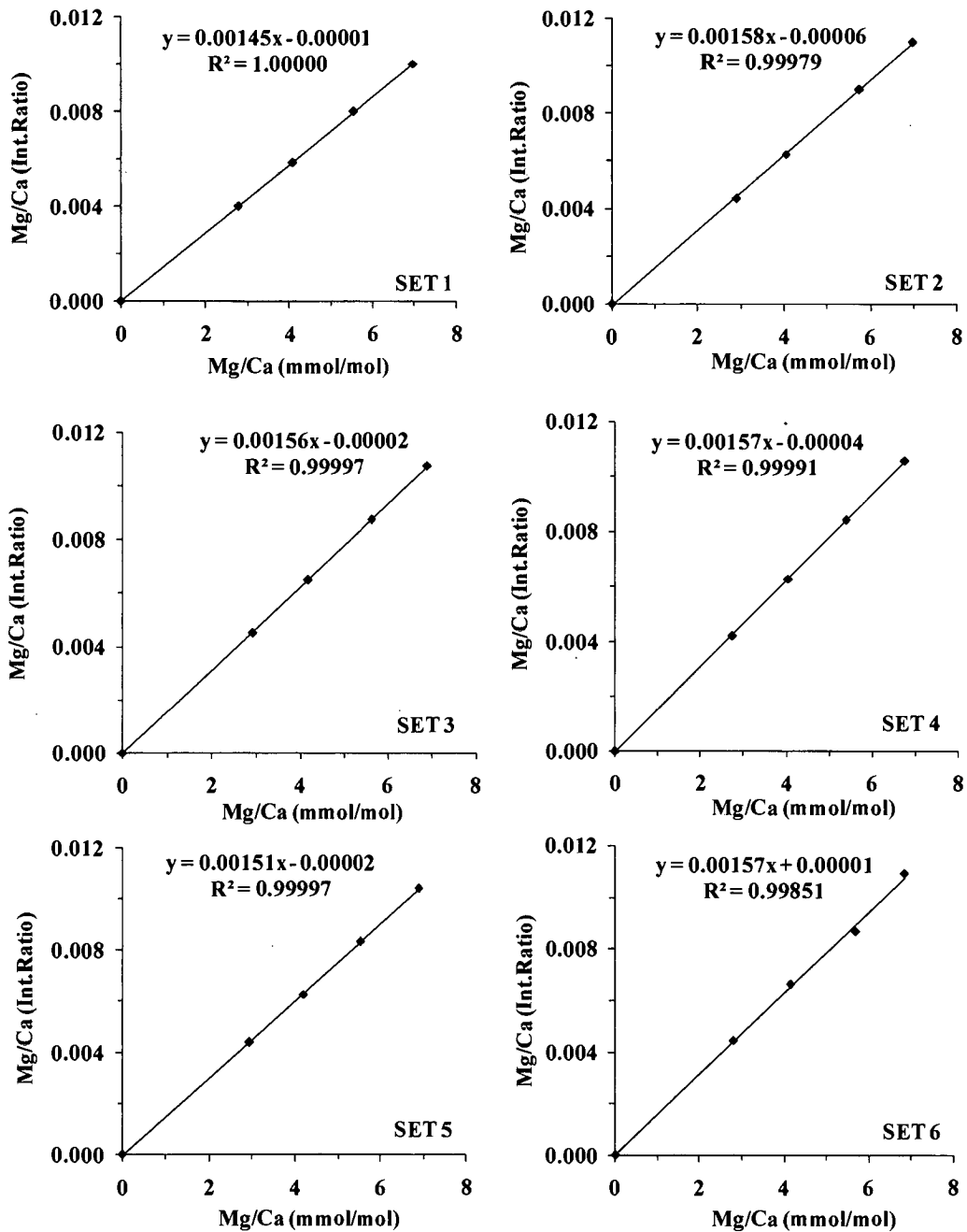
Figure 23. Intensity ratio calibration curves with their line equations used for SK129/CR05 sample solutions analyzed in six sessions.
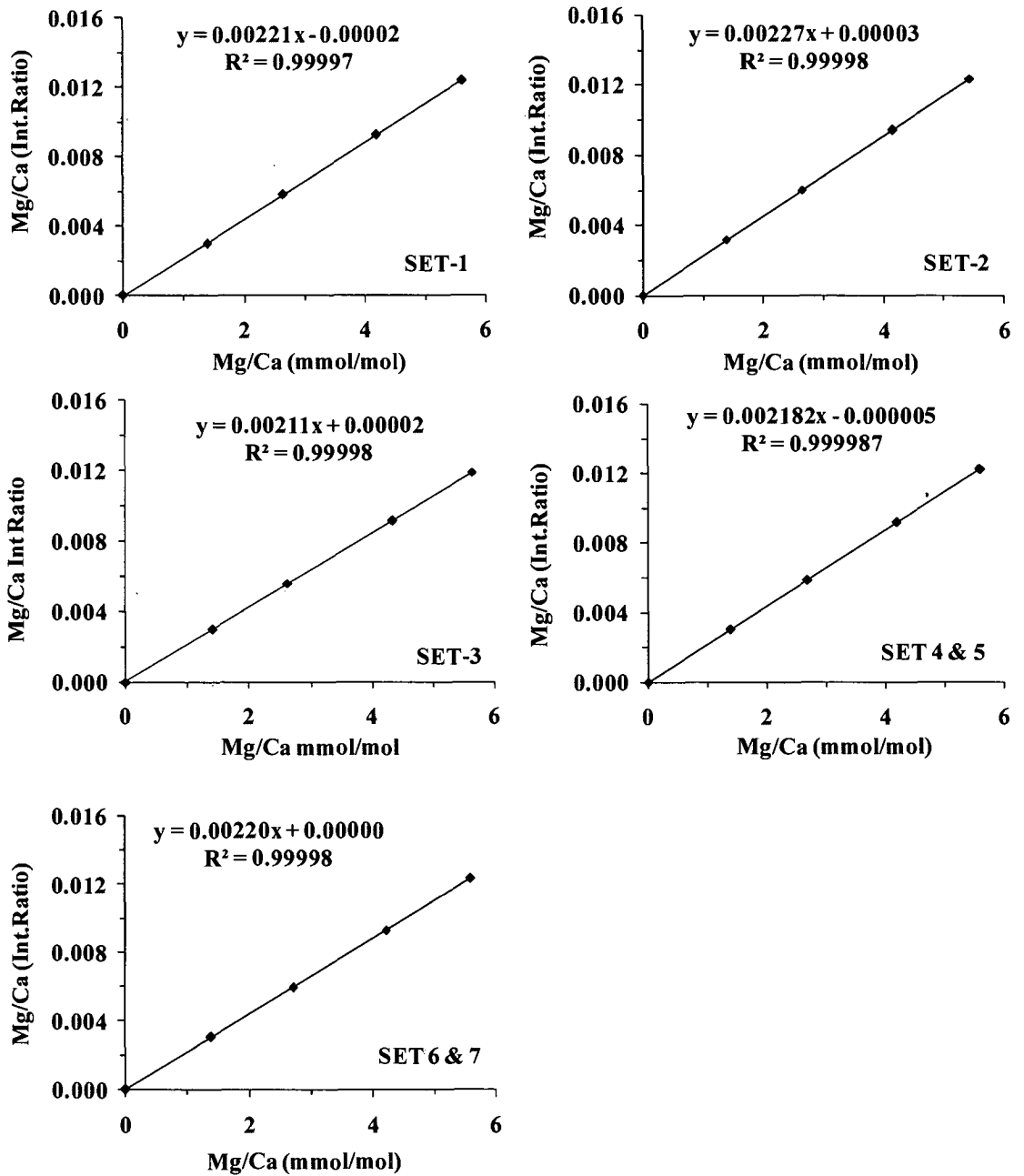
Figure 24. Intensity ratio calibration curves with their line equations used for SK129/CR04 sample solutions analyzed in five sessions.

6.6. Modern surface climatology of the EAS

The heat-budget is critical in dictating SST changes depending upon the seasons. The modern summer monsoons are characterized by strong winds, wet-air and cloud cover resulting in net oceanic heat gain of ~90 W/m^2. On the contrary, the winter monsoons are characterized by moderate winds, dry-air and clear sky resulting in heat-loss of ~20 W/m^2. Inter-monsoons are the periods of significant heat gain > 70 W/m^2 and are warmest. This seasonal trend of heat-balance coupled with upwelling etc., ultimately results in positive annual heat-balance in the entire Arabian Sea with ~30 - 60 W/m^2 net heat-gain (warming) (Wilson et al., 2009). Wilson et al. (2009) also demonstrated that winter monsoons are the only seasonal features that bring basin-wide heat-loss of over 45 W/m^2. In other words, winter monsoon typically cools the surface of the Arabian Sea, while rest of the period of the year normally warms the surface. This seasonal heat budget dynamics defines the SSTs in this region (see Figure 4 for SSTs of all four seasons with annual average).

In the modern salinity setup (see Figure 4 for salinity of all four seasons with annual average), the high salinity water (~37 psu) is evident in the northernmost part of the Arabian Sea and lowest salinity water (~ 34.5 psu) in the southern Arabian Sea (also refer to study area section). This pattern is due to net loss of freshwater due to intense winter evaporation (E-P >1) from the northern region and net gain of freshwater in the southern region. The modern surface climatology of the EAS can be very well understood from salinity maps of all four seasons (Spring, Summer, Fall and Winter: Figure.5). The presence of low-salinity tongue in EAS is distinctly visible during three seasons (Spring-Fall-Winter). The strength of influx of low-salinity water into the EAS is stronger when the sea surface height in BoB is higher than in the Arabian Sea, which is resulted by voluminous input of freshwater to the BoB during summer monsoons. The salinity in EAS is modulated by two factors viz., overhead precipitation and inflow of low-salinity water. The intensity of both these increase when the summer monsoon is intensified.

Modeling and observational results have shown that an increase in monsoon wind intensity, whether summer or winter induces surface cooling along with increased productivity in the open Arabian Sea region (Murtugudde et al., 2007). The expected

hydrographic changes due to monsoon variations would be to, a) enhance surface cooling along with surface freshening (< E-P, i.e., decreased salinity) as a result of intensified summer monsoon, and b) enhance surface cooling along with increased evaporation (> E-P, i.e., increased salinity) as a result of intensified winter monsoon.

If the surface cooling at a given time was associated with increased salinity (i.e., increased $\delta^{18}O_{SEAWATER}$), then it should reflect relatively stronger winter monsoons than the summer monsoons. In case, if the surface cooling was associated with decreased salinity (decreased $\delta^{18}O_{SEAWATER}$), then it indicates stronger summer monsoons. Evolution of such characteristic surface climatology is because the summer monsoons add > 80% of the annual freshwater to the northern Indian Ocean, hence expected to induce surface freshening coupled with surface cooling. With this background, the reconstructed time-series of SST and salinity in the EAS are discussed.

6.6.1. LGM-to-Holocene SST variability

The magnitude of LGM cooling in tropical seas has been of great debate of recent years. The debate is justifiable because, tropical-ocean SSTs are believed to hold key for ocean-atmosphere coupled processes such as monsoons, ENSO etc. Therefore, a clear understanding of the SST variability in past is an essential element of the paleoclimatic reconstructions. The SSTs estimated based on isotopic composition of foraminifera (CLIMAP Members, 1976) indicate < 2°C lowered SSTs throughout much of the equatorial tropics during the LGM. The MAT was applied for planktonic foraminiferal samples from Atlantic, Pacific and Indian oceans, which resulted in marginally lowered annual mean SST for LGM (Prell, 1985; Trend-Staid and Prell 2002). The MARGO reconstructions showed a cooling of 1°C to 4°C in the tropics (MARGO, 2009). These reconstructions provide an important resource for climate variability during the Holocene-LGM time-slice. Further, model inter-comparisons made by PMIP-1 Project Group (Joussaume and Taylor, 2000) using AOGCM showed a modest cooling of 2°C-3°C of tropical ocean surface, and greatest cooling at mid- to high-latitudes in association with increases in sea ice and changes in ocean circulation (Braconnot et al., 2007).

Though large number of paleo-SST datasets are available for the Pacific and Atlantic Ocean (see Rosell-Melé et al., 2004; Barker et al., 2005; Barrows and Juggins, 2005; Kucera et al., 2005), the data for Indian Ocean in general is limited, while it is still sparse for the northern Indian Ocean. The SSTs estimated by Mg/Ca method for northern Indian Ocean are very rare. Only reported records are of Saraswat et al. (2005), Saher et al. (2007), Anand et al. (2008), Banakar et al. (2010), and Govil and Naidu, (2010). Few paleo-SST data for northern Indian Ocean based on alkenones show consistency with CLIMAP reconstruction recording < 2°C cooling in LGM tropics (e.g., Rostek et al., 1993, 1997; Sonzogni et al., 1998; Cayre and Bard, 1999; Banakar et al., 2005).

The Mg/Ca ratios analyzed in the present study vary between 3 and 4.6 mmol/mol (Tables 10 to 13), which translate into SST variation of 27°C to 30°C. The analyzed Mg/Ca ratios are in the expected range of planktic Mg/Ca ranges for tropical oceans (see Lea et al., 2000; Barker et al., 2005; Saraswat et al., 2005; Dahl and Oppo, 2006). The SSTs for core-top sections vary between 29°C and 30°C (Figure 25), which are comparable to the modern SSTs at core locations (see Figure 9). The core-top SSTs are also comparable to alkenone-based SSTs derived for the Holocene sections in a set of sediment cores from EAS (~28°C: Rostek et al., 1993; 28.5°C: Sonzogni et al., 1998: 28.9°C: Cayre and Bard, 1999). These comparisons suggest that estimated SSTs from present sediment cores are reliable.

The Holocene average SSTs are ~29.5°C, while they are ~27.5°C for the last glacial period (~35 kyr BP to 12 kyr BP). That is, the LGM to Holocene SST difference in the EAS is ~2°C. This SST gradient is consistent with those obtained by the CLIMAP group (CLIMAP Project Members, 1981: 2.3°C), MARGO data set (MARGO Project Members, 2009: -1.6 ± 1.1°C) and the PMIP-2 multi-model findings (Bette et al., 2009: 1.7°C to 2.4°C) and are comparable to previous report on alkenone based LGM-SST cooling in the Arabian Sea (2.5°C: Rostek et al., 1993; 2.5°C: Sonzogni et al., 1998) and to other Mg/Ca based LGM-cooling (2.1°C: Saraswat et al., 2005; 2°C: Saher et al., 2007; 3°C: Anand et al., 2008). *These observations indicate that the LGM SSTs were uniformly colder across the entire Arabian Sea by ~2 ± 0.5°C.* A 2°C colder surface of the EAS in particular and northern Indian Ocean in general during the LGM clearly

point towards significantly different ocean-atmosphere coupled dynamics of the region than today.

The increase in EAS-SST from ~27°C during the LGM to ~29°C of the Holocene was not monotonous, but show step structure (Figure 25). This step-increase suggests that during the deglacial transition from LGM to Holocene, the SST rise was rapid for some time followed by a short period of stability. Similar pattern in SST warming has been observed in both western Arabian Sea (Saher *et al.*, 2007) and in EAS (Anand *et al.*, 2008). The rapid increases are evident during ~17 to ~14 cal kyr BP (Figure 25). Although the LGM SSTs exhibit cooling in general, the actual lowest SST band is observed not exactly at the LGM, but between 29 and 24 cal kyr BP in the EAS. If we consider the SPECMAP based isotope boundaries, this period covers late MIS-3 to early MIS-2. If LR04 based isotope boundaries are considered, this period mostly falls within the MIS-2. Whatever the case may be, the overall colder SSTs between 29 and 24 cal kyr BP is observed prior to the actual LGM defined by $\delta^{18}O_{G.\ sacculifer}$. Observed cold SSTs in the EAS are mostly concurrent with growth status of global ice sheets (Clark *et al.*, 2009). Clark *et al.* (2009) have shown that the global ice sheets attained their maximum size much before the actual LGM, i.e., by 26.5 kyr BP and sustained their maximum growth until ~20 kyr BP. That is, the time period between 26.5 and 20 kyr BP should have witnessed conditions quite similar to the LGM. *The coldest SSTs observed much before the LGM ~25 ka BP in the EAS therefore might suggest a response to global climate cooling represented by the then global ice volume maximum.*

Alternatively, other likely cause may be increased upwelling in the EAS during LGM. In order to assess this feature of lowest SST, the published C/N ratios for two sediment cores (SK117/GC08: Banakar *et al.*, 2005 and SK129/CR05: Pattan *et al.*, 2003) are compared with the present SST and salinity records. Further, the abrupt variations in SSTs observed during the period in concurrence with salinity are also discussed separately. The Holocene minimum of lowered SST and salinity, a striking feature observed within the time-slice of 6 and 9 cal kyr BP warrants special consideration and hence discussed separately.
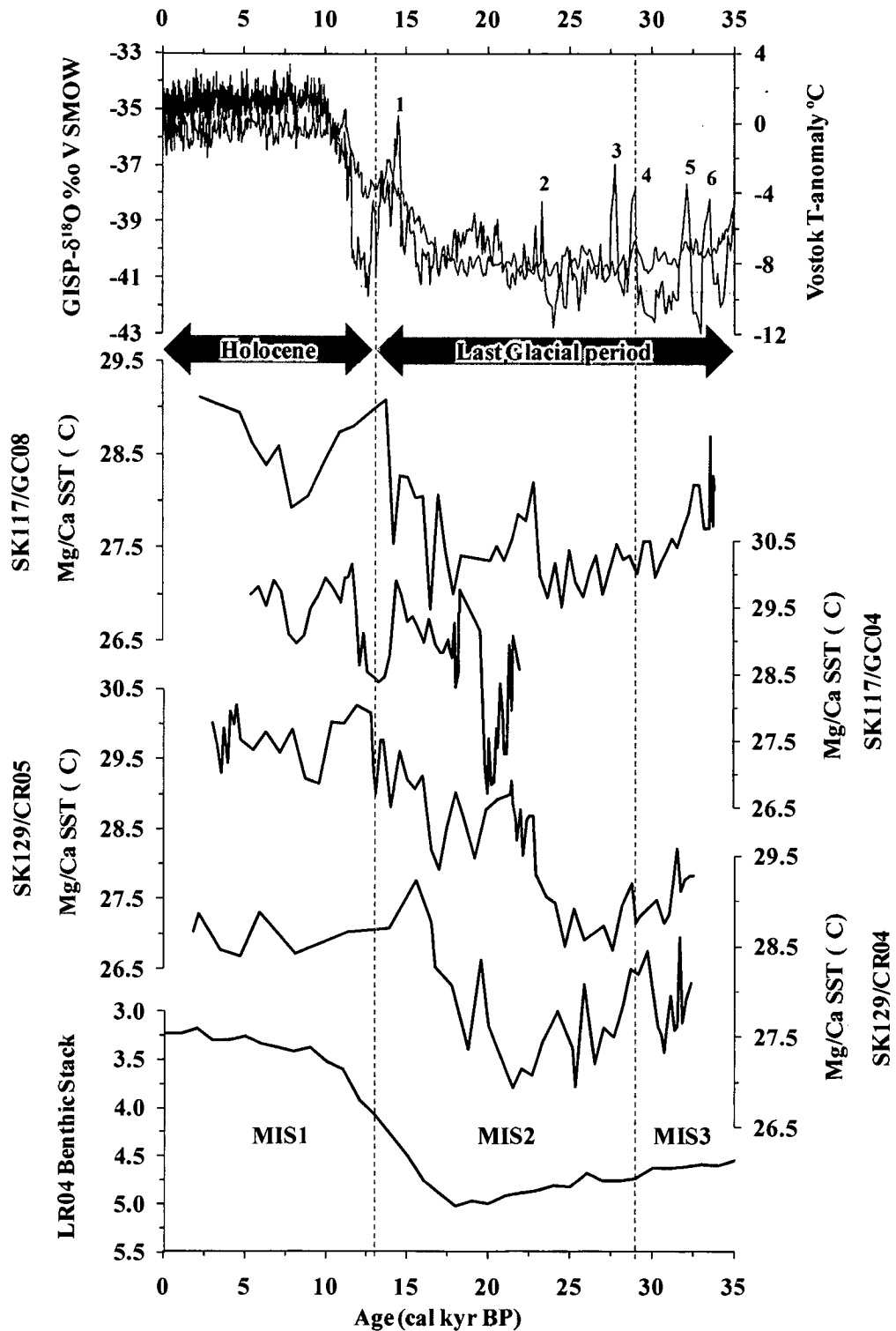
Figure 25. Reconstructed SST time-series from four sediment cores of the EAS are compared with Antarctic temperatures, Greenland Ice oxygen-isotopes and LR04 Benthic Stack. Broken vertical lines indicate MIS 1/2 and 2/3 boundaries. Numbers 1 to 6 represents D-O events.

6.6.2. LGM-to-Holocene surface salinity variability

The past monsoon variability could be understood more clearly through the changes in local salinity. Such salinity time-series of the EAS should reflect in general the past monsoon variability. The salinity (E-P) is a reliable parameter to unscramble the relative dominance of summer and winter monsoons in long-term averaged paleo-records, which, in present case are in the form of averages of few hundreds of years depending upon the time-resolution achieved in each sediment core. This possibility mostly stems from the fact that the seasonally reversing Indian monsoons are two extreme cases of moisture load. The summer monsoons associated with extensive- and intensive- precipitation tend to decrease the E-P, whereas, extremely dry winter monsoon winds tend to increase the E-P (Wyrtki, 1973; Webster and Fasullo, 2002). The 'P' component here covers the total freshwater flux and this flux to the northern Indian Ocean is mostly controlled by summer monsoon precipitation. Further, the sea surface layer (or mixed layer) salinity instantly responds to changes in the E-P, wherein, E tends to increase the salinity and P does the reverse.

The $\delta^{18}O_{G.\ sacculifer}$ and estimated salinity should exhibit co-variation if the estimated salinity from the $\delta^{18}O_{SEAWATER}$ is realistic, because the $\delta^{18}O_{SEAWATER}$ was calculated from the $\delta^{18}O_{G.\ sacculifer}$. The X-Y plots of $\delta^{18}O_{G.\ sacculifer}$ and estimated salinity from all four sediment cores show significant linear relationship with regression coefficient of > 0.7 (Figure 26). This high correlation indicates that, at least in present case (for EAS region), the estimated salinity is reliable and should indicate E-P in the study region. The standard error in salinity estimates is ±1 psu (Rohling, 2007) and hence general salinity changes are discussed here.
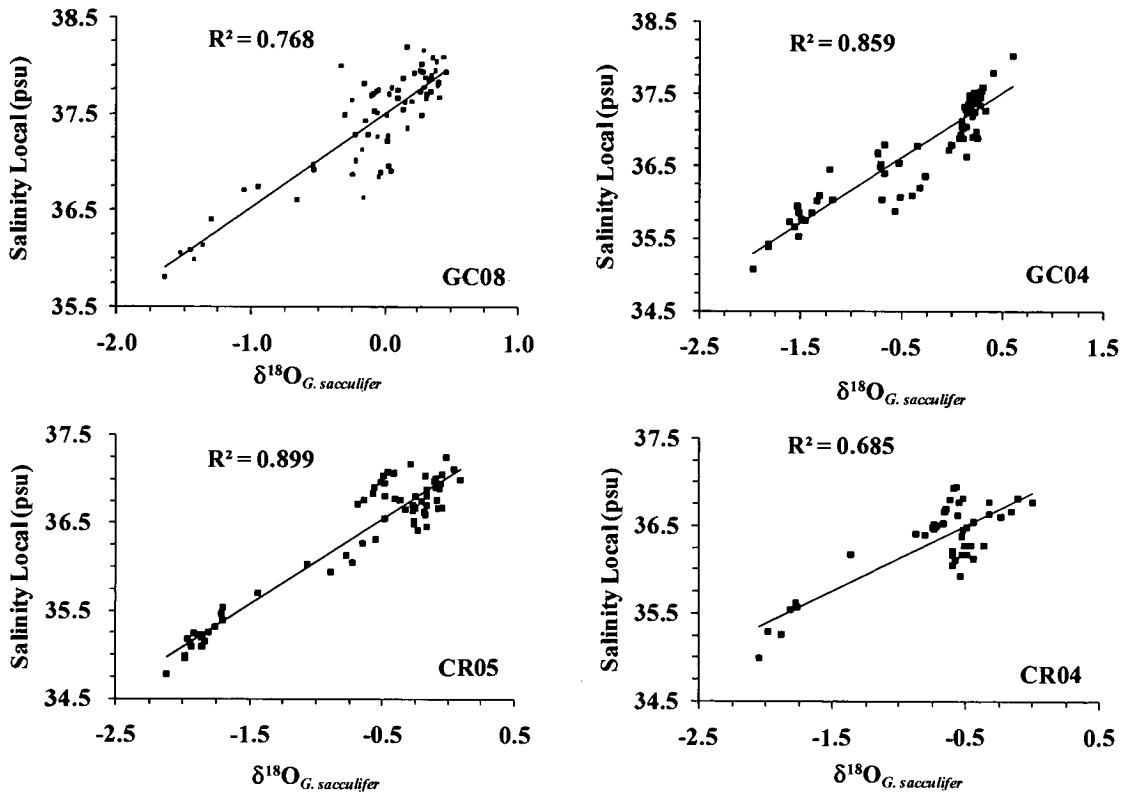
Figure 26. X-Y plots of $\delta^{18}O_{G.sacculifer}$ and salinity for all four sediment cores. Although there is some clustering in the data distribution, the linear trend is invariably evident.

While discussing salinity time-series with respect to monsoon intensity, it is necessary to assess the flow of low salinity water in to the southern Arabian Sea. One of them is the cross-equatorial flow into the southern Arabian Sea (Jensen, 2003) and the other is the inflow of low salinity water from BoB in the form of poleward coastal currents (Shetye *et al.*, 1991; Shankar *et al.*, 2002). These two sources of low salinity water at the outset may lead to dilution of the actual effect of salinity variability in the EAS resulting from the monsoon precipitation. But, the salinity of winter-spring coastal currents originating in BoB is dependent on the summer monsoon precipitation both on India and over BoB. In other words, summer monsoons tend to decrease the salinity of coastal currents responsible for freshening the EAS surface, in a way much similar to the overhead precipitation would contribute to the reduction of EAS salinity. Hence, low-salinity intrusion in to EAS through coastal currents from BoB could be considered as part of the larger freshening component 'P'. Further, the scenario of cross-equatorial

flow of low salinity water is not well established as a major inflow that could significantly alter the surface salinity in EAS, hence can be ignored at this juncture. The past salinity reconstructions for the EAS are very few (Rostek *et al.*, 1993, 1997; Banakar *et al.*, 2010-data presented in this thesis; Govil and Naidu, 2010), hence any new information added to this pool of data is useful.

The salinity estimated from the core-top sections of all four sediment cores vary between 35 and 36.5 psu (Figure 27). As expected, the Holocene is marked by lower salinity, while the LGM sections show higher salinity. This observation is consistent with generally expected climatology of the Arabian Sea during warm-wet Holocene and cold-dry LGM climate. The primary reason for this change is the shift in the E-P due to relative changes in intensities of two seasonal monsoons, which might have reorganized depending upon the climate conditions. *The Holocene's lower salinity recorded in all four sediment cores of the EAS clearly suggests increased freshening (reduced E-P) due to intensified summer monsoons, while the LGM's higher salinity reflects increased evaporation (increased E-P) due to intensified winter monsoons.* The former meteorological conditions indicate intensified moisture laden warm southwesterlies blowing over the Arabian Sea leading to reduced E-P (freshening), while the latter conditions indicate intensified moisture-starved northeasterly cold winds blowing from Indian sub-continent over the Arabian Sea leading to increased E-P. This observation and interpretation are consistent with several previous reported studies based on other proxies.

The overall change in salinity from LGM to Holocene is ~2 psu. The average salinity during the LGM is ~37 psu in all four salinity time-series until the beginning of the deglaciation (~18 cal kyr BP) (Figure 27). This observation suggests that, long sustained intense winter monsoons were characteristic of the LGM resulting in long-term elevated salinity in EAS. On the other hand, a rapid reduction in salinity across the deglaciation (18-10 cal kyr BP) is evident and the lowest salinity of ~36 psu characterized the Holocene EAS. The significantly reduced salinity within 8 kyr of climate transition is a direct indication of intensification of summer monsoons along with weakening of winter monsoon during the deglacial transition. That is, significant

reorganization in the Indian Monsoon system took place during the last climate transition.

The salinity in EAS between 8 and 9 cal kyr BP shows a pulse of further reduction within the Holocene low salinity trend. This pulse occurs at ~6-4 kyr after the SST maxima. Although these two features are not consistent in all four sediment cores, a general lag in salinity minima to that of SST maxima could be noticed (Table 21).

Table 21. Timings of SST maxima and salinity minima recorded in the EAS sediment cores

Core	SST maxima (cal kyr BP)	Salinity minima (cal kyr BP)
SK117/GC08	13.83	8.00
SK117/GC04	14.76	8.25
SK129/CR05	13.42	8.75
SK129/CR04	14.00	8.12

The lowest salinity event occurring after highest SST event has major implication to monsoon dynamics. This data suggests that the warmer sea surface required for initiating summer monsoon convections over the Arabian Sea appear to have optimised few thousand years before the actual intensification of freshwater flux resulting in lowered salinity. *The warm-SST leading lowered-salinity may indicate a meteorological preconditioning of ocean surface required to set in moisture charged summer monsoon circulation.* Such pre-conditioning may be a requirement following major shift in climate from glacial to interglacial conditions. The step-wise increase of SST across the deglacial transition (Figure 25) may also suggest a kind of preconditioning of sea surface before another following SST increase.

Decreasing trend of the salinity that began ~18 cal kyr BP nearly superimposes the beginning of deglaciation evident in LR04 benthic $\delta^{18}O$ stack (see Lisiecki and Raymo, 2005) representing globally averaged deepwater temperatures, in turn global ice-volume. These synchronous changes suggest a link between global climate and regional monsoon precipitation. *Where as, the EAS-SST leading both these global and local changes may suggest a speculative possibility of implicating tropical sea surface warming in triggering global climate shift via reorganizing the monsoon circulations.*

115

The Indian Monsoons form part of much larger ocean-atmosphere coupled phenomena called ENSO. The ENSO system in turn has potential to force global climate due to its vastness. Therefore, it is likely that the tropical SST warming might have preceded the beginning global ice-volume reduction thus terminating the LGM. However, above ocean-atmosphere coupled link is presently tentative and needs thorough validation through more studies from tropical Indian and Pacific oceans.

Another significant feature observed within the early Holocene is that of lowered salinity superimposing lowered SST between 10 to 5 cal kyr BP in both northern and southern EAS (SK117/GC8 and SK129/CR04: Figure 9). This combination of SST and salinity is a reflection of intensified summer monsoons resulting in increased winds-forced surface cooling as well as increased precipitation (Dahl and Oppo, 2006).

The salinity time-series also provide information on the mixing of more saline ASHSW forming in northern Arabian Sea and less saline BoB water advected in the EAS. Because, the SK117/GC04 and SK117/GC08 (northern EAS) are located below the surface layer that is dominated by ASHSW and SK129/CR05 and SK129/CR04 (southern EAS) are located below the surface layer filled entirely by the low salinity water originated in the BoB (also known as low-salinity tongue).

The average salinity obtained for northern and southern EAS for full-Holocene are 36.2 and 35.1 psu respectively. That is a difference of 1.1 psu between the northern and southern locations (Figure 28). During the LGM, the salinity averages are 37.7 psu for northern location and 36.1 psu for southern location. That is a difference of 1.6 psu between northern- and southern-locations. Thus the north to south salinity gradient was ~0.5 psu higher during the LGM than during the Holocene. Higher north-south gradient during the LGM indicates that the BoB water advection in to the EAS was less-fresher than during the Holocene and/or the ASHSW formation was relatively more. Both these scenario suggest reduced precipitation (> E-P) during the LGM. This observation essentially indicates that the summer monsoons and associated precipitation was more intense during the Holocene and the winter monsoons and associated evaporation was more intense during the LGM.
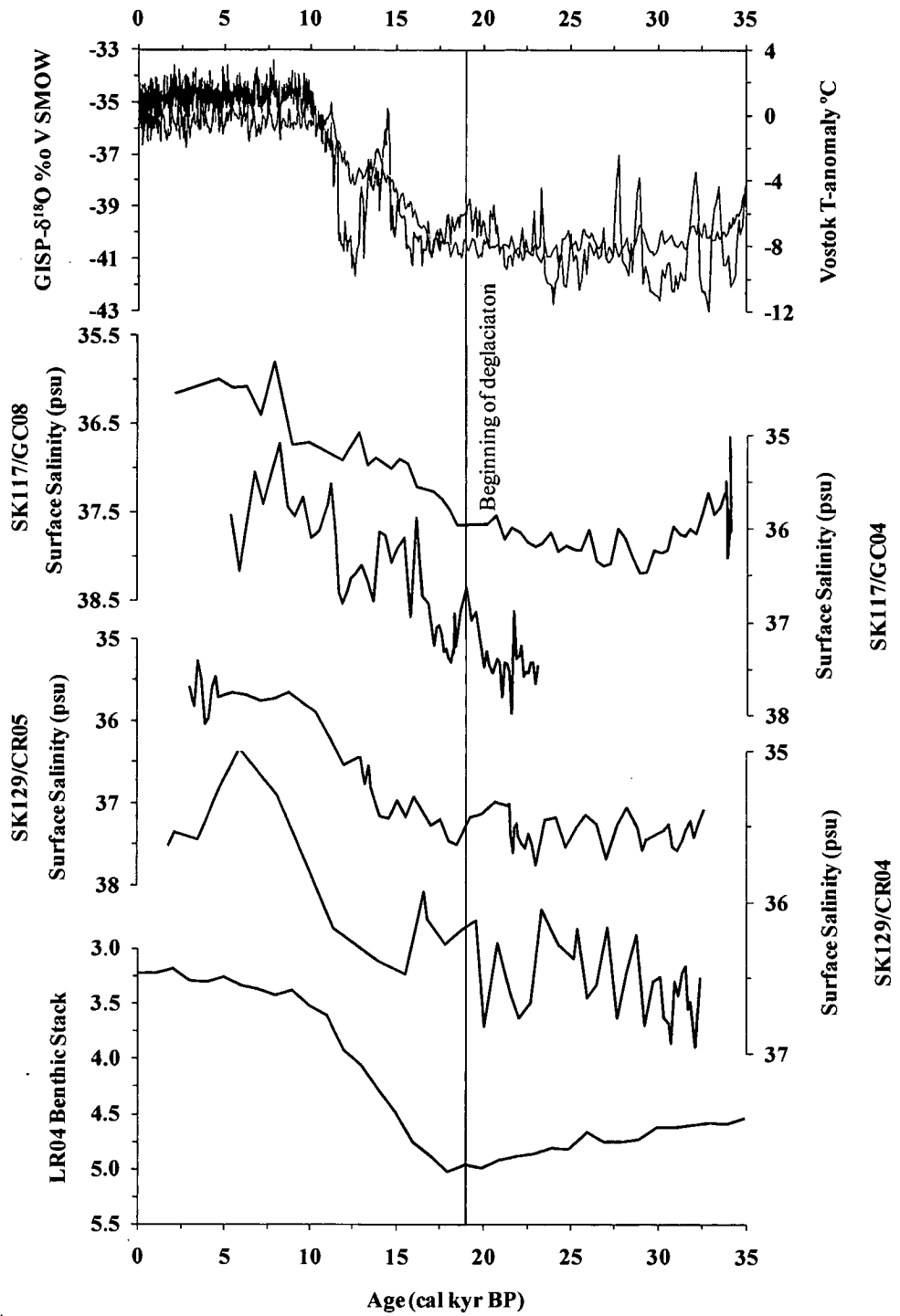
Figure 27. Time-series of surface salinity are compared with Antarctic temperature, Greenland Ice oxygen-isotopes and LR04 Benthic Stack. The straight vertical line represents the beginning of deglaciation.
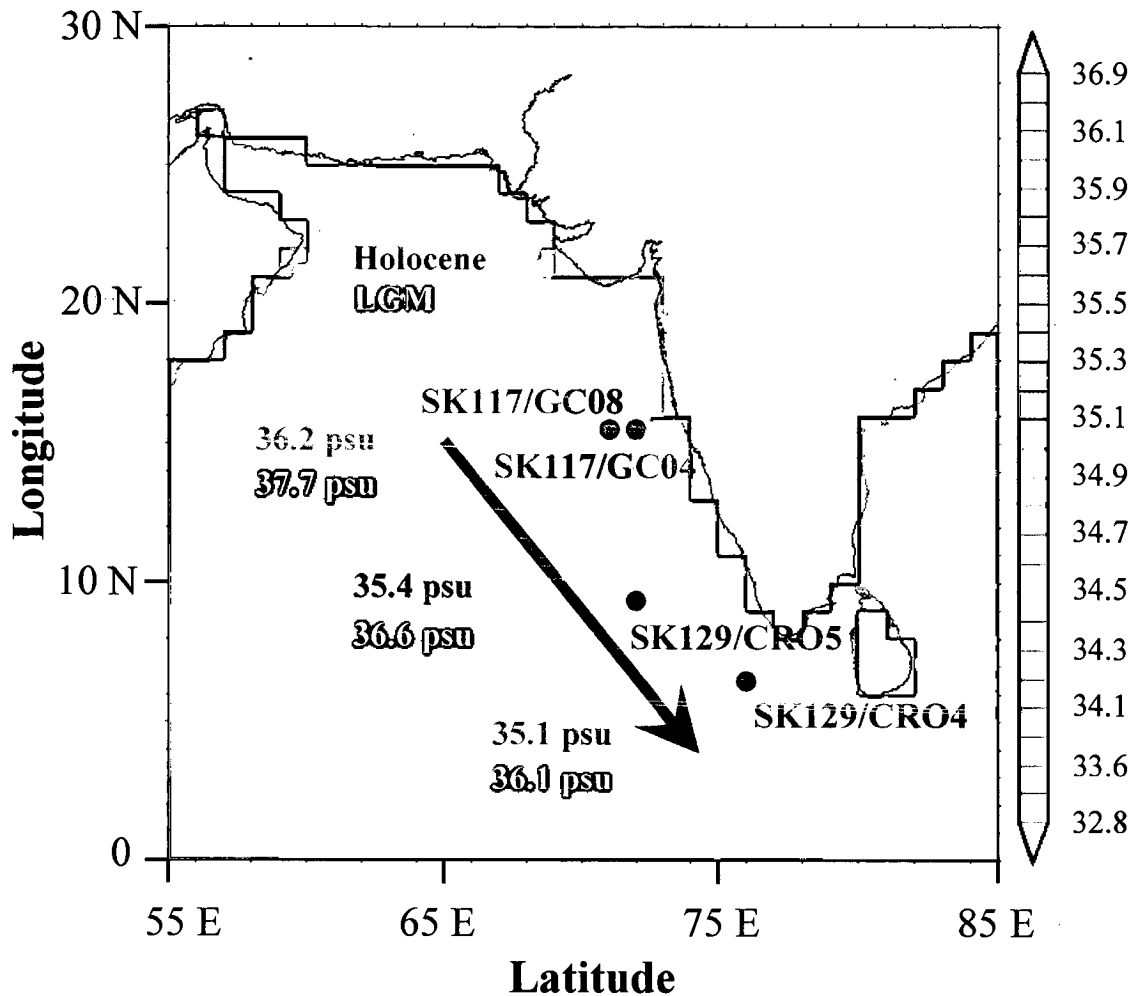
117

Figure 28. Average salinity values in the EAS at core locations during LGM (white font) and Holocene (black font). During both these periods there is north-to-south decreasing salinity is observed, but with variable gradient (i.e., Holocene = 1.1 psu and LGM = 1.6 psu, a difference of 0.5 psu between Holocene and LGM). (Base map source: www.noaa.nodc.gov).

Ideally, the salinity gradient between northern- and southern- EAS would increase if the influence of the ASHSW on northern location and the BoB inflow in southern location is increased at the same time. But, such a setup is highly unlikely because the increased formation of ASHSW indicates intensification of winter evaporation, while increased input of low-salinity water from BoB means increased input of freshwater to BoB, i.e., increased summer monsoon precipitation, which are two contrasting monsoon features. Therefore, an alternative scenario is required to explain increased salinity gradient between northern and southern locations of the EAS during the LGM. A feasible set-up could be an increase in the ASHSW along with reduction in low-salinity water reaching the northern location. The increased influence

118

of ASHSW can result from intensification of winter monsoons. Whereas, to prevent the low salinity water reaching the northern location and restricting it to only southern location can result from weakening the low-salinity tongue or BoB water inflow, which indicate reduced difference in the sea level between BoB and Southern Arabian Sea. This could happen when freshwater flux to BoB is significantly decreased i.e., weakened-summer monsoon freshwater input. *Thus, the increased N-S salinity gradient in the EAS during LGM suggests not only reduced summer monsoons but also relatively intensified winter monsoons. That is, the LGM Arabian Sea appears to have witnessed precisely reversed monsoon system of the modern time.* The intensified summer monsoons not only enhance the low salinity BoB water reaching the northern location but also significantly reduce the ASHSW formation, together resulting in decreased salinity gradient, which characterize the Holocene surface condition in the EAS. This observation is consistent with previously published record of $\delta^{18}O$ gradient between northern and southern EAS (Chodankar *et al.*, 2005).

6.6.3. Abrupt variation in SST and salinity during the glacial period

The SST and salinity variations are not monotonous or smooth, but show rapid fluctuations within the LGM. The fluctuation of SSTs were as much as 1 °C within each of these climate stages, while the salinity exhibits ~0.5 psu variations around the mean climate stage values (see Figure 29). The SST fluctuations during the last glacial period are more distinct than those marginal variations in $\delta^{18}O$ (± 0.2‰: Figure 16; Tables 5 to 8). The increased SSTs quickly return to averaged glacial level (~27°C) approximately within 2 to 4 kyr.

To examine whether the observed fluctuations are specific to the studied locations or inherent property of the paleo-SST records, the present SST time-series of northern-, central-, and southern-EAS were compared with three other published Mg/Ca SST records from the Arabian Sea (see Figure.29: NIOP723: Saher *et al.*, 2007; SK17: Anand *et al.*, 2008; AAS9/21: Govil and Naidu, 2010), which cover the last 35 kyr. Distinct warming events (designated as WE1 and WE2) are recorded within the LGM climate at ~15, and ~20 cal kyr BP exhibiting a rise of ~ 1°C in SSTs above the average LGM SST of ~ 27 °C in all the records, although with certain timing offsets. These

abrupt SST fluctuations are difficult to explain with changes in monsoon strength alone as synchronous changes in salinity are not seen in the salinity time-series. Therefore, these fluctuations are most likely linked to local hydrographic changes and may indicate association with intermittently weakened coastal upwelling in the EAS.
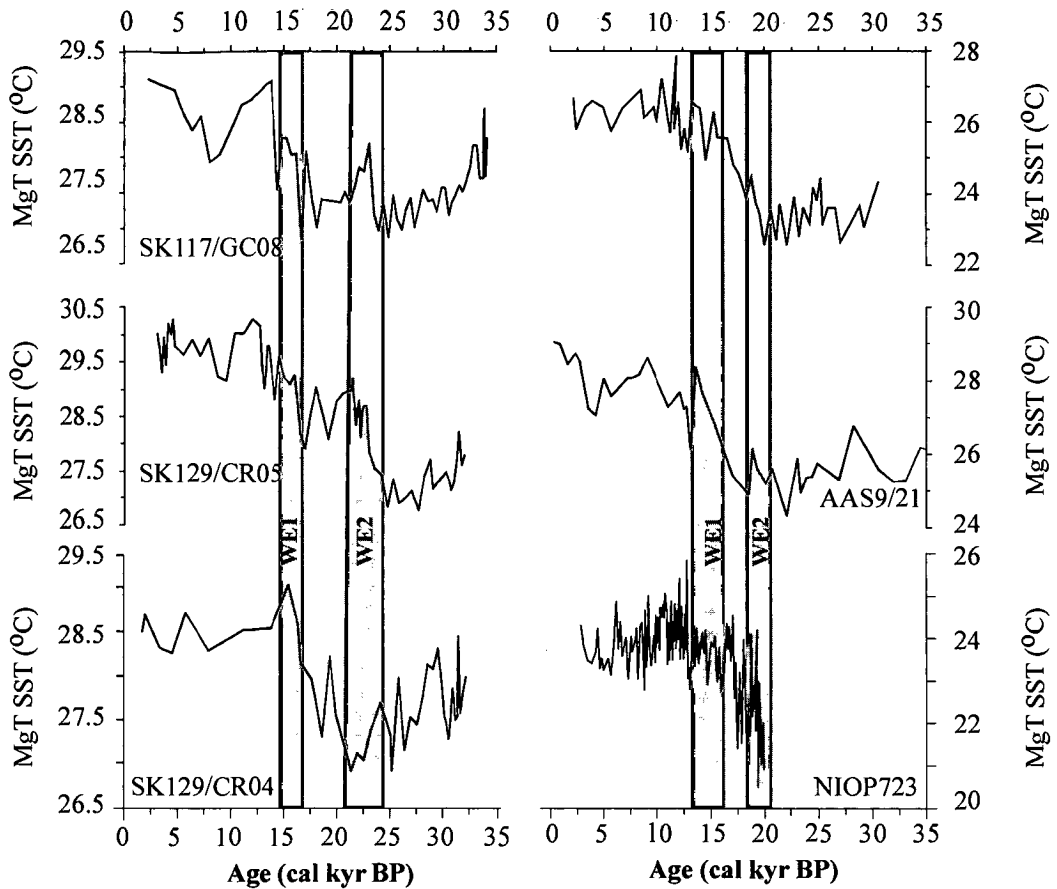

Figure 29. SST time-series from four sediment cores of EAS are compared with three published SST records of the Arabian Sea viz., NIOP929 (Saher *et al.*, 2007), SK17 (Anand *et al.*, 2008) and AAS9/21 (Govil and Naidu, 2010), Warm events within LGM (WE1 and WE2) are represented by shaded bars.

Saher *et al.* (2007) invoked combination of intermittent weakening of winter monsoons, reduced upwelling off Oman and Somalia, and also inflow of warm water of South Equatorial origin to explain the short-lived warmer-SST events in the western Arabian Sea during LGM. The winters during glacial periods are expected to be more intense and more prolonged than during the interglacial times (Hong *et al.*, 2003). The winter monsoon winds have profound influence on SST variations in the Arabian Sea under glacial conditions (Duplessy, 1982; Fontugne and Duplessy., 1986). In flow of south equatorial warm water causing warmer SSTs in the EAS is less likely, because, there is no such known flow path directly leading in to EAS as evident in tracer studies (Jensen, 2003). The reduction of upwelling causing intermittent warm-events also appears unlikely because the EAS is not a major upwelling region. Therefore, increased SST events during the glacial period in the EAS most likely suggest intermittent weakening of glacial winters.

6.6.4. Early Holocene intense summer monsoons

A notable feature observed within the Holocene is a decrease of $\delta^{18}O_{G.\,sacculifer}$ (by 0.3 ‰) between 6 and 9 cal kyr BP, nearly superimposing SST cooling and salinity lowering (Figure 30). This decreased $\delta^{18}O_{G.\,sacculifer}$ event is distinct in both northern EAS sediment cores (SK117/GC08 and SK117/GC04). The SST and salinity also exhibit decrease by about ~1°C and ~0.5 psu respectively during the same time. The $\delta^{18}O_{G.\,sacculifer}$ time-series in southern-EAS cores (SK129/CR04 & CR05) is not very distinct probably due to coarse sampling in this section. However, the SST and salinity lowering is reflected in all the sediment cores (Figure 30). *Concurrently decreased $\delta^{18}O_{G.sacculifer}$, SST and salinity during the early Holocene are a clear reflection of most intense summer monsoons.* This interpretation is based on the facts that the intensification of summer monsoons results in enhanced surface cooling in the Arabian Sea but also increases the freshwater flux reducing the salinity (and hence decreased $\delta^{18}O_{SEAWATER}$). The modeling results in fact have clearly indicated enhanced wind-forced SST cooling during intensified summer monsoons (Murtugudde *et al.*, 2007).

Similar summer monsoon-wind forced surface cooling event has been observed across the entire Arabian Sea (Dahl and Oppo, 2006; Overpeck *et al.*, 1996), and hence appears to be a regional feature. This early Holocene event of lowered SST at the outset could be related to globally prominent cooling event ~8 kyr BP (Barber *et al.*, 1999). But its association with reduction in both salinity and $\delta^{18}O$ argue against it, because, the oceanic response of global cooling would be to increase the salinity and $\delta^{18}O$, which are not seen in this early Holocene event in EAS.
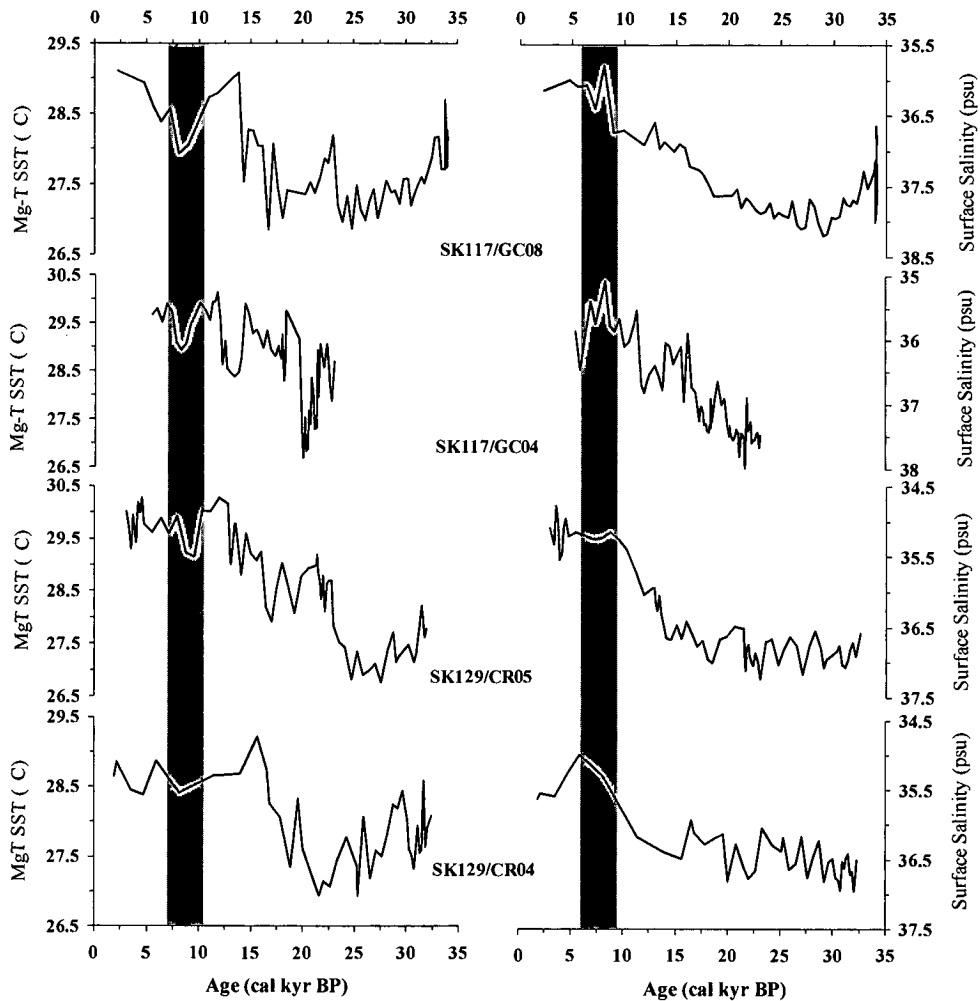

Figure 30. Composite of SST (left panel) and salinity (right panel) time-series for the EAS. Shaded vertical bars encompass the early Holocene event exhibited as concurrently decreased SST and salinity.

To further assess the effect of global climate conditions on the Indian monsoon system, another independent proxy "carbon/nitrogen (C/N) ratio in sedimentary organic matter" is utilized. This ratio is as an indicator of the source of organic matter in marine sediments. The Redfield ratio of C/N in marine phytoplanktons organic matter is 6.6 (Bordowskiy, 1965a). In contrast, terrestrial vascular plants and their derivatives in sediments have C/N ratios of >15 (Bordowskiy, 1965b). Thus, the C/N ratios help in establishing the provenance of the organic matter in the marine sediments.

The colder SSTs observed in EAS between 30 and 19 cal kyr BP (Figure 25) indicate either enhanced surface cooling due to globally colder climate or due to intensified winter monsoon winds. Alternatively, the SST cooling might have been the result of increased coastal upwelling in the EAS during that time. Although the intensified winter monsoon winds during the LGM appear to be the most likely cause of cooling the EAS surface as it significantly enhances the oceanic net heat-loss by evaporation, local upwelling due to intensified glacial winter winds also cannot be ruled-out. Because, the winter-monsoons (land-to-sea) are expected to sweep-off large amount of water from the western Indian coast, which can induce upwelling of thermocline water.

To unscramble the actual cause of this SST cooling during LGM, the C/N ratios of organic matter deposited in the sediment may be useful. The C/N ratios in marine sediment above ~7 (Redfield Ratio for pure marine phytoplankton derived organic matter) is possible only when terrestrial plant biomass having higher C/N ratios (up to 35) (Walsh et al., 1981) is added to the marine sediment. The C/N ratio of ~7 therefore would indicate marine end-member and high C/N of ~35· would be terrestrial end-member. The C/N ratios in the sediment cores SK117/GC08 (Banakar et al., 2005) and SK129/CR05 (Pattan et al., 2003) in general vary marginally ~7 during the entire Holocene period. Whereas, the ratios are significantly increased (> 10 up to 14) during most of the pre-Holocene period (Figure 31: C/N data from Pattan et al., 2003; Banakar et al., 2005). *These higher C/N ratios in the EAS during the last glacial period show association with overall SST cooling and increased salinity (this study), clearly suggesting intensified winter monsoons.* This interpretation confirms Banakar et al.'s (2005) view that suggested significant amount (>10%) of the sedimentary organic

matter in the EAS during the LGM was derived from terrestrial sources and also from soil organic matter from exposed continental shelf due to glacial lowered sea-level (Chodankar, 2004). *Therefore, it is speculated here that, the enhanced nutrients required for increased glacial productivity in this region (Banakar et al., 2005) might have been originated from adjacent soil organic matter and dust supplied to the EAS by intensified winter winds rather than increased injection of nutrient rich-water from below.* If the nutrient injection from the upper thermocline had occurred, then the salinity of upwelled water should have been very high, because this depth in the EAS is filled by inherently very saline ASHSW originating in the northern Arabian Sea, which is expected to be much more saline during the cold glacial conditions than today.

From the SST, salinity and C/N time-series (Figure 31), it is observed that lower SST and higher salinity correspond to higher C/N and *vice-versa*. This in turn suggests that the relative strength of monsoon winds controls the variation of sedimentary C/N ratios in the EAS. The elevated C/N ratios during the glacial period are on expected lines, as the glacial winter monsoons (land towards sea) were intense resulting in increased transfer of terrestrial organic matter in to the EAS. Although not strong, a negative relationship between C/N and SST and positive relationship between C/N and salinity (Figure 32) confirm that the most intense winter winds prevailed during LGM and period prior to this.
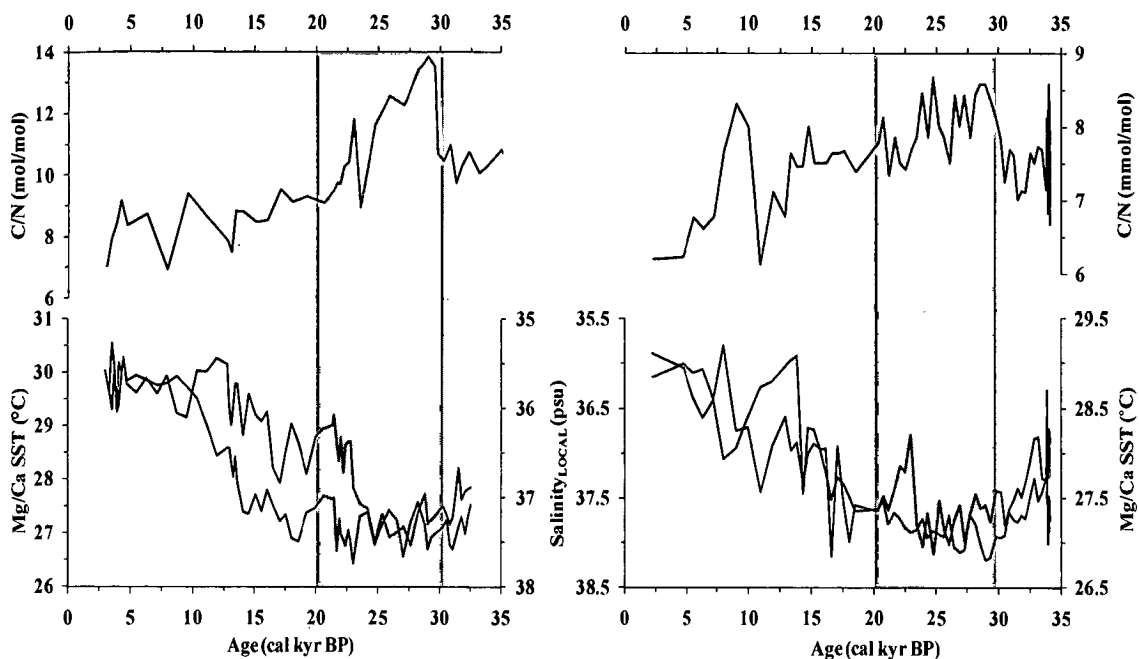
Figure 31. Time series of surface salinity and C/N molar-ratios of organic matter in SK117/GC08 (RHS panel) and SK129/CR05 (LHS panel) sediment cores for the last 35 kyr. The shaded bars represents the period of intense winter winds. (C/N data from Pattan *et al.*, 2003; Banakar *et al.*, 2005).
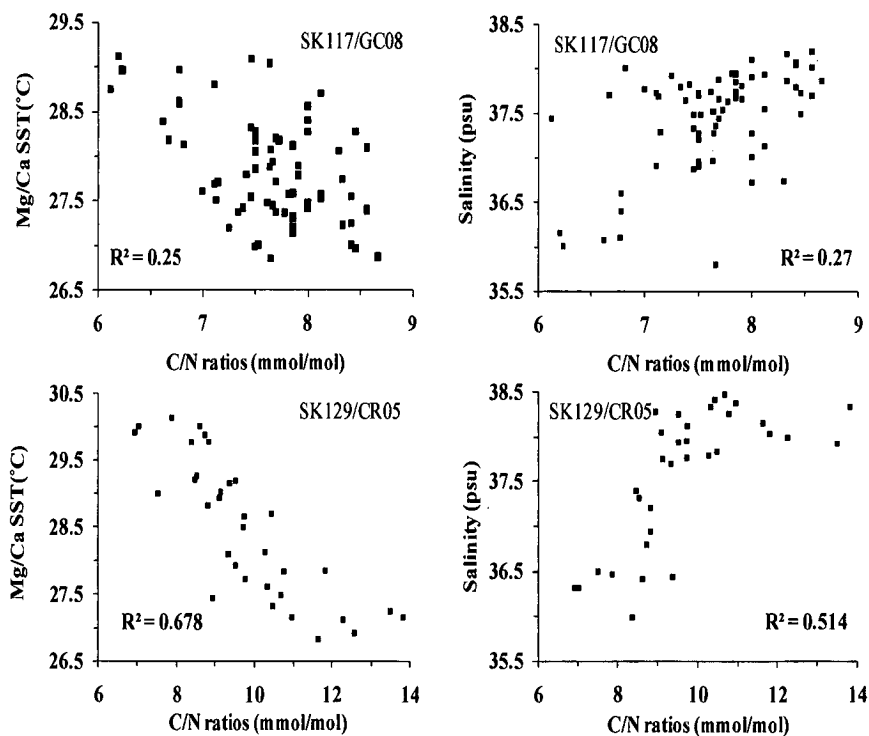

Figure 32. X-Y scatter plots of SST and salinity vs. C/N in the EAS

6.7. Long term variability in EAS climatology

The long-term (past 100 kyr) evolution of surface hydrography recorded in a northern-EAS sediment core (SK117/GC08) and a southern-EAS sediment core (SK129/CR04) is discussed briefly in this chapter. Most of this aspect based on former sediment core has already been published (see Banakar, V. K., Mahesh, B. S., Burr, G., and Chodankar, A. R., 2010. Climatology of the Eastern Arabian Sea during the last glacial cycle reconstructed from paired measurement of foraminiferal $\delta^{18}O$ and Mg/Ca. Quaternary Research, 73: 535-540). As mentioned in the Methods Section, the chronology for sections beyond radiocarbon dated intervals was derived from tuning the oxygen-isotope depth profile to LR04 benthic stack (Lisiecki and Raymo, 2005). The Youngest Toba Tuff (YTT: ~ 71 ka; Zielinski *et al.*, 1996) provided additional tie-point for the chronology. The surface hydrography variations are discussed in context with the monsoonal variations and the global climate.

The $\delta^{18}O_{G.\ sacculifer}$ records of both sediment cores nearly mimic the LR04 benthic stack and are closely comparable to Antarctic atmosphere temperature record (Figure 33). The overall SST variation over the entire 100 kyr is ~2°C, which is comparable to few Arabian Sea sedimentary records published earlier. The SSTs show a gradual decrease from MIS 5 to MIS 2 (Figure 34). During MIS 5, the SSTs varied marginally between 28.5 and 27.9°C. A 1.4°C cooling of SST is evident from MIS 5 to MIS 4. The LGM-SSTs are colder by ~0.8°C compared to MIS 3 average of ~28°C. The difference in the Holocene-LGM SST is ~2°C in both the cores. The SST trends in both northern- and southern-EAS appear similar (Figure 34). The overall variation in salinity for the last 100 kyr is within 2 psu (Figure 35). The salinity variation during the entire last glacial cycle (60 – 18 cal kyr BP) is marginal within the estimation error (±0.2 psu) hence not significant, indicating near consistent variation in the EAS salinity through-out the last glacial cycle.
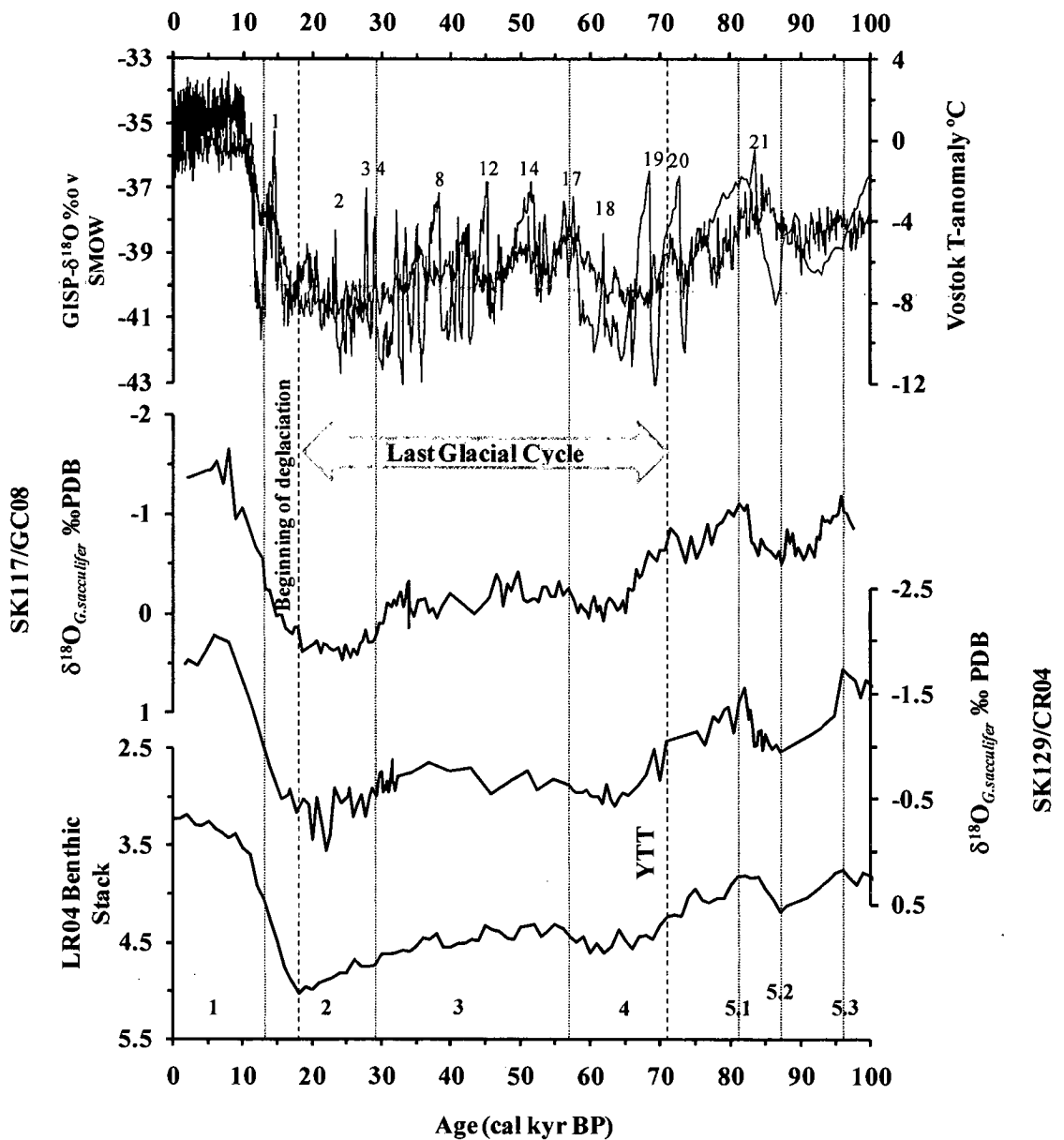
Figure 33. Comparison of last 100 kyr changes in oxygen isotopes with polar climate and ice-volume evolution (LR04). YTT = Youngest Toba Tuff of 71 ka, which was used as an additional control point for the chronology along with radiocarbon dates and oxygen isotope boundaries (vertical dotted lines). Numbered peaks on top panel are the warm interstadials as in D-O oscillations; the numbers on bottom panel are the marine oxygen isotopes stages.

In the last couple of decades, several researchers have brought out significant teleconnections between low-latitude and high-latitude climates. The most important teleconnection with predictive implications is probably the ENSO connection with the global climate. Further, the bipolar see-saw model suggested from vigorous synthesis of Antarctic ice core data and Greenland ice core data by EPICA community members (2006) has documented existence of tight connection between climates of both polar regions.

The link between Indian monsoon and global climate gained significance following publication by Schulz *et al.* (1998), who reported close association between monsoon driven productivity in the Arabian Sea and D-O fluctuations characteristic of the northern high-latitude climate. Several high-resolution studies based on sedimentary proxies from the Arabian Sea indicated that the summer monsoons have responded to high frequency D-O oscillations. The eolian dust input (Leuschner and Sirocko, 2000), $\delta^{13}C$ time series on cellulose and peat bog from Tibet Plateau (Hong *et al.*, 2003), denitrification intensity (Suthhof and Ittekkot, 2001) brought out the correlation of Indian monsoon with global climate system. In all those studies, intensification of summer monsoons was found to have association with warm interstadials in D-O variability. Krishna Kumar *et al.* (1999) and Goes *et al.* (2005) have demonstrated teleconnections of Indian monsoons and ENSO with distant high-latitude climate variations in the modern times. Thus there are evidences to show connection between global climate and Indian monsoon system both in present and in past.

The SST variability recorded in the present sediment cores does not show either distinct glacial-interglacial variability as depicted by the oxygen isotope records or Antarctic atmosphere Temperature record or clearly do not reflect the D-O type variation (Figure 34). Although the time resolution of the analyzed data is not adequate to isolate every D-O events, it is sufficient to recognize net effect of a set of consecutive D-O events. The past SST trends obtained here for EAS appear to qualitatively incorporate mixed signals of both hemisphere climatic signals (Antarctic Temperature: Petit *et al.*, 1999; and Greenland Ice oxygen-isotope: Dansgaard *et al.*, 1993).

In the core SK117/GC08, the coldest SSTs during MIS 4 closely overlap the stadial trend between D-O interstadial events 17-19, and MIS 3's moderately warmer

SSTs follow the broad pattern between interstadials 5-15 (Figure 34). The prominent features such as the D-O interstadials 1, 2, 3, 8, 17 and 21 are identifiable by warm SSTs in both locations of the EAS. On the other hand, the MIS 4, MIS 2, and deglaciation SST trends are consistent with Vostok temperature record.

The overall variation in EAS-salinity for the last 100 kyr appear to follow the Antarctic temperature and LR04 benthic $\delta^{18}O$ variations (Figure 35) and is consistently higher during the last glacial cycle ($\sim 60 - 18$ cal kyr BP). This higher salinity during the entire last glacial period is indicative of weakening of the Poleward Coastal Current system that advects low-salinity water from BoB in to EAS (Chodankar et al., 2005). Therefore, consistently higher salinity in the EAS during the last glacial period suggests influence of global climate on the local circulation.

The SST time-series for the equatorial Indo-Pacific (Lea et al, 2000; Saraswat et al, 2005) and salinity reconstruction for Equatorial Indian Ocean (Rostek et al., 1993) have glacial-interglacial patterns closely comparable to Antarctic temperatures. These two together and EAS salinity exhibiting trends similar to LR04 benthic stack (indicative of global climate) suggest close association of equatorial Indo-Pacific surface hydrography with Antarctic climate.

In light of the above observations, the past variability of EAS climatology can be interpreted as response to processes reflecting both global climate and regional monsoon intensity. The Arabian Sea sedimentary records have shown influence of both Antarctic warming and Greenland warming (D-O interstadials) on strengthening of Indian summer monsoons. This connection probably was a result of coupled north and south polar climates operating in low latitudes via ENSO (Sirocko et al., 1999). In addition, the transmission of sub-antarctic-mode water has been invoked to provide a thermal connection between Southern Hemisphere climate and the Western Indian Ocean (Kiefer et al., 2006). These previously reported observations, along with present time-series of SST and salinity, provide evidence for high-latitude climate influencing the Late Quaternary climatological evolution of the EAS.
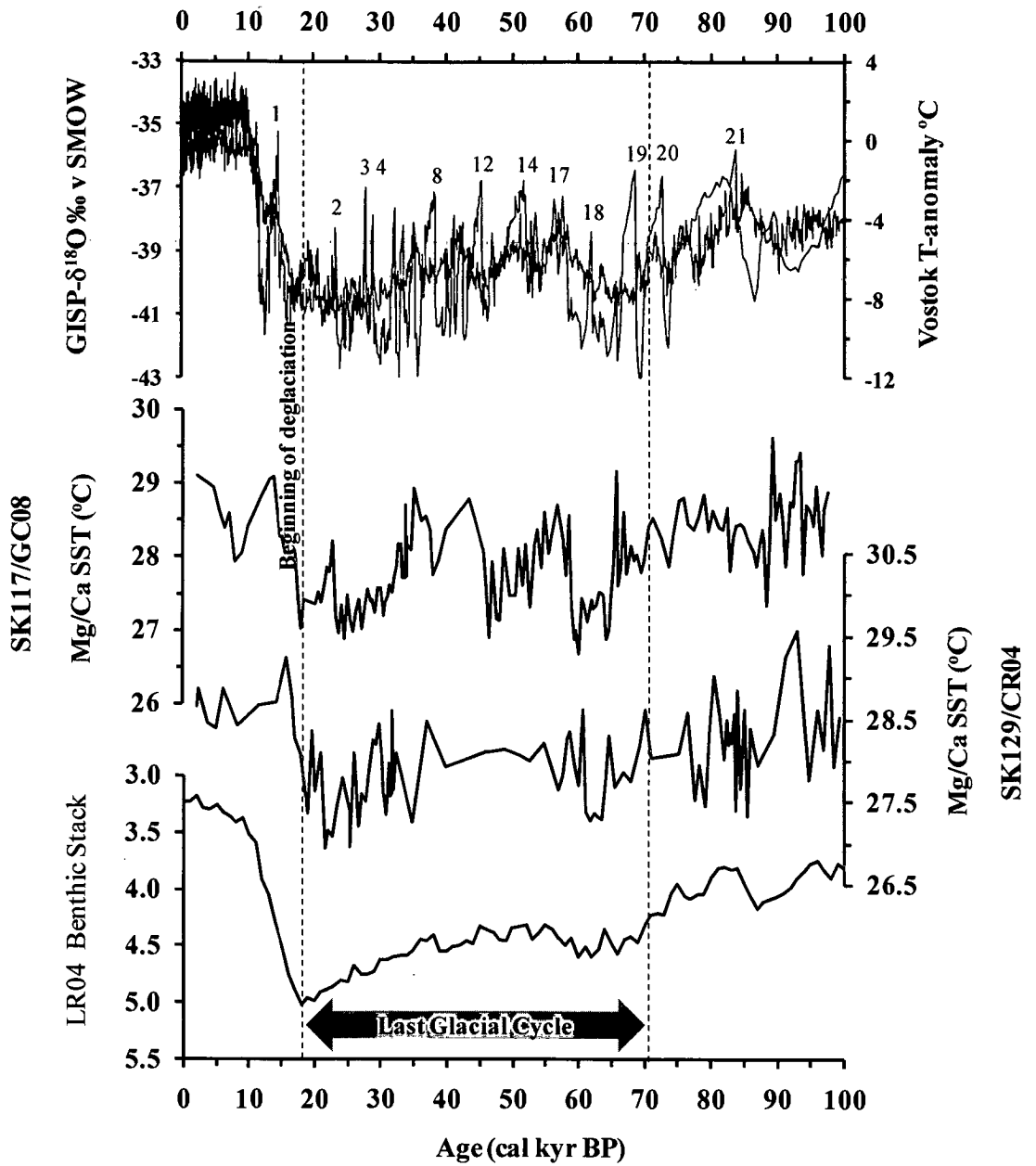
Figure 34. Composite of time-series of Antarctic T- Anomaly, Greenland Ice oxygen-isotopes, EAS SST for the last 100 kyr. The numbers in the top panel represent warm interstadials in D-O type climate.
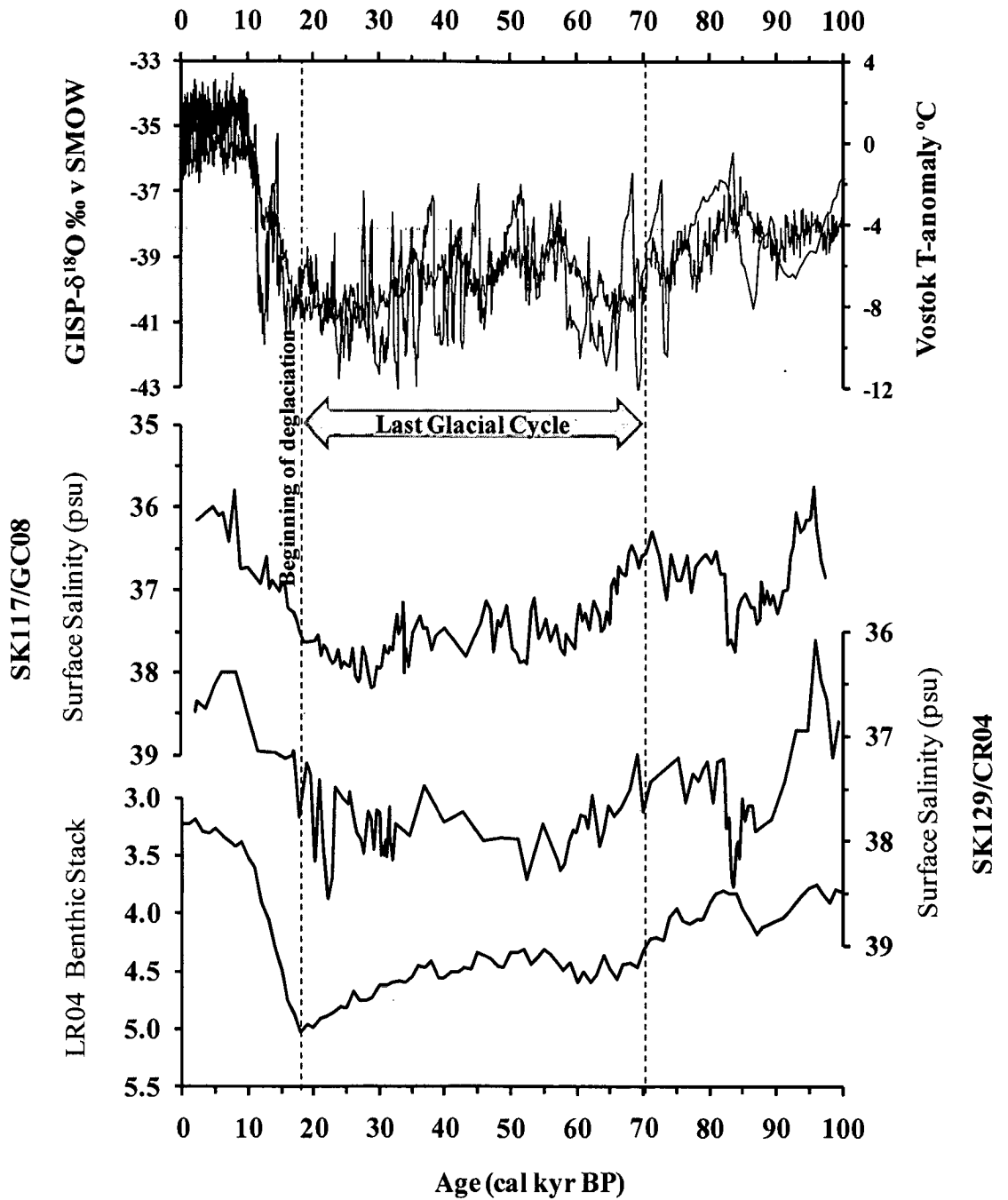
Figure 35. Composite of time-series of Antarctic T- Anomaly, Greenland Ice oxygen-isotopes, LR04 Benthic Stack, and EAS salinity for the last 100 kyr. Broken vertical lines bracket the last glacial period and the numbers in the top panel represents the warm interstadials in D-O type climate.

6.8. SST variations in tropical Indo-Pacific region

In this section, I have compared the present SST time-series of EAS with four other SST records from the Arabian Sea and equatorial Indo-Pacific region (Figure 36). One core is from the EAS (AAS9/21: Govil and Naidu, 2010), one from the equatorial Indian Ocean (EIO: SK157/4: Saraswat et al., 2005) and two cores from Equatorial Pacific (Western Pacific Warm Pool: ODP806B and Eastern Pacific Cold Tongue: T163-19, Lea et al., 2000). This comparison is expected to provide some insights to identify if any common forcing existed for the evolution of global tropical SSTs.

The overall SST variation over the last 100 kyr in the EAS is between ~2°C (present study) and ~4.5°C (Govil and Naidu, 2010). The SST variations in the EAS (present study) and Equatorial Indian Ocean (Saraswat et al., 2005) are similar to the variations recorded in Western Pacific warm Pool (Lea et al., 2000: ODP806B). The comparison of SSTs between all three locations (EAS, EIO and Western Pacific Warm Pool) show similar variation through MIS 1, 2, 4 and 5 (see Table 22 and Figure 37). The SSTs in East Pacific Cold Tongue (TR163-19) are always lower than other records as expected, since the latter is located in intense upwelling region of the east Pacific.

The SSTs of the west Pacific have been interpreted in terms of transmission of Subantarctic thermocline temperatures, which is also evident in carbon-isotope records of the same sediment core (Spero and Lea, 2002). This, along with Kiefer et al.'s (2006) study showing Subantarctic temperature signal transmitting in to EIO, provide a mechanism of transferring the Antarctic temperature signals to tropical oceans.

Table 22. Climate stage averaged SSTs obtained from six sediment cores from tropical Indo- Pacific referred in Figure 36.

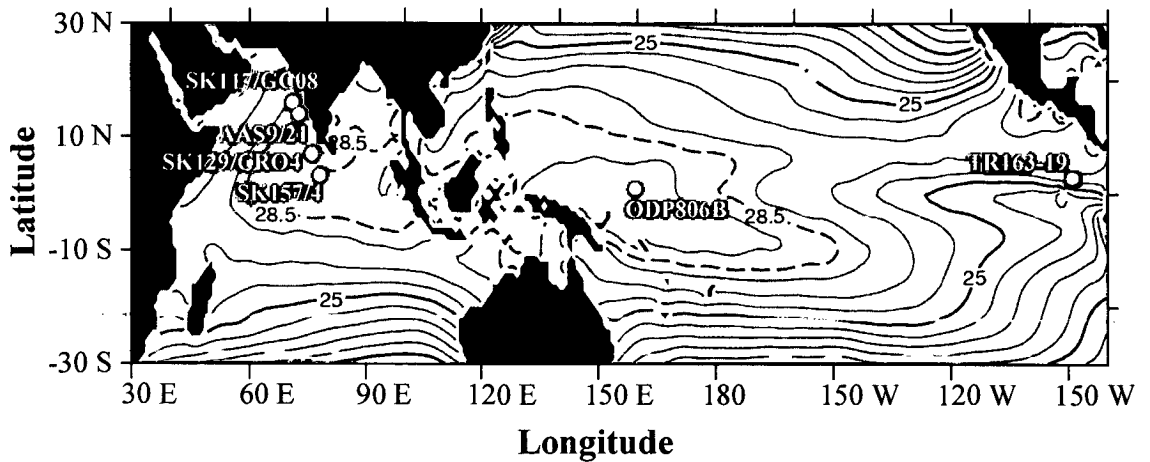| Core.Id	MIS1	MIS2	MIS3	MIS4	MIS5
SK117/GC8	29.1°C	26.9°C	28.0°C	27.0°C	29.0°C
SK129/CR4	29.0°C	27.0°C	28.0°C	27.0°C	28.0°C
SK157/4	29.0°C	26.6°C	28.0°C	27.0°C	28.0°C
ODP 806B	29.0°C	26.3°C	27.0°C	26.5°C	28.4°C
TR163-19	26.0°C	23.5°C	24.0°C	23.0°C	25.0°C
AAS9/21	28.5°C	25.0°C	27.0°C		
Mean	28.4±1.2	25.9±1.4	27±1.55	26±1.7	27.6±1.5

Figure 36. The sediment cores used to compare Mg/Ca SSTs from tropical Indo-Pacific oceans. The background map is modern SST (map source: http://www.nodc.noaa.gov)

The SST time-series of EAS and equatorial Indo-Pacific show internally consistent structures (Figure 37). The D-O type climatic signals are more pronounced in the EAS. Whereas, in the equatorial Indo-Pacific the glacial-interglacial pattern is dominant. The D-O interstadials 1, 2, 3, 4, 8, 12, 14, 17 and 21 occur as either independent or merged features in all records with variable amplitudes and certain timing offsets. This offset might be due to different tuning utilized for chronology or may be due to region-specific lead or lag of the events. *Nevertheless, the important aspect of the SST variability in all these regions is the existence of consistent structure that renders the SST records presented in this thesis as significant contribution to the existing global paleo-SST datasets.*
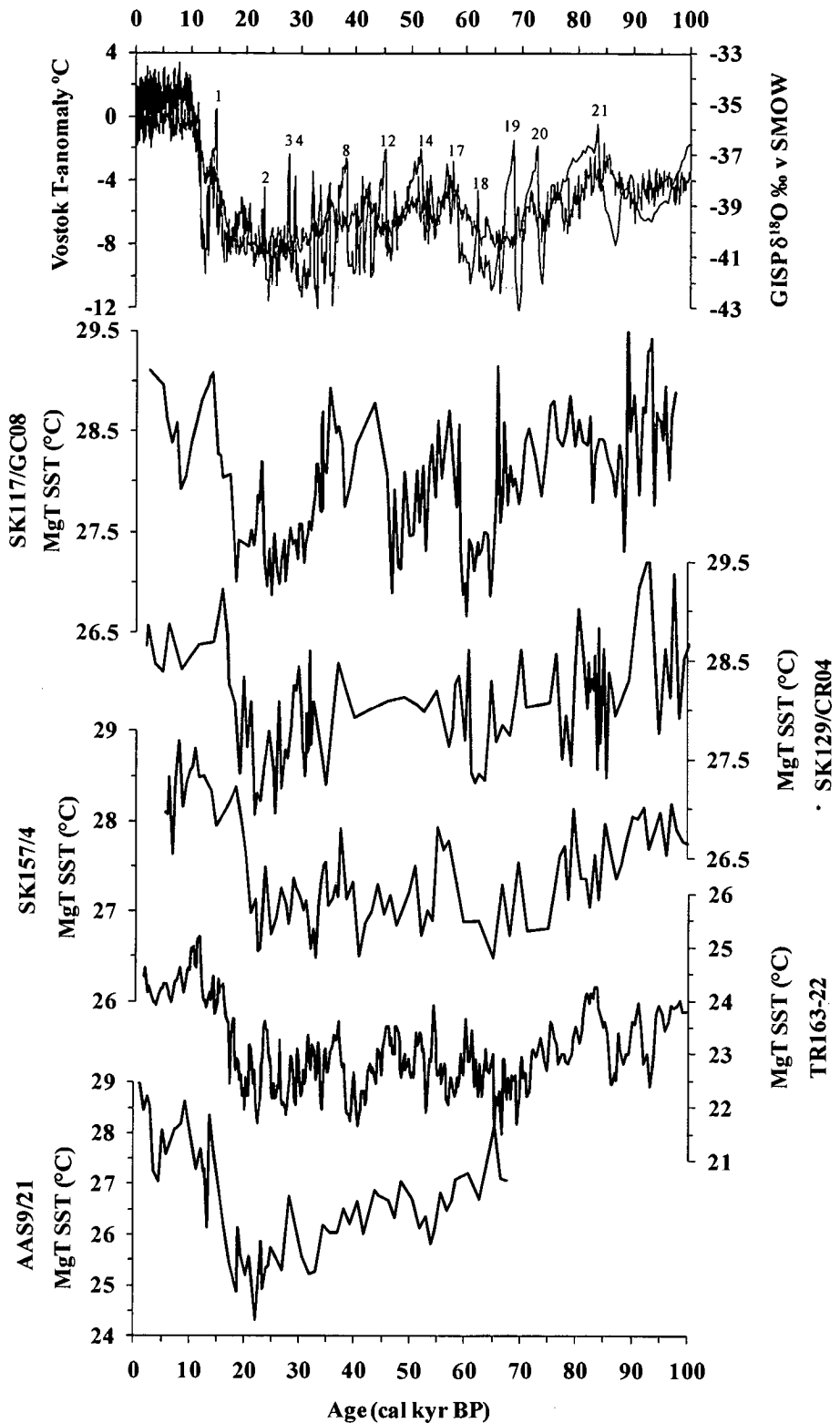
Figure 37. Mg/Ca SST time-series for EAS (Present study), Equatorial Indian Ocean (Saraswat *et al.*, 2005) and Equatorial Pacific (Lea *et al.*, 2000) for the last glacial cycle are compared with polar climates. Note several variable magnitude warming events within the glacial climate in almost all the records.

The internally consistent SST variability in equatorial Indo-Pacific and EAS showing affinity to both polar climates is intriguing. The SSTs of equatorial Pacific (TR163-19 and ODP806B, Lea *et al.*, 2000) tend more towards Antarctic climate, while EAS SSTs tend towards mixed D-O and Antarctic type. The Antarctic warming occurring within the rising phase of northern hemisphere high latitude summer insolation (Kawamura *et al.*, 2007) has further strengthened the north–south polar climate linkages. Therefore, interconnections such as: a) significant heat exchange between a Indian and Pacific Ocean via Indonesian Through Flow (Webster *et al.*, 1998), b) EAS SSTs exhibiting mixed D-O type and Antarctic temperature patterns, c) the Antarctic Ocean communicating with the Indian Ocean via sub-antarctic mode water and finally c) the EAS salinity records showing glacial-interglacial patters, together suggest a comprehensive interconnections of global climate connection with the EAS climatology. The Arctic and Antarctic climates might be acting as two end members in dictating low-latitude surface ocean climatology with relatively variable influence depending upon the relative separation of a study region from the end-member locations (Banakar *et al.*, 2010). This speculation needs further detailed examinations using several sediment records spread along the NS transects in the world oceans.

7. Conclusions

First reconstructions of paleo-SSTs using Mg/Ca thermometry in an Indian laboratory are reported in the present thesis carried out to understand past changes in the Eastern Arabian Sea surface climatology. The surface climatology of this region has potential to provide insights in to the past monsoon variability. Indian monsoon system evolves seasonally due to the sum of many interacting complex mechanisms. Understanding this complex system, how it changes from one state to another or maintains long-term stability, is of crucial importance to make predictions.

The salient features and observations made from the present study, which are significant in understanding the evolution of the surface hydrography of the Eastern Arabian Sea in response to past monsoons as well as global climate systems are listed in this section.

1. *The sedimentation rates* in the EAS provide preliminary information about the relative strength of seasonally reversing Indian monsoons. Higher sedimentation rates during the LGM than during Holocene recorded in this basin indicate stronger winter monsoon and weaker summer monsoons during LGM.

2. *The LGM,* most recent-past coldest event within the radiocarbon dated intervals of the sediment cores, is defined here as a continuous part lasting for ~7 kyr from 26 to 19 cal ky BP that has recorded heaviest $\delta^{18}O_{G.\ sacculifer}$ fluctuating within the measurement precision band of ±0.08‰ within the last glacial cycle.

3. *The beginning* of deglaciation and its transition pattern recorded in the EAS sediment cores are closely comparable to the global benthic $\delta^{18}O$ record (LR04). The timing of initiation and completion of deglacial transition also correlate well with the LGM-Holocene transition recorded in Antarctic ice-core records. These observations suggest that the tropical climate pattern appears to have influenced by changes in global climate.

4. *Non-reflection* of the longest cold interval viz., Younger Dryas (characteristic of D-O type climate) during the last glacial transition in the present $\delta^{18}O_{G.\ sacculifer}$ records and their closely comparable patterns with Antarctic type climate variability may be suggestive of a link between Antarctic climate and EAS hydrography.

5. *The lowest SSTs* were recorded prior to the LGM (i.e., between 29 and 24 cal kyr BP) might suggest a response to global climate cooling represented by then global ice volume maximum as evident in recent rigorous evaluation of global climate models and ice-growth dynamics last glacial cycle.

6. *The warm-SST* leading the lowered-salinity by ~3-5 kyr during deglacial transition may indicate preconditioning of sea surface climatology required to set-in moisture charged summer monsoon circulation.

7. *The striking feature* recorded within the Holocene is a synchronous decrease of SST, surface salinity, and $\delta^{18}O_{G.\ sacculifer}$ within the time-slice of 9-6 cal kyr BP. This combination indicates most intense summer monsoons with the onset of full Holocene conditions in the EAS.

8. *Published* C/N time-series from the same sediment cores along with the present SST and salinity time-series reveal intense winter monsoons during the LGM.

9. *The long-term* EAS SST variations contain diffused pattern of D-O type climate oscillations, while salinity and $\delta^{18}O$ records tend more towards the Antarctic type of climate suggesting both polar climate controls on the local climatology.

Bibliography

Agassiz, L., 1842. The glacial theory and its recent progress. *The Edinburgh New Philosophical Journal*, **33**: 271-283.

Anand, P., and Elderfield, H., 2003. Calibration of Mg/Ca thermometry in planktonic foraminifera from a sediment trap time series. *Paleoceanography*, **18**: 1050.

Anand, P., Kroon, D., Singh, A.D., Ganeshram, R.S., Ganssen, G., and Elderfield, H., 2008. Coupled sea surface temperature–seawater $\delta^{18}O$ reconstructions in the Arabian Sea at the millennial scale for the last 35 ka. *Paleoceanography*, **23**: PA4207.

Anderson, D.M., and Prell, W.L., 1993. A 300 kyr record of upwelling off Oman during the Late Quaternary: Evidence of the Asian Southwest monsoon. *Paleoceanography*, **8**: 193-208.

Banakar, V.K., Gupta, S.M., and Padmavati, V.K., 1991. Abyssal sediment erosion in the Central Indian Basin: Evidence from radiochemical and radiolarian studies. *Marine Geology*, **96**: 167-173.

Banakar, V.K., Parthiban, G., Pattan, J.N., and Jauhari, P., 1998. Chemistry of surface sediment along a north-south transect across the equator in the Central Indian Basin: an assessment of biogenic and detrital influences elemental burial on the seafloor. *Chemical Geology*, **147**: 217–232.

Banakar, V.K., Oba, T., Chodankar, A.R., Kuramoto, K., Yamamoto, M., and Minagawa, M., 2005. Monsoon related changes in sea surface productivity and water column denitrification in the Eastern Arabian Sea during last glacial cycle. *Marine Geology*, **219**: 99-108.

Banakar, V. K., Mahesh, B. S., and Burr, G., 2010. Climatology of the Eastern Arabian Sea during the last glacial cycle reconstructed from paired measurement of foraminiferal $\delta^{18}O$ and Mg/Ca. *Quaternary Research*, **73**: 535-540.

Banse, K., 1968. Hydrography of the Arabian Sea Shelf of India and Pakistan and effects on demersal fishes. *Deep Sea Research*, **15**: 45-79.

Barber, D.C., Dyke, A., Hillaire-Marcel, C., Jennings, A.E., Andrews, J.T., Kerwin, M. W., Bilodeau, G., McNeely, E., Southon, J., Morehead, M. D., and Gagnonk, J. M., 1999. Forcing of the cold event of 8,200 years ago by catastrophic drainage of Laurentide Lake. *Nature*, **400**: 344-348.

Bard, E., Rostek, F., Turon, J., and Gendreau, S., 2000. Hydrological Impact of Heinrich Events in the Subtropical Northeast Atlantic. *Science,* **289**: 1321-1324.

Barker, S., Greaves, M., and Elderfield, H., 2003. A study of cleaning procedure used for foraminiferal Mg/Ca paleothermometry. *Geochemistry Geophysics Geosystems,* **4**: 8407.

Barker, S., Cacho, I., Benway, H., and Tachikawa, K., 2005. Planktonic foraminiferal Mg/Ca as a proxy for past oceanic temperatures: a methodological overview and data compilation for the last glacial maximum. *Quaternary Science Reviews,* **24**: 821-834.

Barrows, T.T. and Juggins, S., 2005. Sea-surface temperatures around the Australian margin and Indian Ocean during the Last Glacial Maximum. *Quaternary Science Reviews,* **24**: 1017-1047.

Bassinot, F.C., Labeyrie, L.D., Vincet, E., Quidelleur, X., Shackleton, N.J., and Lancelot, Y., 1994. The astronomical theory of climate and the age of the Brunhes-Matuyama magnetic reversal. *Earth and Planetary Science Letters,* **126**: 91-108.

Be`, A.W.H., 1960. Ecology of recent planktonic foraminifera, part 2: Bathymetric and seasonal distributions in the Sargasso Sea off Bermuda. *Micropaleontology,* **6**: 373–392.

Be`, A.W.H., 1980. Gametogenic calcification in a spinose planktic foraminfer, *Globigerinoides sacculifer* (Brady). *Marine Micropaleontology,* **5**:283-310.

Bemis, B.E., Spero, H.J., Bijma, J., and Lea, D.W., 1998. Re-evaluation of the oxygen isotopic composition of planktonic foraminifer: Experimental results and revised paleotemperature equations. *Paleoceanography,* **13**: 150-160.

Bender, M., Lorens, R., and Williams, D., 1975. Sodium, magnesium, and strontium in the tests of planktonic foraminifera. *Micropaleontology.* **21**: 448–459.

Berger, W.H., and Winterer, E.L., 1974. Plate stratigraphy and thefluctuating carbonate line. In: Hs. u, K.J., Jenkyns, H.C. (Eds.), Pelagic Sediments: On Land and Under the Sea. Publication No. 1, Blackwell, Oxford; *International Association of Sedimentologists,* pp 11–98.

Bette, L., Otto-Bliesner, Schneider, R., Brady, E.C., Kucera, M., Abe-Ouchi, A., Braconnot, P., Crucifix, M., Hewitt, C., Kageyama, M., Marti, O., Paul, A., Rosell-Melé, A., Weber, S.L., Weinelt, M., and Yu, Y., 2009. A comparison of PMIP2 model simulations and the MARGO proxy reconstruction for tropical sea surface temperatures at last glacial maximum. *Climate Dynamics,* **32**: 799-815.

Bijma, J., and Hemleben, C., 1990. Population dynamics of the planktic foraminifer *Globigerinoides sacculifer* (brady) from the central Red Sea. *Deep-sea Research Oceanographic Research Papers*, **41**: 485-510.

Bijma, J., Faber, Jr W. W., and Hemleben, C., 1994. Temperature and salinity limits for growth and survival of some planktonic foraminifers in laboratory cultures. *Journal Foraminiferal Research*, **20**: 95-116.

Biswas, S.K., 1987. Regional tectonic framework, structure and evolution of the western marginal basins of India. *Tectonophysics*, **135**: 307-327.

Bond, G. C., and Lotti, R., 1995. Iceberg Discharges into the North Atlantic on Millennial Time Scales during the Last Glaciation. *Science*, **267**: 1005-1010.

Bond, G., Showers, W., Cheseby, M., Lotti, R., Almasi, P., Menocal, P., Priore, P., Cullen, H., Hajdas, I., and Bonani, G., 1997. A pervasive millennial-scale cycle in North Atlantic Holocene and glacial climates. *Science*, **14**: 1257-1266.

Bordowskiy, O.K., 1965a. Source of organic matter in marine basins. *Marine Geology*, **3**: 5–31.

Bordowskiy, O.K., 1965b. Accumulation of organic matter in bottom sediments. *Marine Geology*, **3**: 33–82.

Braconnot, P., Otto-Bliesner, B., Harrison, S., Joussaume, S., Peterschmitt, J.-Y. , Abe-Ouchi, A., Crucifix, M., Driesschaert, E., Th. Fichefet, Hewitt, C. D., Kageyama, M., Kitoh, A., Laine, A., Loutre, M.-F., Marti, O., Merkel, U., Ramstein, G., Valdes, P., Weber, S.L., Yu, Y., and Zhao, Y., 2007. Results of PMIP2 coupled simulations of the Mid-Holocene and Last Glacial Maximum - Part 1: experiments and large-scale features. *Climate of the Past*, **3**: 261-277.

Bradley, R.S., and Eddy, J.A., 1991. Records of past global changes. In: *Global changes of the past*, Bradley, R. S., (Ed.). Boulder: *University Corporation for Atmospheric Research*, 5-9.

Broecker, W. S., Andree, M., Bonani, G., Woeli, W., Oeschger, H., Klas, M., Mix, A. C., and Curry, W., 1998. Preliminary estimates for the radiocarbon age of deep water in the glacial ocean. *Paleoceanography*, **3**: 659-669.

Brown, O.B., and Evans. R.H., 1981. Interannual variability of the Arabian Sea surface temperature. In: *Oceanography from Space*, J. F. R. (Ed.). Plenum Press, New York: 135-143 pp.

Brown, S.J., and Elderfield, H., 1996. Variations in Mg/Ca and Sr/Ca Ratios of Planktonic Foraminifera caused by post-depositional dissolution: Evidence of Shallow Mg-Dependent Dissolution. *Paleoceanography*, **11**: 543–551.

Burton, E.A., and Walter, L.M., 1991. The effects of P_{CO2} and temperature on magnesium incorporation in calcite in seawater and $MgCl_2$---$CaCl_2$ solutions. *Geochimica et Cosmochimica Acta,* **55**: 777–785.

Butzin, M., Prange, M. and Lohmann, G., 2005. Radiocarbon simulations for the glacial ocean: the effects of wind-stress, Southern Ocean sea ice, and Heinrich events. *Earth and Planetary Science Letters.* **235**: 45-61.

Cayre, O., and Bard, E., 1999. Planktonic foraminiferal and alkenone records of the last-glaciation from the eastern Arabian Sea. *Quaternary Research,* **52**: 337-342.

Central Water Commission, *Water and Related Statistics,* India - 2007.

Chao, W.C., and Chen, B., 2001. The origin of monsoons. *Journal of the Atmospheric Sciences,* **58**: 3497–3507.

Chave, K.E., 1952. A solid solution between calcite and dolomite. *Journal of Geology,* **60**: 190-192.

Chave, K.E., 1954. Aspects of the Biogeochemistry of Magnesium 1. Calcareous Marine Organisms. *The Journal of Geology,* **62**: 266-283.

Chodankar, A.R., 2004. The Late-Pleistocene sedimentation history in the Eastern Arabian Sea: Climate-Weathering-Productivity linkage. (In.) *Thesis,* Goa University.

Chodankar, A.R., Banakar, V.K., and Oba, T., 2005. Past 100 ky surface salinity gradient response in the Eastern Arabian Sea to the summer monsoon variation recorded by $\delta^{18}O$ of *G. sacculifer. Global Planetary Change,* **47**: 135-142.

Clark, P.U., Dyke, A.S., Shakun, J.D., Carlson, A.E., Clark, J., Wohlfarth, B., Mitrovica, J., Hostetler, S.W., and McCabe, A.M., 2009. The Last Glacial Maximum. *Science,* **325**: 710-714.

Clemens, S.C., and Prell, W.L., 1990. Late Pleistocene variability of Arabian Sea summer monsoon winds and continental aridity: Eolian records from the lithogenic components of deep sea sediments. *Paleoceanography,* **5**: 109-145.

Clemens, S., Prell, W., Murray, D., Shimmield, G., and Weedon, G., 1991. Forcing mechanisms of the Indian Ocean monsoon. *Nature,* **24**: 720-725.

CLIMAP Project Members, 1976. The surface of the ice-age Earth. *Science,* **191**: 1131-1137.

CLIMAP Project Members, 1981. Seasonal reconstruction of the Earth's surface at the last glacial maximum Map Chart Ser. MC-36, *Geological Society of America.*

Croll, J., 1867. On the eccentricity of the earth's orbit and its physical relations to the glacial epoch. *Philosophical Magazine,* ser. 4, **33**: 119-131.

Crowley, T.J., 2003. When Did Global Warming Start? *Climate Change* **61**: 259-260.

Cullen, J.L., and Prell, W.L., 1984. Planktonic foraminifera of the northern Indian Ocean: Distribution and preservation in surface sediments. *Marine Micropaleontology,* **9**: 1-52.

Crutzen, P.J., and Stoermer, E.F., 2000. The Anthropocene. *Global Change Newsletter,* **41**: 17-18.

Currie, R.I., 1963. The Indian Ocean standard net. *Deep-Sea Research,* **10**: 27-32.

Currie, R.I., 1992. Circulation and upwelling off the coast of south-east Arabia. *Oceanologica Acta,* **15**: 43-60.

Dahl, K.A., and Oppo, D.W., 2006. Sea surface pattern reconstructions in the Arabian Sea. *Paleoceanography,* **21**: PA1014.

Dai, A., and Trenberth, K.E., 2003. New Estimates of Continental Discharge and Oceanic Freshwater Transport. *AMS Symposium on Observing and Understanding the Variability of Water in Weather and Climate,* 9-13 Feb. Long Beach, CA.

Dansgaard, W., Johnsen, S.J., Clausen, H. B., Dahl-Jensen, D., Gundestrup, N.S., Hammer, C. U., Hvidberg, S., Steffensen, J. P., Sveinbjornsdottir, A. E., Jouzel, J., and Bond, G., 1993. Evidence for general instability of past climate from a 250 ka ice-core record. *Nature,* **364**: 218-220.

Danzeglocke, U., Jöris, O., and Weninger, B., 2009. CalPal-2007[online]. http://www.calpal-online.de/, 2008-10-05.

Darbyshire, M., 1967. The surface waters off the coast of Kerala, south-west India. *Deep-Sea Research,* **14**: 295-320.

Dekens, P.S., Lea, D.W., Pak, D.K., and Spero, H.J., 2002. Core-top calibration of Mg/Ca in tropical foraminifera: refining paleo-temperature estimation. *Geochemistry Geophysics Geosystems,* **3**: 1022.

Delaney, M.S., Be, A.W., and Boyle, E.A., 1985. Li, Sr, Mg and Na in foraminiferal calcite shells from laboratory culture, sediment traps and sediment cores. *Geochimica et Cosmochimica Acta,* **49**: 1327-1341.

Delaygue, G., Bard, E., Rollion, C., Jouzel, J., Stevenard, M., Duplessy, J.C., and Banssen, G., 2001. Oxygen isotope/salinity relationship in the northern Indian Ocean. *Journal of Geophysical Research*, **106**: 4565-4574.

DeVilliers, S., Greaves, M., and Elderfield, H., 2002. An intensity ration calibration method for the accurate determination of Mg/Ca and Sr/Ca of marine carbonates by ICP-AES. *Geochemistry, Geophysics, Geosystems*, **3**: 2001GC000169.

Dobson, D.P., and Brodholt, J.P., 2005. Subducted banded iron formations as a source of ultralow-velocity zones at the core-mantle boundary. *Nature*, **434**: 371-374.

Duing, W., and Leetma, A., 1980. Arabian Sea cooling: a preliminary heat budget. *Journal of Physical Oceanography*, **10**: 307-312.

Duplessy, J.C., 1982. Glacial to interglacial contrast in the northern Indian Ocean. *Nature*, **295**: 464-498.

Elderfield, H. and Ganssen, G., 2000. Past temperature and salinity using $\delta^{18}O$ of surface ocean water inferred from foraminiferal Mg/Ca ratios. *Nature*, **405**: 442-445.

Emeis, K.C., Anderson, D.M., Kroon, D., and Schulz-Bull, D., 1995. Sea-surface Temperatures and the History of Monsoon Upwelling in the Northwest Arabian Sea during the Last 500,000 years. *Quaternary Research*, **43**: 355-361.

Emiliani, C., 1954. Depth habitats of growth stages of pelagic foraminfera as indicated by oxygen isotope ratios. *American Journal of Science*, **252**: 1315-1325.

Emiliani, C., 1955. Pleistocene temperatures. *The Journal of Geology*, **63**: 538-578.

EPICA Community Members, 2006. One to one coupling of glacial climate variability in Greenland and Antarctica. *Nature*, **444**: 195-198.

Epstein, S., Buchsbaum, R., Lowenstam, H. A., Urey, H. C., 1953. Revised carbonate-water isotopic temperature scale. *Bulletin of Geological Society of America*, **64**: 1315-1325.

Farquhar, J., Bao, H.M., and Thiemens, M., 2000. Atmospheric influence of Earth's earliest sulfur cycle. *Science*, **289**: 756-758.

Fieux, M., 1987. Sections in the western Indian Ocean Variability in the temperature structure. *Deep-Sea Research*, **34**: 601–625.

Fontugne, M.R., and Duplessy, J.C., 1986. Variations of the monsoon regime during the upper Quaternary: Evidence from carbon isotopic record of organic matter in north Indian Ocean sediment cores. *Palaeogeography Palaeoclimatology Palaeoecology*, **56**: 69-88.

145

Frakes, L.A., 1979. Climates through geologic time. *Elsevier*, Amsterdam: 310 pp.

Gadgil, S., 2003. The Indian monsoon and its variability. *Annual Reviews of Earth and Planetary Sciences*, **31**: 429–467.

Goes, J., Prasad, T.G., Helga, R.G., and Fasullo, J.T., 2005. Warming of the Eurasian landmass is making Arabian Sea more productive. *Science*, **308**: 545-547.

Goldsmith, J.R., Graf, D.L., and Joensuu, O.I., 1955. The occurrence of magnesian calcites in nature. *Geochimica et Cosmochimica Acta*, **7**: 212-230.

Govil, P., and Naidu, P.D., 2010. Evaporation-precipitation changes in the eastern Arabian Sea for the last 68 ka: Implications on monsoon variability. *Paleoceanography,* **25**: PA1210.

Graham, D.W., Bender, M.L., Williams, D.F., and Keigwin, L.D., 1982. Strontium–calcium ratios in Cenozoic planktonic foraminifera. *Geochimica et Cosmochimica Acta,* **46**: 1281-1292.

Grootes, P.M., Stuiver M., White, J.W.C., Johnsen, S., and Jouzel, J., 1993. Comparison of oxygen isotope records from the GISP2 and GRIP Greenland ice-cores. *Nature*, **366**, 552-554.

Grootes, P.M., and Stuiver, M., 1997. Oxygen $^{18}O/^{16}O$ variability in Greenland snow and ice with 10^{-3} to 10^5 year time resolution. *Journal of Geophysical Research*, **102**: 455-470.

Groves, D.G., and Hunt, L.M., 1980. *Ocean world Encyclopedia*, McGraw-Hill Company, New York: 159-165.

Hambrey, M.J. and Harland, W.B., 1981. Evolution of climates. In: *The Evolving Earth*, Cocks, L. R. M., (Ed.). British Museum and Cambridge Univ. Press, Cambridge, 137-152 pp.

Harland, W.B., 1964. Critical evidence for a great infra-Cambrian glaciation. *Geologische Rundschau*, **54**: 45-61.

Hathorne, E.C., Alard, O., James, R.H., Rogers, N.W., 2003. Determination of intra-test variability of trace elements in foraminifera by laser ablation inductively coupled plasma-mass spectrometry. *Geochemistry, Geophysics, Geosystems*: **4**: 8408.

Hemleben, C., Spindler, M., Breitinger, I., and Ott, R., 1987. Morphological and physiological responses of *Globigerinoides sacculifer* (BRADY) under varying laboratory conditions. *Marine Micropaleontology*, **12**: 305-324.

Hemleben, C., Spindler, M. and Anderson, O.R. 1989. *Modern planktonic foraminifera.* Springer-Verlag, New York, N.Y.

Hillaire-Marcel, C., and De Vernal, A., (eds) 2007. Proxies in Late Cenozoic Paleoceanography. Developments in Marine Geology Series Volume 1. xviii + 843 pp.

Holland, H.D., 1978. The chemistry of the Atmosphere and the Oceans. New York: John Wiley & Sons, Inc.

Holland, H.D., 1994, Early Proterozoic atmospheric change. In: *Early life on Earth: Nobel Symposium No. 84,* Bengtson, S., (Ed.). New York, Columbia University Press, 237-389 pp.

Hong, Y.T., Hong, B., Lin, Q.H., Zhu, Y.X., Shibata, Y., Hirota, M., Uchida, M., Leng, X.T., Jiang, H.B., Xu, H., Wang, H., and Yi, L., 2003. Correlation between Indian Ocean summer monsoon and north Atlantic climate during the Holocene. *Earth and Planetary Science Letters,* **211**: 371-380.

Imbrie, J., and Imbrie, J.Z., 1979. Modeling the Climatic Response to Orbital Variations. *Science,* **207**: 943-953

Imbrie, J., Hays, J.D., Martinson, D.G., McIntyre, A., Mix, A.C., Moorley, J.J., Pisias, N.G., Prell, W.L., and Shackleton, N.J., 1984. The orbital theory of Pleistocene climate: support from a revised chronology. In: *Milankvovitch and climate, Part-1* Berger, A. (Ed.). Springer, NY, 269-305 pp.

Jensen, T.G., 2003. Cross-equatorial pathway of salt and tracers from the northern Indian Ocean: modeling results. *Deep Sea Research II,* **50**: 2111-2127.

Joussaume, S., and Taylor, K.E., 2000. Modelling Extreme Climates of the Past: What we have learned from PMIP and related Experiments, PAGES Newsletter / CLIVAR Exchanges, 8/5: 18-19.

Katz, A., 1973. The interaction of magnesium with calcite during crystal growth at 25°–90°C and one atmosphere. *Geochimica et Cosmochimica Acta,* **37**: 1563–1586.

Kawamura, K., Parrenin, F., Lisiecki, L., Uemura, R., Vimeux, F., Severinghaus, J.F., Hutterli, M.A., Nakazawa, T., Aoki, S., Jouzel, J., Raymo, M.E., Matsumoto, K., Nakata, H., Motoyama, H., Fujita, S., Goto-Azuma, K., Fujii, Y., Watanabe, O., 2007. Northern hemisphere forcing of climate cycles in Antarctica over the past 360,000 years. *Nature,* **448**: 912-916.

Kennedy, M., 2008. Snowball Earth termination by destabilization of equatorial permafrost methane clathrate. *Nature,* **453**: 642-645.

Kirschvink, J.L., 1992. Late Proterozoic low-latitude global glaciation: the Snowball Earth. In: *The Proterozoic Biosphere*, Schoff, J. W. and Klein, C. (Eds.), Cambridge University Press, New York, 51-52 pp.

Kiefer, T. and Kienast, M., 2005. Patterns of deglacial warming in the Pacific Ocean: A review with emphasis on the time interval of Heinrich event 1. *Quaternary Science Reviews,* **24**: 1063-1081.

Kiefer, T., McCave, I.N., and Elderfield, H., 2006. Antarctic control on tropical Indian Ocean sea surface temperature and hydrography. *Geophysical Research Letters,* **33**: L24612.

Kolla, V, Ray, P.K., and Kostecki, J., 1981. Surficial sediments of the Arabian Sea. *Marine Geology*, **41**: 183-204.

Krishna kumar, K., Rajgopalan, B., and Cane, M.A., 1999. On the weakening relationship between the Indian monsoon and ENSO. *Science*, **284**: 2156-2159.

Krey, J., and Babenerd, B., 1976. *Phytoplankton Production Atlas of the International Indian Ocean Expedition*, Landes Vermessungsamt Schleswig-Holstein, Kiel, 1-70 pp.

Kucera, M., Rosell-Melé, A., Schneider, R., Waelbroeck, C., and Weinelt, M., 2005. Multiproxy approach for the reconstruction of the glacial ocean surface (MARGO). *Quaternary Science Reviews*, **24**: 813-819.

Kucera, M., and Schönfeld, J., 2007. The origin of modern oceanic foraminiferal faunas and Neogene climate change. In: M. Williams, A.M. Haywood, F.J. Gregory and D.N. Schmidt, Editors, *Deep Time Perspectives on Climate Change: Marrying the Signal from Computer Models and Biological Proxies, The Micropalaeontological Society, Special Publication.* **2**: 409–426.

Kutzbach, J.E., Prell, W.L., and Ruddiman, W.F 1993. Sensitivity of Eurasian climate to surface uplift of the Tibetan Plateau. *Journal of Geology*, **101**: 177-190.

Lang, C., Leuenberger, M., Schwander, J., and Johnson, S., 1999. 16°C rapid temperature variation in central Greenland 70,000 years ago. *Science*, **286**: 934-937.

Langen, P.J., Pak, D.K., Spero, H.J., and Lea, D.W., 2005. Effect of temperature on Mg/Ca in neogloboquadrinid shells determined by live culturing, *Geochemistry Geophysics Geosystems,* **6**: Q10P03.

Lea, D.W., Mashiotta, T.A., Spero, H.A., 1999. Controls on magnesium and strontium up-take in planktonic foraminifera determined by living culturing, *Geochimica et Cosmochimica Acta*, **63**: 2369-2379.

Lea, D.W., Pak, D.K., and Spero, H.J., 2000. Climate Impact of late Quaternary equatorial Pacific sea-surface temperature variations. *Science*, **289**: 1719-1724.

Leuschner, D.C and Sirocko, F., 2000. The low-latitude monsoon climate during Dansgaard-Oeschger cycles and Heinrich Events. *Quaternary Science Reviews*, **19**: 243-254.

Levitus, S., and T.P. Boyer., 1994. World Ocean Atlas 2005, vol. 4, Temperature, NOAA Atlas NESDIS, vol. 4, 129 pp., NOAA, Silver Spring, Md.

Libby, W.F., 1946. Atmospheric Helium Three and Radiocarbon from Cosmic Radiation. *Physical Review,* **69:** 671–672.

Lisiecki, L.E., and Raymo, M.E., 2005. A Pliocene-Pliestocene stack of 57 globally distributed benthic $\delta^{18}O$ records. *Paleoceanography*, **20**: PA1003.

Loeblich, A.R., Jr., and H. Tappan., 1964. Foraminiferal Classification and Evolution. *Journal of the Geological Society of India* **5**:5-39.

Madhupratap, M., Kumar, S.P., Bhattatri, M.A., Kumar, M.D., Raghukumar, S., Nair, K.K.C., and Ramaiah, N., 1996. Mechanism of biological response to winter cooling in the northeastern Arabian Sea. *Nature*, **384**: 549-552.

Manabe, S., and Broccoli, A.J., 1985. The influence of continental ice sheets on the climate of an ice age. *Journal of Geophysical Research,* **90**: 2167.

MARGO Project Members, 2009. Constraints on the magnitude and patterns of ocean cooling at the Last Glacial Maximum. *Nature Geoscience*, **2**:127-132.

Martinson, D.G., Pisias, N.G., Hays, J.D., Imbrie, J., Moore, T.C., and Shackleton, N.J., 1987. Age dating and the orbital theory of the ice ages: Development of a high-resolution 0 to 300,000-year chronostratigraphy. *Quaternary Research*, **27**: 1-29.

Masarik, J., and Beer, J., 1999. Simulation of particle fluxes and cosmogenic Nuclide production in the Earth's atmosphere. *Journal of Geophysical Research,* **104**: doi: 10.1029/1998JD200091.

Mascarelli, A.L., 2009. Quaternary geologists win timescale vote. *Nature*, **459**: 654.

Mashiotta, T.A., Lea, D.W., and Spero, H.J., 1999. Glacial-interglacial changes in subantarctic sea surface temperature and $\delta^{18}O$ water using foraminiferal Mg. *Earth and Planetary Science Letters,* **170:** 417-432.

Mayewski, P.A., Meeker, L.D., Twickler, M.S., Whitlow, S.I., Yang, Q. and Prentice, M., 1997. Major features and forcing of high latitude northern hemisphere atmospheric circulation over the last 110,000 years. *Journal of Geophysical Research,* **102:** 345-362.

McConnell, M.C., and Thunell, R.C., 2005. Calibration of the planktonic foraminiferal Mg/Ca paleothermometer: sediment trap results from the Guaymas Basin, Gulf of California, *Paleoceanography,* **20:** doi: 10.1029/2004PA001077.

McCrea, J.M., 1950. On the Isotopic Chemistry of Carbonates and a Paleotemperature Scale. *Journal of Chemical Physics,* **18:** 849.

McCreary, J.P., and Kundu. P.K., 1988. A numerical investigation of the Somali Current during the southwest monsoon. *Journal of Marine Research,* **46:** 25-58.

McKenna, V.S., and Prell, W.L., 2004. Calibration of the Mg/Ca of *Globorotalia truncatulinoides* (R) for the reconstruction of marine temperature gradients, *Paleoceanography,* **19:** PA2006.

Milankovitch, M., 1941, Cannon of insolation and ice age problem (in German): Acad. Royale Serbe, Belgrade Spec. Pub. 133 (English translation 633 p., Israel Program for Scientific Transla-tion, Jerusalem, 1969).

Miller, J.C., and Miller, J.N., 1988. *Statistics for Analytical Chemistry,* 2nd ed. Ellis Horwood, Chichester, England, 202 pp.

Millero, F.J., 1996. *Chemical Oceanography.* CRC / Taylor & Francis pp: 496.

Mix, A.C., Bard, E., and Schneider, R., 2001. Environmental processes of the ice age: land, oceans, glaciers (EPILOG). *Quaternary Science Reviews,* **20:** 627-657.

Mucci, A., and Morse, J.W., 1990. Chemistry of low temperature abiotic calcites: Experimental studies on co-precipitation, stability and fractionation. *Reviews in Aquatic Sciences,* **3:** 217-254.

Murtugudde, R., Seager, R., and Thoppil, P., 2007. Arabian Sea response to monsoon variations. *Paleoceanography,* **22:** PA4217.

Nurnberg, D., 1995. Magnesium in tests of Neogloboquadrina pachyderma sinistral from high northern and southern latitudes. *Journal of Foraminiferal Research,* **25:** 350-368.

Nurnberg, D., Bijma, J., and Hemleben, C., 1996. Assessing the reliability of magnesium in foraminiferal calcite as a proxy for water mass temperature. *Geochimica et Cosmochimica Acta*, **60**: 803-814.

Oomori, T., Kaneshima, H., and Maezato, Y., 1987. Distribution coefficient of Mg^{2+} ions between calcite and solution at 10-50 °C. *Marine Chemistry,* **20**: 327-336.

Overpeck, J., Anderson, D., Trumbore, D., and Prell, W., 1996. The southwest Indian Monsoon over the last 18000 years. *Climate Dynamics*, **12**: 213-225.

Owens, N.J.P., Burkill, P.H., Mantoura, R.F.C., Woodward, E.M.S., Bellan, I.E., Aiken, J. and Llewellyn, R.J.M., 1993. Size-fractionated primary production and nitrogen assimilation in the northwestern Indian Ocean. *Deep-Sea Research II*, **40**: 711-736.

Pattan, J.N., Masuzawa, T., Naidu, P.D., Parthiban, G., and Yamamoto, M., 2003. Productivity fluctuations in the southeastern Arabian Sea during the last 140 ka. *Paleogeography Paleoclimatology Paleoecology*, **193**: 575-590.

Pena, L.D., Calvo, E., Cacho, I., Eggins, S., and Pelejero, C., 2005. Identification and removal of Mn–Mg-rich contaminant phases on foraminiferal tests: implications for Mg/Ca past temperature reconstructions. *Geochemistry Geophysics Geosystems*, **6**: Q0902.

Petit, J.R., et al., 1999. Climate and atmospheric history of the past 420,000 years from Vostok ice core, Antarctica. *Nature*, **399**: 429-436.

Prasanna Kumar, S., and Prasad, T.G., 1999. Formation and spreading of Arabian Sea high salinity water mass. *Journal of Geophysical Research*, **104**: 1455-1461.

Prasanna Kumar, S., Ramaiah, N., Gauns, M., Sarma, V.V.S.S., Muraleedharan, P.M., Raghukumar, S., DileepKumar, M., and Madhupratap, M., 2001. Physical forcing of biological productivity in the northern Arabian Sea during the northeast monsoon. *Deep-Sea Research II: Topical Studies in Oceanography*, **48**: 1115-1126.

Prasanna Kumar, S., Narvekar, J., Kumar, A., Shaji, C., Anand, P., Sabu, P., Rijomon, G., Josia, J., Jayaraj, K. A., Radhika, A., and Nair, K. K. C. 2004. Intrusion of the Bay of Bengal water into the Arabian Sea during winter monsoon and associated chemical and biological response. *Geophysical Research Letters*, **31**: L15304, doi:10.1029/2004GL020247.

Prasad, T.G., 1997. Annual and seasonal buoyancy flux for the tropical Indian Ocean. *Current Science*, **73**: 667-673.

Prell, W.L., 1985. The stability of low-latitude sea-surface temperatures: An evaluation of the CLIMAP reconstruction with emphasis on the positive SST anomalies. Washington, D. C., Department of Energy, 60pp.

Prell, W.L., and Van Camp, E., 1986. Coherent response of Arabian Sea upwelling and pollen transport to late Quaternary monsoonal winds. *Nature*, **323**: 526 - 528.

Prell, W.L., Imbrie, J., Martinson, D.G., Morley, J.J., Pisias, N.G., Shackleton, N.J., and Streeter, H.F., 1986. Graphic Correlation of Oxygen Isotope Stratigraphy Application to the Late Quaternary. *Paleoceanography*, **1**: 137-162.

Raman, S., Alapati, K., and Madala, R.V., 1992. Role of the air-sea interaction processes on the Indian southwest monsoon dynamics. In: *Oceanography of the Indian Ocean*, Desai, B. N. (Ed.). Oxford and IBH Pub. Co., New Delhi. 637-645 pp.

Ramasastry, A.A., and Myrland, P., 1959. Distribution of temperature, salinity and density in the Arabian Sea along the south Malabar coast during the past - monsoon season. *Indian Journal of Fisheries*, **6**: 223-235.

Ramsey, M.H., Thompson, M., and Walton, S.J., 1987. Self matrix effects as a cause of calibration curvature in inductively coupled plasma atomic emission spectrometry. *Journal of Analytical Spectrometry*, **2**: 33–38.

Rao, R.R., Molinari, R.L. and Festa, J.F., 1989. Evolution of the climatological near-surface thermal structure of the tropical Indian Ocean: Description of mean monthly mixed layer depth, sea surface temperature, surface current and surface meteorological fields. *Journal of Geophysical Research*, **94**: 801-815.

Reichart, G.J., Lournes, L.J., and Zachariasse, W.J., 1998. Temporal variability in the northern Arabian Sea Oxygen Minimum Zone (OMZ) during the last 225,000 years. *Paleoceanography*, **13**: 607-621.

Reverdin, G., 1987. The upper equatorial Indian Ocean: The climatological seasonal cycle. *Journal of Physical Oceanography*, **17**: 903-927.

Rochford, D.J., 1964. Salinity maxima in the upper 1000 metres of the North Indian Ocean. *Australian Journal of Marine Freshwater Research*, **15**: 1-24.

Rohling, E.J., 2000. Paleosalinity: confidence limits and future applications. *Marine Geology*, **163**: 1–11.

Rohling, E.J., 2007. Progress in paleosalinity: Overview and presentation of a new approach. *Paleoceanography*, **22**: PA3215.

Rosell-Melé, A. et al., 2004. Sea surface temperature anomalies in the oceans at the LGM estimated from the alkenone-UK' 37 index: Comparison with GCMs. *Geophysical Research Letters,* **31**: L03208.

Rosenthal, Y., Boyle, E.A., and Slowey, N., 1997. Temperature control on the incorporation of magnesium, strontium, fluorine, and cadmium into benthic foraminiferal shells from Little Bahama Bank: Prospects for thermocline paleoceanography. *Geochimica et Cosmochimica Acta,* **61**: 3633-3643.

Rosenthal, Y., Lohmann, G.P., Lohmann, K.C., and Sherrell, R.M., 2000. Incorporation and preservation of Mg in *Globigerinoides sacculifer*: Implications for reconstructing the temperature and $^{18}O/^{16}O$ of seawater. *Paleoceanography,* **15**: 135-145.

Rosenthal, Y., and Lohmann, G.P., 2002. Accurate estimation of sea surface temperatures using dissolution corrected calibrations for Mg/Ca paleothermometry. *Paleoceanography,* **17**: 1044.

Rosenthal, Y., Oppo, D.W., and Linsley, B.K., 2002. The amplitude and phasing of climate change during the last deglaciation in the Sulu Sea, western equatorial Pacific. *Geophysical Research Letters,* **3**: 1428.

Rostek, F., Ruhland, G., Bassinot, F C., Muller, P.J., Labeyrie, L.D., Lancelot, Y., and Bard, E., 1993. Reconstructing sea surface temperature and salinity using $\delta^{18}O$ and alkenone records. *Nature,* **364**: 319-321.

Rostek, F., Bard, E., Beaufort, L., Sonzogni, C., and Ganssen, G., 1997. Sea surface temperature and productivity for the past 240 kyr in the Arabian Sea. *Deep Sea Research II,* **44**: 1461-1480.

Russell, A.D., B. Hoenisch, H.J. Spero, and Lea. D.W., 2004. Effects of seawater carbonate ion concentration and temperature on shell U, Mg, and Sr in cultured planktonic foraminifera. *Geochimica et Cosmochimica Acta,* **68**: 4347-4361.

Ruben, S., and Kamen, M.D., 1941. Long-Lived Radioactive Carbon: C14. *Physical Review* **59**: 349–354.

Saher, M.H., Peeters, F.J.C., and Kroon, D., 2007. Sea surface temperatures during the SW and NE monsoon seasons in the western Arabian Sea over the past 20,000 years. *Palaeogeography, Palaeoclimatology, Palaeoecology,* **249**: 216–228.

Saher, M.H., Jung, S.J.A., Elderfield, H., Greaves, M., and Kroon, D., 2007. Sea surface temperatures of the western Arabian Sea during the last deglaciation. *Paleoceanography,* **22**: PA2208.

Saji, N.H., Goswami, B.N., Vinaychandran, P.N., and Yamagata, T., 1999. A dipole mode in the tropical Indian Ocean. *Nature*, **401**: 360-363.

Sankaranarayanan, V.N., and Qasim, S.Z., 1969. Influence of some hydrographical factors on the fisheries of the Cochin area. In: *Symposium on Indian Ocean, Bulletin of National Institute of Science India*, **38**: 846-853.

Saraswat, R., Nigam, R., Weldeab, S., Mackensen, A., and Naidu, P.D., 2005. A first look at past sea surface temperatures in the equatorial Indian Ocean from Mg/Ca in foraminifera. *Geophysical Research Letters*, **32**: L24605.

Sarker, R.P., 1966. A dynamical model of orographic rainfall. *Monthly Weather Review*, **94**: 555-572.

Sarnthein, M., 1978, Sand deserts during glacial maximum and climate optimum. *Nature*, **272**: 43-46

Savin, S.M., and Douglas, R.G., 1973. Stable isotope and magnesium geochemistry of recent planktonic foraminifera from the south Pacific. *Geological Society of America Bulletin*, **84:** 2327–2342.

Schmidt, M.W., Spero, H.J., and Lea, D.W., 2004. Links between salinity variation in the Caribbean and North Atlantic thermohaline circulation. *Nature*, **428**: 160-163.

Schott, F., and Quadfasel, D., 1982. Variability of the Somali Current and associated upwelling. *Progress in Oceanography*, **12**: 357-381.

Schott, F., 1983. Monsoon response of the Somali Current and associated upwelling. *Physical Oceanography*, **12**: 357-382.

Schulz, H., Von Rad, U., and Erlenkeuser, H., 1998. Correlation between Arabian Sea and Greenland climate oscillations of past 110000 years. *Nature*, **393**: 54-57.

Shackleton, N.J., and Opdyke, N.D., 1973. Oxygen isotope and paleomagnetic stratigraphy of equatorial Pacific core V28-238: oxygen isotope temperatures and ice volume on 10^5-10^6 year scale. *Quaternary Research*, **3**: 39-55.

Shackleton, N.J., 1974. Attainment of isotopic equilibrium between ocean water and the benthonic foraminifera genus Uvigerina: Isotopic changes in the ocean during the last glacial. *Cent. Nat. Rech. Sci. Colloq. Int.*, **219**: 203-209.

Shackleton, N.J., Lamb, H.H., Worssam, B. C., Hodgson, J.M., Lord, A.R., Shotton, F.W., Schove, D.J., and Cooper, L.H.N., 1977. The oxygen isotope stratigraphic record of the Late Pleistocene, *Philosophical Transactions of the Royal Society*

of London. Series B, Biological Sciences, Vol. 280, No. 972, A Discussion on the Changing Environmental Conditions in Great Britain and Ireland During the Devensian (Last) Cold Stage. (Aug. 17, 1977), 169-182 pp.

Shackleton, N.J., 1987. Oxygen isotopes, ice volume and sea level. *Quaternary Science Reviews*, **6**: 183-190.

Shackleton, N.J., Berger, A., and Peltier, W.R., 1990. An alternative astronomical calibration of the lower Pleistocene timescale based on ODP Site 677, *Symposium on the late Cenozoic ice age*, Edinburgh , Royaume-Uni, **81**: 251-261.

Shackleton, N.J., 2000. The 100,000 year ice-age cycle identified and found to lag temperature, carbon dioxide and orbital eccentricity. *Science,* **289**: 1897-1902.

Shankar, D., Vinaychandran, P.N., and Unnikrishnan, A.S., 2002. The monsoon currents in the north Indian Ocean. *Progress in Oceanography*, **52**: 63-120.

Shankar, R., Prabhu, C.N., Warrier, A.K., Vijaya Kumar, G.T., and Sekar, B., 2006. A multidecadal rock magnetic record of monsoonal variations during the past 3700 years from a tropical Indian tank, *Journal of the Geological Society of India* **68**: 447–459.

Sharma, G.S., 1978. Upwelling off the southwest coast of India, *Indian Journal of Marine Sciences*, **7**: 209-218.

Shetye, R.S., 1984. Seasonal variability of the temperature field off the south-west coast of India. *Earth and Planetary Science Letters*, **93**: 399-411.

Shetye, S.R., Gouveia, A.D., Shenoi, S.S.C., Sundar, D., Michael, G.S., Almeida, A.M., and Sanatanam, K., 1990. Hydrography and circulation off the west coast of India during the southwest monsoon. *Jorunal of Marine Research*, **48**: 259-378.

Shetye, S.R., Gouveia, A.D., Shenoi, S.S.C., Michael, G.S., Sundar, D., Almeida, A.M., and Santanam, K., 1991. The coastal current off western India during the northeast monsoon. *Deep Sea Research Part A. Oceanographic Research Papers*, **38**: 1517-1529.

Shukla, J., 1975. Effect of Arabian Sea surface temperature on anomaly on Indian summer monsoon: A numerical experiment with GFDL model. *Journal of Atmospheric Science*, **32**: 503-511.

Sirocko, F., Luischner, D., Staubwasser, M., Maley, J., and Heusser, L., 1999. High-frequency oscillations of the last 70000 years in the tropical/subtropical and

polar climates. (In): *Mechanism of global climate change at millennial time scale*, Geophysical Monograph **112:** *American Geophysical Union*, 113-126 pp.

Sirocko, F., Garbe-Schonberg, D., and Devey, C., 2000. Processes controlling trace element geochemistry of Arabian Sea sediments during the last 25,000 years. *Global and Planetary Change*, **26:** 217-303.

Slingo, J., 2002. Monsoons: Overview. In: *Encylopedia of atmospheric Sciences*, Academic Press, **3:** 1365-1370 pp.

Somayajulu, B.L.K., Rhushan, R., Sarkar, A., Burr , G.S., and Jull, A.J.T., 1999. Sediment deposition rates on the continental margins of the eastern Arabian Sea using ^{210}Pb, ^{137}Cs and ^{14}C. *Science of Total Environment* **237:** 429–439.

Sonzogni, C., Bard, E., and Rostek, F., 1998. Tropical sea surface temperatures during the last glacial period: a view based on alkenones in Indian Ocean sediment. *Quaternary Science Review*, **17:** 1185-1201.

Spero, J.H., and Lea, D.W., 2002. The Cause of Carbon Isotope Minimum Events on Glacial Terminations. *Science,* **296:** 522-525.

Stephen, S., Cacho, I., Benway, H., and Tachikawa, K., 2005. Planktonic foraminiferal Mg/Ca as a proxy for past oceanic temperatures: a methodological overview and data compilation for the Last Glacial Maximum. *Quaternary Science Reviews,* **24:** 821–834.

Stuiver, M., and Braziunas, T.F., 1993. Sun. Ocean, climate and atmospheric ^{14}CO$_2$: An evaluation of causal and spectral relationships. *The Holocene,* **3:** 289-305.

Sumitra-Vijayaraghavan and Kumari, L.K., 1989. Primary productivity in the southeastern Arabian Sea during the southwest monsoon. *Indian Journal of Marine Sciences,* **18:** 30-32.

Suthhof, A., and Ittekkot, V., 2001. Millenial-scale oscillation of denitrification intensity in the Arabian Sea during the late Quaternary and its potential influence on atmoshpheric N$_2$O and global climate. *Global Biogeochemical Cycles,* **15:** 637-649.

Swallow, J.C., Molinari, R.L., Bruce, J.G., Brown, O.B., and Evans, R.H., 1983. Development of near-surface flow pattern and water mass distribution in the Somali Basin in response to the southwest monsoon of 1979. *Journal of Physical Oceanography,* **13:** 1398-1415.

Thamban, M., Rao, V.P., Schneider, R.R., and Grootes, P.M., 2001. Glacial to Holocene fluctuations in hydrography and productivity along the southwestern continental margin of India. *Palaeogeography Palaeoclimatology Palaeoecology*, **165**: 113–127.

Thompson, P.R., Be`, A.W.H., Duplessy, J., and Shackleton, N.J., 1979. Disappearance of pink-pegmented *Globigerinoides ruber* at 120,000 yr BP in the Indian and Pacific Oceans. *Nature*, **280**: 354-358.

Trend-Staid, M. and Prell, W.L., 2002. Sea surface temperature at the Last Glacial Maximum: A reconstruction using the modern analog technique. *Paleoceanography*, **17**: doi:10.1029/2000PA000506.

Tomczak, M., and Godfreay, J.S., 1994. Regional Oceanography: An Introduction. Pergamon, 193-251 pp.

Tripati, A., Backman, J., Elderfield, H., and Ferretti, P., 2005. Eocene bipolar glaciation associated with global carbon cycle changes. *Nature*, **436**: 341-346.

Urey, H.C., 1947. The thermodynamic properties of isotopic substances. *Journal of Chemical Society*, 562 - 581.

Valdiya, K.S., 1993. Uplift and geomorphic rejuvenation of the Himalaya in the Quaternary period. *Current Science*, **64**: 873-885.

Valdiya, K.S., 1998. Dynamic Himalaya. *Universities Press, Hyderabad.* 178 pp.

Varadachari, V.V.R., 1961. On the process of upwelling and sinking on the east coast of India. Prof. Mahadevan Shastiabdapurti Commemoration. Os. Univeristy Press. 159-162 pp.

Venetz, I., 1821. Temperature Variation in the Swiss Alps. *The Helvetic Society of Natural Sciences.*

Walker, J. C. G., 1977. Evolution of the Atmosphere. Macmillan, New York, NY.

Walker, G., 2003. Snowball Earth. Bloomsbury, 269 pp.

Walsh, J.J., Premuzic, E.T., and Whitledge, T.E., 1981. Fate of nutrient enrichment on continental shelves as indicated by C/N content of bottom sediments. In: *Ecohydrodynamics,* Nihoul, J. C. J. (Ed.). Elsevier, 13–49 pp.

Warrier,, A.K., and Shankar, R., 2009. Geochemical evidence for the use of magnetic susceptibility as a paleorainfall proxy in the tropics. *Chemical Geology*, **265**: 553-562.

Webster, P.J., Magaña, V. O., Palmer, T.N., Shukla, J., Tomas, R.A., Yanai, M., and Yasunari, T., 1998: Monsoons: Processes, predictability, and the prospects for prediction. *Journal of Geophysical Research*, **103**: 451-510.

Webster, P.J., and Fasullo, J., 2002. Monsoons-Dynamic theory, in: Encyclopedia of atmospheric Sciences. *Academic Press*, **3**: 1370-1385.

Weldeab, S., Schneider, R.R., and Kolling, M., 2006. Comparison of foraminiferal cleaning procedures for Mg/Ca paleothermometry on core material deposited under varying terrigenous-input and bottom water conditions. *Geochemistry Geophysics Geosystems*, **7**: Q0412.

Weller, R.A., Baumgartner, M.F., Josey, S.A., Fischer, A.S., and Kindle, J.C., 1998. Atmospheric forcing in the Arabian Sea during 1994-95: observations and comparisons with climatology and models. *Deep-Sea Research II*, **45**: 1961-1999.

Whittington, H.B., 1979. Early arthropods, their appendages and relationships. In M. R. House (Ed.), The origin of major invertebrate groups. The Systematics Association Special Vol. 12. London: Academic Press, pp. 253–268.

Wilson, R.C.L., Drury, S.A., and Chapman, J.L., 2000. (In.) The Great Ice Age - climate change and life. The Open University and Routledge Taylor and Francis Group, London and New York, pp. 267.

Wilson-Diaz, D., Mariano, A.J., and Evans, R.H., 2009. On the heat budget of the Arabian Sea. *Deep Sea Research Part I: Oceanographic Research Papers*, **56**: 141-165.

Wyrtki K., 1971. *Oceanographic Atlas of the International Indian Ocean Expedition*, National Science Foundation,Washington. DC, 531 pp.

Wyrtki, K., 1973. The biology of the Indian Ocean. In: *Physical Oceanography of the Indian Ocean*, Zeitzschel, B. (Ed.). Springer, Berlin, 18-36 pp.

Xie, S.P., Xu, H., Saji, N.H., Wang, Y., and Liu, W.T., 2006. Role of narrow mountains in large-scale organization of Asian monsoon convection. *Journal of Climate* **19**: 3420-3429.

Yokoyama, Y., Lambeck, K., De Deckker, P., Johnston, P., and Fifield, L.K., 2000. Timing of the last glacial maximum from observed sea-level minima. *Nature*, **406**: 713–716.

Zalasiewicz, J., Williams, M., Smith, A., Barry, T.L., Coe, A.L., Bown, P.R., Brenchley, P., Cantrill, D., Gale, A., Gibbard, P., Gregory, F.J., Hounslow, M.S., Kerr,

A.C., Pearson, P., Knox, R., Powell, J., Waters, C., Marshall, J., Oates, M., Rawson, P., and Stone, P., 2008. Are we now living in the Anthropocene? *Geological Society of America Today,* **18**: 4-8.

Zielinski, G.A., Mayewski, P.A., Meeker, L.D., Whitlow, and S., Twickler, M.S., 1996. Potential atmospheric impact of the mega-eruption 71000 y ago. *Geophysical Research Letters.* **23**: 837–840.

http://home.comcast.net/~rhaberlin/glmod.htm

http://calib.qub.ac.uk/marine/

www.cwc.nic.in

www.intcal.qub.ac.uk

www.museum.state.il.us

www.noaa.nodc.gov/WOA009

List of Publications

1. Banakar, V. K., Mahesh, B. S., and Burr, G., 2010. Climatology of the Eastern Arabian Sea during the last glacial cycle reconstructed from paired measurement of foraminiferal $\delta^{18}O$ and Mg/Ca. *Quaternary Research*, **73**: 535-540.

2. Mahesh, B., Banakar, V.K., and Burr, G., 2011. Paired Measurements of Foraminiferal $\delta^{18}O$ and Mg/Ca Ratios of Indian Monsoons Reconstructed from Holocene to Last Glacial Record. *Acta Geologica Sinica*, **85**: 950–956.

List of Conference Abstracts

1. Reconstruction of Holocene-Last Glacial monsoons from Eastern Arabian Sea foraminiferal $\delta^{18}O$ and Mg/Ca ratios". In Abstract Volume Ocean Science Meeting, February 2010, held at Portland, USA.

2. Last 32 000 years record of Indian monsoon variability reconstructed from paired measurements of foraminiferal $\delta^{18}O$ and Mg/Ca ratios". In Abstract Volume, 7th Annual Meeting AOGS, 5 to 9 July, 2010, held at Hyderabad-India.

3. Latitudinal changes in sea surface temperature and salinity within the Eastern Arabian Sea during the Holocene and Last Glacial Period. In Abstract Volume 7th International Conference on Asian Marine Geology, October 2011, held at NIO, Goa-India.

ELSEVIER

Climatology of the Eastern Arabian Sea during the last glacial cycle reconstructed from paired measurement of foraminiferal δ¹⁸O and Mg/Ca

V.K. Banakar [a,*], B.S. Mahesh [a], G. Burr [b], A.R. Chodankar [a,1]

[a] National Institute of Oceanography (CSIR), Dona Paula, Goa-403 004, India
[b] NSF-Arizona AMS Facility, 1118 E, 4th Street, Tucson, AZ85721-0081, USA

ARTICLE INFO

ABSTRACT

Paired measurements of Mg/Ca and $\delta^{18}O$ of *Globigerenoides sacculifer* from an Eastern Arabian Sea (EAS) sediment core indicate that sea-surface temperature (SST) varied within 2°C and sea-surface salinity within 2 psu during the last 100 ka. SST was coldest (~27°C) during Marine Isotope Stage (MIS) 4 and 2. Sea-surface salinity was highest (~37.5 psu) during most of the last glacial period (~60–18 ka), concurrent with increased $\delta^{18}O_{G.sacculifer}$ and C/N ratios of organic matter and indicative of sustained intense winter monsoons. SST time series are influenced by both Greenland and Antarctic climates. However, the sea-surface salinity time series and the deglacial warming in the SST record (beginning at ~18 ka) compare well with the LR04 benthic $\delta^{18}O$-stack and Antarctic temperatures. This suggests a teleconnection between the climate in the Southern Hemisphere and the EAS. Therefore, the last 100-ka variability in EAS climatology appears to have evolved in response to a combination of global climatic forcings and regional monsoons. The most intense summer monsoons within the Holocene occurred at ~8 ka and are marked by SST cooling of ~1°C, sea-surface salinity decrease of 0.5 psu, and $\delta^{18}O_{G.sacculifer}$ decrease of 0.2‰.

© 2010 University of Washington. Published by Elsevier Inc. All rights reserved.

Introduction

The glacial–interglacial variability and Dansgaard–Oeschger (D–O) oscillations observed in the Indian monsoon proxy records (Duplessy, 1982; Clemens and Prell, 1990; Anderson and Prell, 1993; Schulz et al., 1998; Reichart et al., 2002; Hong et al., 2003; Banakar et al., 2005; Chodankar et al., 2005, and references therein) demonstrate teleconnection between high-latitude climates and Indian monsoons. The intensified southwest monsoons were found to coincide with shifts in surface temperature regimes of the Atlantic and Europe and the extent of ice sheets in northern hemisphere, not only during the Holocene (Overpeck et al., 1996) but also apparently continuing into modern times (see Goes et al., 2005).

These studies indicate the existence of complex teleconnections and possibly feedbacks between Indian monsoons and global climate (Krishnakumar et al., 1999), which are yet to be clearly understood. Therefore, the past variation in the Indian monsoon needs further study incorporating paired multi-proxy investigations and comparative assessment in the context of the global climate system. Time-series records of surface hydrographic and biogeochemical variability in the Arabian Sea provide valuable insights into past monsoon variability.

In this study we present paired measurements of oxygen isotopes and Mg/Ca-SST and estimated the residual $\delta^{18}O_{SEAWATER}$ (representing local salinity) for the EAS from SK117/GC8 sediment core. These climatological time series are further compared with previously published past global climate records and local productivity patterns to understand processes involved in driving the local climatology.

Mg/Ca ratios in planktonic calcite have been shown to preserve the ambient water temperature with considerable fidelity (Lea et al., 1999; Elderfield and Ganssen, 2000; Rosenthal et al., 2000; Dekens et al., 2002; Eggins et al., 2003; Sagawa et al., 2006), and salinity can be calculated using seawater $\delta^{18}O$ (Rostek et al., 1993; Delaygue et al., 2001; Dahl and Oppo, 2006). However, Rohling (2000) has demonstrated that the level of confidence in palaeo-salinity estimation from seawater $\delta^{18}O$ is poor, and hence we emphasize residual $\delta^{18}O_{SEAWATER}$ as opposed to absolute salinity to signify local change, unless otherwise warranted.

Materials and methods

A 410-cm-long gravity core (SK117-GC8) was retrieved on board the *ORV Sagar Kanya* from the EAS (off Goa, India: 15°29′N; 72°51′E) at a water depth of 2500 m (Fig. 1) for the present study. The AMS ¹⁴C dating for the core-top section was obtained from the Van der Graaf Laboratory (Utrecht University, The Netherlands), and additional seven depth sections from the upper 150-cm sections were dated at the NSF-AMS facility of the Arizona University (USA). The AMS ¹⁴C dates were corrected for the local reservoir age of

* Corresponding author. Fax: +91 832 245 0609.
  E-mail address: banakar@nio.org (V.K. Banakar).
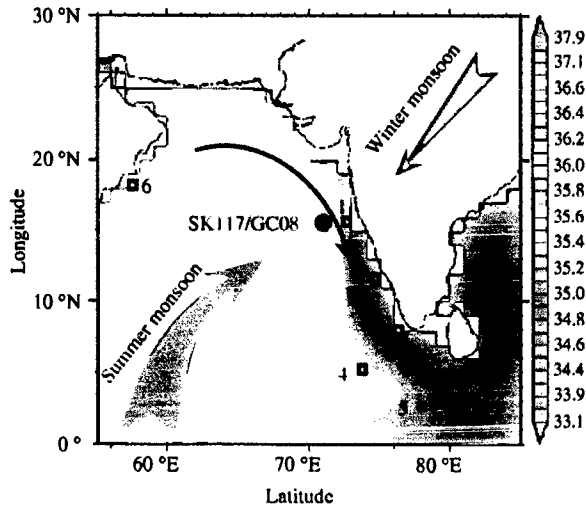[1] Present address: B-6, Datta Apartments, Porvorim, Goa-403 008, India.

Figure 1. Location of SK117/GC8 sediment core (filled circle). The shaded block arrows indicate modern reversing monsoon winds. Solid (broken) arrow indicates surface circulation during summer (winter) monsoons (Shankar et al., 2002). The numbered open boxes are the locations for which last glacial to Holocene SST gradient of <2.5°C was recorded (1–3 and 6, Uk_{37} SST: Sonzogni et al., 1998; 4, Uk_{37} SST: Rostek et al., 1993; 5, Mg-SST: Saraswat et al., 2005. The 175 ka SST record (4) from southeastern Arabian Sea does not exhibit clear glacial-interglacial or D–O patterns. Records 1–3 and 6 are only the last glacial and Holocene sections. The base map of annual surface salinity is adopted from www.nodc.noaa.gov/WOA05.

500 yr (http://intcal.qub.ac.uk) before converting to calendar age using the CalPal-2005 program (Weninger et al., 2005). For radiocarbon dating, ~10 mg of calcite was obtained by mixing two planktonic foraminifer species (*G. ruber* and *G. sacculifer*) of 100–350 µm sizes.

The core-top section (0–2 cm) yielded an age of 2259 ± 64 cal yr BP. The *G. sacculifer* oxygen isotopes, organic carbon and C/N records for the present sediment core are from Banakar et al. (2005). The *G. sacculifer* oxygen-isotope depth series is tuned with eight radiocarbon dates, LR04 Benthic Oxygen-Isotope Stack (Lisiecki and Raymo, 2005) and Youngest Toba Tuff (YTT: 71 ka) (Zielinski et al., 1996) (Fig. 2) to establish an improved time scale over the previously published SPECMAP-based relative chronology (Banakar et al., 2005; Chodankar et al., 2005).

The Mg/Ca measurements were made using the same species (*G. sacculifer* without terminal sac), size range (250–350 µm), and sediment depth intervals documented previously for the oxygen isotopes (Banakar et al., 2005; Chodankar, 2004). The *G. sacculifer* is

relatively more resistant to dissolution as compared to other planktonic foraminifera (Delaney et al., 1985; Dekens et al., 2002) and has nearly uniform distribution of Mg between multiple chambers (Eggins et al., 2003), and hence is well suited for Mg/Ca-based SST reconstruction.

Around fifty visibly clean tests were picked under microscope and subjected to cleaning following the protocol of Elderfield and Ganssen (2000) as later refined by Barker et al. (2003). The tests were first gently crushed between two glass plates to break open all chambers and homogenized in a drop of water. Only the cleanest fragments were isolated from clay lumps, Mn-coated fragments, stained fragments and mineral grains using a fine brush. As this step greatly reduces the chance of oxide contamination, no separate Mn-reduction step was incorporated. The calcite fragments were repeatedly washed with ultrapure water followed by methanol to remove clays. The organic coatings were removed by treating the clay-free fragments in buffered H_2O_2 in a boiling water bath. To remove any secondary calcite deposition on the skeletons, the Mg-polishing was done by treating the clay and coating free fragments with 0.001 N HNO_3. Every step in the cleaning protocol was followed by 30–60 s of sonication. Before the final dissolution in 1 ml of suprapure 0.75 M HNO_3, the cleaned fragments were examined under the microscope to ensure only pristine calcite was taken for dissolution. The solutions were analyzed at the National Institute of Oceanography, India, on a Perkin-Elmer Optima 2000 DV ICP-OES calibrated with five multi-element calibration standards.

The Mg/Ca (mmol/mol) was obtained following intensity-ratio calibration (DeVilliers et al., 2002). A quality control (QC) solution with Mg/Ca of 2.75 mmol/mol was prepared in 0.75 M HNO_3 and analyzed after every fifth sample. The long-term average of QC ($n = 72$) measured over a period of one month during the analytical period was 2.72 ± 0.06 mmol/mol, yielding a precision of ± 0.6°C for estimated SSTs. The Fe/Ca, Al/Ca and Mn/Ca (mmol/mol) were used for monitoring contamination. The scatter plots of the above ratios vs Mg/Ca (mmol/mol) yielded insignificant correlations ($R^2 = 0.09$, 0.24 and 0.02 respectively) suggesting that the measured Mg/Ca ratios were not influenced by contaminants.

The Mg/Ca ratios were translated into SST following Dekens et al. (2002) *G. sacculifer*PACIFIC calibration (Mg/Ca = 0.37 exp 0.09 [T − 0.36 (Core Depth in km) − 2°C]). We have assumed that the Mg/Ca–SST calibration for the same species as found in the tropical Pacific is appropriate for EAS, because these two regions are connected within the El Niño–Southern Oscillation (ENSO) monsoon system and experience more or less similar ocean–atmosphere coupled processes (Webster and Fasullo, 2002). The standard errors on SST estimates associated with this calibration are 1.4°C. The sea-surface salinity was
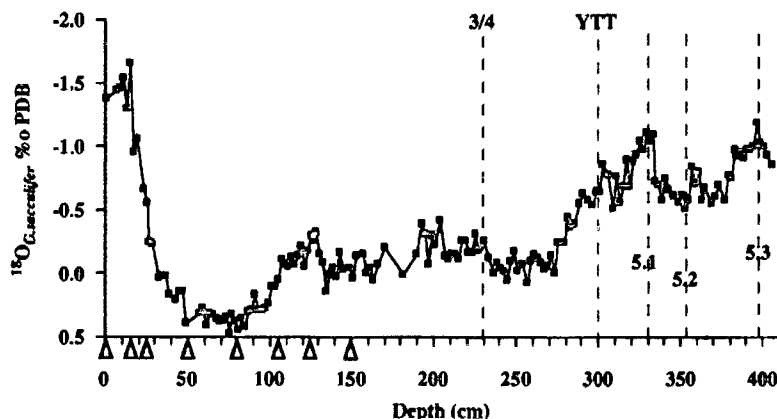

Figure 2. Age model for SK117/GC8 based on a) eight radiocarbon dates (filled triangles: 1 cm = 2259 ± 64 cal yr BP; 15 cm = 8000 ± 37 cal yr BP; 25 cm = 12,887 ± 100 cal yr BP; 49 cm = 18,519 ± 298 cal yr BP; 79 cm = 25,214 ± 393 cal yr BP; 103 cm = 30,180 ± 307 cal yr BP; 125 cm = 33,905 ± 433 cal yr BP; 149 cm = 34,124 ± 402 cal yr BP), b) Marine Isotope Stage events (broken vertical lines labeled as MIS 3/4, 5.1, 5.2, 5.3) defined in LR04 benthic stack (Lisiecki and Raymo, 2005), and c) Youngest Toba Tuff (broken vertical line labeled as YTT) recorded in the Greenland ice cores at ~71 ka (Zielinski et al., 1996).

calculated using a salinity–$\delta^{18}O_{SEAWATER}$ relationship from the Arabian Sea (Dahl and Oppo, 2006). For this, the local seawater $\delta^{18}O$ was obtained using the equation of Epstein et al. (1953) after correcting

the $\delta^{18}O_{G.sacculifer}$ for the global ice effect (Shackleton, 2000). Thus, the $\delta^{18}O_{SEAWATER}$ reflects the local surface salinity (henceforth, 'salinity') in the EAS. The standard errors in salinity estimation are 0.2 psu,
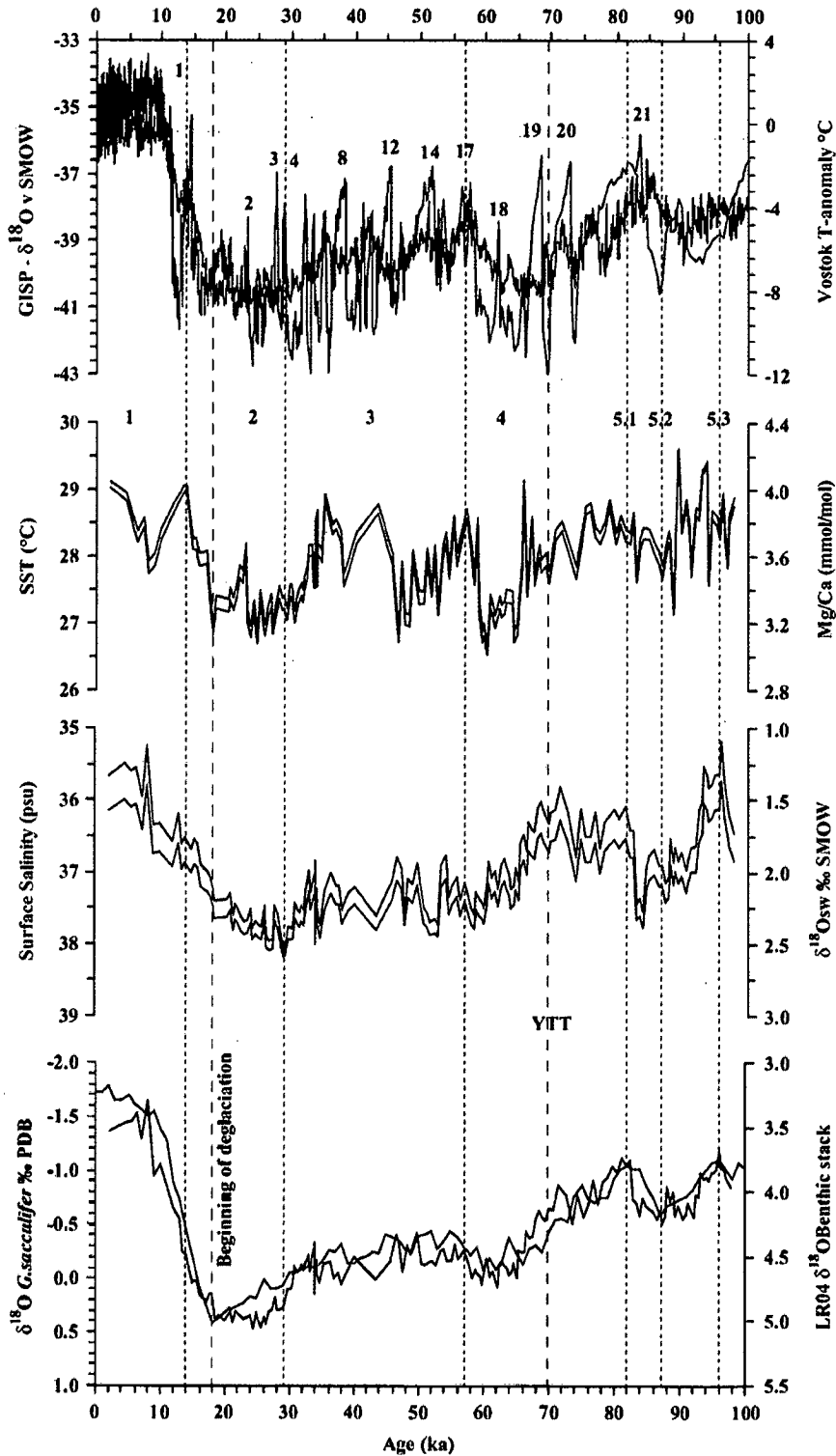

Figure 3. Composite time series (from bottom to top) of oxygen isotopes (SK117/GC8 and LR04 benthic stack); Residual (R) $\delta^{18}O_{SEAWATER}$ and estimated surface salinity; Mg/Ca ratios and estimated SST and Antarctic temperatures (Petit et al., 1999) and Greenland ice-core oxygen isotopes (Dansgaard et al., 1993). Dotted vertical lines indicate marine isotope stage (bold numbered) boundaries and MIS5 peak interstadial and stadial events as recorded in LR04. The initiation of last deglaciation and YTT is shown with broken lines. The Greenland interstadials are labeled with small numbers. The G. sacculifer oxygen-isotope data for SK117/GC8 is from Banakar et al. (2005) and Chodankar et al. (2005). The coherency between residual $\delta^{18}O_{SEAWATER}$ and salinity, and Mg/Ca ratios and SST throughout the last 100 ka, indicate robustness of sedimentary proxies and calibrations used to extract past surface climatology of the EAS.

hence we do not discuss salinity changes <0.4 psu. Although we are aware of the limitations in salinity estimation from local $\delta^{18}O_{SEAWATER}$ (Rohling, 2000), an approximate quantification of past variation of salinity may be useful to understand the responses of EAS climatology to global and local forcing. The procedures followed for oxygen-isotope, organic-carbon and organic-nitrogen measurements are standard and available elsewhere (Banakar et al., 2005; Chodankar et al., 2005).

Results and discussion

The Mg/Ca ratios vary between 2.8 and 4.2 mmol/mol, which is in the expected range of planktic Mg/Ca ranges for tropical oceans (Lea et al., 2000; Barker et al., 2005; Dahl and Oppo, 2006; Saraswat et al., 2005, and references therein). The SST obtained from the core-top (29.1°C: Fig. 3) is comparable to the modern SST (~28.5°C) at the core location (www.nodc.noaa.gov), and also to the Uk$_{37}$ SSTs of Holocene sections in a set of sediment cores from the EAS (~28.5°C: Sonzogni et al., 1998: see Fig. 1).

The Glacial Termination-1 marking the beginning of the Holocene occurred at 13 cal ka BP, and the commencement of the last glacial maximum (LGM= MIS2) is recorded at 29 cal ka BP (Fig. 3). The former event shows a delay of 1 ka, while the latter shows excellent agreement with oxygen-isotope boundaries defined by the LR04 benthic stack (see Lisiecki and Raymo 2005). As per the oxygen-isotope time series on a calendar-year time scale, the deglaciation began ~18 cal ka BP and the Holocene optimum was reached at ~9 cal ka BP. The coldest period of the LGM, marked by heaviest $\delta^{18}O$ (0.3 ± 0.1‰), spans a time interval between 27 and 18 cal ka BP (Fig. 3). The LGM–Holocene shift in $\delta^{18}O_{G.sacculifer}$ after correcting for global ice volume is ~0.8‰, which could be accounted for by glacial–interglacial change in SST and salinity due to monsoon variability. This change is consistent with several other published oxygen-isotope records for the Arabian Sea. The climate events identified in the present sediment core could be considered as typical for the EAS because the structure of $\delta^{18}O_{G.sacculifer}$ record is highly consistent with the robust LR04 benthic stack (Lisiecki and Raymo, 2005) (Fig. 3), and timings of the climate events are based on radiocarbon ages.

Eastern Arabian Sea surface hydrographic variability and global climate

The overall SST variation for the last ~100 ka is within 2°C, which is comparable to the glacial cooling of <2.5°C extracted from several Arabian Sea sedimentary records (see Fig. 1 caption). The SST exhibits subdued glacial–interglacial variability relative to $\delta^{18}O$ (Figs. 2 and 3). Although our time resolution is not adequate to define D–O fluctuations, the SST trends seen in Figure 3 appear to qualitatively incorporate mixed signals of both northern and southern polar climates as depicted in the Vostok Temperature record (Petit et al., 1999) and the Greenland ice sheet oxygen-isotope record (Dansgaard et al., 1993). The coldest SSTs during MIS 4 closely overlap the stadial trend between D–O interstadial events 17–19, and MIS 3's moderately warmer SSTs follow the broad pattern between interstadials 5–15. On the other hand, the MIS 4, MIS 2, and deglaciation data are consistent with the Vostok temperature record (Fig. 3).

The ice-volume-corrected salinity (local surface salinity) approximately follows the trend observed in the Antarctic temperature record and LR04 benthic $\delta^{18}O$ stack (Fig. 3) and is consistently higher during the last glacial period (~60–18 ka BP). The EAS salinity depends largely on inflow of low-salinity water from the Bay of Bengal (BoB) through winter-spring poleward coastal currents (Shetye et al., 1991; Shankar et al., 2002). The reasons for higher salinity in the EAS during the last glacial period might indicate weakened coastal currents as a result of either intensified winter monsoons (Chodankar et al., 2005) or weakened summer monsoons. The net effect is increased salinity in the bay and reduced sea-level difference between the BoB and EAS,

namely a reduction in pressure gradient that drives the winter–spring coastal currents, which are largely responsible for freshening the EAS surface (Shetye et al., 1991; Shankar et al., 2002). Therefore, consistently higher salinity in the EAS during the last glacial period suggests influence of global climate on the local circulation.

In light of above observations, we interpret the past variability of EAS climatology as response to processes reflecting global climate and monsoon intensity. The faint impressions of Antarctic warming as stages of strong summer monsoons, in addition to clear reflection of D–O fluctuations in the Arabian Sea sedimentary records and other oceanic regions, has suggested coupled north–south climate operating in low latitudes influenced by ENSO forcing (Sirocko et al., 1999). In addition, the transmission of subantarctic-mode water has been invoked to provide a thermal connection between Southern Hemisphere climate and the Western Indian Ocean (Kiefer et al., 2006). These previously reported observations, along with our present time series of SST and salinity, provide evidence for high-latitude climate influences on the late Quaternary climatological evolution of the EAS.

A tight connection between northern and southern high-latitude climate following a bipolar seesaw model has been documented in ice cores (EPICA Community Members, 2006). The Antarctic warming occurring within the rising phase of northern hemisphere high-latitude summer insolation (Kawamura et al., 2007) has further strengthened the north–south polar climate linkages. In our opinion, this linkage might be acting as two forcing end members for low-latitude climates, with relatively variable influence depending upon the relative separation of a region from the end-member locations. The superposition of effects of monsoons and associated circulation on the influence of global climate appears to have resulted in observed mixed and complex responses in the surface climatology of the EAS.

Eastern Arabian Sea surface hydrographic variability and monsoon climate

The summer monsoon intensity is mainly responsible for high productivity all over the Arabian Sea, due to associated intense upwelling in the western Arabian Sea and lateral advection of nutrient-rich upwelled water (Wyrtki, 1973). On the other hand, intense winter mixing and deepening of the mixed layer in the northern region together increase the productivity during winter monsoons (Madhupratap et al., 1996). These observations are consistent with the coupled physical–biological modeling results for the Indian monsoon system, which demonstrated that intensified monsoons (summer or winter) may be expected to cause cooling of the sea surface and increase in productivity together in most parts of the Arabian Sea (Murtugudde et al., 2007).

Isolating the relative importance of past variability in summer and winter monsoons is not feasible from SST records. SST variability also incorporates the global climate effect along with monsoon-forced surface cooling. Hence, there is a need for another robust proxy, such as salinity, to isolate the relative dominance of summer and winter monsoons during a given climate stage.

It is well known that the Indian summer monsoons are extremely moist, while winter monsoons are extremely dry (Wyrtki, 1973). This contrasting moisture load results in distinct changes in salinity of the northern Indian Ocean during summer and winter monsoons (Slingo, 2002; Webster and Fasullo, 2002). In addition, the BoB is relatively more sensitive to salinity changes as it receives enormous amount of freshwater from Ganges-Brahmaputra river discharge during the summer monsoon. We examine our multi-proxy data essentially in the light of the preceding observation.

The salinity time series shows variation up to 2 psu during the last 100 ka, and the largest gradient occurs between ~18 and ~9 cal ka BP (deglacial period) (Fig. 4). During most of the last glacial cycle (MIS 4 through MIS 2) the EAS has witnessed salinity higher by over 1 psu than the present (~36 psu). This high-salinity feature could be expected only if there existed long-sustained intense winter monsoons and weakened
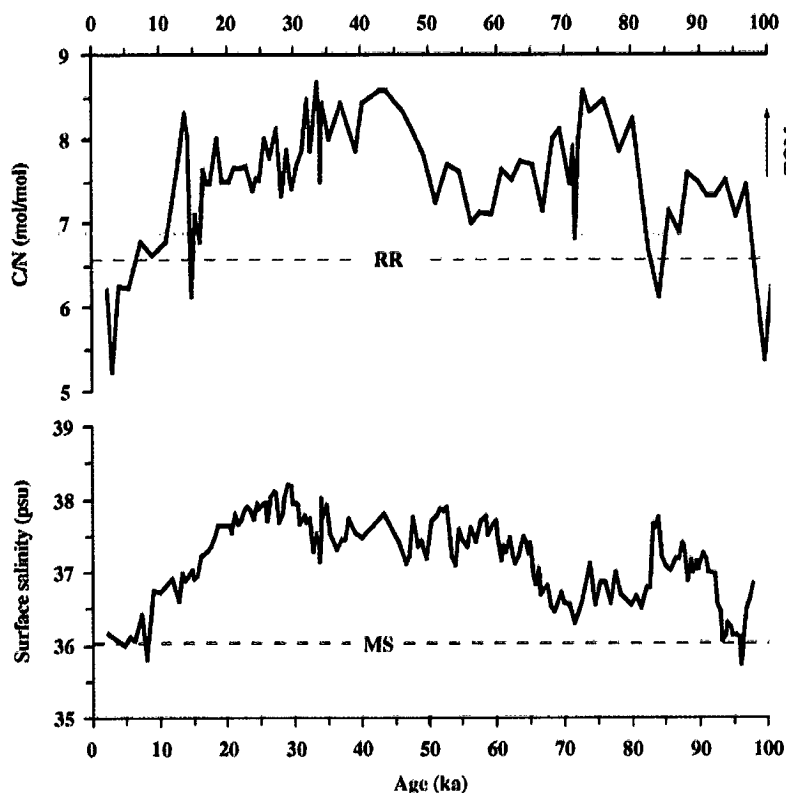
Figure 4. Time series of surface salinity and C/N ratios of organic matter in the studied sediment core. The horizontal broken line on the C/N-panel is the maximum expected Redfield Ratio (RR) for marine organic matter and upward arrow on the right-hand side denotes increasing contribution of terrestrial organic matter (TOM). The broken line on the salinity panel marks the modern surface salinity (MS) in the location of the sediment core (see Fig. 1). C/N data are from Banakar et al. (2005).

summer monsoons. In addition, advection of low-salinity water from BoB into the EAS was reduced during the last glacial period due to intensified winters (Chodankar et al., 2005). These two regional processes appear to have resulted in long-sustained higher salinity in the EAS during most of the last glacial period.

The intensification of winter monsoon can be confirmed by elevated C/N ratios of the sedimentary organic matter in the same sediment core spanning the last glacial cycle (Fig. 4). The Redfield ratio of C/N for pure marine organic matter is ~6.6. The ratios above this are possible only when terrestrial plant biomass or organic matter from exposed shelf region during glacial-lowered sea level having higher C/N ratios (up to 35) (Walsh et al., 1981) are added to the marine sedimentary reservoir.

The preferential fractionation of N during post-depositional diagenesis (Walsh et al., 1981) resulting in temporal variability of present C/N data may be ruled out because the X–Y scatter diagram for C and N in the present sediment core exhibits a tight linear correlation ($R^2 = 0.93$) (Fig. 5). Therefore, the time series of C/N (Fig. 4) is attributed to temporally varied mixing of marine and terrestrial organic matter in the EAS. The calculated proportion of terrestrial organic matter, considering mixing of two end members with C/N 6.6 and 35, is around 10% during the last glacial cycle and nearly absent during the Holocene and last warm period. The increased input of terrestrial organic matter during the cold climate is expected because glacial winter winds (land towards sea: see Fig. 1) are likely to have been stronger than the interglacial winter winds. Distinctly higher salinity during the last glacial cycle associated with increased terrestrial organic matter input and productivity in EAS (Banakar et al., 2005) together suggest that the basin has experienced significant reduction in freshwater flux due to weakened summer monsoons, but it has remained productive due to enhanced winter

upwelling and nutrient supply from surrounding land caused by intense winter winds.

The deglacial warming in the Antarctic atmosphere, monotonic increase of SST, and decrease of salinity in EAS until the commencement of the Holocene (Fig. 3) are consistent with the evolution of Indian summer monsoons, which began to strengthen with global climate warming following the LGM. Within the Holocene, the sea-surface cooling of ~1°C and freshening of ~0.5 psu along with ~0.2‰-lowered $\delta^{18}O_{G.sacculifer}$ (Fig. 3) centered on 8 cal ka BP indicate the strongest summer monsoons of the Holocene. This ~8 cal ka BP event appears to be characteristic of the Holocene monsoon history of the Arabian Sea, as the event has also been
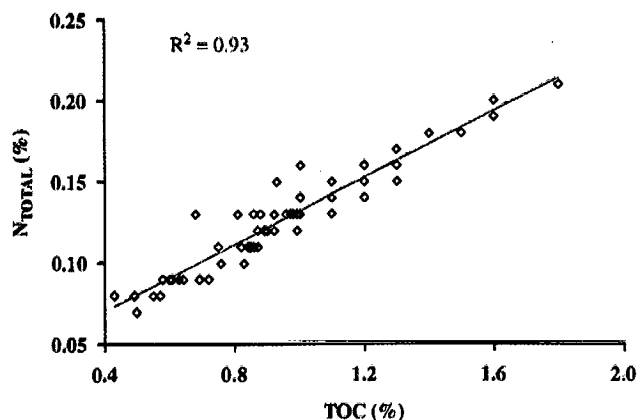

Figure 5. X–Y scatter plot of total organic carbon and organic nitrogen (data from Chodankar, 2004).

reflected in previous high-resolution multi-proxy studies (Overpeck et al., 1996; Dahl and Oppo, 2006).

Conclusions

Past variability of the SST and salinity in the Eastern Arabian Sea appear to have influenced by both global climate and local monsoons. On one hand, the time series of SST exhibits a pattern comparable to likely pattern emerging from a combination of southern and northern high-latitude climates. On the other hand, the time series of salinity and C/N ratios exhibit glacial–interglacial variability.

Sea-surface warming by ~2°C and freshening by ~1 psu concurrently occurring during the deglaciation indicate rapid reorganization of regional monsoons with global climate transition from cold to warm. A synchronous decrease of sea-surface temperature, surface salinity, and $\delta^{18}O_{G.sacculifer}$ at ~8 cal ka BP indicate most intense summer monsoons with the onset of full Holocene conditions in the EAS.

Acknowledgments

References

Anderson, D.M., Prell, W.L., 1993. A 300 ka record of upwelling off Oman during the late Quaternary: evidence of the Asian southwest monsoon. Plaeoceanography 8, 193–208.

Banakar, V.K., Oba, T., Chodankar, A.R., Kuramoto, T., Yamamoto, M., Minagawa, M., 2005. Monsoon related changes in sea surface productivity and water column denitrification in the Eastern Arabian Sea during last glacial cycle. Marine Geology 219, 99–108.

Barker, S., Greaves, M., Elderfield, H., 2003. A study of cleaning procedures used for foraminiferal Mg/Ca paleothermometry. Geochemistry Geophysics Geosystems 4, 8407.

Barker, S., Cacho, I., Benway, H., Tachikawa, K., 2005. Planktonic foraminiferal Mg/Ca as a proxy for past oceanic temperatures: a methodological overview and data compilation for the Last Glacial Maximum. Quaternary Science Reviews 24, 821–834.

Chodankar, A. R., 2004. Late Pleistocene sedimentation history in the Eastern Arabian Sea: Climate-productivity-weathering linkages. Ph.D. Thesis, National Institute of Oceanography-Goa University, pp. 126.

Chodankar, A.R., Banakar, V.K., Oba, T., 2005. Past 100 ky surface salinity gradient response in the Eastern Arabian Sea to the summer monsoon variation recorded by $\delta^{18}O$ of G. sacculifer. Global Planetary Change 47, 135–142.

Clemens, S.C., Prell, W.L., 1990. Late Pleistocene variability of Arabian Sea summer monsoon winds and continental aridity: Eolian records from the lithogenic components of deep-sea sediments. Paleoceanography 5, 109–145.

Dahl, K.A., Oppo, D.W., 2006. Sea surface pattern reconstructions in the Arabian Sea. Paleoceanography 21, PA1014. doi:10.1029/2005PA001162.

Dansgaard, W., Johnsen, S.J., Clausen, H.B., Dahl-Jensen, D., Gundestrup, N.S., Hammer, C.U., Hvidberg, S., Steffensen, J.P., Sveinbjornsdottir, A.E., Jouzel, J., Bond, G., 1993. Evidence for general instability of past climate from a 250 ka ice-core record. Nature 364, 218–220.

Delaney, M.L., Be, A.H.W., Boyle, E.A., 1985. Li, Sr, Mg, Na in foraminiferal calcite shells from laboratory culture, sediment traps and sediment cores. Geochimica et Cosmochimica Acta 49, 1327–1341.

Delaygue, G., Bard, E., Rollion, C., Jouzel, J., Stevenard, M., Duplessy, J.C., Ganssen, G., 2001. Oxygen isotope/salinity relationship in the northern Indian Ocean. Journal of Geophysical Research C106, 4565–4574.

Dekens, P.S., Lea, D.W., Pak, D.K, Spero, H.J., 2002. Core-top calibration of Mg/Ca in tropical foraminifera: refining paleo-temperature estimation. Geochemistry Geophysics Geosystems 3, 1022.

DeVilliers, S., Greaves, M.J., Elderfield, H., 2002. An intensity ratio calibration method for the accurate determination of Mg/Ca and Sr/Ca of marine carbonates by ICP-AES. Geochemistry Geophysics Geosystems 3, 1001.

Duplessy, J.C., 1982. Glacial-interglacial contrasts in the northern Indian Ocean. Nature 295, 494–498.

Eggins, S., De Deckker, P., Marshall, J., 2003. Mg/Ca variation in planktonic foraminifera tests: implication for reconstructing paleo-seawater temperature and habitat migration. Earth and Planetary Science Letters 212, 291–306.

Elderfield, H., Ganssen, G., 2000. Past temperature and $\delta^{18}O$ of surface ocean water inferred from foraminiferal Mg/ca ratios. Nature 405, 442–445.

EPICA Community Members, 2006. One to one coupling of glacial climate variability in Greenland and Antarctica. Nature 444, 195–198.

Epstein, S., Buchsbaum, R., Lowenstam, A., Uray, H.C., 1953. Revised carbonate-water isotopic temperature scale. Bulletin of Geological Society of America 64, 1315–1325.

Goes, J., Prasad, T.G., Helga, R.G., Fasullo, J.T., 2005. Warming of the Eurasian landmass is making Arabian Sea more productive. Science 308, 545–547.

Hong, Y.T., Hong, B., Lin, Q.H., Zhu, Y.X., Shibata, Y., Hirota, M., Uchida, M., Leng, X.T., Jiang, H.B., Xu, H., Wang, H., Yi, L., 2003. Correlation between Indian Ocean summer monsoon and north Atlantic climate during the Holocene. Earth and Planetary Science Letters 211, 371–380.

Kawamura, K., Parrenin, F., Lisiecki, L., Uemura, R., Vimeux, F., Severinghaus, J.F., Hutterli, M.A., Nakazawa, T., Aoki, S., Jouzel, J., Raymo, M.E., Matsumoto, K., Nakata, H., Motoyama, H., Fujita, S., Goto-Azuma, K., Fujii, Y., Watanabe, O., 2007. Northern hemisphere forcing of climate cycles in Antarctica over the past 360, 000 years. Nature 448, 912–916.

Kiefer, T., McCave, I.N., Elderfield, H., 2006. Antarctic control on tropical Indian Ocean sea surface temperature and hydrography. Geophysical Research Letters 33, L24612.

Krishnakumar, K., Rajgopalan, B., Cane, M.A., 1999. On the weakening relationship between the Indian monsoon and ENSO. Science 284, 2156–2159.

Lea, D.W., Mashiotta, T.A., Spero, H.J., 1999. Controls on magnesium and strontium uptake in planktonic foraminifera determined by living culturing. Geochimica et Cosmochimica Acta 63, 2369–2379.

Lea, D.W., Pak, D.K., Spero, H.J., 2000. Climate impact of late Quaternary equatorial Pacific sea surface temperature variation. Science 289, 1719–1724.

Lisiecki, L.E., Raymo, M.E., 2005. A Pliocene–Pliestocene stack of 57 globally distributed benthic d18O records. Paleoceanography 20, PA1003. doi:10.1029/2004PA001071.

Madhupratap, M., Kumar, S.P., Bhattatri, M.A., Kumar, M.D., Raghukumar, S., Nair, K.C., Ramaiah, N., 1996. Mechanism of biological response to winter cooling in the northeastern Arabian Sea. Nature 384, 549–552.

Murtugudde, R., Seager, R., Prasad, T., 2007. Arabian Sea response to monsoon variations. Paleoceanography 22, PA4217.

Overpeck, J., Anderson, D., Trumbore, D., Prell, W., 1996. The southwest Indian Monsoon over the last 18000 years. Climate Dynamics 12, 213–225.

Petit, J.R., Jouzel, J., Raynaud, D., Barkov, N.I., Barnola, J.M., Basile, I., Bender, M., Chappellaz, J., Davis, M., Delaygue, G., Delmotte, M., Kotlyakov, V.M., Legrand, M., Lipenkov, Y.V., Lorius, C., Pepin, L., Ritz, C., Saltzman, E., Steivenard, M., 1999. Climate and atmospheric history of the past 420,000 years from Vostok ice core. Antarctica. Nature 399, 429–436.

Reichart, G.J., Nortier, J., Versteegh, G., Zachariasse, W.J., 2002. In: Clift, P.D., et al. (Ed.), Periodic breakdown of Arabian Sea oxygen minimum zone caused by deep convective mixing: The Tectonic and Climate Evolution of the Arabian Sea Region, Geological Society of London, Special Publication, vol. 195, pp. 407–419.

Rohling, E.J., 2000. Paleosalinity: confidence limits and future applications. Marine Geology 163, 1–11.

Rosenthal, Y., Lohmann, G.P., Lohmann, K.C., Sherell, R.M., 2000. Incorporation and preservation of Mg in Globigerinoides sacculifer: implication for reconstructing the temperature and $^{18}O/^{16}O$ of seawater. Paleoceanography 15, 135–145.

Rostek, F., Ruhland, G., Bassinot, F.C., Muller, P.J., Labeyrie, L.D., Lancelot, Y., Bard, E., 1993. Reconstructing sea surface temperature and salinity using $\delta^{18}O$ and alkenone records. Nature 364, 319–321.

Sagawa, T., Toyoda, K., Oba, T., 2006. Sea surface temperature record off central Japan since the last glacial maximum using planktonic foraminiferal Mg/Ca thermometry. Journal of Quaternary Science 21, 63–73.

Saraswat, R., Nigam, R., Weldeab, S., Mackensen, A., Naidu, P.D., 2005. A first look at past sea surface temperatures in the equatorial Indian Ocean from Mg/Ca in foraminifera. Geophysical Research Letters 32, L24605. doi:10.1029/2005GL024039.

Schulz, H., von Rad, U., Erlenkeuser, H., 1998. Correlation between Arabian Sea and Greenland climate oscillations of past 110000 years. Nature 393, 54–57.

Sirocko, F., Luischner, D., Staubwasser, M., Maley, J., Heusser, L., 1999. High-frequency oscillations of the last 70000 years in the tropical/subtropical and polar climates. Mechanism of global climate change at millennial time scale. Geophysical Monograph, vol. 112. American Geophysical Union, pp. 113–126.

Shackleton, N.J., 2000. The 100, 000 year ice-age cycle identified and found to lag temperature, carbon dioxide and orbital eccentricity. Science 289, 1897–1902.

Shankar, D., Vinayachandran, P., Unnikrishnan, A.S., 2002. The monsoon currents in the north Indian Ocean. Progress in Oceanography 52, 63–120.

Shetye, S.R., Gouveia, A.D., Shenoi, S.S.C., Micheal, G.S., Sundar, D., Almeida, A.M., Santanam, K., 1991. The coastal currents off western India during the northeast monsoon. Deep Sea Research 38, 1517–1529.

Slingo, J., 2002. Monsoons: Overview. Encyclopedia of atmospheric Sciences, v.3. Academic Press, pp. 1365–1370.

Sonzogni, C., Bard, E., Rostek, F., 1998. Tropical sea surface temperatures during the last glacial period: a view based on alkenones in Indian Ocean sediment. Quaternary Science Reviews 17, 1185–1201.

Walsh, J.J., Premuzic, E.T., Whitledge, T.E., 1981. Fate of nutrient enrichment on continental shelves as indicated by C/N content of bottom sediments. In: Nihoul, J. C.J. (Ed.), Ecohydrodynamics. Elsevier, pp. 13–49.

Webster, P.J., Fasullo, J., 2002. Monsoons—Dynamic theory. Encyclopedia of atmospheric Sciences. Academic Press, pp. 1370–1385. v. 3.

www.nodc.noaa.gov/WOA05: Levitus and Boyer's Annual salinity and temperature online maps.

Weninger, B., Joris, O., Danzeglocke, U., 2005. Cologne radiocarbon calibration and palaeoclimate research package-online: www.calpal-online.de.

Wyrtki, K., 1973. Physical oceanography of the Indian Ocean. In: Zeitzschel, B. (Ed.), Biology of the Indian Ocean. Springer, pp. 18–36.

Zielinski, G.A., Mayewski, P.A., Meeker, L.D., Whitlow, S., Twickler, M.S., 1996. Potential atmospheric impact of the mega-eruption 71000 y ago. Geophysical Research Letters 23, 837–840.

Paired Measurements of Foraminiferal $\delta^{18}O$ and Mg/Ca Ratios of Indian Monsoons Reconstructed from Holocene to Last Glacial Record

Badanal MAHESH[1, *], Virupaxa BANAKAR[1] and George BURR[2]

1 *National Institute of Oceanography (CSIR), Dona Paula, Goa 403 004, India*

2 *National Science Foundation-Arizona Accelerator Mass Spectrometer Facility, 1118 East 4th Street, Tucson, AZ85721-0081, USA*

Abstract: The effect of seasonally reversing monsoons in the northern Indian Ocean is to impart significant changes in surface salinity (SS). Here, we report SS changes during the last 32 kyr in the Lakshadweep Sea (southeastern Arabian Sea) estimated from paired measurements of $\delta^{18}O$ and sea surface temperature (SST) using *Globigerinoides sacculifer*, an upper mixed layer dwelling foraminifera. The heaviest $\delta^{18}O_{G.sacculifer}$ (−0.07±0.08‰) is recorded between 23 and 15 ka, which could be defined as the last glacial maximum (LGM). The $\delta^{18}O_{G.sacculifer}$ shift between the LGM and Holocene is 2.07‰. The SST shows an overall warming of 2C from the LGM to Holocene (28°C to 30°C). However, coldest SSTs are observed prior to LGM, i.e., ~27 ka. The SS was higher (~38 psu) throughout most of the recorded last glacial period (32.5–15 ka). This high salinity together with generally lower SSTs suggests a period of sustained weaker summer or stronger winter monsoons. The deglacial warming is associated with rapid reorganization of monsoons and is reflected in decreased salinity to a modern level of ~ 36.5 psu, within a period of ~5 kyr. This indicates intensification of summer monsoons during cold to warm climate transition.

Key words: paleoclimate, oxygen isotopes, Mg/Ca thermometry, monsoon variability, Arabian Sea

1 Introduction

Semiannually reversing monsoon winds over the Arabian Sea (AS) modulate sea surface temperature (SST), surface salinity (SS) and productivity in space and time (Wyrtki, 1973). Modeling results have shown that an increase in monsoon wind intensity, whether summer or winter, induces surface cooling along with increased productivity in the AS (Murtugudde et al., 2007). The SS structure in the Eastern AS (EAS) is largely dictated by the presence of low-salinity tongue extending up to 15°C latitude (Fig. 1). The summer monsoons during interglacial periods were stronger than the glacial periods during which the winter monsoons were probably overwhelming (Duplessy, 1982; Prell and Van Campo, 1986; Clemens and Prell, 1990; Anderson and Prell, 1993; Rostek et al., 1993; Emeis et al., 1995; Reichart et al., 1998; Banakar et al., 2005). The robust proxy to monitor monsoon intensity could be the variation in SS as it instantly responds to changes in evaporation-precipitation. The SS can be reconstructed from the $\delta^{18}O$ of seawater. The SST is an

important component to be corrected while estimating $\delta^{18}O$ of seawater from foraminiferal calcite. Reliable SSTs can be obtained using Mg/Ca ratios in planktonic foraminifera (Bijma et al., 1990; Numberg et al., 1996; Bemis et al., 1998; Elderfield and Ganssen, 2000). Only few SST estimates from the Mg/Ca method are available for the AS (Dahl and Oppo, 2006; Saher et al., 2007; Anand et al., 2008). In this paper we report the past-SST and -SS variations in the southeastern AS (Lakshadweep Sea) using *G. sacculifer* picked from a sediment core and discuss their implication with respect to monsoon variability.

2 Materials and Methods

An upper 150 cm section of a 552 cm long sediment core (SK129-CR05) retrieved on board ORV *Sagar Kanya* at 9° 21' N; 71° 59' E (Lakshadweep Sea: off Kochi, India) from a water depth of 2300 m (Fig. 1) is used for the present study. The sediment core was sub-sampled at 2-cm intervals except for the top peneliquid section, which was 4 cm thick. The calendar ages for the core are based on 10 AMS-^{14}C dates measured at the National Science
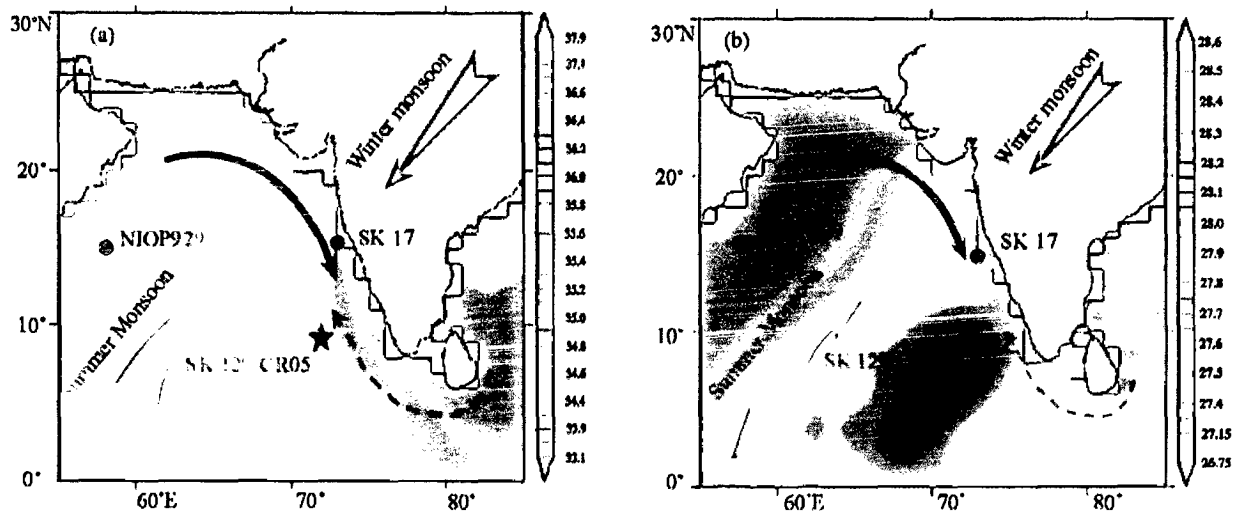
* Corresponding author. E-mail: mahe687@gmail.com

Fig. 1. SK129/CR05 sediment core location (star), shown on annual sea surface salinity (a) and surface temperature (b) maps of the Arabian Sea (AS) (www.nodc.noaa.gov).

Note the maximum SST region in which the present core lies. The northwestern AS shows the lowest sea surface temperature (SST) (blue color code), while higher SSTs (red color code) are observed over the southwestern AS. Presence of low-salinity tongue along the west coast of India is evident by isohaline bordering the blue color region. The shaded block-arrows indicate modern reversing monsoon winds. Solid (broken) arrow indicates surface circulation during summer (winter) monsoons (Shankar et al 2002). The numbered filled circles are the locations of other sediment cores studied for Mg/Ca SST reconstructions (SK17 [Anand et al 2008]; NIOP929 [Saher et al 2007]).

Foundation-Accelerator Mass Spectrometer facility, University of Arizona, USA. The radiocarbon dates were corrected for local reservoir age (600 years) (http://intcal.qub.ac.uk) and converted to calendar ages using the CalPal2007_HULU calibration (Danzeglocke et al., 2007). The last dated section (149–151 cm) has yielded an age of 32564±86 cal y BP. The age of the core-top section (0–4 cm) is 3048±67 cal y BP (Fig. 2).

Around one hundred *G. sacculifer* tests (without terminal sac, size: 250–355 µm) from each section were handpicked under a binocular microscope. The tests were broke-open by gently pressing between two glass plates and homogenized with a fine brush. One third of the aliquot was used for oxygen isotope analysis and the remaining two thirds was subjected to cleaning required before Mg/Ca measurement. We have selected this particular species since the *G. sacculifer* is not only less susceptible to dissolution as compared to other planktonic species (Delaney et al., 1985; Dekens et al., 2002), but also the inter-chamber distribution of Mg/Ca is nearly uniform (Eggins et al., 2003). The SSTs were estimated using Dekens et al. (2002) *G.sacculifer*$_{TROPICAL PACIFIC}$ calibration (Mg/Ca = 0.37exp 0.09[*T*–0.36 (core depth in km) –2°C]). This calibration is favored because the ocean-atmosphere coupled processes over the northern Indian Ocean are similar to that of the western tropical Pacific warm-pool (Webster and Fasullo, 2002). The Mg/Ca analyses were
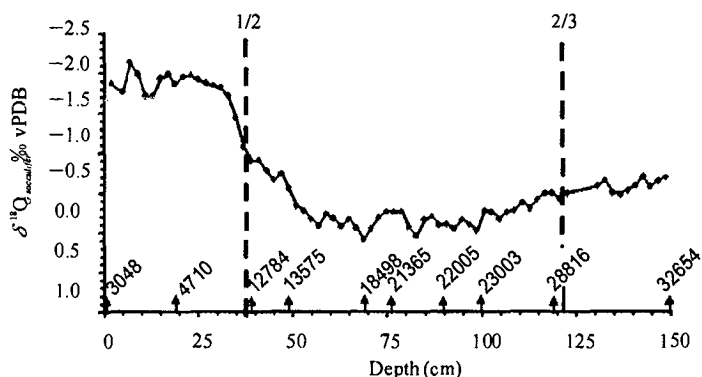

Fig. 2. The $\delta^{18}O_{G.sacculifer}$ variation plotted against core depth (cm).

The upward triangles along the depth axis are the radiocarbon dated sections shown along with their calibrated calendar ages. The ages for remaining sections of the sediment core were obtained by calculating the sedimentation rates between two adjacent ^{14}C dated sections. The broken vertical lines denote the marine oxygen isotope stage (MIS) boundaries.

done at the inductively coupled plasma-optical emission spectrometer ICP-OES) laboratory of the National Institute of Oceanography (Goa), India. The oxygen isotope measurements were done at the Godwin Laboratory for Paleoclimate Research, University of Cambridge, UK. The measured $^{18}O/^{16}O$ ratios are expressed as $\delta^{18}O$ with reference to Vienna Pee Dee Belemnite (PDB). The precision of the $\delta^{18}O$ measurements was ±0.08‰. Previously published organic-carbon and -nitrogen data for the same sediment core (Pattan et al., 2003) were used to assess the monsoon-productivity relationship in the study region.

The cleaning steps for Mg/Ca analysis were performed following the method described by Barker et al. (2003). In

brief, the stained and oxide-coated calcite fragments, visible clay lumps, and mineral grains were physically separated from the crushed aliquot and discarded. The clean fragments were washed five times with deionized water followed by methanol to remove clays. Organic coating was removed by treating the fragments with a buffered H_2O_2. The pre-dissolution Mg-polishing was done using 0.001 M HNO_3. Before the dissolution in 1.5 mL of 0.75 M HNO_3, the fragments were examined under the microscope to ensure that only the clean calcite was taken for dissolution. As the Mn-coated and stained fragments were removed initially, the oxide removal step was not incorporated. Finally the solution was centrifuged at ~10 000 rpm (~3354 g) in order to eliminate even the faint possibility of contamination by sub-micron (very fine) clay suspension.

All reagents used were of supra-pure quality. The solutions were analyzed on a Perkin-Elmer Optima 2000 DV ICP-OES calibrated with five multi-element calibration standards. The Mg/Ca ratios were obtained following the intensity-ratio calibration techniques described by DeVilliers et al. (2002). A quality control (QC) solution of Mg/Ca (=5.144 mmol/mol) was analyzed after every six samples. The analytical error for Mg/Ca was within ±0.6%. The long-term average of QC (n=67) measured during the analytical period yielded a mean of 5.111±0.097 mmol/mol. The error on long term average of QC is 1.9%. The Fe, Mn and Al were also measured to monitor the contamination. The scatter plots of Fe/Ca, Al/Ca and Mn/Ca (mmol/mmol) vs. Mg/Ca (mmol/mol) yielded insignificant correlations (R^2= 0.011; 0.121 and 0.178) suggesting that the measured Mg/Ca ratios were free from contamination.

Local SS was estimated from the residual $\delta^{18}O_{seawater}$. The residual $\delta^{18}O_{seawater}$ was calculated from the $\delta^{18}O_G$. $_{sacculifer}$ using Epstein et al. (1953) equation after subtracting the contribution from global ice volume (Shackleton, 2000) and measured SST. The residual $\delta^{18}O_{seawater}$ was translated into salinity using Dahl and Oppo (2006) empirical equation. However, Rohling et al. (2000) have demonstrated that salinity estimation from seawater $\delta^{18}O$ is less reliable than $\delta^{18}O_{seawater}$ itself. Therefore, we place more emphasis on estimated $\delta^{18}O_{seawater}$ than on the estimated salinity. The error on the salinity estimate is ±0.2 psu, hence we discuss only those SS variations that are above this limit.
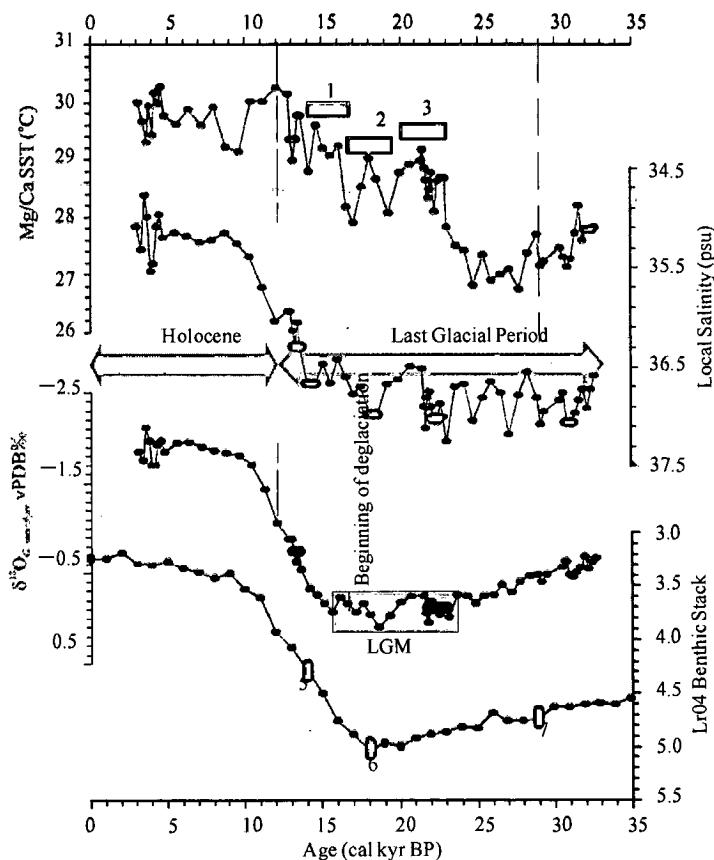

Fig. 3. Composite plot of oxygen-isotope, sea surface temperature (SST) (Red) and surface salinity (SS: blue) variations recorded in SK129/CR05 compared with LR04 benthic-$\delta^{18}O$ record (Lisiecki and Raymo, 2005). Vertical broken lines are the MIS 1/2 and 2/3 boundaries. Last glacial maximum (LGM) (shaded box) is the presently defined coldest event depicted by the heaviest $\delta^{18}O_{G.sacculifer}$ variation. Only latest part of the MIS-3 is covered by the radiocarbon dated interval. The shaded boxes 1 to 3 in the SST panel represent three warming events within the LGM. The numbered (4–6) blue color filled squares on LR04 benthic record indicate MIS boundaries: 4 = MIS1/MIS2, 5 = Beginning of deglaciation; 6 = MIS2/MIS3.

3 Results and Discussion

Based on the depth variation of $\delta^{18}O_{G.sacculifer}$, the beginning of Holocene is recorded at 37 cm depth dating to 12 ka. The beginning of deglaciation occurs at a depth of 57 cm (~16 ka). The Marine Isotope Stage (MIS) 3/2 boundary is evident at 121 cm depth dating to 29 ka (Fig. 2). The LGM-Holocene $\delta^{18}O_{G.sacculifer}$ difference is 2.07‰ This $\delta^{18}O$ gradient incorporates 1.2‰ changes due to expanded global ice sheets during the glacial maximum and the remainder of 0.87‰ should therefore indicate changes in the local SS and SST. Conventionally, the recent-most heaviest $\delta^{18}O_{G.sacculifer}$ event has been considered as the LGM. Instead, we have defined the LGM as a period recording the heaviest $\delta^{18}O_{G.sacculifer}$ (−0.07‰) within the measurement precision band of ±0.08‰ that covers a time-span of 23–15 ka. A similar observation has been made by Banakar et al. (2010) in another sediment core from the EAS. The $\delta^{18}O_{G.sacculifer}$ transition from LGM to Holocene occurs as a rapid

negative excursion beginning at 16 ka, leading into Holocene-minimum at 12 ka. The timings of LGM/Holocene and MIS-3/2 boundaries and the beginning of deglaciation are nearly consistent with the LR04 benthic $\delta^{18}O$ (Lisiecki and Raymo, 2005).

The overall Mg/Ca varies between 3.1 and 4.5 mmol/mol, which translate into SST change of 27°C to 30°C. The SST obtained for core-top section (3.05 ka) is 30°C (Fig. 3) and is comparable to the modern SST at the core location, which falls in the equatorial warm-pool (Fig. 1: http://www.nodc.noaa.gov/WOA01). The warmest average SST (~30°C) is recorded during most of the Holocene and the colder SST (~28°C) during the LGM and the coldest (~27°C) during the late MIS-3 and early MIS-2 (32–24 ka). The observed SST increase of 2°C from LGM to Holocene is comparable with previously published SST gradients of 2°C–3°C in the AS (Rostek et al., 1993; Saraswat et al., 2005; Banakar et al., 2010).

The time-series of SST exhibits step-increase from the coldest conditions (27°C) to attain warmest Holocene conditions (~30°C) at ~12 ka. The LGM SSTs show a fluctuation of 1°C around an average of ~28°C (Fig. 3). Within the warm Holocene, an event of SST lowering of ~1°C is recorded between 8.5 and 9.5 ka (Fig. 3) and is closely comparable with previous observation in the EAS (Banakar et al., 2010). This SST cooling within the Holocene appears to be a regional feature occurring across the AS, which has been interpreted as the surface cooling resulting from intensified monsoons (Overpeck et al., 1996; Dahl and Oppo, 2006).

There are three distinct warming events recorded within the LGM climate at ~21, ~18 and ~16 ka, which exhibit ~1° C elevated SSTs above the average LGM SST of ~28°C (Fig. 3). These warming events are similar to the warming events observed in western AS (WAS; Saher et al., 2007) though with some timing offsets. Intermittent weakening of winter winds, reduced upwelling in WAS, and inflow of warm water of South Equatorial origin have been invoked as the cause for these SST warming events (Saher et al., 2007). The winters during glacial periods are expected to be more intense and prolonged than during the interglacial times. The winter monsoon winds have profound influence on the SSTs of the AS under glacial conditions (Duplessy, 1982; Fontugne and Duplessy, 1986) and hence increased SSTs during the LGM period at the outset might suggest weakening of glacial winters. However, the carbon/nitrogen (C/N) ratios (Fig. 4) do not clearly reflect any
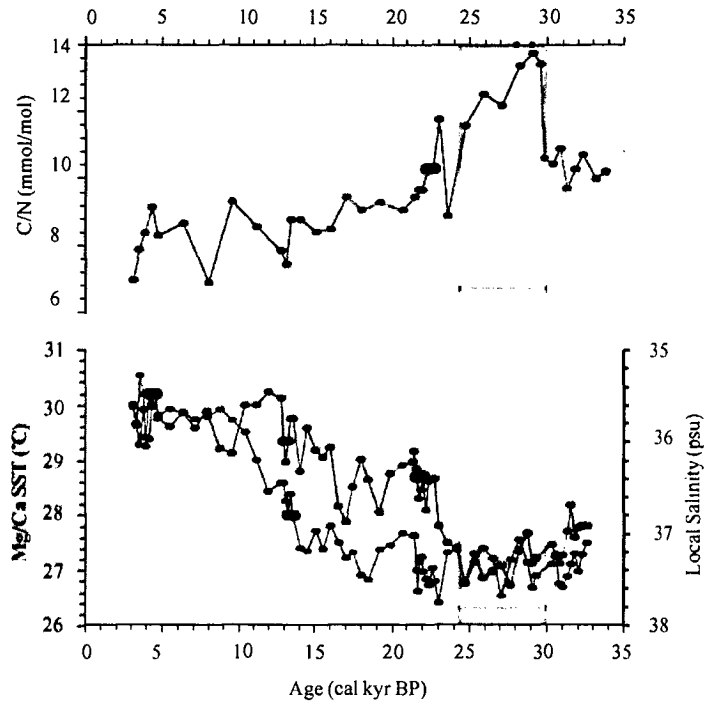

Fig. 4. Time-series of sea surface temperature (SST) (red), salinity (blue) and C/N ratios of sedimentary organic matter (black) in the studied sediment core.

The C/N data are from Pattan et al. (2003). The shaded region indicates period of upwelling (high productivity) and intensified surface cooling (see text for details).
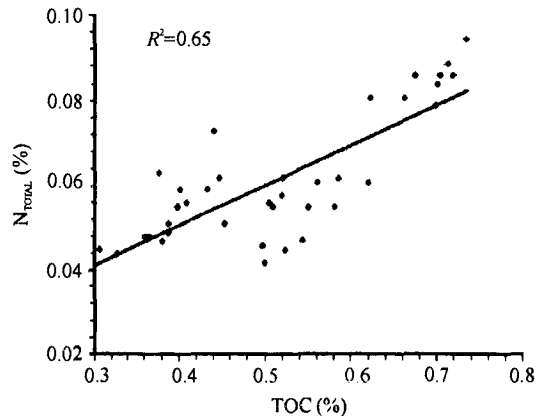

Fig. 5. Scatter plot of total organic carbon vs. nitrogen.

change expected during the period of weakened winter winds. Therefore, these warm-SST events within the LGM warrant detailed explanation that is presented in the later part of the discussion.

Though the LGM SSTs were colder by ~1.5°C as compared to Holocene average SST, the coldest SSTs (~27.5°C) are observed at 32–25 ka, i.e., prior to LGM. The lowest SSTs prior to LGM (late MIS 3 and early MIS 2) might have been the result of major cooling in response to most intense winter winds. A recent study of Clark et al. (2009) has show that the growth of global ice sheets to their maximum has occurred between ~33 and 26.5 ka and
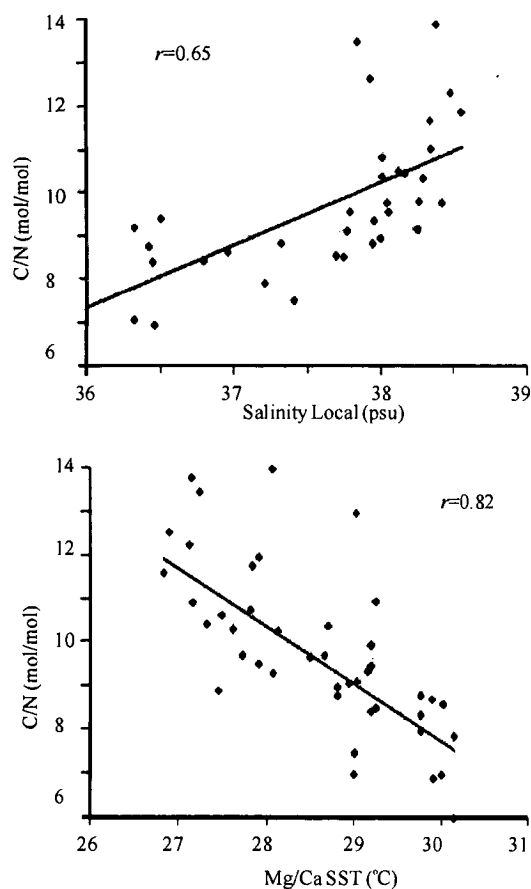
Fig. 6. Scatter plots of C/N vs. sea surface temperature (SST) and surface salinity (SS).

sustained at their maximum growth until ~20 ka. That is, the time period between 26.5 and 20 ka appears to be the actual global glacial maximum. The coldest SSTs observed during 32 to 25 ka in the present record may indicate influence of global climate cooling. However, such cooling appears unlikely in the present case because winter winds should have been most intense leading to increased basin-wide evaporation resulting in increased SS. On the contrary, the SS does not show any significant increase during 33–20 ka and remains nearly uniform around 37 psu until the beginning of deglaciation (Fig. 3). This observation suggests that the observed coldest SSTs were probably the result of intense upwelling in the EAS. This interpretation could be supported by an increased flux of biogenic-calcite and -opal during late MIS 3 recorded in the same sediment core (Pattan et al., 2003). The marginal fluctuations in SS prior to LGM may indicate intermittently varied upwelling primarily from the upper thermocline that consists mainly of high salinity water originated in northern AS (Prasanna Kumar and Prasad, 1999). The role of low-salinity water inflow from the Bay of Bengal dictating observed SS fluctuations may be ruled out during this time

as it was significantly reduced during the last glacial period (Chodankar et al., 2005).

The C/N ratios are ~8 throughout the Holocene and reach values up to 14 during the late MIS 3 (Pattan et al., 2003), which also records minimum SST. The Redfield ratio of C/N in marine organic matter is ~7 and >20 for terrestrial organic matter (Meyers, 1994). The diagenetic alteration of organic matter may also cause a variation in C/N ratios. However, the strong positive correlation between the C and N (r=0.81; n=39, Fig. 5) rules out such alteration possibility. Hence, the higher C/N ratios during late MIS 3 must have been caused by increased abundance of terrestrial organic matter in the sediment. From the X-Y plot of SST and SS against the C/N ratios (Fig. 6), it is observed that higher SSTs and lower SS correspond to lower C/N ratios and vice-versa. This in turn suggests that the relative strength of monsoon winds controls the variation of sedimentary C/N ratios in the EAS. The elevated C/N ratios during the glacial period are expected, as the glacial winter winds (land towards sea) might have been intense resulting in increased transfer of terrestrial organic matter in to the EAS (Banakar et al., 2005). An inverse relationship between SST and C/N ratios confirm that the most intense winter winds prevailed prior to LGM during which an upwelling event is also evident. The coherent association of C/N ratios with SSTs (r=0.83) further strengthen the interpretation that stronger winter winds prevailed during the late MIS 3. The lower C/N ratios associated with higher SSTs of the Holocene indicate the dominance of summer monsoons over winter monsoons leading to reduction in high C/N terrestrial organic matter in the sediment.

The SS estimated for the core-top section is 35.1 psu, which is similar to the modern SS at the core location (Fig. 1). The average Holocene SS is ~35.2 psu, while it is 37.2 psu for the last glacial period. The SS time series shows marginal variation of ±0.2 psu during the Holocene. The overall glacial-interglacial variability in SS is ~2 psu, which is comparable with the previously observed SS gradient in the EAS (Banakar et al., 2010). The SS reaches the Holocene plateau at ~ 10 ka, i.e., 3 ka later than the SST maximum. The decreasing trend of SS started at ~18 ka, which is consistent with the beginning of deglaciation in the LR04 Benthic record of Lisiecki and Raymo (2005). Also, the deglaciation and the Holocene plateau in SS trends follow the LR04 records.

Based on the observations made from the SS time-series (Fig. 3), it can be inferred that the E-P in the EAS has varied marginally during the Holocene. Within the LGM, the SS time-series shows distinct increase in salinity by about 0.2 to 0.6 psu occurring concurrently with the SST warming events of 21, 18 and 16 ka (Fig. 3). The coupled increases
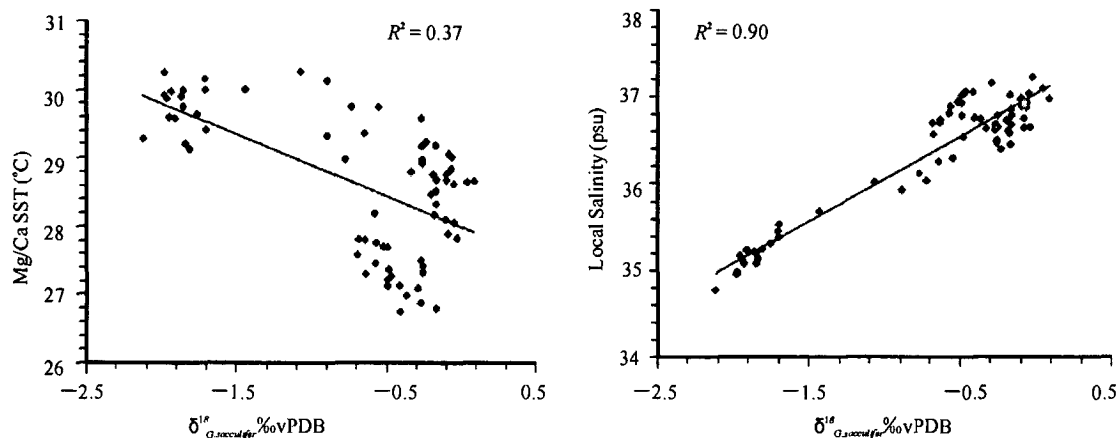
Fig. 7. Scatter plots of SST and SS vs. $\delta^{18}O_{G.sacculifer}$.

of SST and SS during the above events suggest distinctly different E-P balance than generally expected. In the modern or Holocene climate set-up the increased SSTs are associated with intensified summer monsoons, i.e., increased freshwater flux resulting in basin-wide decrease in the SS. We examine this set-up in light of a previously suggested mechanism of warm-SST events within the cold LGM (Saher et al., 2007). The advection of south equatorial warm water into the EAS can warm the SST, but cannot enhance the salinity because it is inherently less-saline water. If the warm-SST events were the result of intermittent weakening of the winter monsoons then also the salinity would decrease because of reduced evaporation. Interestingly, a recent study has identified regional sub-surface temperature inversion in the present study area (Lakshadweep Sea), where the sub-surface (~40 m) is warmer than the surface water (temperature inversion) and also saltier (see Nisha et al., 2009). Assuming an existence of this sub-surface temperature and salinity inversion during the LGM, the coupled increases in SST and SS in the Lakshadweep Sea may suggest vigorous mixing of sub-surface water with the surface layer. Durand et al. (2004) estimated that the heat trapped in the subsurface inversion in the Lakshadweep Sea could result in regional SST warming of over 1°C due to mixing. Therefore, the observed coupled increases in SST and SS at 21, 18 and 16 ka may indicate relatively intensified summer winds (intensified sub-surface mixing) within the LGM.

We examined the relationship of SST and SS with $\delta^{18}O_{G.sacculifer}$ (Fig. 7). The SS association is found to be highly coherent and significant with $\delta^{18}O_{G.sacculifer}$ (r=0.94; n=73), while SST exhibits relatively less coherency (r=0.60; n=73). This observation suggests that the SST variability was mostly due to changes in local processes. The general trend of the SS time-series overlapping the

$\delta^{18}O_{G.\ sacculifer}$ time-series as well as the LR04 benthic oxygen isotope records indicate a close relationship between the evolution of SS and global ice-volume. However, the influences of local processes are also evident, which are reflected as short-term distinct increases in SS during the glacial period as described above.

4 Conclusions

The SST time-series for Lakshadweep Sea (southeastern Arabian Sea) does not exhibit distinct glacial-interglacial variability, suggesting dominance of local processes. The coupled increase in SST and SS within the LGM appears to be the result of mixing of warmer and saltier sub-surface water. Lowest SSTs prior to LGM likely indicate an intense upwelling. The SST cooling at ~9 ka within the warm Holocene is consistent with previous observation and indicates intensified monsoon winds. Our reconstructions indicate that the latest Holocene (3–4.7 ka) has witnessed rapid fluctuation in the summer monsoon intensity as evident in concomitant cooling of SST, lowering of SS, and decreasing $\delta^{18}O_{G.\ sacculifer}$.

References

Anand, P., Kroon, D., Singh, A.D., Ganeshram, R.S., Ganssen, G., and Elderfield, H., 2008. Coupled sea surface temperature-seawater $\delta^{18}O$ reconstructions in the Arabian Sea at the millennial scale for the last 35 ka. *Paleoceanography*, 23: PA4207, doi: 10.1029/2007PA001564.

Anderson, M.D., and Prell, L.W., 1993. A 300 ka record of upwelling off Oman during the Late Quaternary: Evidence of the Asian Southwest monsoon. *Paleoceanography*, 8: 193–208.

Banakar, V.K., Mahesh, B.S., and Burr, G., 2010. Climatology of the Eastern Arabian Sea during the last glacial cycle reconstructed from paired measurement of foraminiferal $\delta^{18}O$ and Mg/Ca. *Quaternary Research*, 73: 535–540.

Banakar, V.K., Oba, T., Chodankar, A.R., Kuramoto, K., Yamamoto, M., and Minagawa, M., 2005. Monsoon related changes in sea surface productivity and water column denitrification in the Eastern Arabian Sea during last glacial cycle. *Marine Geology*, 219: 99–108.

Barker, S., Greaves, M., and Elderfield, H., 2003. A study of cleaning procedure used for foraminiferal Mg/Ca paleothermometry. *Geochemistry Geophysics Geosystems*, 4: doi: 10.1029/2003GC000559.

Bijma, J., Faber, Jr W.W., and Hemleben, C., 1990. Temperature and salinity limits for growth and survival of some planktonic foraminifers in laboratory cultures. *Journal Foraminiferal Research*, 20: 95–116.

Bemis, B.E., Spero, H.J., Bijma, J., and Lea, D.W., 1998. Re-evaluation of the oxygen isotopic composition of planktonic foraminifer: Experimental results and revised paleotemperature equations. *Paleoceanography*, 13: 150–160.

Chodankar, A.R., Banakar, V.K., and Oba, T., 2005. Past 100 ka surface salinity gradient response in the Eastern Arabian Sea to the summer monsoon variation recorded by $\delta^{18}O$ of *G. sacculifer*. *Global Planetary Change*, 47: 135–142.

Clark, P. U., Dyke, A.S., Shakun, J. D., Carlson, A.E., Clark, J., Wohlfarth, B., Mitrovica, J., Hostetler, S.W., and McCabe, A. M., 2009. The Last Glacial Maximum. *Science*, 325: 710–714.

Clemens, S.C., and Prell, W.L., 1990. Late Pleistocene Variability of Arabian Sea Summer Monsoon Winds and Continental Aridity: Eolian Records from the Lithogenic Component of Deep-Sea Sediments. *Paleoceanography*, 5: 109–145.

Dahl, A,K., and Oppo, D.W., 2006. Sea surface temperature pattern reconstructions in the Arabian Sea. *Paleoceanography*, 21: PA1014, doi: 10.1029/2005PA001162.

Danzeglocke, U., Jöis, O., and Weninger, B., 2008. CalPal-2007online. http://www.calpal-online.de/, 2008-10-05.

DeVilliers, S., Greaves, M., and Elderfield, H., 2002. An intensity ration calibration method for the accurate determination of Mg/Ca and Sr/Ca of marine carbonates by ICP-AES. *Geochemistry Geophysics Geosystems*, 3: 2001GC000169.

Dekens, P.S., Lea, D.W., Pak, D.K., and Spero, H.J., 2002. Core-top calibration of Mg/Ca in tropical foraminifera: Refining paleo-temperature estimation. *Geochemistry Geophysics Geosystems*, 3: 1022, doi: 10.1029/2001gC000200.

Delaney, M.S., Be, A.W., and Boyle, E.A. 1985. Li, Sr, Mg and Na in foraminiferal calcite shells from laboratory culture, sediment

traps and sediment cores. *Geochimca et Cosmochimica Acta*, 49: 1327–1341.

Duplessy, J.C., 1982. Glacial to interglacial contrast in the northern Indian Ocean. *Nature*, 295: 464–498.

Durand, F., Shetye, S.R., Vialard, J., Shankar, D., Shenoi, S.S.C., Ethe, C., and Madec, G., 2004. Impact of temperature inversions on SST evolution in the South Eastern Arabian Sea during the pre - summer monsoon season. *Geophysical Research Letters*, 31: L01305, doi: 10.1029/2003GL018906.

Eggins, S., Deckker, P., and Marshall, J., 2003. Mg/Ca variation in planktonic foraminifera tests: Implications for reconstructing palaeo-seawater temperature and habitat migration. *Earth Planetary Science Letters*, 212: 291–306.

Elderfield, H., and Ganssen, G., 2000. Past temperature and salinity using $\delta^{18}O$ of surface ocean water inferred from foraminiferal Mg/Ca ratios. *Nature*, 405: 442–445.

Emeis, K.C., Anderson, D.M., Doose, H., and Schulz, D., 1995. Sea-Surface Temperatures and the History of Monsoon Upwelling in the Northwest Arabian Sea during the Last 500,000 Years. *Quaternary Research*, 43: 355–361.

Epstein, S., Buchsbaum, R., Lowenstam, A., and Urey, H.C., 1953. Revised carbonate-water isotopic temperature scale. *Bulletin of Geological Society of America*, 64: 1315–1325.

Fontugne, M.R., and Duplessy, J.C., 1986. Variations of the monsoon regime during the upper Quaternary: Evidence from carbon isotopic record of organic matter in north Indian Ocean sediment cores. *Palaeogeography Palaeoclimatology Palaeoecology*, 56: 69–88.

Lisiecki, L.E., and Raymo, M.E., 2005. A Pliocene-Pliestocene stack of 57 globally distributed benthic $\delta^{18}O$ records. *Paleoceanography*, 20: PA1003: doi: 10.1029/2004PA001071.

Meyers, P.A., 1994. Preservation of elemental and isotopic identification of sedimentary organic matter. *Chemical Geology*, 144: 213–302.

Murtugudde, R., Seager, R., and Thoppil, P., 2007. Arabian Sea response to monsoon variations. *Paleoceanography*, 22: doi: 10.1029/2007PA001467.

Nisha, K., Suryachandra, A.R., Gopalakrishna, V.V., Rao, R.R., Girishkumar, M.S., Pankajakshan, T., Ravichandran, M., Rajesh, S., Girish, K., Johnson, Z., Anuradha, M., Gavaskar, S. S.M., Suneel, V., Krishna, S.M., 2009. Reduced Near-Surface Thermal Inversions in 2005–06 in the Southeastern Arabian Sea (Lakshadweep Sea). *Journal of Physical Oceanography*, 39: 1184–1199.

Nurnberg, D., Bijma, J., and Hemleben, C., 1996. Assessing the reliability of magnesium in foraminiferal calcite as a proxy for water mass temperatures. *Geochimica et Cosmochimica Acta*, 60: 803–814.

Overpeck, J.T., Anderson, D.M., Trumbore, S., and Prell, W.L., 1996. The southwest Indian monsoon over the last 18,000 years. *Climate Dynamics*, 12: 213–225.

Pattan, J.N., Masuzawa, T., Naidu, P.D., Parthiban, G., and Yamamoto, M., 2003. Productivity fluctuations in the southeastern Arabian Sea during the last 140 ka. *Paleogeography Paleoclimatology Paleoecology*, 193: 575–590.

Prasanna Kumar, S., and Prasad, T.G., 1999. Formation and spreading of Arabian Sea high salinity water mass. *Journal of Geophysical Research*, 104: 1455–1461.

Prell, W.L., and Campo, E.V., 1986. Coherent response of Arabian Sea upwelling and pollen transport of late Quaternary

monsoonal winds. *Nature*, 323: 526–528.

Reichart, G.J., Lournes, L.J., and Zachariasse, W.J., 1998. Temporal variability in the northern Arabian Sea Oxygen Minimum Zone (OMZ) during the last 225,000 years. *Paleoceanography*, 13: 607–621.

Rohling, E.J., 2000. Paleosalinity: confidence limits and future applications. *Marine Geology*, 163: 1–11.

Rostek, F., Ruhland, G., Bassinot, F.C., Muller, P.J., Labeyrie, L. D., Lancelot, Y., and Bard, E., 1993. Reconstructing sea surface temperature and salinity using $\delta^{18}O$ and alkenone records. *Nature*, 364: 319–321.

Saraswat, R., Nigam, R., Weldeab, S., Mackensen, A., and Naidu, P.D., 2005. A first look at past sea surface temperatures in the equatorial Indian Ocean from Mg/Ca in foraminifera. *Geophysical Research Letters*, 32: doi: 10.1029/2005GL024039.

Saher, M.H., Jung, S.J.A., Elderfield, H., Greaves, M., and Kroon, D., 2007. Sea surface temperatures of the western Arabian Sea during the last deglaciation. *Paleoceanography*, 22: PA2208, doi: 10.1029/2006PA001292.

Shackleton, N.J., 2000. The 100000 year ice-age cycle identified and found to lag temperature, carbon dioxide and orbital eccentricity. *Science*, 289: 1897–1902.

Shankar, D., Vinayachandran, P.N., and Unnikrishnan, A.S., 2002. The monsoon currents in the north Indian Ocean. *Progressive Oceanography*, 52: 63–120.

Webster, P.J., and Fasullo, J., 2002. *Monsoons-Dynamic theory*. In: Encyclopedia of atmospheric Sciences. Academic Press, 3: 1370–1385.

Wyrtki, K., 1973. Physical oceanography of the Indian Ocean. In: Zeitzschel, B., (Ed.), *The Biology of the Indian Ocean*, Berlin: Springer-Verlag, 18–36.

www.nodc.noaa.gov/WOA01: Levitus and Boyer's Annual salinity and temperature online maps.